# Assessment and Detection of Landslide-Generated Tsunamis through Numerical Modelling and Instrumental Data

By

Fatemeh Nemati

B.Sc., Amirkabir University of Technology, 2009
M.Sc., Amirkabir University of Technology, 2013
M.Sc., University of Rhode Island, 2018

A Dissertation Submitted in Partial Fulfillment of the
Requirements of the Degree of

DOCTOR OF PHILOSOPHY

in the School of Earth and Ocean Sciences

Assessment and Detection of Landslide-Generated Tsunamis through Numerical Modelling and Instrumental Data

By

Fatemeh Nemati
B.Sc., AmirkKabir University of Technology, 2009
M.Sc., Amirkabir University of Technology, 2013
M.Sc., University of Rhode Island, 2018

## Supervisory Committee

Dr. Lucinda Leonard, Supervisor
(School of Earth and Ocean Sciences)

Dr. Tania Lado Insua, Departmental Member
(School of Earth and Ocean Sciences)

Dr. Gwyn Lintern, Additional Member
(Natural Resources Canada)

Dr. Richard Thomson, Additional Member
(Fisheries and Oceans Canada)

Dr. Eva Kwoll, Outside Member
(Department of Geography)

## Abstract

This PhD dissertation focuses on improving the understanding and mitigation of landslide-generated tsunamis in coastal British Columbia. With a history of landslide tsunamis, much of the coast is at risk of future damage. Here, I demonstrate the hazard of tsunami waves triggered by a large potential landslide in the Strait of Georgia, and develop a proof-of-concept methodology for the detection of landslides and triggered tsunami waves in the Douglas Channel region, using data from a network of seismic, hydroacoustic, and bottom pressure instruments.

The first study details numerical simulations of a potential large subaerial landslide on the coast of Orcas Island and resultant tsunami waves in the Strait of Georgia. Landslide motion and tsunami generation are modelled using the non-hydrostatic physics-based NHWAVE model. The simulated failure moves downslope at up to 13.6 m/s, traveling 732 m before coming to rest after 85 s. Tsunami propagation is continued using the fully nonlinear and dispersive Boussinesq wave model FUNWAVE-TVD in a succession of layered and nested grids. In the near-source region, modelled waves have peak amplitudes of 15-20 m, current speeds up to 10 m/s, and up to 30 m runup. Significant waves occur throughout the region surrounding Orcas Island. In the tsunami propagation direction, runup reaches 7.5 m at Neptune Beach near Lummi Bay. Both initial and reflected waves cause significant runup (> 1.5 m) along much of the shoreline between Point Roberts and Lummi Bay. The findings show that significant coastal impacts may result from landslide-generated waves in the region. Such waves would arrive with little or no warning, highlighting the need to improve tsunami hazard assessment and mitigation strategies.

The second study investigates the use of seismic, hydroacoustic, and hydrostatic pressure instrumental data, to determine an optimal method for landslide detection in the Douglas Channel region, with potential future application in a system to provide early warning of landslide-generated tsunami waves. A new landslide detection method was developed, integrating a Deep-Learning AI model known as EQT with the pre-existing SSNAP earthquake detection model to form the SSNAP-EQT model. Using waveform data from a network of 8 broadband seismic stations, the model was tested to determine if it could detect and locate a number of landslides documented in the region in 2017, 2022 and 2023. The results demonstrate the effectiveness of SSNAP-EQT in detecting landslides and even microseismic earthquakes. Limitations of the existing system include gaps in the station distribution and in data availability that affect the accuracy of event detection and location. Event detections were validated through the analysis of hydroacoustic data from a hydrophone near Kitimat. Analysis of hydroacoustic spectrograms shows great promise in enabling further characterization of landslide events. Data from a bottom pressure sensor near Kitamaat Village were used to demonstrate an effective method to detect and measure potential tsunami waves. An expanded network of hydrophones, pressure sensors, and seismic stations, strategically distributed across the study area, would significantly enhance the precision of landslide detection and enable effective early warning of triggered tsunami waves.

# Table of Contents

# List of Tables

# List of Figures

# List of Abbreviations

| | |
|---|---|
| AI: | Artificial Intelligence |
| BPSs: | Bottom Pressure Sensors |
| BC: | British Columbia |
| BB: | Broadband |
| CGVD2013: | Canadian Geodetic Vertical Datum 2013 |
| CD: | Chart Datum |
| CTD: | Conductivity, Temperature, and Depth |
| CWT: | Continuous Wavelet Transform |
| DART: | Deep-Ocean Assessment and Reporting of Tsunamis |
| DEMs: | Digital Elevation Models |
| DL: | Deep-Learning |
| DONET: | Dense Ocean floor Network system for Earthquakes and Tsunamis |
| EDT: | Equal-Differential-Time |
| EMD: | Empirical Mode Decomposition |
| EOF: | Empirical Orthogonal Function |
| EQT: | Earthquake Transformer |
| FFT: | Fast Fourier Transform |
| HF: | High-Frequency |
| HHT: | Hilbert-Huang Transform |
| HHWMT: | Higher High Water Mean Tide |
| IMFs: | Intrinsic Mode Functions |
| LGTs: | Landslide-Generated Tsunamis |
| LHS: | Left Hand Side |
| LF: | Low-Frequency |
| MF: | Mass Failures |
| MHHW: | Mean Higher High Water |
| MPI: | Message Passing Interface |
| MWL: | Mean Water Level |
| NCBC: | North Coast of British Columbia |
| NE: | Northeast/ Northeastern |
| NRCan: | Natural Resources Canada |
| NRCEC: | Natural Resources Canada Earthquake Catalog |
| NTHMP: | National Tsunami Hazard Mitigation Program |
| OBPGs: | Offshore-Bottom Pressure Gauges |
| OBSs: | Ocean-Bottom Seismometers |
| ONC: | Ocean Networks Canada |
| PSD: | Power Spectral Density |
| RHS: | Right-Hand Side |
| SAL: | Subaerial Landslide |
| SALGT: | Subaerial Landslide-Generated Tsunami |
| SSA: | Source-Scanning Algorithm |
| SSNAP: | Seismicity-Scanning based on Navigated Automatic Phase-picking |
| STEAD: | STanford EArthquake Dataset |

## Acknowledgments

I would like to express my gratitude to all those who have supported me on my PhD journey.

First and foremost, I extend my heartfelt thanks to my advisor, Dr. Lucinda Leonard, for her knowledge, patience, guidance, and support. Her expertise, encouragement, and motivation have been very important in the successful completion of this thesis. Dr. Lucinda Leonard, your support has been invaluable, and I am sincerely grateful.

I also want to acknowledge my other committee members who played unofficial supervisory roles, Dr. Gwyn Lintern and Dr. Richard Thomson, for providing me with the opportunity to undertake this research and for their ongoing guidance and encouragement throughout the project.

My sincere appreciation goes to the members of my committee, Dr. Tania Insua and Dr. Eva Kwoll, for generously sharing their time, experience, advice, and feedback on my thesis.

I am particularly indebted to Fengzhou Tan for his invaluable guidance and creative ideas, which greatly contributed to the success of the second part of my research. His contributions were crucial in the development of the SSNAP-EQT model for detecting landslides from seismic signals.

I am deeply grateful to my parents and siblings, particularly my younger sister, Arefeh, for their unconditional support, inspiration, and steadfast belief in me.

I am grateful for the support provided by Natural Resources Canada (NRCan) for this research, as well as the University of Victoria graduate fellowship. The Orcas Island research was partially funded by the Canadian Safety and Security Program (CSSP) as part of the Coastal Flood Mitigation Canada Project (CSSP-2018-CP-2352) and by the Geological Survey of Canada's Public Safety Geoscience Program. Additionally, I extend my appreciation to the Department of Fisheries and Ocean (DFO) Canada for their partial support.

Special thanks to Robert Kung at the Pacific Geoscience Centre (PGC) for his assistance in acquiring datasets crucial to my research. I also want to express my gratitude to Camille Brillon for her assistance in resolving seismic queries and for her insightful discussions and advice. Special thanks to Ocean Networks Canada (ONC) for granting access to the hydrophone and pressure sensor data. Most of the maps in Chapters 1 and 3 were generated using GeoMapApp (http://www.geomapapp.org), with topography data from Ryan et al. (2009).

Thanks to my Iranian friends in UVic family housing who gave me the feeling of a warm family in the overseas life; thank you all!

Lastly, I am immensely proud and thankful to my beloved spouse, Soroush, for his patience, support, and assistance throughout my PhD journey. I dedicate this thesis to him with all my heart.

# Chapter 1 Introduction

This thesis focusses on the hazard of landslide-generated tsunamis in British Columbia, Canada. This introductory chapter provides background information on the hazard (Section 1.1), on the range of landslide triggers (Section 1.2) and mass movement types in the region (Section 1.3). Section 1.4 outlines the thesis objectives, and Section 1.5 explains the structure of the following thesis chapters.

## 1.1 The hazard of landslide-generated tsunamis

In a worldwide context, the sudden geological phenomena of earthquakes and mass movements (i.e., landslides) are the most triggers of oceanic tsunamis. Among these occurrences, subaerial and submarine landslides stand out as localized but important tsunami sources, with the potential to cause widespread destruction in coastal areas. The possibility of locally huge waves, combined with the difficulty of issuing timely warnings, make landslide-generated tsunamis particularly dangerous. Examples of devastating tsunamis induced either partially or entirely by landslides include the following events: the 1998 Papua New Guinea (Tappin & Grilli, 2021), 1999 Izmit Bay, Turkey (Gasperini et al., 2022), 2011 Tohoku, Japan (Sugawara, 2021), 2018 Palu, Indonesia (Schambach et al., 2021), and 2018 Sunda Strait, Indonesia (Grilli et al., 2019; Widiyanto et al., 2020).

The type, size, and proximity of tsunami sources to coastal settlements all affect how much damage may result. British Columbia (BC)'s coastline, spanning a network of straits, basins, fjords, sounds, passes, and narrows totaling approximately 27,300 kilometers, has the highest tsunami hazard in Canada, based mainly on earthquake sources (Leonard et al., 2014). The prevalence of steep slopes and unstable deltaic and nearshore sediments also enhances the potential for landslides and landslide-generated waves. Submarine/subaerial landslides into water bodies such as fjords, bays, lakes, rivers, mine pits, and reservoirs have the potential to generate waves of considerable height, posing imminent threats to both life and infrastructure (Blais-Stevens & Septer, 2008; Stephenson & Rabinovich, 2009; Van Zeyl et al., 2015). Coastlines of the Strait of Georgia and Juan de Fuca Strait (which together with Puget Sound comprise the Salish Sea), as well as the heads of inlets (e.g., Kitimat), have significant populations at risk of damage from landslide tsunamis (Figure 1.1). Factors such as glaciation, rapid erosion due to steep onshore topography, the presence of unconsolidated sediments on local steep gradients, tidal fluctuations which cause drastic changes in sediment pore pressures, and semi-enclosed marine basins contribute to the heightened risk of damage due to subaerial and submarine landslides and associated tsunamis. If combined with high tide and/or storm surges, the damage potential is even higher. Regular onshore and offshore geologic mapping is essential to monitor and assess the probability of future landslide tsunamis.

Submarine landslides present an outstanding hazard to assets and life in southwestern BC, since much of the human population lives near the coasts of the restricted marine basins of the Salish Sea. Furthermore, the financial state of Vancouver is crucially dependent on natural gas pipelines, highways, rail lines, and electrical transmission lines that pass through steep-sided mountain valleys and that could be damaged or destroyed by landslides triggered by rainfall or by a large earthquake. The city's international airport, the ferry terminal connecting Vancouver Island and mainland BC, and the largest coal export facility in North America are all located on liquefiable soils at the front of the Fraser River delta (Clague, 2002). Transmission cables that supply all of the electricity to Vancouver Island extend throughout the submarine front of the Fraser delta, with the potential for landslides and associated tsunami waves (Hamilton & Wigen, 1987; Rabinovich et al., 2003; Dunbar & Harper, 2009). Much of Canada's grain and lumber exports, as well as imports of cars and trucks from Japan and Korea, pass through Vancouver, and any lengthy interruption of the port or rail lines would hurt the economy of the whole country.

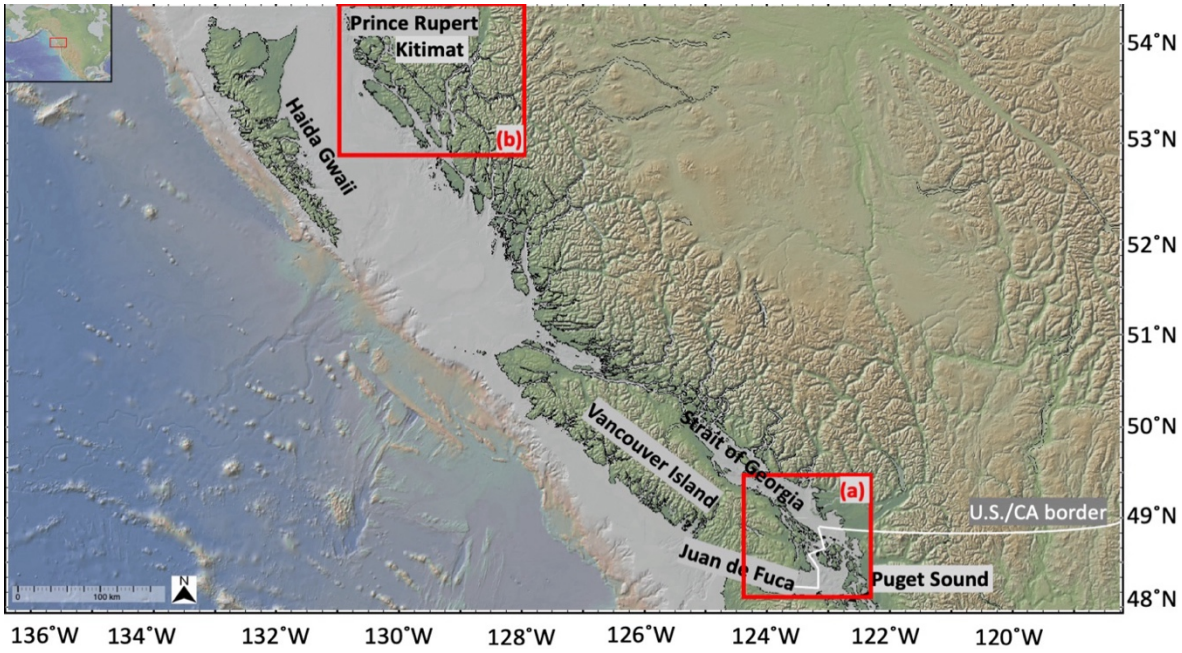


Figure 1.1. Focus areas of thesis, at risk of damage from landslide tsunamis. Box (a): Study area for Orcas Island/Boundary Bay landslide tsunami modelling project described in Chapter 2; Box (b): Study area for Douglas Channel landslide detection project described in Chapter 3.

Further north along the BC coast, population density is much lower, but there are also communities at risk, particularly those along and at the heads of inlets, e.g., Kitimat, which was damaged in a landslide tsunami in 1975 (Murty & Brown, 1979; Skvortsov & Bornhold, 2007; Kirby et al., 2016). Such communities and an increasing amount of infrastructure are at risk from future landslide-generated waves (Huntley et al., 2020). Tsunamis caused by landslides commonly occur along the inlets and narrow straits of North America's Pacific coast, sometimes with exceptionally

large run-up. The 1853-1854 (120 m runup), 1874 (24 m), 1899 (60 m), 1936 (150 m), and 1958 (525 m) Lituya Bay, Alaska tsunamis (Miller, 1960; Rabinovich et al., 2023), as well as the 1952-1968, 1971, and 1975 (>8 m wave height) Kitimat Arm, BC tsunamis (Johns et al., 1985), are a few of the historical landslide tsunamis that occurred in this region (Figure 1.2). Additional locations of tsunamis caused by landslides along with the year they occurred are displayed in Figure 1.2. These locations include Puget Sound in Washington State (Baum et al., 2005), Yakutat, Russel Fjord, and Skagway Harbor (all in southeast Alaska) (Kulikov et al., 1996).

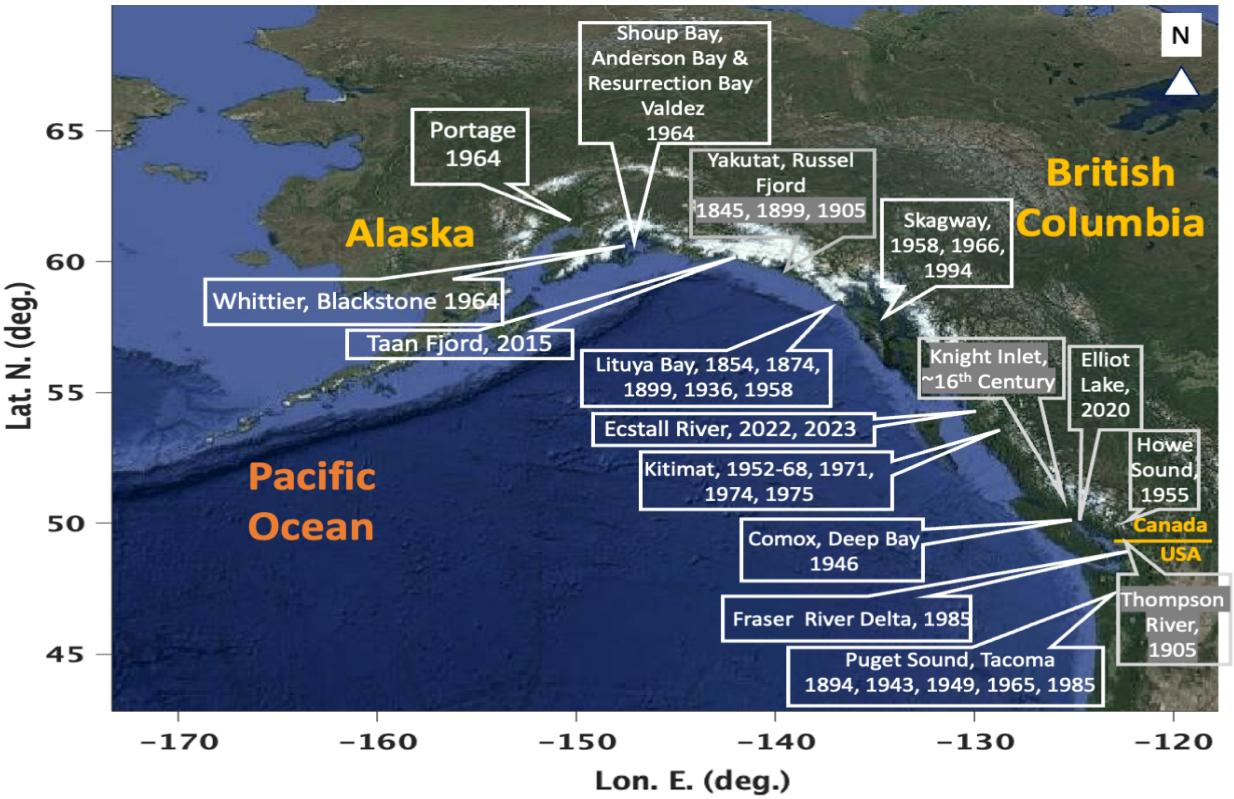


Figure 1.2. Locations of known historical landslide-generated tsunamis along the coast of Alaska, British Columbia, and Washington (Rabinovich et al., 2003).

Various tsunami hazard studies have been carried out for the Pacific coast of BC, including the inner coastal region of Juan de Fuca Strait and the Strait of Georgia. However, most of these studies are based on numerical simulations of seismically generated tsunamis caused by distant or regional earthquakes beneath the Pacific Ocean (Cherniawsky et al., 2007; Fine et al., 2008; Gao et al., 2018). Mosher et al. (2004) illustrated that submarine landsliding is possible and even expected in many coastal parts of BC, triggered by even moderately low ground accelerations. Rabinovich et al. (2003) examined two zones of potentially unstable sediment deposits: the eastern slope of Texada Island in Malaspina Strait and Roberts Bank on the Fraser River delta front in the southern Strait of Georgia (Figure 1.3). Numerical models of the 1975 landslide event and accompanying tsunami in Kitimat Arm, BC, are presented by Skvortsov and Bornhold (2007) and

Kirby et al. (2016). The structure, stability, potential failure mechanism, and tsunami hazard of a rock slope in Knight Inlet, BC (Figures 1.2 and 1.4), were studied by Van Zeyl et al. (2015). Knight Inlet was the site of a rock avalanche-generated tsunami that destroyed the village of Kwalate around 1570 (Bornhold et al., 2007). The necessity for reliable methods to predict the amplitudes of landslide-generated waves and to detect landslides becomes evident.

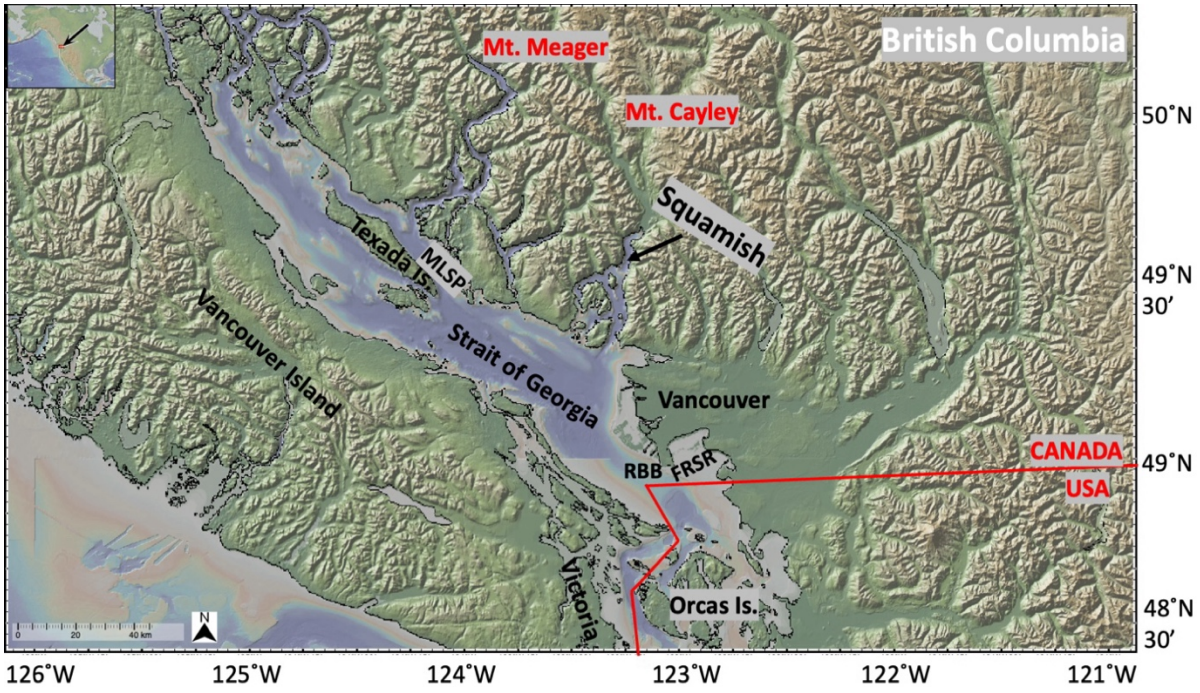


Figure 1.3. Map of southwestern BC including: Texada Island, Malaspina Strait (MLSP), Roberts Bank (RBB) on the Fraser River (FRSR) delta front, Vancouver, Squamish, Mount Meager, Mount Cayley.

Compared to the west coast of Vancouver Island, the Strait of Georgia and Puget Sound are relatively sheltered from tsunamis generated by megathrust earthquakes on the offshore Cascadia subduction zone (Clague et al., 2000; Rabinovich et al., 2020, 2023). However, a few Holocene-active faults have been identified within the Salish Sea, located between the southern coast of British Columbia, Canada, and the northwestern coast of Washington state, United States, that could host large ($M_w$~7) earthquakes and trigger significant tsunami waves via tectonic displacement of the seafloor (e.g., Johnson et al., 2001; Koshimura et al., 2002; Kelsey et al., 2012; Barrie & Greene, 2018; Caston, 2021). Such earthquakes could also trigger subaerial or submarine landslides (e.g., Karlin et al., 2004), increasing the possibility of anomalous waves, especially when landslides impact limited or semi-confined water basins. The M7.3 onshore earthquake on Vancouver Island in 1946 caused at least two landslide-generated tsunamis, resulting in one fatality (Hodgson, 1946; Evans, 1989).

Landslide-generated waves have a more localized impact than earthquake-caused tsunamis, but can be extreme in height, with significant impacts, highlighting the necessity of regional and

local emergency response strategies. The Tsunami Warning System for the Pacific coast of Canada, which is part of the International Tsunami Warning System for the Pacific Ocean, is roughly sufficient for the outer coast (Rapatz & Murty, 1987; Anderson & Gow, 2004; Insua et al., 2015). However, no warning system currently exists for tsunamis generated locally in the Salish Sea, or in inlets along the mainland BC coast.

## 1.2 Range of known triggers of past damaging/tsunamigenic landslides in British Columbia

Future development requires safe and secure locations for infrastructure installations and communities, particularly along BC's northwest coastline region (Huntley et al., 2020). The challenge for managing environmental and infrastructure protection and site reclamation will be to accommodate future extreme weather events, climate change, and damage from earthquakes, landslides, and tsunamis (Huntley et al., 2020). Between 1900 and 2018, there were 278 verified deaths in BC due to landslides (Kirschbaum et al., 2015; Blais-Stevens et al., 2018). The damage to infrastructure was substantial, with average annual costs ranging from $75 to 200 million CDN in 2019 dollars (Guthrie et al., 2013; Sobie, 2020). To better understand the hazard of future landslides, it is important to review the causes of past landslides in BC. Common triggers of historical landslides are outlined in the following sections.

### 1.2.1 Rainfall

In BC, rainfall is the primary cause of landslides (Sobie, 2020). Most landslides globally are caused by short-duration precipitation, and BC is no exception (Jakob & Weatherly, 2003; Guthrie et al., 2010; Sobie, 2020). It is anticipated that the frequency and intensity of landslides will rise in tandem with the effects of climate change on precipitation (Westra et al., 2014; Gariano & Guzzetti, 2016; Sobie, 2020). Moreover, the possibility of landslide occurrence increases due to complex interaction of climatic conditions, soil types, geology, terrain, vegetation, and topography (Sobie, 2020).

According to Jacob & Lambert (2009), antecedent precipitation (prior to a triggering event) has contributed to ground saturation, enabling subsequent precipitation events to trigger landslides in urban Vancouver, Howe Sound, and the North Shore Mountains over 40 years of observations. Future projections suggest that landslide hazard frequency will increase from 16 days per year to 21 days per year (32%) on average by the 2050s for landslide susceptible regions in BC (Sobie, 2020). Areas with the most frequent landslide hazards, including the west coast and northern Rocky Mountains, are expected to see between 8 and 11 additional hazardous days per year (49-61% increase; Sobie, 2020). Most of the increased hazard frequency occurs during fall and winter, reflecting those seasons with the largest projected increases in single and multi-day precipitation

(Sobie, 2020). Risk assessments for regions in BC vulnerable to landslides will need to account for increasing hazard due to climate change-altered precipitation (Sobie, 2020).

### 1.2.2 Earthquakes

Although rainfall is the dominant trigger of landslides in BC, many small and regional-scale landslides have been triggered by earthquakes (Barth et al., 2020). Ground shaking can directly trigger numerous landslides and reduce soil and rock strength, increasing susceptibility to instability over time (Lin et al., 2006; Barth et al., 2020). Submarine landsliding, for instance, can be triggered by shaking in many coastal areas of BC, even with moderately low ground accelerations (Mosher et al., 2004). Particularly strong earthquakes may induce submarine landslides near the Fraser delta front, possibly resulting in the generation of tsunamis (Hincks et al., 2011).

The possibility of tsunamis in the Strait of Georgia is also related to crustal earthquakes near the seismically active region (Caston, 2021). For example, the Mw 7.3 1946 Vancouver Island earthquake (Figure 1.4) triggered many hundreds of local landslides and slumps along the coast of Vancouver Island, some of which generated tsunami waves, representing hazards to human life, and to seafloor installations and coastal infrastructures (Mosher et al., 2004; Stacey et al., 2019). The only death in BC associated with the 1946 event was caused when a slump-generated tsunami wave overturned a small boat near Deep Bay, eastern Vancouver Island (Rabinovich et al., 2003; Huntley et al., 2020). The 1958 Lituya Bay rockslide and tsunami, as well as a similar event in 1899, were triggered by strong earthquakes (Figure 1.2) (Rabinovich et al., 2003).

Haida Gwaii is located in the northeast Pacific Ocean and along the Pacific-North America tectonic plate boundary, the most seismically active region in Canada; the islands are prone to heavy rainfall, strong earthquakes, and frequent landslides (Barth et al., 2020). The area experienced a notable spike in landslides during and following the Mw 7.8 2012 earthquake (Barth et al., 2020). Of the 446 landslides identified between 2007 and 2018, 244 were determined to be seismically induced (Barth et al., 2020). Following the 2012 earthquake, the number of landslides identified in imagery averaged about 18 landslides per 100 $km^2$, covering a total area of 461 ha. In subsequent years, the number and area of landslides per year decreased (Barth et al., 2020).

The Puget Sound region of Washington State (Figure 1.1) lies in the forearc basin of the Cascadia convergent continental margin (e.g., Karlin et al., 2004). Large-scale and widely distributed landslides are among the most obvious manifestations of large earthquakes in this region (Karlin et al., 2004). Prehistoric earthquakes on the Seattle fault triggered coseismic uplift and tsunamis in Puget Sound, along with landslides and debris flow in Lake Washington that may also have been tsunamigenic (Karlin et al., 2004).

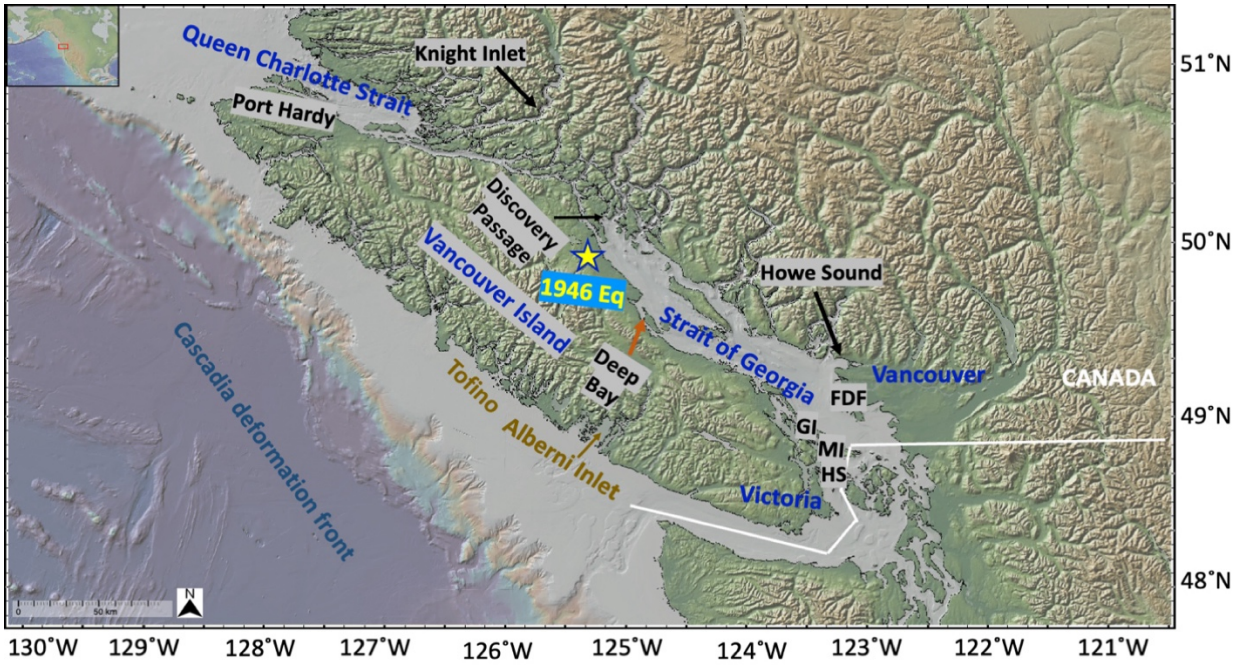


Figure 1.4. Map showing the epicenter of the 1946 earthquake (yellow star) that triggered landslide tsunamis and other sites mentioned in the text. FDF: Fraser delta front; GI: Galiano Island; HS: Haro Strait; MI: Mayne Island.

In the Strait of Georgia, high-resolution bathymetry data revealed the existence of recent landslide deposits on the seafloor adjacent to northeast Orcas Island (Greene et al., 2018). These deposits indicate the possibility of future landslides caused by seismic activity along the neighboring Skipjack Island fault zone, which has been active in the Holocene and may experience earthquakes of magnitude 7 or higher (Greene et al., 2018; Caston, 2021). A further rapid subaerial collapse along the steep northeastern shore of Orcas Island can be expected to create tsunami waves that might strike nearby coastal portions of the Gulf and San Juan Islands, as well as the mainland to the east/northeast. The impacts of such a failure are explored in Chapter 2.

While there are descriptions of earthquake-triggered tsunami deposits from southwest BC there are still significant knowledge gaps regarding the frequency and size of paleo-seismic and paleotsunami events for a large portion of the province's coastal regions (Huntley et al., 2020).

### 1.2.3 Sediment loading

This section focusing on the BC coastline consistently highlights the high instability of deltaic and nearshore sediments. Submarine landslides are typically triggered either by seismic loading or by regional processes like gradual sediment loading from rivers (Rabinovich et al., 2003). Particularly concerning are the vast accumulations of unstable sediments found in deltas of North American rivers such as the Fraser, Skeena, and Nisqually, which pose significant hazards (Rabinovich et al., 2003). Along the marine coasts of BC, thick deposits of unconsolidated or semi-lithified sediment are prevalent, often overlain by human development (Mosher et al., 2004).

Landslide-generated tsunamis tend to be concentrated along rivers or lakes with steep slopes of unconsolidated Pleistocene sediments, as well as in fjords and glacially carved valleys with steep bedrock slopes (Roberts et al., 2013).

Recent studies have underscored that fjords and inlets along the BC coast, even when far from the source of an incoming tsunami, can amplify the waves through resonance amplification (Rabinovich et al., 2020). Locally damaging waves are closely associated with landslides along the Pacific coast, with fjords especially vulnerable due to the potential failure of their steep walls or submarine delta fronts. Even minor failures can generate significant run-up in these elongated basins (e.g., Leonard et al., 2014).

The Strait of Georgia, including low-lying parts of Greater Vancouver, faces potential risks from submarine landslide tsunamis, especially from the foreslope of the Fraser River delta (Clague & Orwin, 2005). With the Fraser River depositing about 17 million tons of sediment annually into the Strait of Georgia, the accumulation on the delta's steep frontal slope poses significant tsunami-generating potential (Clague & Orwin, 2005). The unconsolidated sediments forming the delta front may fail tsunamigenically, even without seismic triggers (Clague & Orwin, 2005). Rabinovich et al. (2003) analyzed two possible styles of failure at the Fraser Delta front. They concluded that a large slide could produce tsunami waves up to 18 m high on the eastern shores of Galiano and Mayne islands, with smaller waves on the eastern shores of the Georgia Strait.

In Howe Sound, seismic and/or sediment loading could also lead to tsunamigenic submarine slides at the Squamish River delta front (Figure 1.3) (Clague & Orwin, 2005), as occurred in October 2006 (Stephenson & Rabinovich, 2009). The seaward edge of this growing delta, being steep and unstable, is particularly susceptible to submarine landslides (Stephenson & Rabinovich, 2009).

### 1.2.4 De-buttressing of slopes due to deglaciation

In various regions of BC, unstable conditions on steep slopes are attributed to glacial deposits, which can fail due to external perturbations (Evans & Clague, 1994). Rockfalls, deep-seated gravitational slope deformation, and catastrophic rock avalanches are more likely when paraglacial de-buttressing is paired with glacio-isostatic rebound, tectonic faulting, and/or the thawing of permafrost (Huntley et al., 2020). The growth of cracks results from the release of stress caused by the loss of glacial ice buttressing steep slopes (Huntley et al., 2020).

The rapid variation in daily temperature or freeze-thaw cycles in alpine and rocky slopes can induce fractures and melt snow and ice, decrease glaciated and permafrost areas, and then lead to more unconsolidated materials in periglacial areas and instability. Receding ice sheets and glaciers have left loosely consolidated deposits in many areas of BC (Geertsema et al., 2006; Clarke et al., 2015).

The findings of an InSAR analysis conducted between 2017 and 2019 in the vicinity of Hawkesbury Island and Hartley Bay, BC indicate that, over relatively short time periods (around

10,000 years), various geological processes such as stress release, reduction of fjord side wall support, glacio-isostatic rebound, tectonic faulting, and thawing of permafrost during deglaciation have influenced the landscape (Huntley et al., 2020).

Recent events, such as the evolution of a combined landslide, tsunami, outburst flood, and sediment plume event in the southern Coast Mountains of BC, underscore the impact of environmental changes in the region (Geertsema et al., 2022). This event occurred on November 28, 2020, near the head of Elliot Creek, a tributary of the Southgate River (Geertsema et al., 2022). A massive rockslide descended 1,000 m from a steep valley wall, crossing the toe of a glacier before crashing into a glacier lake, causing a tsunami with over 100 m of run-up. The Elliot Creek event not only impacted terrestrial, riverine, and marine environments but also devastated critical salmon spawning habitats in the Southgate River and lower Elliot Creek, crucial food sources for the Homalco First Nations. Although the landslide affected a relatively small area of about 1 $km^2$ the ensuing tsunami and outburst flood wreaked havoc on approximately 3 $km^2$ of forest, burying soil along their paths. This event, along with similar occurrences elsewhere in BC, highlights the potential hazards posed by rapid deglaciation in high mountains, underscoring the importance of understanding and mitigating such risks in increasingly developed and touristic areas. Glacier retreat in the southern Coast Mountains, which contain over 8,000 $km^2$ of glacier-covered terrain, is contributing to increased rates of glacier mass loss, with implications for landslide frequency (Geertsema et al., 2006, 2022; Friele et al., 2020).

Rapid glacier melting may exacerbate the risk of high mountain landslides that cause tsunamis, floods, and fast-moving mass flow events by increasing the quantity and size of lakes beneath potentially unstable slopes in alpine valleys undergoing ice retreat (Geertsema et al., 2022). Recent increases in rockslides and rock avalanches in deglaciation-prone terrains support the link between glacier retreat and landslide occurrence (Friele et al., 2020). Glacier retreat can also reveal basins where ice-contact or proglacial lakes emerge, sometimes resulting in catastrophic collapses and massive floods. Although previous glacial retreat occurrences in Western Canada have not resulted in fatalities, rising rates of resource development, tourism, and city growth increase the future risk presented by these phenomena (Geertsema et al., 2022).

### 1.2.5 Volcanic eruption

In western Canada, despite being situated in an area of active tectonics and volcanism, the sparse population has experienced few eruptions due to the remote locations of the volcanoes and their limited activity (Stasiuk et al., 2003). Consequently, there's a misconception that Canada's volcanoes are extinct (Stasiuk et al., 2003). Landslides linked to eruptions are facilitated by steepened slopes resulting from ground deformation, increased steam venting, and sustained shaking caused by shallow seismic events (Stasiuk et al., 2003). Many Canadian volcanoes, situated on basement rocks with steep relief, are already weakened by poor consolidation and hydrothermal alteration (Stasiuk et al., 2003). These conditions have led to numerous failures

unrelated to eruptive events (Stasiuk et al., 2003). Instances in southwestern BC include the Dusty Creek and Avalanche Creek landslides at Mount Cayley, the collapse of the Barrier Lava, and frequent small landslides, along with occasional large ones, at Mount Meager (Figure 1.3).

A significant landslide at Mount Meager claimed four lives in 1975 (Stasiuk et al., 2003). Mount Meager also hosted a massive rockslide-debris flow in August 2010; the potential for a subsequent outburst flood led to the evacuation of 1500 people, and costs are estimated at ~10 M CAD (Guthrie et al., 2012). The Mount Meager Volcanic Complex, a glacier-clad stratovolcanic system, experienced its last major explosive eruption over 2400 years ago (Warwick et al., 2022). Despite being Canada's most recent significant explosive eruption, research on Mount Meager has predominantly focused on its extensive landslides, leading to an understudied understanding of its volcanic hazard characteristics (Warwick et al., 2022). Although the mentioned landslides are not directly triggered by eruptive events, these incidents would not occur in the absence of the volcanoes and hence are considered secondary volcanic hazards (Stasiuk et al., 2003).

### 1.2.6 Anthropogenic activities

Landslide-induced tsunamis may, in some cases, be initiated by human activities such as pile driving, deforestation, forest road construction, or land development activities. A significant tsunami (9-11 m run-up) that occurred on November 3, 1994, in Skagway, Alaska, was caused by an underwater landslide triggered by the collapse of a cruise ship wharf under construction at the head of Taiya Inlet, causing one fatality and significant damage (Kulikov et al., 1996). The failure has been attributed to the construction causing overloading of delta slope sediments, combined with an extreme low tide (Rabinovich et al., 1999). Construction-induced sediment loading and tidally-induced drawdown may also have contributed to triggering the 1975 submarine slide in Kitimat Arm that triggered tsunami waves with >8 m runup, causing substantial damage amounting to $1.75 million to wharves and other shore facilities (Johns et al., 1986; Bornhold et al., 2004). The de-stabilizing role of low tide conditions is explained further in the next section.

### 1.2.7 Low tide and pore pressure

Coastal BC is at risk of significant subaerial landslide hazards, particularly concerning forestry operations, which are primarily vulnerable to shallow, saturated debris avalanches and channelized debris flows (Jakob et al., 2006). These hazards are predominantly triggered by elevated pore water pressures resulting from various factors such as rainfall, snowmelt, and alterations in drainage patterns (Jakob et al., 2006). In the submarine environment, in addition to elevated pore pressures, steep slopes, and weak sedimentary conditions, slope instability is often increased by low tide conditions (Mosher et al., 2004). During periods of low tide, submarine deposits experience heightened pore pressures, further predisposing coastal slopes to failure

(Mosher et al., 2004). This dynamic interaction between low tide events and excess pore pressure underscores the complex nature of submarine slope stability. Under these conditions, even moderate seismic events, such as a magnitude 5 earthquake occurring at a distance of 10 km, have the potential to trigger submarine landslides in this region (Jakob et al., 2006).

The Kitimat submarine slides and tsunamis (1952-1975) and some of the Lituya Bay subaerial failure-triggered tsunamis (1854, 1874, and 1936) occurred during seismically calm times (Figure 1.2) (Huntley et al., 2020). As previously mentioned, coastal construction activities coincided with low tides both in association with the 1975 Kitimat Arm failure and subsequent tsunami (Johns et al., 1985; Kulikov et al., 1996; Huntley et al., 2020), and the 1994 Skagway event; an anomalously low tide also occurred during a previous event in Skagway Harbor in 1966 (Huntley et al., 2020).

Mosher et al. (2004) documented two notable submarine landslide events on April 28, 1998, and April 21, 1999 at Mapleguard Spit near Deep Bay (Figure 1.4). Remarkably, the occurrence of these landslide events coincided with periods of spring tide, with the first event transpiring during a spring tide characterized by a recorded low tide of 0.95 m. Subsequently, the second landslide event occurred two days after the spring tide, coinciding with a recorded low tide of 1.23 m (Mosher et al., 2004). Despite extensive scrutiny, no immediate additional trigger mechanism has been conclusively identified to explain the occurrence of these submarine landslides. The enigmatic aspect of the events underscores the complexity inherent in submarine slope instability phenomena, necessitating further interdisciplinary research efforts to unravel the underlying mechanisms driving such occurrences.

## 1.3 Range of landslide types in British Columbia and their influence on tsunamigenesis

Different types of mass failure are categorized according to the material that failed, the failure mechanism, and the rate of movement. The varieties of slope failure are described and explained in the following sections, with examples from BC and consideration of their influence on tsunamigenesis.

### 1.3.1 Rock avalanches

Rock avalanches, characterized by the rapid movement of fragmented rock suspended on an air cushion, move at a very high velocity, exceeding 10 m/s. Remote and sparsely populated coastal areas of BC are commonly sensitive to tsunamis generated by rock avalanches and other subaerial mass movements (Stephenson & Rabinovich, 2009). Subaerial landslides in southwest BC and northern Washington State have been associated with numerous tsunamis, as documented in the scientific literature (Figure 1.5) (e.g., Roberts et al., 2013). However, it is important to note that the event record is biased towards residential areas and the recent historic

period, leading to an incomplete understanding of the frequency and characteristics of these events (Roberts et al., 2013).

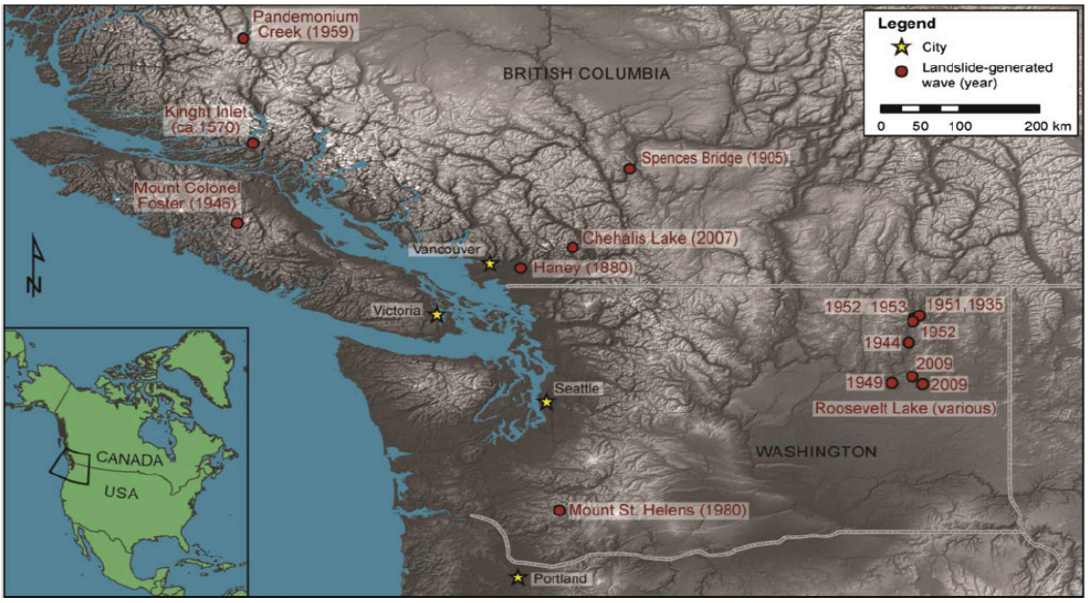


Figure 1.5. Locations where tsunamis resulting from landslides have been recorded in southwest BC and northern Washington State (Roberts et al., 2013).

Most of the documented events, with the exception of the Knight Inlet event reported by Bornhold et al. (2007), have occurred only since European colonization in the mid-1800s, indicating that many prehistoric events are likely missing from the record (Roberts et al., 2013). Despite these limitations, the available data suggest some commonalities among rock avalanche-generated tsunamis in the region. While most failures have no noticeable triggers, notable exceptions include tsunamis triggered by the Mount St. Helens rock avalanche associated with the 1980 volcanic eruption (Roberts et al., 2013), and the Mount Colonel Foster rock avalanche triggered by the M7.3 earthquake on Vancouver Island in 1946 that generated damaging tsunami waves in what is now known as Landslide Lake (Evans, 1989). With a length of 125 km, Knight Inlet is one of the longest inlets on the BC coast (Figure 1.4). An 840-m high rock avalanche plunged into the water and generated a tsunami which destroyed the First Nations Village of Kwalate on the other side of the inlet, approximately 400 years ago (Bornhold et al., 2007). This tsunami is thought to have killed 100 or more residents (Stephenson & Rabinovich, 2009).

### 1.3.2 Rockfalls and rockslides

Rockfalls are characterized by rock fragments, exhibiting a vertical or near-vertical descent, often accompanied by bouncing, with a very fast rate of motion exceeding 10 m/s in many instances. Rockslides are similar, except that movement is parallel to the slope, and may not be near-vertical.

Howe Sound is one of the southernmost fjords on the mainland coast of BC (Figure 1.4). It joins the Strait of Georgia immediately north of the City of Vancouver. An investigation by Jackson et al. (2014) aimed to identify potential sources of tsunami waves within Howe Sound, focusing on the presence of large rockslide deposits on the seafloor. Their analysis revealed only one notable rockslide deposit, situated off the northwest side of Bowen Island, with no evidence of similar events occurring in the late Holocene period. Additionally, Westmar (2005) estimated the maximum possible rockslide-generated tsunami height in Howe Sound to be 2 m above sea level, with a return period ranging from 100 to 1000 years.

However, examination of swath multibeam bathymetry (SMB) imagery in Howe Sound by Jackson et al. (2008) revealed conspicuous submarine rockslide run-out deposits in Collingwood Channel west of Bowen Island. This discovery raised concerns regarding the potential for future landslide activity in the region, which could generate displacement waves capable of impacting nearby communities and marine traffic (Hermanns et al., 2014). Subsequent assessments of slope stability along Bowen Island, including investigations of sediment deposits beneath Howe Sound, were undertaken to better understand the geological hazards associated with Mount Gardner (Jackson et al., 2008, 2014). The sedimentary deposits found on the seafloor beneath Mount Gardner likely resulted from one or multiple minor rockslides or debris flows originating from nearby unstable areas, prompting a need for additional exploration into the potential risks associated with these occurrences (Jackson et al., 2008).

Further north, in the Douglas Channel region, examination of extended InSAR data sets could uncover gradual slope movement and instances of rockfall activity in the area surrounding vital infrastructure and communities (Huntley et al., 2020). Hawkesbury Island is characterized by glacial erosional features including cirque basins, horns, arêtes, truncated spurs, deeply carved U-sd valleys, and hanging valleys that drain into the Kitimat fjord. With bedrock slope angles exceeding 35 degrees, these terrains are susceptible to erosion and rockfall events, evidenced by the accumulation of talus deposits at their base.

### 1.3.3 Debris flows and debris avalanches

Debris flows are characterized by the presence of sand, gravel, and larger fragments, often with a significant water content. They flow downslope with a rapid velocity of up t0 10 m/s. Debris avalanches typically involve a sudden failure of rock, soil, and other debris on a steep slope. They can travel long distances, sometimes reaching speeds of hundreds of kilometers per hour.

Debris flows and debris avalanches stand out as the predominant and most perilous forms of landslides along the rugged terrain of the north coast of BC (Jakob et al., 2006). These hazardous events, often triggered by intense rainfall, pose significant risks to forestry workers, particularly in sparsely populated regions where development is limited (Jakob et al., 2006).

In the challenging landscape of BC's north coast, shallow landslides up to 1 m thick, commonly referred to as debris avalanches, present a substantial threat (Jakob et al., 2006). These debris

avalanches, as classified by Hungr et al. (2001), frequently evolve into debris flows through the channelization of the displaced debris, exacerbating the hazard further.

One notable region of concern is Howe Sound (Figure 1.4), characterized by its intricate fjord-like features and substantial freshwater discharge compared to other fjords in the vicinity (Jackson et al., 2008). Howe Sound has hosted numerous instances of submarine and subaerial sediment movements, including debris slides, turbidity currents, slumps, and debris flows (Jackson et al., 2008). These events, documented extensively by Jackson et al. (2008) and Blais-Stevens & Septer (2008) have resulted in significant damage to infrastructure and even fatalities since records began in the early 1900s.

Among the notable incidents in Howe Sound is the failure of the sand and gravel delta at Woodfibre in 1955, a well-known case study in subaqueous sediment failure (Blais-Stevens & Septer, 2008). Additionally, debris avalanches and flows originating from the Mt. Cayley complex (location in Figure 1.3) have intermittently obstructed the Squamish River, posing further risks to local communities and forestry operations (Jackson et al., 2014).

The impact of these landslide events extends beyond property damage, often resulting in injury or loss of life for forestry workers caught in their path. Historical records indicate a significant toll, with approximately 80 recorded deaths attributed to landslides in northern BC since the mid-1800s (Jakob et al., 2006). Notable catastrophes, such as debris flows in 1881 that struck two canneries along Inverness Channel, northern BC, causing approximately 50 deaths, and a debris avalanche at Prince Rupert in 1957 that killed seven people, underscore the grave consequences of these natural hazards (Jakob et al., 2006).

Two debris flow episodes that took place in the neighborhood of Hartley Bay (Douglas Channel region, Figure 1.1 (a)) during autumn or winter storm events between September 2017 and January 2018 are captured by SAR images (Huntley et al., 2020). During this time, flooding in a nearby lake basin is also shown by SAR imaging. Through ground observations and public interaction, the extent to which the debris flows identified affected local watersheds has not yet been assessed.

Vegetation and thin organic soil (Folisol) are removed to the Douglas Channel by elongated debris flows or slides that are less than 0.8 $km^2$, on high terrestrial bedrock slopes (Huntley et al., 2020). In bottom profile surveys of the fjord, folisolic slides and rockfalls create subsurface talus cones, slumps, and slide blocks (Maynard et al., 2017; Huntley et al., 2020). These smaller-volume, more frequent failures are not expected to produce significant tsunamis. On the other hand, the marine sediments that have been deposited in bays at the head of the fjord beyond storm berms (Huntley et al., 2020) serve as a record of tsunamis that were caused by distant earthquakes or large-scale landslides that occurred locally.

### 1.3.4 Submarine slumps

Slumps are characterized by downslope movement of thick deposits (ranging from meters to tens of meters) of unconsolidated sediment. The motion involves movement as a unit along a curved surface, indicative of rotational sliding.

The 1946 Vancouver Island earthquake did not result in a significant tectonically-generated tsunami (Rabinovich et al., 2003). However, it triggered local landslides and slumping, leading to minor water level disturbances along the coast (Rabinovich et al., 2003; Huntley et al., 2020). E.g., a sandy spit slumped off during the earthquake, creating displacement waves and leading to the only event fatality in BC (Hodgson, 1946).

In many parts of coastal BC, exposed glaciolacustrine sediments indicate the transport of weakly lithified sediments downslope as subaqueous debris flows, likely evolving from slumps and slides involving coherent sediment masses (Eyles, 1987). During the Late Wisconsin period (before 30,000 B.P.), ice-sheet lobes moved opposite to the regional drainage flow, forming extensive lakes, some reaching up to 5000 $km^2$, in the Upper Fraser River Valley of BC (Eyles, 1987). It is probable that the Fraser River debris flows were generated by large-scale sliding or slumping of coherent masses of Tertiary sediment progressively breaking up during downslope movement (Eyles, 1987).

As mentioned in Section 1.2, submarine slumps on the Kitimat River delta front in 1974 and 1975 caused a sequence of tsunamis that destroyed residential homes in the neighboring towns of Kitimat and Kitamaat as well as maritime infrastructure that was under construction (e.g., Lintern et al., 2019). Evidence of tsunami events, as well as older recurrent marine inundation events linked to displacement waves caused by landslides on steep coastal slopes, storm surge waves, flood events from glacierized Cordilleran watersheds, and great earthquake-generated tsunamis, are preserved in clastic deposits in tidal peat marshes and forest soils of Douglas Channel (Huntley et al., 2018, 2020).

Postglacial submarine debris slides and slumps, triggered by factors like extreme tides and high sedimentation rates, are common in Douglas Channel (Huntley et al., 2020). They range from smaller events on terrestrial slopes to larger slumps on the Kitimat River delta front (Lintern et al., 2019; Huntley et al., 2020). While landslide features on Hawkesbury Island have been determined to be stable and to pose minimal hazard, coastal communities remain vulnerable to damage from large volume submarine slumps (Huntley et al., 2020). The distribution of marine inundation deposits indicates that these events primarily affect outer channels and peninsulas, with colluvial terrain near the shoreline posing a moderate to high risk of landslides (Huntley et al., 2020). Overall, while smaller events like rockfalls and debris flows do not typically generate tsunamis, larger landslides or distant earthquakes can trigger significant local tsunamis, highlighting the ongoing risk to coastal development in Douglas Channel (Huntley et al., 2018, 2020).

## 1.4 Thesis objectives

In this thesis, I focus on two coastal study areas (Box (a) and (b) shown in Figure 1.2), with the overall goal of advancing the hazard assessment and mitigation of landslide-generated tsunamis in BC. The objective of the first study is to demonstrate the hazard posed by potential landslide-generated tsunamis in the Strait of Georgia. I present an accurate numerical simulation of both a large potential subaerial landslide and its resultant tsunami waves as they propagate from the source and inundate coastlines in the southern Strait of Georgia. In the second phase of my research, my objective is to evaluate the effectiveness of instrumental seismic, hydroacoustic, and bottom pressure sensor data in detecting landslides and potentially-triggered tsunami waves in Douglas Channel and Gardner Canal. The main objective of the second study is to provide a proof-of-concept methodology for detecting both landslides and tsunami waves that may result. This methodology, based on a network of instruments, aims to pave the way for future applications in a comprehensive landslide tsunami early warning system. The background, motivation, and specific objectives for the two studies are outlined in the sections below.

### 1.4.1 Numerical simulation of landslide-generated tsunami waves

Tsunami assessment is a critical problem for hazard mitigation and long-term planning (Bernard, 1998; Mofjeld et al., 1999), including planning for new construction in coastal areas, for approximating tsunami risk, and to enable generation of inundation maps for endangered communities (Preuss & Hebenstreit, 1998). Early tsunami warning requires rapid detection and evaluation of the mechanisms of tsunami generation (e.g., earthquakes and/or landslides) as well as detection of the tsunami itself as soon as possible after its generation (Grilli et al., 2016). Therefore, progress in tsunami science and engineering is demanded for mitigating this deadly hazard (Skvortsov & Bornhold, 2007). Prompt detection is crucial when the tsunami source is located close to coastal zones, and thus both energy spreading is low and propagation time is short (Tinti, 2003; Ioualalen et al. 2007; Grilli et al., 2013).

As most mass failure tsunamis are generated at or near shoreline regions, they have short propagation times towards coastlines, and hence short warning times. Tsunami hazard assessment can be improved with the use of hydrodynamic numerical modeling of potential sources. Local authorities, informed by tsunami hazard information, then play a key role in disaster management plans, land use control, public education, and warning systems.

The first part of my study focuses on the southern Strait of Georgia, near the US/Canada border, with a specific emphasis on the potential for a large tsunamigenic subaerial failure off Orcas Island (Box (a) in Figure 1.2). Understanding the recurrent nature of landslides and their potential to trigger tsunamis is crucial for coastal hazard assessment.

Despite the absence of documented tsunamigenic landslides in the historical record, indications of recent landslide activity, including a rockfall debris apron and distinct deposits on

the seafloor adjacent to northeast Orcas Island, underscore the need for further investigation (Greene et al., 2018). These deposits suggest the possibility of future landslides triggered by seismic activity along the nearby Skipjack Island fault zone, which has been active in the Holocene and may host earthquakes up to magnitude 7 or higher (Greene et al., 2018; Caston, 2021). A rapid collapse along the steep northeastern coast of Orcas Island is anticipated to generate tsunami waves capable of impacting the neighbouring coastal regions of the Gulf and San Juan Islands, as well as the adjacent mainland. Detailed modeling is necessary to evaluate this potential impact.

Various parameters, including slide volume, Froude number, slide velocity, water depth, bottom friction, dispersion, coastal geometry, and seafloor topography, influence tsunami wave heights. To specify the characteristics of landslide-generated tsunamis, different parameters must be considered in numerical simulation. Some of these factors are more important than others, and small miscalculations or wrong assumptions can lead to large errors. For example, the correct shape of the landslide should be considered in numerical modeling as it will influence the generated wave height. For rigid slides, the semi-elliptical shape represents the worst-case scenario, at least for submarine landslides. On the contrary, the shape of a subaerial landslide does not substantially affect the generated waves (Yavari-Ramshe & Ataie-Ashtiani, 2017). In this study, ArcGIS 10.7 software was employed to compute physical properties of the subaerial landslide, including geometry, center of mass, and volume. NHWAVE and FUNWAVE-TVD models were selected for the numerical simulations. The NHWAVE model, governed by non-hydrostatic Navier-Stokes equations, provided precise modeling of wave generation during the landslide. These equations are fully dispersive, which is critical for landslide simulation. However, due to its complexity and computational cost, it was selectively used for the generation phase of the tsunami. The model allows the choice between rigid and deformable landslides, influencing the resultant wave height. In parallel, the FUNWAVE-TVD model, employing high-order Boussinesq-type wave equations, focused on accurate simulations of wave propagation and coastal-scale inundation predictions. This fully nonlinear and dispersive model considered both the landslide body and surface wave interaction during slide motion. This model simulated tsunami wave propagation toward the shoreline, enabling determination of inundation, runup heights, and current velocities.

Next, a coupling method was implemented. Wave generation was simulated using the NHWAVE model, which solves the Navier-Stokes equations due to the more complex behaviour of flow near the landslide source; far-field wave propagation was simulated using a simpler model rather than the full 3D model as FUNWAVE_TVD.

The main objective of the study is to provide insights into potential tsunamigenic subaerial failures off Orcas Island, contributing to coastal hazard mitigation efforts. Specific objectives are to model, as accurately as possible, (1) a large potential subaerial failure of a slope that has undergone similar failures in the past, and (2) the resultant tsunami waves as they propagate in

both the near-source region and further afield, computing time series of wave heights and current velocities, and estimating maximum runup at affected coastlines.

### 1.4.2 Landslide and potential tsunami detection

As there is currently no system in place to detect or provide early warnings for landslides or landslide-generated tsunami waves in BC, the second part of my research focuses on assessing the use of instrumental seismic and hydroacoustic data for landslide detection and bottom pressure sensor data for tsunami detection in Douglas Channel and Gardner Canal (Box (b) in Figure 1.2). This is the first study of its kind in Canada. Additionally, the automated landslide detection method developed in this study based on an AI machine learning model, is a novel approach not seen in previous studies elsewhere in the world.

Based on previous studies in comparable settings (Heesemann et al., 2014; Dziak et al., 2015; Igarashi et al., 2016; Tepp et al., 2019; Clare et al., 2024; Tepp & Dziak, 2021), the combination of data from seismometers, hydrophones, and bottom pressure sensors is ideal for enabling detection of landslides and possible tsunamis.

Seismic events originating from sources such as landslides, debris flows, rockfalls, and snow avalanches generate ground vibrations as material descends under the influence of gravity (Suriñach et al., 2005; Kao et al., 2012). These vibrations can be detected by seismometers, and analyzing the waveforms proves valuable for identifying seismic signals associated with these events in real time or near real time (Suriñach et al., 2005). Hydrophones, converting underwater sound waves into electrical impulses, play a crucial role in enabling prompt data analysis and generating calibrated waveform information (Madhusudhana et al., 2022). They unveil distinct spectral banding and signal duration across various stages of landslides (Caplan-Auerbach et al., 2014). This distinctive feature renders hydrophones essential for early warning systems (Chierici et al., 2017). Recognizing ground movements and acoustic emissions resulting from friction during landslide deformation enhances the efficacy of these devices in foreseeing and mitigating potential resultant hazards, including tsunamis (Chierici et al., 2017). In contrast to seismometers, which can capture landslide seismic signals within a 150 km range of the source, hydrophones can detect signals beyond 500 km, contingent on the type and size of the landslide source (Tepp et al., 2019).

To identify potential tsunamis in a warning system, data from bottom pressure sensors (BPSs) are critical (Chierici et al., 2017). Once the data are processed and specific thresholds are established, BPSs become well-suited for tsunami detection (Chierici et al., 2017). The recording of hydrostatic bottom pressure over time within the water column, just above the pressure sensor, enables accurate measurements of sea level variations and detection of abrupt changes in water level (Chierici et al., 2017). As a result, BPSs play a crucial role in accurately measuring sea levels, offering the capability to identify sudden changes, which is particularly valuable for the detection of tsunami waves (Chierici et al., 2017). A network of BPSs is an important component

of a tsunami early warning system (Comfort et al., 2012; Kurkin et al., 2016). These sensors provide an additional/alternative method of monitoring systems on unstable rock slopes since they are capable of detecting all potential tsunamis in fjords or lakes (Harbitz et al., 2014). The seismic signal and deep-water pressure sensor technique, commonly used in oceanic earthquake tsunami warning systems, is insufficient for fjords or lakes due to different source processes and shorter tsunami travel durations from rockslide locations to risk-prone zones (Harbitz et al., 2014).

Considering the information provided earlier, the implementation of integrated networks onshore and offshore, featuring broadband seismometers, hydrophones, and underwater pressure-monitoring sensors, has emerged as a viable solution, especially in remote regions (Brillon et al., 2018; Clare et al., 2024). For instance, the hydroacoustic network of the International Monitoring System (IMS), which consists of cabled hydrophone arrays in the water and T-phase-optimized seismic stations on land, is essential for identifying submarine eruptions (Tepp & Dziak, 2021). A notable experiment package of hydrophone, seismometer, and pressure sensor components was highlighted by the Hawaii Undersea Geo-Observatory (HUGO) system deployment at Lo'ihi Seamount in 1991 (Caplan-Auerbach & Duennebier, 2001; Matsumoto et al., 2023). This comprehensive monitoring approach holds the promise of enhancing early warning systems by detecting subaerial and submarine landslides and potential resultant tsunamis and gauging the subsequent dynamics of the waves (Brillon et al., 2018).

The main objectives of my research are to establish a methodology for detecting the location and timing of landslides in the study area using seismic and hydroacoustic data. Additionally, the aim is to develop an algorithm capable of capturing water level changes for the detection of tsunami waves. The ultimate goal of this research as a future work is to integrate sophisticated signal processing techniques from seismic, hydroacoustic, and pressure sensor data to enable real time detection, paving the way for a real time detection and prospective landslide tsunami early warning system.

## 1.5 Thesis outline

This thesis consists of four chapters, with three additional chapters beyond the current one. Chapter 2 presents the results of numerical simulations focusing on a potential subaerial landslide along the Orcas Island coast and the resulting tsunami waves in the southern Strait of Georgia. Chapter 3 introduces a new method for landslide detection and shares the outcomes of utilizing different types of instrumental data, including seismic, hydroacoustic, and hydrostatic pressure data. The goal is to determine an optimal method for landslide detection and its potential application for tsunami early warning within Douglas Channel and Gardner Canal, with applicability elsewhere in the world. Chapter 4 summarizes the main findings of this research, its implications, and limitations and provides recommendations for future work.

# Chapter 2 Numerical modeling of a potential landslide-generated tsunami in the southern Strait of Georgia

## 2.1 Article information

This chapter was published in the journal Natural Hazards. I led the project development, performed the numerical simulations, wrote the manuscript, and generated the figures. Lucinda Leonard, Gwyn Lintern, and Richard Thomson contributed to project development, reviewed the findings, and assisted in data interpretation. Richard Thomson supervised all technical details. Manuscript drafts were edited by Lucinda Leonard and Richard Thomson. Soroush Kouhi assisted with ArcGIS analysis. The last revision was approved by all writers.

### 2.1.1 Citation

Nemati, F., Leonard, L., Thomson, R., Lintern, G., Kouhi, S., Numerical modeling of a potential landslide-generated tsunami in the southern Strait of Georgia. Natural Hazards 117, 2029–2054 (2023). https://doi.org/10.1007/s11069-023-05854-w

### 2.1.2 Authors Names and Affiliations

F. Nemati[1], L. Leonard[1], R. Thomson[2], G. Lintern[3], S. Kouhi[4]

[1] School of Earth and Ocean Sciences, University of Victoria, 3800 Finnerty Rd, Victoria, BC V8P 5C2, Canada

[2] Institute of Ocean Sciences, Fisheries and Oceans Canada, 9860 West Saanich Road, Sidney, BC V8L 4B2, Canada

[3] Geological Survey of Canada-Pacific, Natural Resources Canada, 9860 W Saanich Rd, Sidney, BC V8L 4B2, Canada

[4] Applied Science Solutions, Ocean Networks Canada, 2474 Arbutus Rd, Victoria, BC V8N 1V8, Canada

## 2.2 Abstract

We report results of numerical simulations of a potential subaerial landslide on the coast of Orcas Island and the resultant tsunami waves in the southern Strait of Georgia near the US/Canada border. A likely trigger is strong ground shaking during large earthquakes on the nearby Holocene-active Skipjack Island fault zone. For a worst-case scenario, we assume a rigid subaerial failure on the steep northeast coast of the island, spanning the ~5 km between previous landslide deposits on the adjacent seafloor. The landslide motion and resulting tsunami

generation are modelled using the three-dimensional (3D) non-hydrostatic physics-based NHWAVE model. The simulated failure moves downslope with a peak velocity of 13.64 m/s and travels 732 m before coming to rest after 85 s in 75-m water depth. Tsunami propagation is then continued using the 2D fully nonlinear and dispersive Boussinesq wave model FUNWAVE-TVD in a succession of layered and nested grids. The modeling reveals susceptible locations, particularly as waves will arrive with little or no warning. In the near-source region, modelled waves have peak amplitudes of 15-20 m, current speeds of up to 10 m/s, and runup of up to 30 m. Smaller, but significant, wave amplitudes and runup occur throughout the region surrounding Orcas Island. In the tsunami propagation direction, runup reaches 7.5 m at Neptune Beach near Lummi Bay. Both initial and reflected waves cause significant runup (> 1.5 m) along much of the shoreline between Point Roberts and Lummi Bay.

## 2.3 Introduction

The coastline of British Columbia (BC) is at risk from tsunami waves generated by a range of different sources, with most studies focusing on seismically generated tsunamis that have the potential to cause the most widespread damage (e.g., Cherniawsky et al., 2007; Fine et al., 2008; Gao et al., 2018). However, it is also critical to assess and mitigate the tsunami risk posed by subaerial and underwater landslides.

Several events over the past century have demonstrated that mass movements such as submarine slumps and subaerial rockfalls play a far more significant role in tsunami generation than previously thought. Many “tsunami earthquakes” are followed by landslides, which locally increase the tsunami waves generated by tectonic displacements (Iwasaki et al., 1996). Examples include the 1922 Flores Island (Imamura & Gica, 1996), 1998 Papua New Guinea (Imamura et al., 2001), 1999 Kocaeli, Turkey (Altinok et al., 1999), and 2011 Tohoku, Japan (Grilli et al., 2013) events. Landslide-generated tsunamis (LGTs) are far more confined than those induced by earthquakes, and they can cause extreme coastal runup and associated damage, particularly when the wave energy is retained by inlets or semi-enclosed embayments (Rabinovich et al., 2003). Tsunami runup resulting from subaerial landslides can be particularly high, as evidenced by several historical events with runup exceeding 100 m (e.g., Higman et al., 2018).

Landslides and triggered waves tend to recur regularly in some areas. After the 525 m runup tsunami in Lituya Bay, Alaska in 1958, field surveys indicated that LGTs had previously occurred in the bay in 1853–54 (120 m), 1874 (24 m), 1899 (60 m), and 1936 (150 m) (Miller, 1960; Rabinovich et al., 2003). Other recurring LGT sites along the west coast of North America include Kitimat Arm, BC (Johns et al., 1985), Yakutat, Russell Fjord, Skagway Harbor (all in Southeast Alaska) (Kulikov et al., 1996), and Puget Sound (Washington State) (Baum et al., 2005).

Local subaerial (e.g., Knight Inlet: 1999) and submarine (e.g., Kitimat Arm: 1975) failures, larger continental slope failures off the west coast of Vancouver Island, and those associated with the deformation front of the Cascadia subduction zone, with the potential to increase the size of

megathrust-generated tsunamis, are the most pertinent potential sources of a landslide tsunami for the west coast of Canada (Clague et al., 2003; Goff et al., 2020; Leonard et al., 2014; Murty, 1979). Potential far-field landslide tsunami sources include the Aleutian trench and volcanic flank collapses in Hawaii or other Pacific islands (e.g., Leonard et al., 2014).

The shores of BC have the highest tsunami hazard in Canada, with a significant population at risk, particularly along coastlines of the Strait of Georgia and Juan de Fuca Strait (which together with Puget Sound comprise the Salish Sea), as well as at the heads of inlets (e.g., Kitimat). This region also features a complex maritime environment as well as high onshore terrain, local steep slopes, and tidal variation, all of which contribute to a high risk of damage from subaerial and submarine landslides and related tsunamis. The damage risk increases if paired with high tide and/or storm surges.

The hazard of landslide tsunamis on the west coast of Canada remains poorly understood; the historical and geological record of slope failures is incomplete, as much of the seafloor remains to be mapped or studied in detail (Lintern et al., 2020). Only a few landslide tsunami modeling studies have been completed for the region, including the 1975 submarine failure in Kitimat Arm (Skvortsov and Bornhold, 2007), the sixteenth-century subaerial failure in Knight Inlet (Bornhold et al., 2007), and potential submarine failures of the Fraser delta front (Dunbar & Harper, 1993; Rabinovich et al., 2003), and offshore Texada Island (Rabinovich et al., 2003).

This study focusses on the potential for a large tsunamigenic subaerial failure off Orcas Island in the Strait of Georgia (Figure 2.1). This work forms part of a larger project to assess coastal flooding hazards in Boundary Bay, near the US/Canada border, from a variety of sources. Although no tsunamigenic landslides have been documented in the short written historical record (~< 200 yr), recent landslide activity is indicated by a rockfall debris apron as well as two distinct landslide deposits on the seafloor adjacent to northeast (NE) Orcas Island (Figure 2.1; Greene et al., 2018).

Both slides initiated subaerially on the steep NE side of the island, and one of the slides has a 450-m runout (Greene et al., 2018). A likely trigger for future slides here is strong ground shaking during large earthquakes on the nearby Skipjack Island fault zone, which has been active in the Holocene and may host earthquakes up to magnitude 7 or higher (Caston 2021; Greene et al., 2018). A sudden collapse along the steep NE coast of Orcas Island is expected to cause tsunami waves with the potential to strike nearby coastal areas of the Gulf and San Juan islands and the adjacent mainland—modeling is needed to assess this potential.

We carry out numerical simulations of a potential subaerial landslide on NE Orcas Island and the resultant tsunami waves to simulate their potential impacts on nearby coastlines in the southern Strait of Georgia near the US/Canada border (Figure 2.1). Using ArcGIS 10.7 software, we first compute the physical properties of the subaerial landslide (SAL), such as geometry (length, width), center of mass, and volume (Section 2.4.1). The kinematic characteristics of the landslide, such as initial acceleration and final velocity, are calculated using the law of motion in Section 2.4.2. Simulation of the subaerial landslide-generated tsunami (SALGT) is then performed

using NHWAVE software (Ma et al., 2012) (Sections 2.4.3 and 2.4.4), and the results of the numerical simulations are interpolated to the FUNWAVE–TVD (Total Variation Diminishing) variant of the fully nonlinear Boussinesq wave model (FTVD) (Kirby et al., 2013; Shi et al., 2012).

This model simulates tsunami wave propagation toward the shoreline (Sections 2.4.3 and 2.4.4), enabling us to determine inundation, runup heights, and current velocities that are described in Section 2.5.

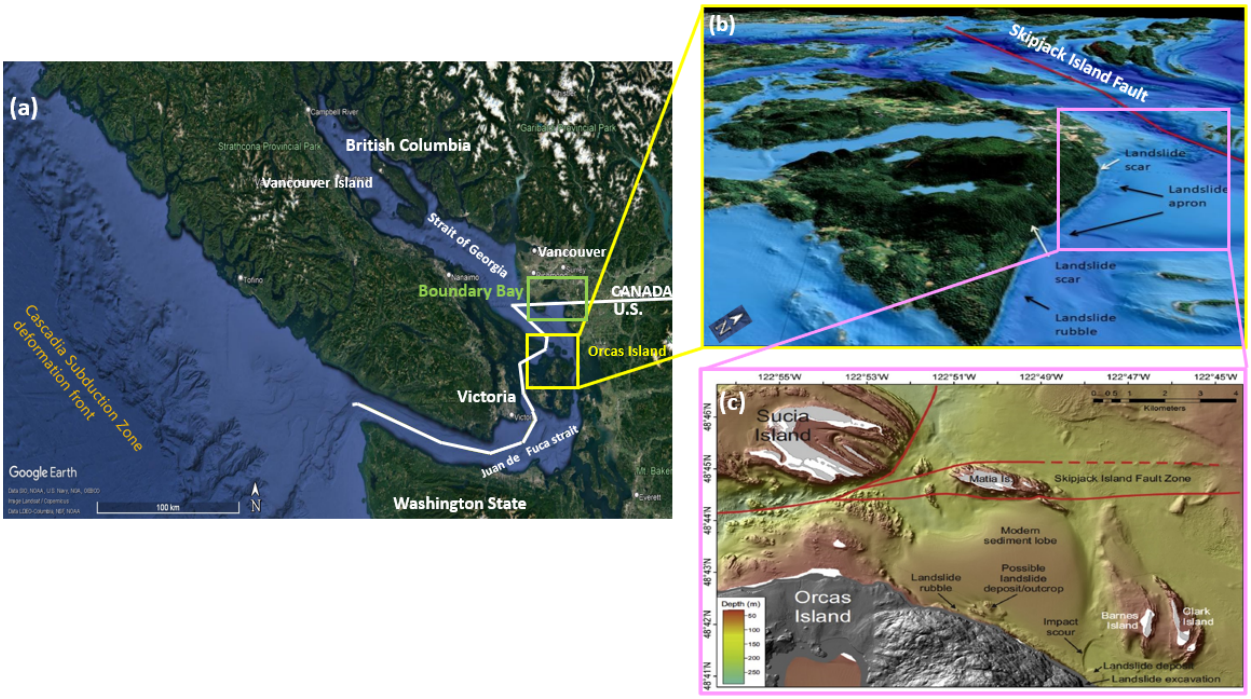


Figure 2.1. (a) Map of the study area, highlighting the locations of the landslide source (Orcas Island) and Boundary Bay as the focus for assessing tsunami impacts; (b) evidence of subaerial landslide failures near Orcas Island (modified after Greene (2019)); and (c) high resolution multibeam echosounder (MBES) bathymetric and land LiDAR images indicating the area of the Skipjack Island fault zone and evidence of past landslides along northeastern (NE) Orcas Island (modified after Greene et al., 2018).

## 2.4 Subaerial landslide-generated tsunami (SALGT) modeling

### 2.4.1 Location and volume of the potential landslide

The boundaries, form, and volume of a landslide must be approximated for accurate numerical modeling. Subaerial slides have a greater tsunamigenic potential than submarine slides of equal volume and shape (Fornaciai et al., 2019). The most significant factor affecting the evolution of a slide-generated tsunami and associated wave heights is the slide volume (Chen et al., 2014; Løvholt et al., 2020).

In our modeling, we consider the largest likely tsunamigenic subaerial landslide on NE Orcas Island. Given the occurrence of two large landslide deposits on the adjacent seafloor and a debris

apron that extends between the deposits, we postulate that the entire steep slope of NE Orcas Island between the two large deposits is susceptible to a future failure. This failure is considered to be a worst-case scenario. To pinpoint the position of the probable landslide, geological mapping data were merged with digital elevation models (DEMs) obtained from multibeam bathymetric and topographic survey data. The potential failure area is shown in Figure 2.2; its cross-slope width and downslope length are estimated to be ~5840 m and 1080 m, respectively.

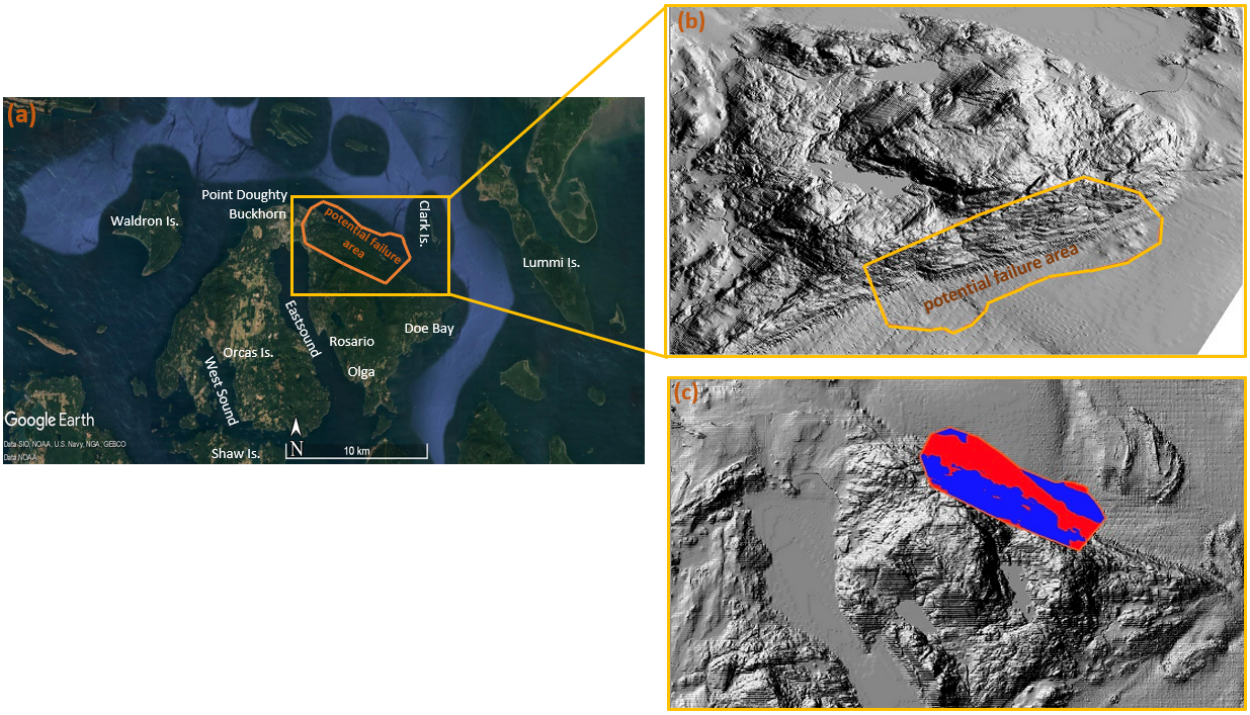


Figure 2.2. (a) Site of the potential subaerial landslide (SAL) failure area based on DEM data and the extent of previous failures as documented by Greene et al. (2018); (b) Orange polygon showing the potential failure area in the DEM; and (c) SAL volume evaluation for the orange polygon. Summation of the negative and positive values provides the total volume estimate of the failed slope. Red denotes net gain (positive values) and blue denotes net loss (negative values).

The volume of the potential landslide was calculated by approximating a post-failure surface that is based on an interpolation between the existing large landslide deposits and analyzing the volume difference between the pre- and post-failure DEMs. The volume was computed using the ESRI ArcGIS 10.7 GIS software's "Spatial Analyst Cut Fill" technique to calculate projected net-loss volumes. This method generates a map based on two input raster surfaces of the potential slide area, one before and one after the slide occurrence; the seafloor map is characterized by the difference between the pre-slide bathymetry and a virtual plane (the approximated post-failure surface) (e.g., Verbovšek et al., 2017). The difference between the pre- and post-failure surfaces on the seafloor is then subtracted from a digitized polygon representing the onshore potential failure area in order to produce the post-failure subaerial surface. We used a global polynomial

trend interpolation set with a polynomial order of three (P3) to create the virtual plane surfaces. The pre- and post-failure surfaces were then run through the "Cut Fill" processing tool to calculate the volume of the potential slide (Verbovšek et al., 2017). The tool compares the heights of raster values in each cell. The volume difference is given as positive if the material was removed (blue in Figure 2.2c) or negative if the material was added (filled) (red in Figure 2.2c). This estimated volume approach does not take into account the other more complex strategy of anticipating volumes for un-failed slides, e.g., using data from core profiling or seismic surveys, as no such data are available. The volume of the potential worst-case landslide is estimated at 0.17 $km^3$ (Table 2.1).

Table 2.1. Orcas Island SAL specifications and volume estimation from ArcGIS 10.7 and analytical equations.

| Parameter | |
|---|---|
| Cross-slope width, $w\ (m)$ | $5,840$ |
| Downslope length, $b\ (m)$ | $1{,}080$ |
| Maximum thickness, $T\ (m)$ | $75.7$ |
| Azimuthal direction of motion, $\theta\ (°)$ | $32$ |
| Initial elevation, $h0\ (m)$ | $120$ |
| Center of Mass $(°E, °N)$ | $(-122.8192, 48.6893)$ |
| Total Area $(m^2)$ | $4{,}665{,}720$ |
| Volume $(m^3)$ | $168{,}037{,}890$ |
| Volume, $V_s\ (km^3)$ | $0.17$ |

## 2.4.2 Kinematic and geometric parameters of the subaerial landslide

As previously noted, landslide volume is the most important factor determining tsunamigenesis, but other variables such as landslide frontal area and landslide dynamics including velocity, Froude number, and acceleration also play a significant role (Løvholt et al., 2020).

Sliding and slumping are the two most common mechanisms for subaerial and submarine mass failures (MF), as rigid or deforming translations down a flat slope (Grilli & Watts, 2005). The MF center of mass motion is determined by geometric, hydrodynamic, and geotechnical characteristics, depending on whether the MF is rigid or deforming (Grilli & Watts, 2005).

Using the estimated geometry of the Orcas Island SAL, we numerically modeled the tsunami generation and propagation. No mass (material) was extracted from the bathymetric data before the simulations. We assume a worst-case failure scenario consisting of a slump, a rigid and impulsive subaerial landslide. Rigid landslides are more tsunamigenic and create more inundation than deformable landslides (Schambach et al., 2019). In addition, a rigid landslide can be

characterized in numerical simulations as a mound with a "Quasi-Gaussian" cross-sectional shape of elevation $\zeta(\xi, \chi, t)$, an elliptical footprint of downslope length "$b$" and cross-slope width "$w$", and a maximum thickness "$T$" (Grilli et al., 2015).

The geometric parameters and beginning position determined for the modeled landslide are given in Table 2.1 and Figure 2.3. We can only make estimates about the probable landslide thickness due to a lack of geophysical and morphological knowledge about the landslide site. The maximum thickness, $T = 75.7$ m, is determined using the volume produced from ArcGIS 10.7 software, the elliptical footprint of the landslide (Table 2.1), and the $V_s = 0.351\ bwT$ equation (Grilli et al., 2015). These dimensions provide a $T/b$ value of 0.07, which lies at approximately the lower end of the $T/b$ validity range of [0.1, 0.15] determined by Watts et al. (2005) based on 12 numerical simulations of underwater slumps.

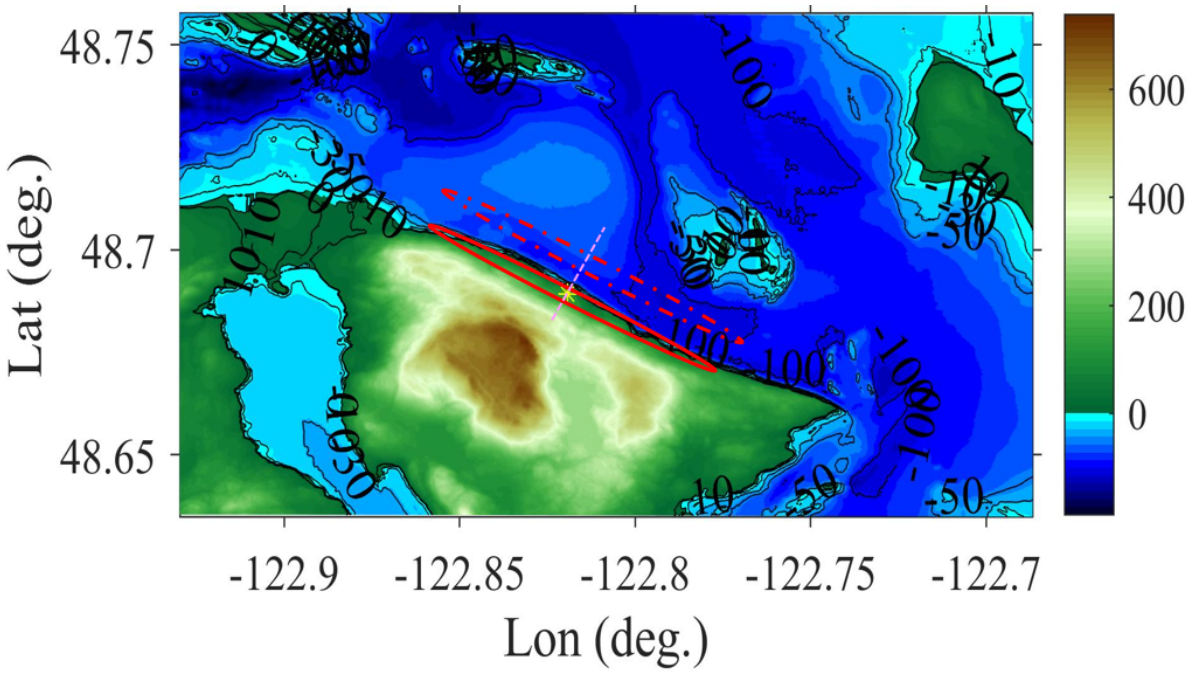


Figure 2.3. As simulated in NHWAVE, red ellipses depict the footprint of an imagined landslide before and after failure (solid/ chained); yellow star represents the centroid of the subaerial landslide (SAL). The pink dashed line depicts the landslide's downward path to the sea. Depths and elevations are in meters.

The coordinate transformation to the local MF slope-parallel coordinate system $(\xi, \chi)$ is specified based on the MF starting center of mass position (Table 2.1), in global axes $(x, y)$ and azimuthal direction of motion, $\theta$ (as defined in Schambach et al., 2020).

Grilli and Watts (2005) addressed 3D problems in the vertical plane for slices of width "$w$" since it is assumed that mass failures are homogeneous in width. Further assumptions include the absence of isolated high Reynolds number flows near moving MFs, which allows the fluid to be assumed to be inviscid and irrotational (Grilli & Watts, 2005).

The kinematic properties of the rigid subaerial slump are calculated using the analytical rules given by Grilli & Watts (1999, 2005) and Watts et al., (2005). The kinematics for the rigid body motion are identical to its center of mass motion, $S_c(t)$ (provided by Eq. (2.1) below), in azimuthal direction $\theta = 32°$ on the surface of uniform slope $\alpha_s = 34°$.

$$S_c(t) = S_0\left(1 - cos\frac{t}{t_0}\right) \quad for \quad 0 \le t \le t_f \tag{2.1}$$

where $S_0 = S_f/2$, $t_f$ is the runout time, $t_0 = t_f/\pi$, and $S_c(t) = S_f$ for $t > t_f$ (where the MF starts moving at t = 0 ) (Grilli et al., 2015).

Based on prior research (Locat et al., 2009), it can be shown that the maximum displacement (runout) $S_f$, is rather small in its leading direction of movement down the slope $(S_f < b)$ throughout its tsunamigenic movement, spanning an indeterminate length of activity, $t_f$ (Grilli & Watts, 2005).

$U_{max} = S_0/t_0$ is the maximum slump velocity (Schambach et al., 2020). Similarly, the slump acceleration $A(t)$ is calculated using Eq. (2.1), where $A_0$ is the starting acceleration (Grilli et al., 2015). $U_{max}$, $A_0$, and other kinematic parameters estimated for the Orcas Island SAL are given in Table 2.2.

Table 2.2. Parameters used to define the rigid (mass failure, MF) slump kinematics simulated in NHWAVE (see Table 2.1 for other parameters).

| Parameter | |
|---|---|
| MF shape | Quasi-Gaussian |
| Runout time, $t_f$ $(s)$ | 84.3 |
| Runout distance, $S_f$ $(m)$ | 731.89 |
| Maximum velocity, $U_{max}$ $(\mathrm{m/s})$ | 13.64 |
| Starting acceleration, $A_0$ $(\mathrm{m}/s^2)$ | 0.51 |

Although landslide velocity is important for tsunamis generated by impulsive slides, such as fast-moving SALs, it is well recognized that landslide acceleration dictates the initial tsunami elevation generated by translational landslides (Løvholt et al., 2015). In other words, the starting acceleration, which impacts initial elevation in the event of a lengthy run-out, is the most important kinematic parameter for a tsunamigenic landslide (Løvholt et al., 2015).

SALs, unlike totally submerged landslides, frequently entail significant Froude numbers and nonlinearity (Løvholt et al., 2020). The landslide Froude number also serves as the most important kinematic property for determining the height of the resultant tsunami for SALs and slumps where the runout distance is sufficiently short in relation to the slide length (Løvholt et

al., 2015). As a result, the landslide moves erratically, producing shorter and higher waves and causing frequency dispersion (Løvholt et al., 2015).

Due to the low velocity and modest amplitude of motion, little hydrodynamic drag is anticipated for rigid slumps (Grilli et al., 2015). Thus, inertia comprises both the MF mass $M_s = \rho_s V_s$, with $\rho_s$ representing the slide bulk density, and the specific density $\gamma_s = \rho_s/\rho_w$, with $\rho_w$ denoting the water density, as well as an added mass $\Delta M_s = C_M \rho_w V_s$, defined by way of an added mass coefficient $C_M$. For rigid slumps failing in a circular motion of high radius $R$ and modest angular displacement $\Delta\Phi$, we can also assume constant basal friction. By formulating a dynamic balance between weight, buoyancy, inertia, and basal friction forces Grilli et al. (2015) developed an analytical rule of motion for the center of mass:

$$S_0 = \frac{R\Delta\Phi}{2}, \qquad t_0 = \sqrt{\frac{R}{g}\frac{\gamma+C_M}{\gamma-1}} \text{ with } \qquad R \cong \frac{b^2}{8} \tag{2.2}$$

where "$g$" represents earth's gravitational acceleration. The radius of the slump motion is calculated using the semi-empirical formula provided by Watts et al. (2005) as a function of slump downslope length and maximum thickness.

We may deduce from Eq. (2.1) to (2.2) that the slump law of motion is a function of runout distance $S_f$, and the slump time of motion $t_f$ is a function of $\gamma = \rho_s/\rho_w$, the specific density (Grilli et al., 2015).

In our study, we assumed a slide material density of $\rho_s = 1790\ kg/m^3$, an average sea water density of $\rho_w = 1025\ kg/m^3$ (so, $\gamma = 1.75$) and $C_M = 1$, a hydrodynamic added mass coefficient.

Using Eq. (2.2), a radius of nearly circular motion $R$, characteristic time $t_0$, and characteristic distance of motion $S_0$, are estimated. Then, the maximum displacement ($S_f$) and runout time ($t_f$) can be derived from Eq. (2.1), giving $S_f = 732$ m and $t_f = 84$ s in azimuthal direction $\theta = 32°$ (Table 2.2).

Parameters computed in Table 2.1 and 2.2 are used in the slump law of motion in addition to slump geometry to assign the bottom boundary condition in NHWAVE, described in Section 2.4.4 (Grilli et al., 2015; Schambach et al., 2019, 2020).

### 2.4.3 Computational grids, and bathymetry/topography data

Based on guidelines from the US National Tsunami Hazard Mitigation Program (NTHMP) (Dunbar & Weaver, 2015), the resolution in coastal regions for evaluating coastal runup should be 10 m or better. Use of a coarser resolution grid along the coast cannot properly predict tsunami coastal inundation and runup; e.g., coarse resolution may create obstructions that prevent waves from entering a port and limit the maximum wave height and inundation (Nemati et al., 2019).

In this study, we integrate and interpolate the best available bathymetry and topography data into five horizontal Cartesian grids of different resolutions (Figure 2.4; Table 2.3). We used 10 m topo-bathymetry data from Natural Resources Canada (2021) to create a seamless topographic/bathymetric DEM for the grid G0 region with 160-m resolution. For the other grids, G1, G2a, G2b, and G3N, we utilized data from a cross-border 3-m resolution DEM compiled by various government agencies (Amante et al., 2020; Carignan et al., 2019). The resulting bathymetry and grid areas are shown in Figure 2.4.

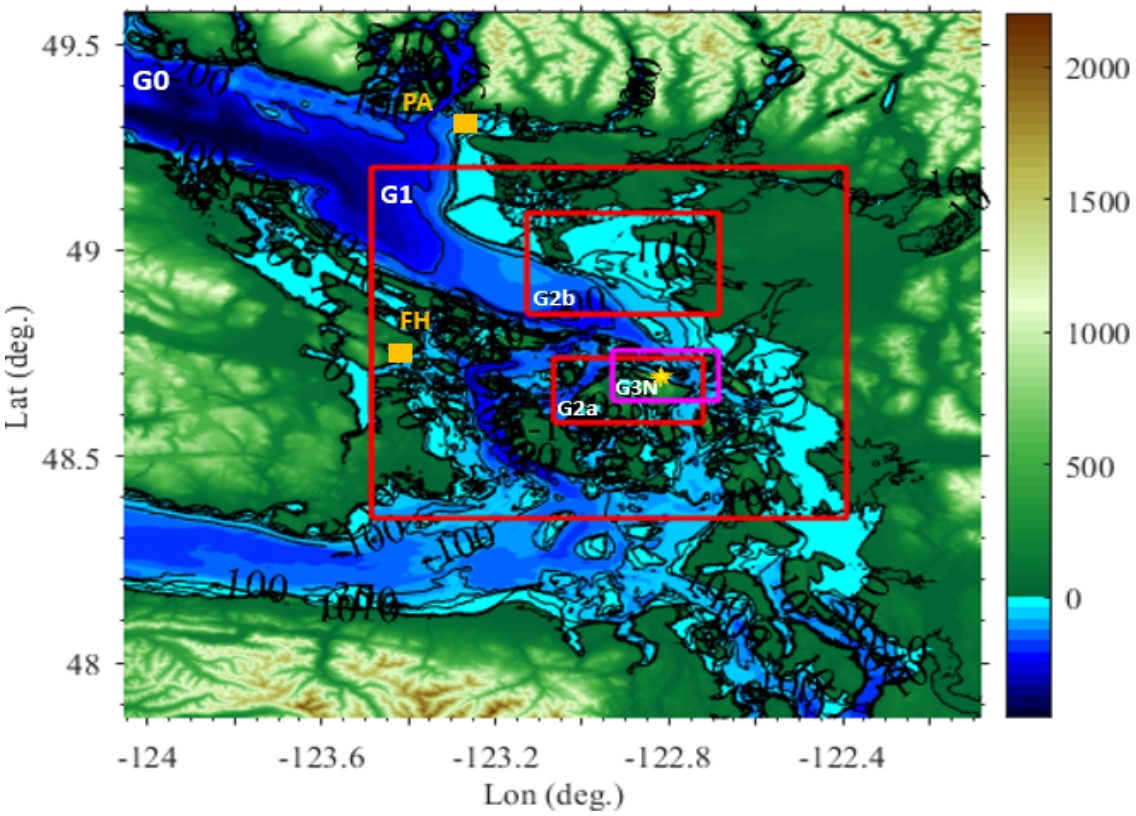


Figure 2.4. Computational grid footprints for the landslide and tsunami simulations (red and pink boxes; details in Table 2.3); color scale and black contours in meters. Chart Datum bathymetry/topography data are from Natural Resources Canada (2021) + 1.5 m for the tide (Higher High Water Mean Tide; HHWMT) for grid G0; red boxes (G0, G1, G2a, and G2b) are modelled in FTVD, and pink box (G3N) is simulated in NHWAVE with 5 vertical σ–layers. The yellow star marks the centroid of the subaerial landslide (SAL). Orange squares denote tide gauge sites: Point Atkinson (PA) and Fulford Harbour (FH).

G0, G1, G2a, and G2b nested grids, with resolutions of 160 m, 40 m, 10 m, and 10 m, respectively, are utilized in the FTVD simulations (Figure 2.4; Table 2.3). The grid G0 covers the largest area, including northern Washington State, southern Vancouver Island, eastern Juan de Fuca Strait, southern Strait of Georgia, and the adjacent BC mainland; G1 encompasses the southernmost portion of the Strait of Georgia and adjacent parts of the mainland and Vancouver Island. The two 10-m resolution grids, G2a and G2b, are nested in order to more rigorously simulate tsunami inundation and runup in two areas of particular interest: (1) the coastal parts

of Orcas Island, and (2) the Boundary Bay region. G3N, also at 10-m resolution, covers the eastern sector of Orcas Island and is used to model landslide generation in the NHWAVE model, with five evenly spaced boundary fitted layers in the vertical (from the sea surface to the seabed).

Table 2.3. Parameters of computational grids used in simulations with NHWAVE (G3N), FTVD (G0-G2a, b) (Figures 2.4, 2.5). The projection origin is at the center of each grid.

| Grid | Mesh size $(M, N)^a$ | Resolution $(m)$ | Projection origin (Lat., Lon.) |
|---|---|---|---|
| G3N | 1792, 136 | 10 | 48.6965° $N$, -122.8083° $E$ |
| G0 | 924, 1192 | 160 | 48.718° $N$, -123.0518° $E$ |
| G1 | 2008,2368 | 40 | 48.7759° $N$, -122.9392° $E$ |
| G2a | 2532,1744 | 10 | 48.6607° $N$, -122.8939° $E$ |
| G2b | 3256,2736 | 10 | 48.9679° $N$, -122.9058° $E$ |

$^a$ M and N are the number of cells in the x and y directions, respectively

The effect of ocean tides on inundation and runup is another important component in tsunami modeling; a higher tide at the time of the landslide leads to greater inundation for the same tsunami source. We used a tide level of Higher High Water Mean Tide (HHWMT), the average of all Higher High Water projections at a site over the previous 19 years; this is equivalent to Mean Higher High Water (MHHW) in the USA, typically used in tsunami modeling (e.g., Suleimani et al., 2005). The reference level in the topo-bathymetry dataset (grid G0) is chart datum (CD), roughly comparable to the lowest astronomical tide level (Vancouver Fraser Port Authority, 2020); thus, the dataset must be corrected to HHWMT.

The reference level of topo-bathymetry data for all the other grids (G1, G2a, G2b, and G3N) is based on the Canadian Geodetic Vertical Datum 2013 (CGVD2013), which is deemed comparable to Mean Water Level (MWL), but with an offset of − 0.2 m.

The next step in the modeling was to add the Higher High Water Mean Tide (HHWMT) level to CD or CGVD2013 levels in order to incorporate the static tide influence into the topo-bathymetry data. In this case, we used the HHWMT from the Canadian tide and current tables (Canadian Hydrographic Service, 2022), which is based on CD, for the Fulford Harbour and Point Atkinson stations, which are the closest stations to the study area (see Figure 2.4 for locations). Fulford Harbour, on the southeast coast of Salt Spring Island, BC, has an HHWMT value of 3.3 m, whereas Point Atkinson, in West Vancouver, has an HHWMT value of 4.5 m. Grid G0 bathymetry is updated with the average HHWMT of these stations (3.9 m). The other grids are based on MWL, so must be corrected for the difference between MWL and HHWMT. This difference, the tidal amplitude, is 1 m at Fulford Harbour and 1.4 m at Point Atkinson; we use the average of 1.2 m to correct the reference level of the topo-bathymetry data. This result is also consistent with prior research conducted by Fine and Thomson (2020).

### 2.4.4 Numerical models and tsunami modeling methodology

Tsunami waves generated by landslides are more challenging to model than those generated by earthquake displacements (Løvholt et al., 2015). Landslide collapse at the water body boundaries causes impulsive waves that spread outward and migrate along shorelines (Romano et al., 2019). The relative wave amplitude of a SALGT depends on both the Froude number (F) and the slide thickness, as confirmed in numerous studies (e.g., Fritz et al., 2004; Heller & Hanger, 2010; Fornaciai et al., 2019; Sarlin et al., 2021).

The tsunamigenic potential of a slide is determined by both the Froude number (F) and the slide thickness (Fornaciai et al., 2019). In order to determine how effectively landslides generate waves, we must calculate the Froude number, which is the ratio of landslide speed to wave speed (linear shallow water wave celerity = $\sqrt{gh}$ where h is the depth of the water). Wave generation is most efficient if the landslide and tsunami waves travel at the same velocity, whereby F = 1. As the Froude number decreases below unity, wave generation becomes less efficient (Fornaciai et al., 2019). In the case of the Orcas Island landslide, the maximum velocity of the landslide as it moves downward to the sea is around 13.64 m/s, and the water depth adjacent to the failure area is 75 m. Consequently, the Froude number is about 0.5, indicating moderately effective wave generation due to the landslide.

To model the Orcas Island landslide and subsequent tsunami, we use a coupled modeling approach, similar to that used in recent studies on landslide processes (e.g., Grilli et al., 2013, 2015; Schambach et al., 2019, 2020, 2021). Based on the dimensions determined in Sections 2.4.1 and 2.4.2, a simplified landslide form and plane geometry were computed on grid G3N (Figure 2.3).

The landslide failure movement and resulting tsunami production are modeled using the three-dimensional (3D) non-hydrostatic numerical wave model NHWAVE (Ma et al., 2012). In the horizontal direction, the model employs a Cartesian system ($\Delta x, \Delta y$), and in the vertical direction it uses a $\sigma$-layer boundary fitted grid (Schambach et al., 2020). With fully nonlinear free-surface boundary conditions, NHWAVE solves the inviscid Euler equations (viscous and turbulent effects can be incorporated if needed) (Ma et al., 2012). In most cases, because tsunami waves are approximately 2D, only a few $\sigma$-layers are needed (Schambach et al., 2020). Adding more $\sigma$-layers better quantifies wave dispersion, especially where the depth to wavelength ratio is relatively high. For coastal landslide tsunami simulations, five $\sigma$-layers appear to suffice (Grilli et al., 2015; Schambach et al., 2019, 2021). The use of three $\sigma$-layers in NHWAVE results in the same dispersive features as a 2D Boussinesq model (Schambach et al., 2020).

In the near field, five boundary-fitted vertical layers in the G3N grid are taken to estimate the lateral collapse landslide and the resulting tsunami production in the NHWAVE setup. Using NHWAVE to simulate wave generation helps us to improve the assessment of dispersive effects and horizontal velocities. In landslide tsunami generation and propagation models, the availability

of a frequency dispersion option has a substantial impact. Dispersion governs phase speed, wave-wave interactions during propagation, and tsunami impact (Schambach et al., 2021). Undular bores (also known as dispersive shock waves) are thought to be caused by dispersion across the crest and trough of prolonged shoaling tsunami waves near coasts, boosting coastal impact (Schambach et al., 2021; Madsen et al., 2008).

The modeled landslide occurs on the steep NE coastline of Orcas Island. When tsunami waves occur in shallow water, the relationship between the waves and the sloping seafloor is a crucial element to consider (Romano et al., 2019). The waves can be refracted or trapped (Romano et al., 2019). Therefore, the simulation begins on grid G3N (10-m resolution) with the most recent version of NHWAVE (v. s3.0), which can evaluate vertical acceleration impacts in the slide layer (Zhang et al., 2021a, b); this NHWAVE advancement is especially important on steep slopes (Grilli et al., 2019; Schambach et al., 2021).

Once the tsunami waves are generated, the waves are input to nested grids of increasing resolution toward the shore using the 2D fully nonlinear and dispersive Boussinesq wave model FTVD (Shi et al., 2012). The model simulates propagation from the near field to the surrounding coastlines in the far field.

Both directly forced waves and freely propagating waves occur during the landslide. The waves radiating away from the slide will encounter modified depths associated with the slide volume. It is these waves that need to take into account the changes in seafloor depth due to the slide. Unlike FTVD, NHWAVE can simulate moving bottom-generated waves in three dimensions at each time step, allowing velocities to be captured with more precision, as they change with depth during wave formation. As a result, landslide tsunami generation may be precisely simulated. On the other hand, coastal wave changeovers, such as wave breaking and dissipation, as well as incorporation of a shifting coastline, can be evaluated more precisely in FTVD. Furthermore, the use of a 2D grid in FTVD means that the computational time is a factor of three less than the required time for an identical horizontal resolution for a NHWAVE simulation. Owing to its spherical implementation, FTVD may be used for far-field tsunami propagation, whereas NHWAVE can only examine a Cartesian horizontal grid, limiting its applicability to near-field tsunami generation. These are the justifications for using linked modeling approaches in our research (more detail in Grilli et al., 2015). NHWAVE and FTVD are both open source (available on Github) and parallelized with Message Passing Interface (MPI) to operate effectively on big computer clusters (Schambach et al., 2020). According to NTHMP standards, the model has been fully verified based on laboratory and field benchmarks for both coseismic and rigid landslide tsunami generation and propagation (Ma et al., 2012; Tehranirad et al., 2012).

A similar coupled modeling strategy was previously used to simulate the coastal effect of transoceanic tsunamis along the US east coast, such as those resulting from a potential collapse of the Cumbre Vieja volcano in the Canary Islands (Abadie et al., 2012), for which the SAL tsunami source was computed using the multi-fluid 3D Navier–Stokes solver THETIS (Abadie et al., 2010).

Grilli et al. (2013) used an equivalent NHWAVE/FTVD coupling approach to model the Tohoku 2011 tsunami, where the seismic source was located as a time- and space-varying bottom boundary condition.

The Orcas Island landslide-generated tsunami was modeled using the initial landslide geometry and net-loss volume, kinematic parameters, and 10-m resolution bathymetry data. The modeled landslide stopped moving after runout time $t_f$ = 85 s, and modeling the tsunami waves was continued in NHWAVE for an additional 15 s. There is no need to continue modeling in NHWAVE for a longer time, since landslides are not tsunamigenic after they have stopped moving. An animation of the NHWAVE model simulation (VideoNo01.mp4) is provided in Online Resource 2 of the Natural Hazards paper.

After 100 s, tsunami simulation is continued using FTVD, with initial conditions based on the NHWAVE simulation results. Surface elevation, horizontal velocity, and after failure bathymetry are interpolated in grid G0, G1, and G2a. Tsunami propagation is then simulated from the source location to surrounding coastlines in a succession of layered and nested grids, with increased resolution in the areas of particular interest, as outlined in Section 2.4.3.

Absorbing (sponge) layers define open boundary conditions in both models. To prevent reflection at open boundaries, sponge layers are allocated, being 5 km wide at the west and 1 km at the south and north boundaries of grid G0. These widths appear adequate, as no reflection occurs at the boundaries in our results.

FTVD can compute inundation and runup with high precision at coastal locations by taking into account the impacts of bottom friction, dissipation, wave breaking, and the moving shoreline algorithm in the model (Shi et al., 2012). Where water depths are shallow, such as between Orcas Island and Boundary Bay, landslide-generated tsunami waves may not be widely dispersed in the beginning. The dispersive impact is also reduced if the landslide footprint is large in relation to the depth (Ma et al., 2012; Schambach et al., 2019, 2021). The footprint of the landslide in grids G2a and G2b is substantially larger (5.8 km width and 1.08 km length) than the maximum depth, which is roughly 180 m inside these grids. As a result, minimal wave dispersion occurs in those grid simulations.

In deeper water, as waves migrate away from shallow water locations, dispersion becomes more important. Significant dispersion occurs for the deeper-water grids G0 and G1.

We use a number of grid boundary stations (details not provided here) and tide gauge stations (Table 2.4; Figure 2.5, 2.6) to ensure data coupling between the grids. The boundary conditions for finer grids are based on the grid data at a time zero, i.e., the time series of boundary station elevation and horizontal velocity computed in grid G0 are given as the boundary condition for the nested grid G1, and the time series computed in grid G1 provide boundary conditions for the finer nested grids G2a and G2b.

In the NHWAVE and FTVD model simulations, bottom friction associated with coarse material is assumed ($C_d$ = 0.0025).

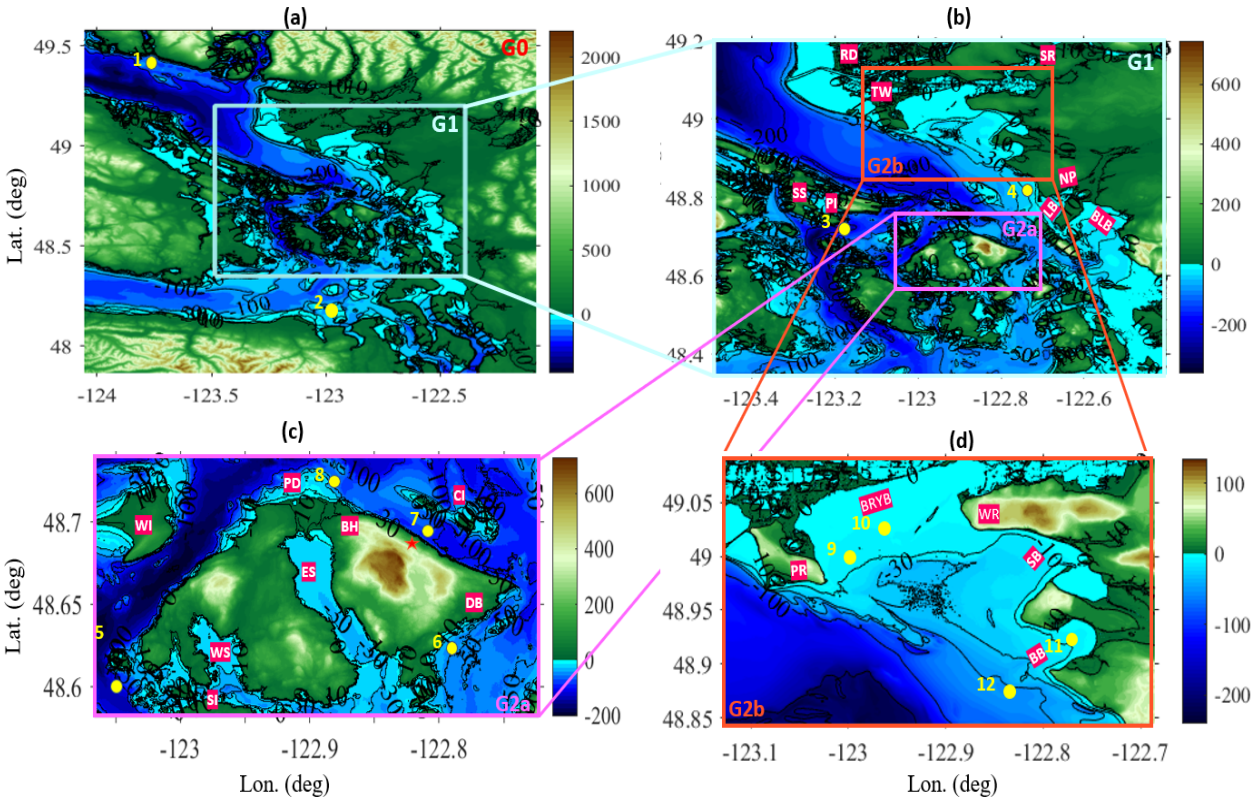


Figure 2.5. Footprints of nested computational grids and locations of the numbered stations (yellow circles) for which surface elevation time series are computed (Figure 2.6; Table 2.4). (a) grid G0 with stations 1,2 simulated in FTVD with 160 m resolution with footprint of grid G1 in light blue box; (b) grid G1 with stations 3,4 simulated in FTVD with 40 m resolution with footprints of grid G2a in pink and G2b in red; (c) grid G2a with stations 5-8 simulated in FTVD at 10 m resolution; red star shows the landslide center of mass; and (d) grid G2b with stations 9-12 simulated in FTVD at 10 m resolution. Color scales are bathymetry (< 0) and topography (> 0) in meters; black lines are bathymetric contours. BB = Birch Bay, BH= Buckhorn, BLB = Bellingham Bay, BRYB = Boundary Bay, CI= Clark Island, DB = Doe Bay, ES = Eastsound, LB = Lummi Bay, PD = Point Doughty, PI = Pender Island, PR = Point Roberts, RD = Richmond, SB = Semiahmoo Bay, SI = Shaw Island, SR = Serpentine River, TW = Tsawwassen, WI = Waldron Island, WR = White Rock, WS = Westsound.

## 2.5 Tsunami modeling results

The modeled tsunami waves generated by the potential Orcas Island landslide are shown and described in this section. Water surface elevations are shown as time series for the 12 selected stations in Figure 2.6 (with plots for a total of 34 stations provided in Online Resource 1 of the Natural Hazards paper), and on maps in Figure 2.7 and 2.8. Maps of current velocities are shown in Figure 2.9 and 2.10 and the maximum tsunami runup within the high-resolution grid areas in Figure 2.11. Table 2.4 contains characteristics of the modeled tsunami waves at the 12 selected stations.

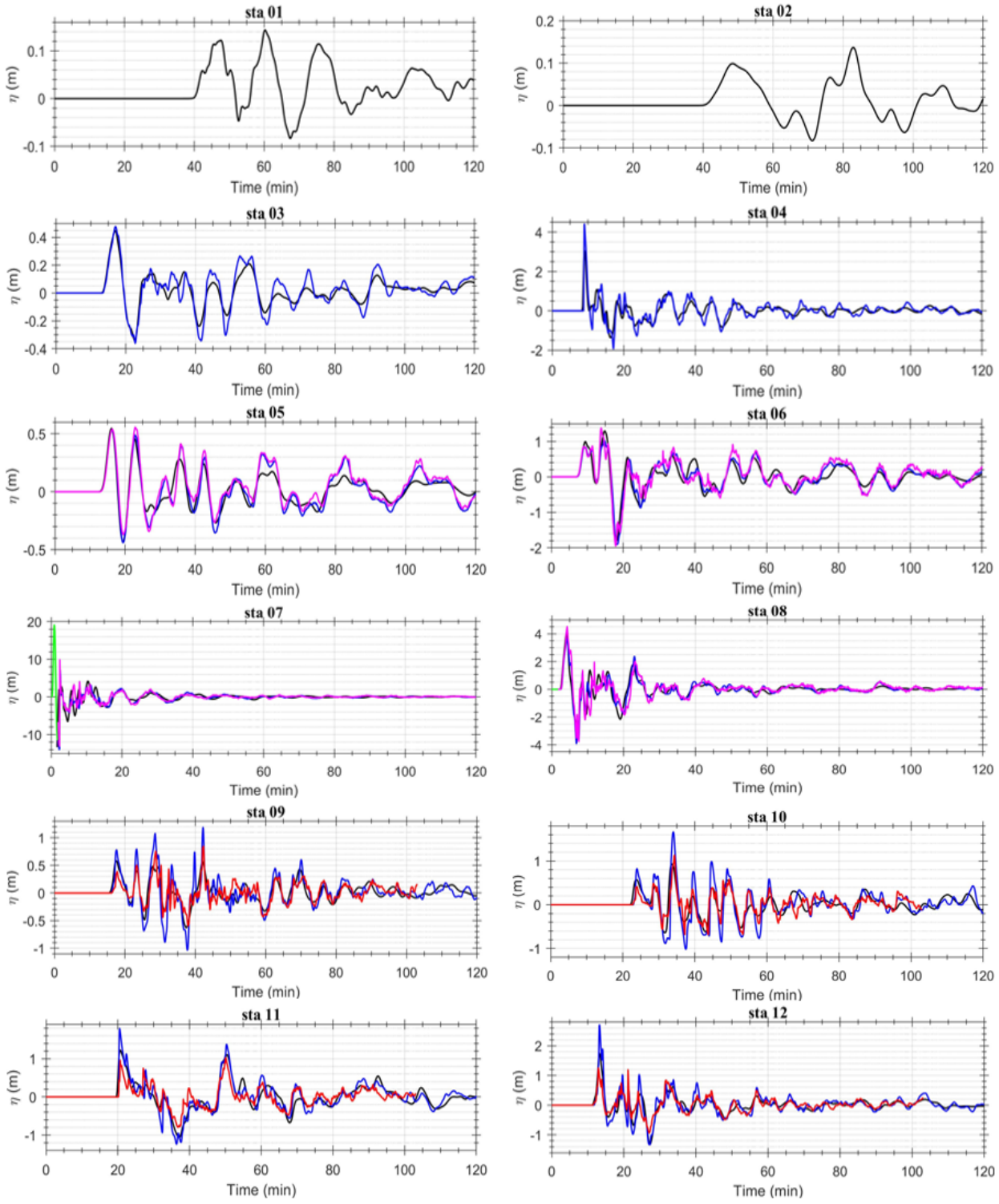


Figure 2.6. Time series of surface wave elevations in grid G0 (black), G1 (blue), G2a (pink), G2b (red) and G3N (green) at stations: 1 to 12 (Figure 2.5, Table 2.4).

Table 2.4. Locations and modelled tsunami wave characteristics at numbered stations for which surface elevation time series are shown in Figure 2.6.

| Sta. No. | Lon. ($°E$) | Lat. ($°N$) | Depth (m) | Arrival Time (min) | Max. wave ampl. (m) | Time of max. (min) | Typical period (min) | Max. current speed (m/s) | Grid used |
|---|---|---|---|---|---|---|---|---|---|
| 01 | -123.755 | 49.417 | 187.6 | 40 | 0.14 | 3.1 | 16 | 0.02 | G0 |
| 02 | -123.003 | 48.157 | 56.0 | 40.2 | 0.14 | 83 | 33.7 | 0.08 | G0 |
| 03 | -123.178 | 48.718 | 254.7 | 13.1 | 0.47 | 17.2 | 11.1 | 0.13 | G0, G1 |
| 04 | -122.751 | 48.818 | 36.8 | 8.8 | 4.41 | 9 | 6.3 | 2.17 | G0, G1 |
| 05 | -123.052 | 48.593 | 138.1 | 13 | 0.55 | 16.2 | 8 | 0.2 | G0, G1, G2a |
| 06 | -122.792 | 48.620 | 49.2 | 7.3 | 1.35 | 13.2 | 5.8 | 0.52 | G0, G1, G2a |
| 07 | -122.804 | 48.693 | 88.7 | 0.08 (5 s) | 19.13 | 0.8 (50 s) | 2 | 6 | G0, G1, G2a, G3N |
| 08 | -122.877 | 48.728 | 57.1 | 2.3 | 4.7 | 4.3 | 5.7 | 2.6 | G0, G1, G2a, G3N |
| 09 | -122.992 | 48.990 | 9.6 | 16.3 | 0.84 | 42.3 | 6.1 | 0.48 | G0, G1, G2b |
| 10 | -122.939 | 49.011 | 6.2 | 22.7 | 1.13 | 34.3 | 7.5 | 1.3 | G0, G1, G2b |
| 11 | -122.766 | 48.920 | 9.2 | 20.2 | 1.03 | 50.1 | 6.7 | 0.98 | G0, G1, G2b |
| 12 | -122.839 | 48.874 | 5.5 | 11.7 | 1.26 | 12.9 | 5.8 | 0.56 | G0, G1, G2b |

The 3D movement of the Orcas Island SAL is simulated in the NHWAVE model; the slide material flows downslope to the ocean, where the water depth is 75 m. During the northeastward propagation of the tsunami waves, the water depth remains uniform over a 1.7 km distance (Figure 2.5). The depth then shallows to 40 m for about 1.4 km near Clark Island, before returning to a consistent depth of 100 m for another 2.16 km (to Lummi Island).

Surface elevation estimates from NHWAVE and FTVD up to t = 100 s show good agreement especially for the crest-to-trough heights of the leading waves. This is an indication that the two models are well coupled.

In grid G2a, immediately adjacent to the simulated subaerial landslide site, a huge initial tsunami wave is generated, with a wave crest amplitude of ∼20 m (Figure 2.6-station 07, 7-b). The initial crest is followed by a ∼12-m trough. Tsunami wave reflection and shoaling are primarily regulated by nearshore bathymetry, and the details of the tsunami source fade as the waves move away from the source region (Grilli et al., 2019). Hence, in the near-source region, the tsunami waves have very small wavelengths, with a period of approximately 400 s, and dissipate to near-zero amplitudes after 40 min due to a near-uniform depth, relatively high bottom friction, and marked dissipation along the shoreline (see Figure 2.6-Stations 07, 08). As was previously indicated, a short runout distance with respect to the slide length may be the cause of the shorter wave duration, higher waves, and fast wave dissipation. Although the majority of wave energy propagates away from Orcas Island with the leading wave, some tsunami waves are re-directed by bathymetry and surrounding islands to eventually run up on shoreline areas around Orcas Island, away from the source location.

In the Eastsound and Westsound regions (see Figure 2.5 for locations), the leading wave is 0.4 m and subsequent wave surface elevations increase to 1.24 m (detailed time series in the Online

Resource 1 of the Natural Hazards paper, station 23); this occurs due to shoaling and wave buildup inside these semi-enclosed shallow areas that can occur due to the potential resonance of trapped waves (Nemati et al., 2019). Nearshore amplification effects are common and are often connected to bathymetric control (producing wave convergence/divergence) and coastline form (i.e., causing potential resonance) (Nemati et al., 2019).

Further from the source location, the maximum wave crests do not exceed 6 m (e.g., Figure 2.6-stations 08 and 07). Near Waldron Island, west of Orcas Island (Figure 2.6-station 05), and in the southern part of Eastsound, near Doe Bay (Figure 2.6-station 06), maximum wave heights vary from 0.45 to 1.2 m (Figure 2.5, 2.6, and Natural Hazards paper Online Resource 1-stations 26, 28).

In Grid G2b, the landslide-generated waves arrive at the southern section of the Fraser River Delta, south of Point Roberts, 13 min (780 s) after the landslide collapse, with roughly 0.3 m wave amplitude (Figure 2.7). The greatest wave amplitude near the shoreline of Boundary Bay (Figure 2.6-stations 09, 10) is around 1.2 m, with a 15-min arrival time. The highest wave elevation between White Rock and Semiahmoo Bay is around 1.04 m, with arrival times of about 25 min (more detail in Natural Hazards paper Online Resource 1). The tsunami reaches Birch Bay (Figure 2.5, 2.6-stations 11, 07) within 20 min; the first two waves have amplitudes of 1–1.1 m. The region near Lummi Bay (e.g., Figure 2.5, 2.6-stations 12, 07) has the largest maximum amplitudes in grid G2b, of about 1.2 m, with a 12-min arrival time. In semi-enclosed locations, such as harbors or shorelines where the geometry is complicated, the reflected waves can undergo many oscillations. For example, at stations 09 and 10, the leading waves (max 0.45 m) are smaller than the crests of later waves (max 1.14 m); at these locations, the maximum wave height occurs 27 min and 10.3 min, respectively, after the leading wave arrival (Figure 2.5). The explanation for this might be the location of the Serpentine River on the NE side of Grid G2b, where waves propagate to a shallower location and are not slowed by dry regions near Boundary Bay. Also, tsunami travel time to shore is governed by wave celerity, which is determined by water depth, and landslide-generated short waves are controlled by wave frequency (e.g., Grilli et al., 2019). The large leading waves at nearshore stations in grid G2b are accompanied by oscillations with a short average period of 400 s. This suggests that dispersion has less influence in shallow water zones. The dissipation begins after 100 min at all nearshore stations, and the wave heights gradually decrease.

In grid G1 (Figure 2.5), the first wave arrives near Victoria, after 20 min, with the largest amplitude of 0.3 m occurring 6 min later (detailed time series in Online Resource 1 of the Natural Hazards paper). South of Orcas Island, the maximum wave surface elevation is less than 0.5 m. At station 03, located NW of Orcas Island near Pender Island (Figure 2.5), the leading tsunami wave arrives within 15 min with an amplitude of almost 0.5 m; wave amplitudes decrease over time (Figure 2.6). Within grid G1, in areas removed from the source and from the direct path of wave propagation, maximum wave amplitudes do not exceed ∼0.5 m. In contrast, the leading wave at station 04 near Lummi Bay (Figure 2.5) has an amplitude of ∼4.4 m, with a subsequent 1-m

trough, followed by smaller waves (Figure 2.6). This station is positioned in the direct path of the waves generated by the tsunami source, with no dry regions or islands to scatter or deflect the wave motion. The wave amplitude reduces as it approaches the shore due to increased bottom friction and energy loss via breaking.

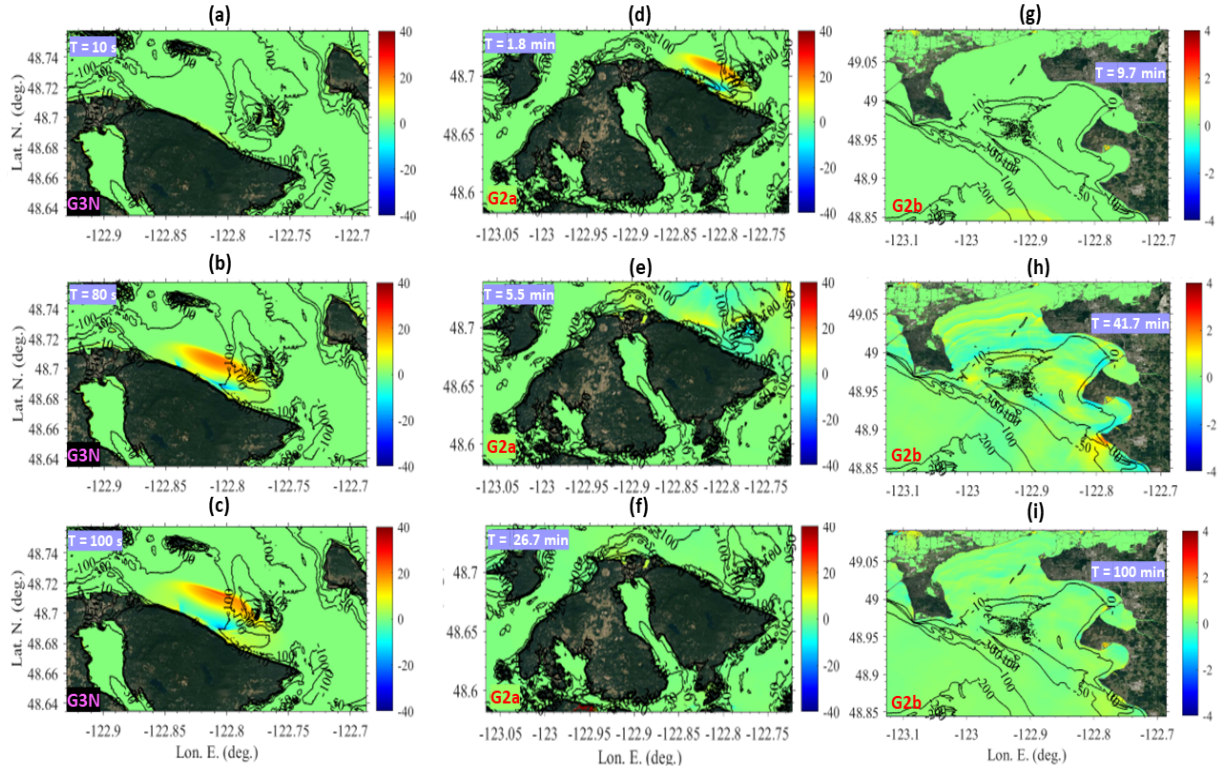


Figure 2.7. Instantaneous tsunami wave elevations (color scale in meters) simulated using NHWAVE in grid G3N for the 0.17 $km^3$ rigid Orcas Island landslide collapse at: (a) t = 10 s; (b) t = 80 s; and (c) t = 100 s. (d-i) Instantaneous wave elevations simulated in grids G2a,b using FTVD at timesteps from t = 110 s (d) to t = 6000 s (100 min) (i); reference level is Higher High Water Mean Tide (HHWMT). Maps created using MATLAB version 2021b and the bathymetry/topography dataset; topography from GOOGLE EARTH georeferenced satellite photos was incorporated in these maps using an API key: GOOGLE EARTH, 2019 DigitalGlobe.

The time series at stations 01 and 02, located in the northern (01) and southern (02) areas of grid G0, ~105 km and ~65 km from the source, provide examples of the minimal far-field impact of the tsunami (Figures. 2.5, 2.6). At both sites, the leading wave arrives after ~40 min, and wave amplitudes reach 0.14 m.

The propagation of the tsunami waves is illustrated for the high-resolution grids as a time sequence, up to 100 min following the initial landslide, of surface elevations in Figure 2.7 and current speeds in Figure 2.9. Full animations are also provided in Online Resource 2 of the Natural Hazards paper. Over the first ~100 s, large leading waves (20 m high) propagate in all directions, but primarily toward the NE. At time t = 80 s (near the t = 85 s landslide runout time) tsunami waves are travelling in several directions, resulting in a complex tsunami wave pattern.

Interactions between waves, bathymetry, the shoreline, and neighboring islands cause multiple wave reflections.

Figure 2.8 shows the maximum tsunami amplitudes from the Orcas Island simulation. The largest amplitudes generally occur close to the Orcas Island source, with amplitudes generally > 15 m. The maximum wave height is 19 m at 50 s after landslide initiation. In the direction of wave propagation, including the southern Boundary Bay region, particularly from Lummi Bay to Neptune Beach (Figure 2.5), amplitudes exceed 4 m (max. 4.41 m at 9 min). The region is distinguished by its numerous small inlets and semi-enclosed embayments, where tsunami waves can be amplified and potentially cause more damage. A reduction in water depth that causes wave shoaling and/or resonance, as well as limiting area, can contribute to wave amplification.

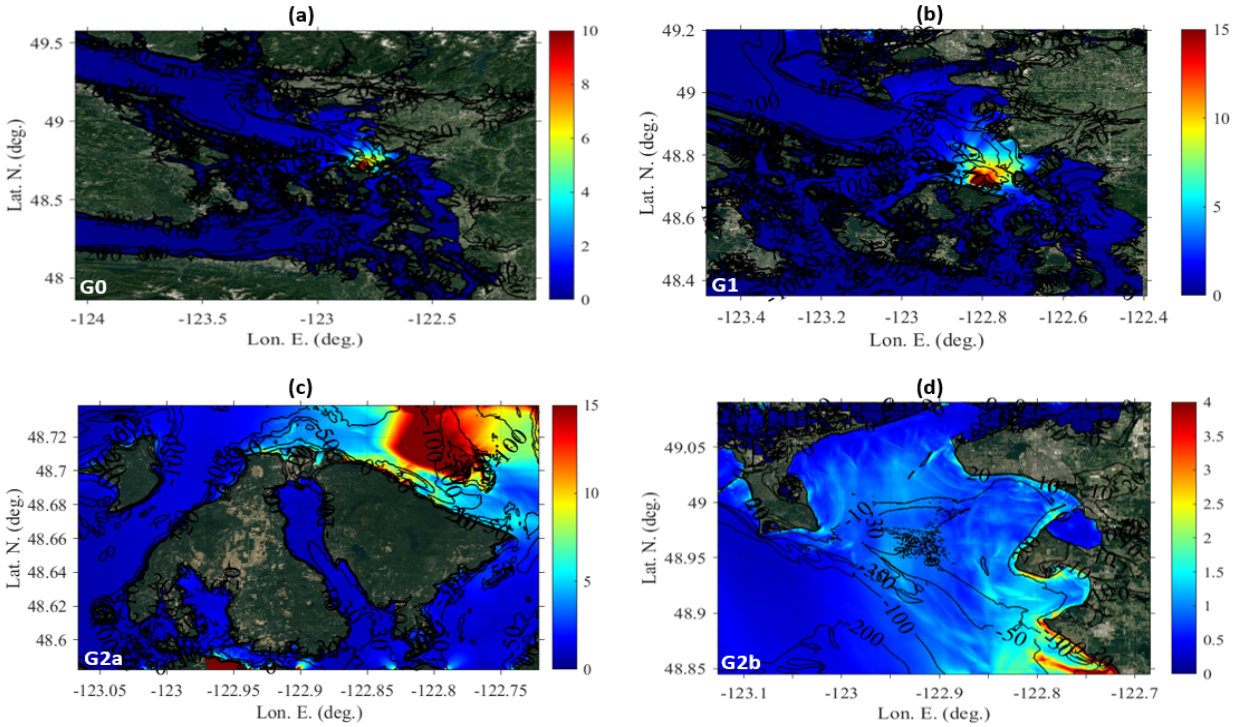


Figure 2.8. Maximum modelled surface elevations for the tsunami generated by the Orcas Island subaerial landslide (SAL) (color scale in meters) in grid: (a) G0, (b) G1; (c) G2a; and (d) G2b. Reference level is Higher High Water Mean Tide (HHWMT). Maps created as in Figure 2.7.

The strongest currents, up to 10 m/s (e.g., 9 m/s at station 07), coincide with the largest wave amplitudes in the near-source region (Figures 2.8-2.10). Strong modeled currents occur in coastal areas near the source region, as well as further to the NE within Boundary Bay, Semiahmoo Bay, and Birch Bay. Simulated currents are less than 4 m/s elsewhere in the region and are relatively weak in more remote areas of the model domain. Specifically, tsunami-induced currents throughout Boundary Bay have typical speeds of less than 1–1.5 m/s and do not exceed 3 m/s.

Figure 2.10 depicts the maximum modeled current velocities. Fast current velocities (e.g., higher than 1.5 m/s) are forecast over the whole east, north, and south coast of Orcas Island in

grid G2a (Figure 2.10c). However, the results in the south part (Shaw Island) may be artefacts because they are at the grid's edge. The highest current velocities from Lummi Bay to Boundary Bay can be seen in Figure 2.10d. Due to shallower depths and the narrow constrictions between the many islands in the direction of wave propagation, particularly fast, hazardous currents are predicted near Point Doughty, Buckhorn, and Clark Island in grid G2a, and Neptune Beach, Birch Bay, Semiahmoo Bay, White Rock, Boundary Bay, Point Roberts, Tsawwassen, and Richmond in grid G2b.

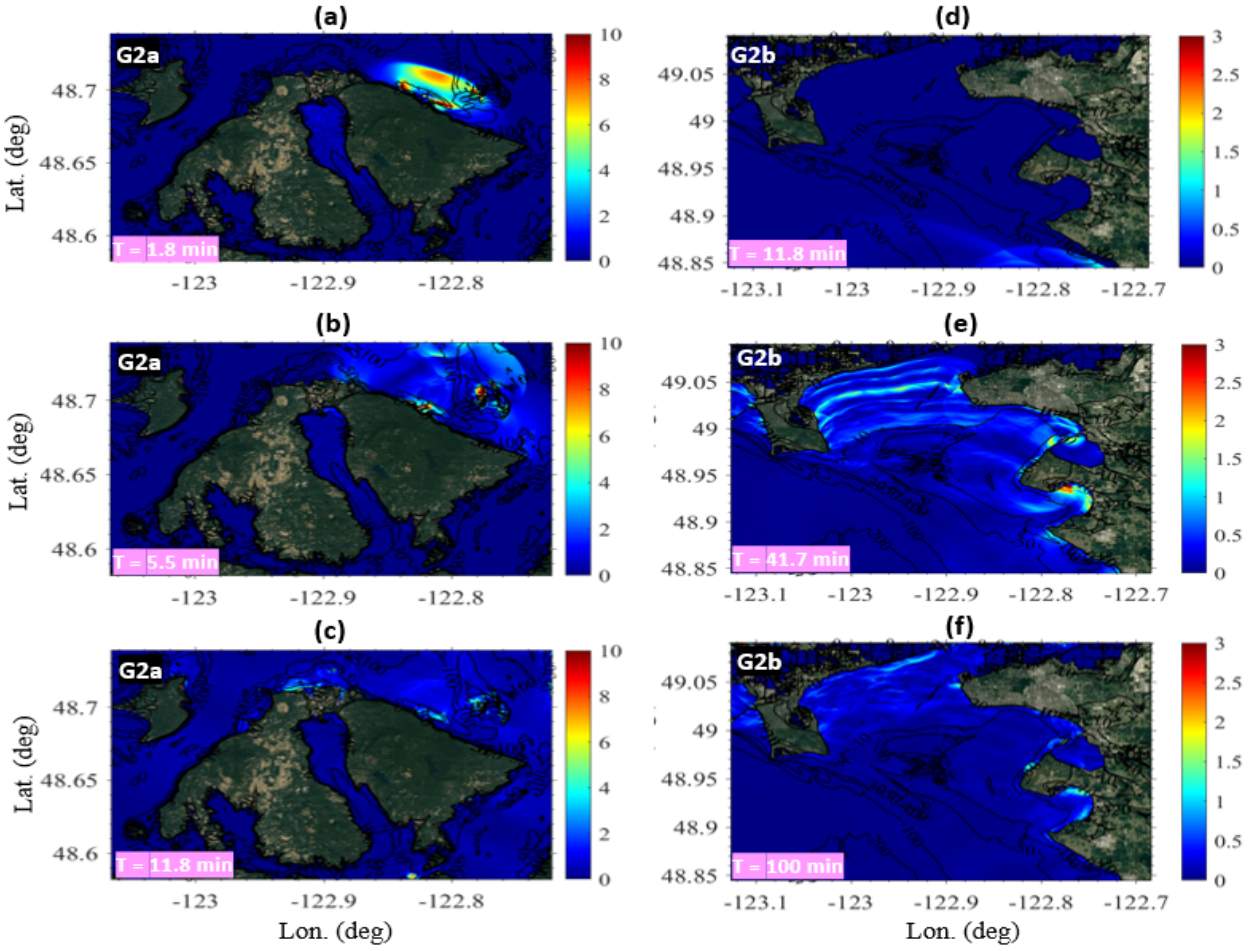


Figure 2.9. Maximum modelled current velocities for the tsunami waves generated by the Orcas Island subaerial landslide (SAL). Current velocities (color scale in m/s) simulated using FTVD in grid G2a at: (a) t = 110 s; (b) t = 330 s; and (c) t = 710 s. (d-f) Current velocities simulated in grid G2b using FTVD at: (d) t = 710 s; (e) t = 2500 s; and (f) t = 6000 s (100 min). Reference level is Higher High Water Mean Tide (HHWMT). Maps created as in Figure 2.7.

Maximum tsunami runup is shown in Figure 2.11 for the two high-resolution areas of interest. Starting from the north and moving clockwise (toward Buckhorn and Doe Bay), the runup is initially high in the near-source region, ~30 m, then lowers to less than 5 m before dramatically increasing to a local maximum of 30 m on Shaw Island, surprising given its location far removed from the source area (Figure 2.11a, b). This extreme runup might be caused by being located on

the boundary of computing grid G2a, which could lead to some inaccuracy and artificial amplified wave height, causing a spurious runup prediction in this area. Due to refraction surrounding the landslide, runups on Point Doughty, which is located approximately perpendicular to the primary collapse direction, still reach 10–16 m. Smaller, but still significant, runup occurs throughout the region surrounding Orcas Island. Further afield to the NE (Figure 2.11c, d), runup reaches 7.5 m at Neptune Beach near Lummi Bay. Both initial and reflected waves cause significant runup (> 1.5 m) along much of the shoreline between Point Roberts and Lummi Bay.

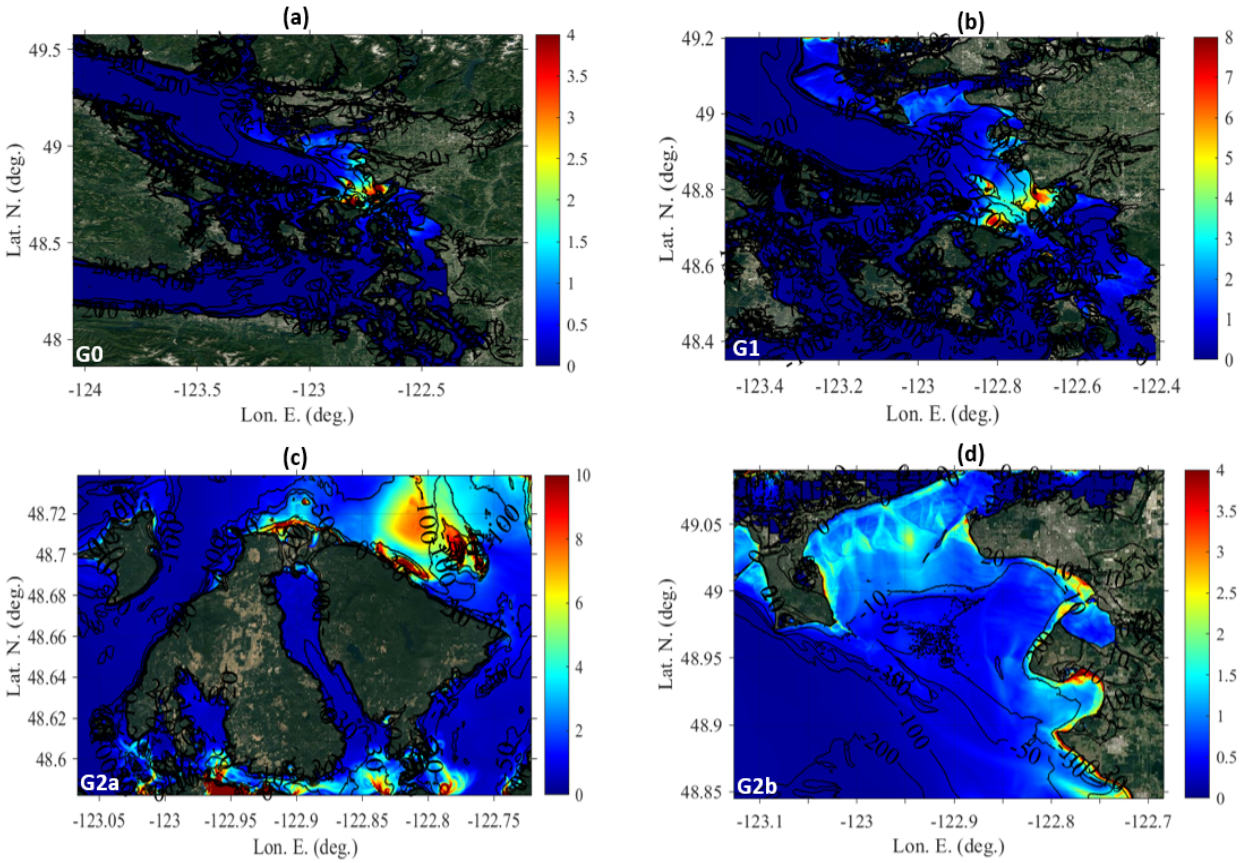


Figure 2.10. Maximum total modelled current velocities (m/s) for the tsunami waves generated by the Orcas Island subaerial landslide (SAL) (color scale in $m/s$ in grid: (a) G0; (b) G1; (c) G2a; and (d) G2b. Reference level is Higher High Water Mean Tide (HHWMT). Maps created as in Figure 2.7.

## 2.6 Discussion

In this study, we simulated tsunami waves triggered by a potential subaerial rigid landslide on NE Orcas Island, using NHWAVE (Ma et al., 2012) and FTVD (Kirby et al., 2013; Shi et al., 2012) software.

Landslide extent and volume were determined based on a worst-case scenario: large-scale failure of NE Orcas Island for the full length between previous landslide deposits. Small differences in volume or rheology are expected to have little effect on a tsunami coastal impact

projection (Grilli et al., 2019). The sensitivity of the numerical results to model formulation, seabed topography, bottom friction, and other physical factors, as well as to tsunami wave resonances and attenuation time scales, requires more investigation.

Grids G0 and G1, which include areas of relatively deep water, were used to run simulations with dispersive effects. Initial testing showed that it was not necessary to include dispersion for simulations in the shallower regions of the G2a and G2b grids. All simulations in FTVD were performed out to t = 7200 s (120 min), which was long enough to capture the maximum runup throughout the Orcas Island and Boundary Bay regions.

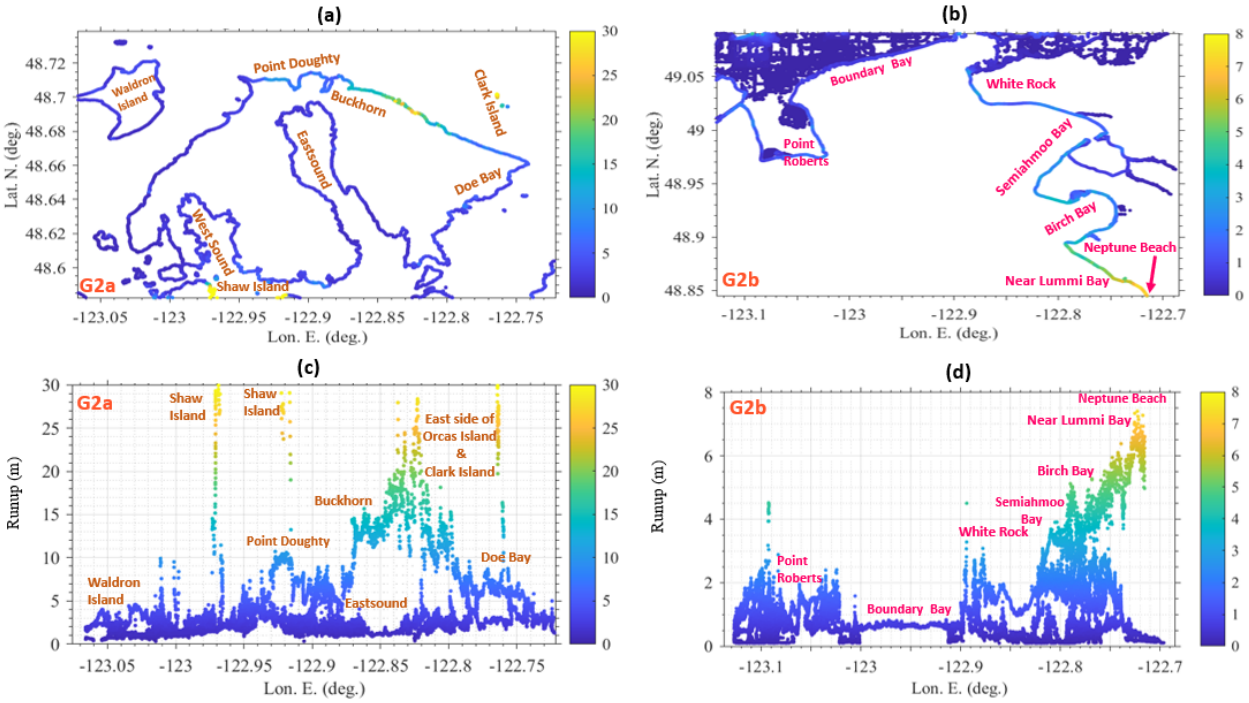


Figure 2.11. Maximum modelled runup (color scales in meters) in map view for grids G2a (a) and G2b (b), and plotted against longitude for grids G2a (c) and G2b (d).

Tsunamis generated by submarine landslides begin with a trough (negative wave), whereas subaerial landslide-generated tsunamis (SALGTs) commence with a crest (positive wave) followed, as in Figure 2.6, by a trough of similar or greater magnitude (Fornaciai et al., 2019). According to Løvholt et al. (2015), the leading wave tsunami amplitudes caused by SALs decay more slowly than those caused by totally submerged landslides. The far-field propagation of tsunamis caused by rockslides in fjords has comparatively unique properties compared to offshore occurrences, due to the multiple reflections that make the propagation less efficient (Løvholt et al., 2015). Except for the near-source region offshore Orcas Island (stations 07 to 08), these characteristics of SALG waves are plainly visible at stations within our study area (Figure 2.6). Dispersion and geometric spreading may be the two primary explanations for the relatively rapid decrease in surface elevation near the tsunami source for stations 07 and 08 during wave propagation. As the

waves travel to the northeast from the source, these variables, together with the transfer of tsunami energy into channels, result in rapid attenuation of the waves. These factors can also have an influence on runup.

The effect of waves on the shore is not only directly connected to the source from which they originate, but also highly influenced by topography and bathymetry. The distance from the tsunami source does not have a linear connection with wave height or runup. Bathymetry is critical since it may lead to a significant increase in wave height in a given region. Topography, which is equally crucial, defines the inundation zone.

The highest runup is captured by the finer grids G2a,b rather than the coarser grids G0 and G1 (more detail in Online Resource 3 of the Natural Hazards paper), justifying the use of nested grids in FTVD. As shown in Figure 2.11, the expected tsunami impact is considerable along the east coast of Orcas Island, near the source, and for much of the mainland coast between White Rock, BC and Lummi Bay, Washington, an area that is positioned directly in the tsunami propagation path, without intervening islands to cause damping. Elsewhere, wave heights (and runup) are damped by islands or diminished with distance due to dispersion and geometric spreading.

We can compare our numerical modeling results with the maximum near-field wave amplitude predicted by experiment-based equations. Mulligan and Take (2017) first examined the condition of the bulk fluid upon landslide impact using a one-dimensional technique. The hydrostatic pressure gradient formed by a near-instantaneous vertical water-level displacement over a short timescale $\Delta t_e = t\left(g/h\right)$ and length scale $L_e$ expresses the momentum imparted to the water in this situation. The initial pressure gradient is calculated from the difference in water surface elevation $\eta(x,t)$ between two locations in the landslide impact zone and the zone unaffected by the slide, which has a maximum positive wave amplitude above the still water depth h. The analysis yields

$$a_q = \sqrt{h^2 + \frac{2\rho_s T u_{max} cos\alpha L_e}{\rho g \Delta t_e}} - h, \tag{2.3}$$

where $a_q$ denotes the maximum near-field wave amplitude derived from a quadratic equation, h is the still water depth, $\rho_s$ is the sediment density, $T$ is landslide thickness, $\alpha$ is slope angle, $u_{max}$ is maximum velocity parallel to the slope, $\rho$ the fluid density, and $g$ is gravitational acceleration (Mulligan et al., 2018). In the case of the Orcas Island landslide, the near-field water depth is 75 m, and the other parameter values are as follows: $\rho_s$= 1750 $kg/m^3$, $u_{max}$=13.64 m/s, $\alpha$ = 34°, $L_e$ = 732 m, $\Delta t_e$= 85 (calculated based on the period of the first crest at station 07 as 10 sec) which gives a maximum near-field amplitude of about 15.8 m. This is slightly smaller than the maximum amplitude of ~19 m in our model results (e.g., Figure 2.6-station 07).

## 2.7 Conclusion

In this study, we used the dispersive numerical tsunami models NHWAVE (Ma et al., 2012) and FTVD (Kirby et al., 2013; Shi et al., 2012) to simulate tsunami waves generated by a large potential subaerial landslide on the NE coast of Orcas Island.

Modeling of the subaerial landslide (SAL) necessitated the use of high (3 m)-resolution bathymetry data (cf., Amante et al., 2020; Carignan et al., 2019). The simulated SAL travelled approximately 732 m before coming to rest in water depths of around 75 m. Based on an assumed friction drag coefficient of 0.0025 between the slide and the underlying seafloor, the modeled slide moved downslope with a peak velocity of 13.64 m/s before coming to rest after a duration of about 85 s. According to our numerical simulations, the SAL would generate tsunami waves with peak amplitudes of 15–20 m, current speeds of up to 9 m/s, and wave periods of roughly 6.6–8 min.

The modeled tsunami waves experience many reflections and a significant degree of dispersion due to their relatively short wavelengths and the complicated coastline and bathymetry in the Strait of Georgia. The most powerful waves and currents will occur at the shorelines adjacent to the failure on Orcas Island and opposite to it, near Lummi Bay. Wave amplitudes then rapidly attenuate with distance from the source due to the dispersion effect, geometric spreading, and transfer of tsunami energy to the surrounding water and coastline in semi-enclosed areas. The wave amplitude near the tsunami source is about 17–19 m and the current speed and the maximum runup are roughly 9 m/s and 30 m, respectively. The simulated waves reach Lummi Bay (station 04, 15.5 km from the source region) in 8.5 min, with a propagation speed of approximately 31 m/s, maximum amplitude of ∼4 m, runup of ∼7.5 m, and current speeds of 2.17 m/s. Modeled tsunami waves reach the entrance of Boundary Bay in less than 12 min and arrive at Semiahmoo Bay in less than 15 min, with wave amplitudes of up to 1 m, accompanying currents of up to 1.5 m/s, and maximum runup of 4.5 m.

Studies of past tsunami events (e.g., Melgar, 2021; Whitmore et al., 2008; Williamson et al., 2020) demonstrate that coastal damage is possible even for tsunami amplitudes as low as 0.5 m, with more severe damage and inundation occurring for amplitudes or runup exceeding ∼1.5 m. Runup maps (Figure 2.11) reveal that areas closest to the source area, including Point Doughty, Buckhorn, and Clark Island, would be the most impacted (runup > 12 m), while other locations on and near Orcas Island, including Eastsound, Westsound, and Waldron Island, would be less impacted with runup less than 5 m. The modeling shows that Clark Island, which hosts a marine state park and campground, could be completely overwhelmed by waves within ∼2.5 min of the landslide. High runups (up to ∼7.5 m) and strong currents (up to 4 m/s) would affect Semiahmoo Bay, Birch Bay, and Neptune Beach, which are located at the southern end of the Boundary Bay region. In contrast, Point Roberts, Boundary Bay, and White Rock would experience lesser wave effects with maximum runup of up to 3.5 m.

# Chapter 3 Detection of landslides and tsunamis in Douglas Channel and Gardner Canal

## 3.1 Introduction

In British Columbia, there is currently no system in place for the detection or early warning of landslides or landslide-generated tsunami waves. Recent research has revealed the presence of tsunami deposits along the north coast of British Columbia (NCBC) indicating the past occurrence of earthquake and/or landslide-generated waves (Geertsema et al., 2006a; Huntley et al., 2018). A large portion of the coastline is susceptible, as also evidenced by a number of damaging historical events, as outlined in Chapter 1. An earthquake early warning system has recently been developed for southwestern BC, to warn of damaging seismic waves from offshore earthquakes before they arrive in communities (Schlesinger et al., 2021); for megathrust events, tsunami early warning is effectively also provided. For far-field events (e.g., sourced in Alaska) BC receives tsunami warnings from the U.S. National Tsunami Warning Center, which relies on a network of offshore DART buoys and coastal tide gauges.

Seafloor deposits throughout the Douglas Channel region provide evidence of previous submarine landslide events, as detailed by Conway et al. (2012) and Stacy et al. (2020). A submarine landslide in April 1975 triggered tsunami waves in Kitimat Arm at the northern end of Douglas Channel (Figure 3.1; e.g., Skvortsov & Bornhold, 2007). These waves, observed to reach a height of over 8 m at the inlet's head, resulted in the destruction of a dock and a newly-built barge terminal (e.g., Murty, 1979; Kirby et al., 2016).

Today, the NCBC is a developing region that makes a major contribution to the country's economy. Many important infrastructure projects, such as ports, gas pipelines, oil and gas pipeline termini, and other waterfront initiatives, have been proposed for the coastal districts of Kitimat Arm (e.g., Brillon et al., 2018; Lintern et al., 2019). The area remains vulnerable to geohazards including earthquakes, landslides, and ensuing tsunamis, all of which could have a negative impact on the region (Brillon et al., 2018). Subaerial landslides of varying sizes are a regular occurrence in the area, as noted by Maynard et al. (2017).

Submarine landslides triggered by events such as earthquakes, rock avalanches, or volcanic eruptions, possess the potential to initiate local yet destructive tsunamis, even when they are relatively small and occur in shallow-water or coastal regions (Tinti et al., 2005; Walter et al., 2019; Casalbore et al., 2020). Notable recent events worldwide include the following: The 2018 Sulawesi-Palu tsunami, where multiple waves were triggered by a combination of a large earthquake and earthquake-triggered landslides, caused over 2000 fatalities (Sassa, 2023). A rainfall-induced landslide in southern Chile in 2022 generated a tsunami causing significant infrastructure damage (Aránguiz et al., 2023; Sassa, 2023). A heavy rainfall-induced coastal

landslide in Vietnam in 2017 (Minh Duc et al., 2020) and a water level rise-induced landslide in China's Three Gorges Reservoir in 2003 (Yin et al., 2015) triggered tsunami waves, leading to fatalities and economic losses. In Norway (2014), a coastal landslide induced a tsunami, damaging port facilities (Glimsdal et al., 2016). In 2018, a period of moderate eruptions of the Anak Krakatau volcano, Indonesia triggered a massive flank failure and submarine landslide, which in turn generated a tsunami that caused the deaths of 437 people (Walter et al., 2019; Casalbore et al., 2020). In 2002, landslide-induced tsunamis occurred at the coast of the volcanic island of Stromboli, in the Tyrrhenian Sea, Italy; one person died and six were injured (Tinti et al., 2005). A final example is a rock avalanche that occurred in Karrat Fjord, Greenland in 2017, resulting in a destructive tsunami that left several individuals missing (Sassa, 2023), further exemplifying the diverse triggers and impacts of such events.

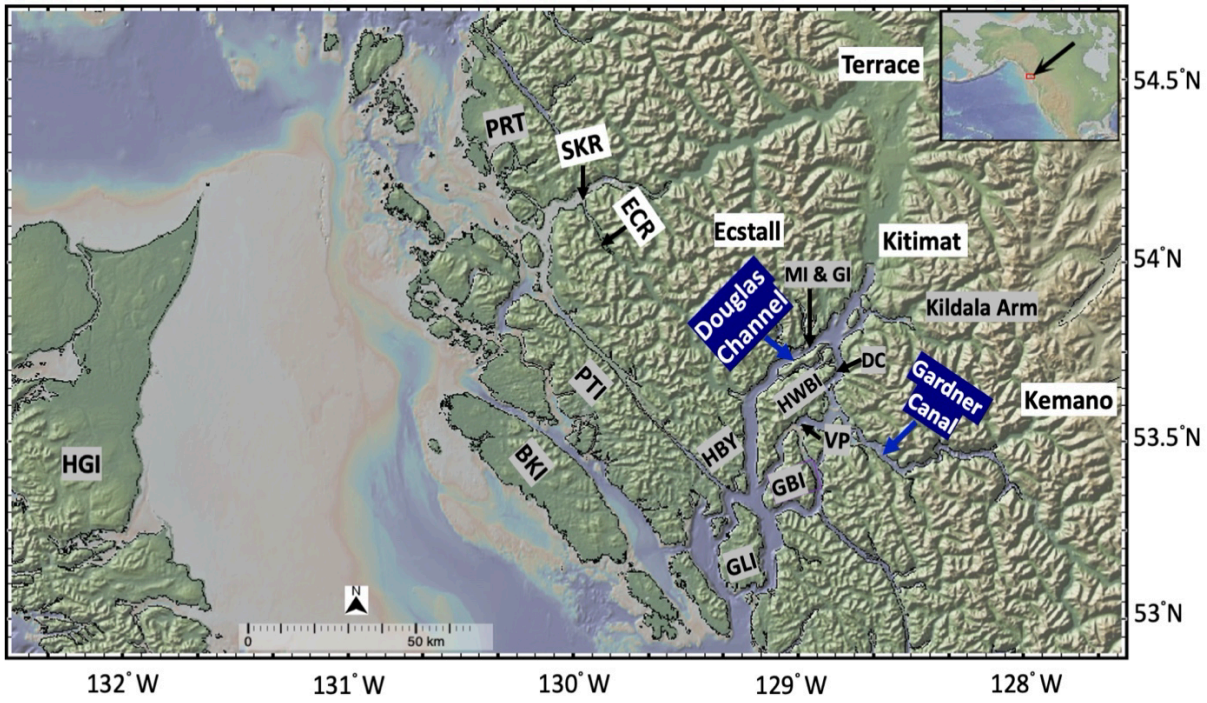


Figure 3.1. Locations of population centers and other sites in the Douglas Channel region, including Terrace, Kitimat, Kemano, Hartley Bay (HBY), Skeena River (SKR), Ecstall R (ECR), and Hawkesbury Island (HWBI). Banks Island (BKI), Devastation Channel (DC), Gil Island (GLI), Gilttoyees Inlet (GI), Gribbell Island (GBI), Miskatla Island (MI), Pitt Island (PTI), Prince Rupert (PRT), Varney Passage (VP), and the Haida Gwaii Islands (HGI) are also labelled.

Globally, there is increasing focus on the substantial danger of coastal and seabed infrastructure damage/destruction from even small landslides. The NCBC area saw little attention paid to local-scale landslides prior to 2013 (Brillon et al., 2018; Stacey et al., 2020). The extent of damage from landslides is mostly determined by their volume and speed (Lin, 2015). Due to difficulties in surveying shallow-water regions in remote locations, smaller landslides are frequently disregarded in marine environments even though they represent major hazards (Casalbore et al., 2021). Notably, these small landslides have a greater recurrence probability than

bigger events, which increases their potential hazard (e.g., Di Roberto et al., 2010; Casalbore et al., 2020).

The 320-kilometer long Douglas Channel fjord complex is situated in NCBC, and hosts a few population centers including Hartley Bay, Kitimat, and Kitamaat Village (Figure 3.1). Gardner Canal is a 90-kilometer side-inlet of Douglas Channel. Accessible by Varney Passage or Devastation Channel, the canal is located behind Hawkesbury Island and is the site of the Kemano Generating Station, developed to provide power to an Alcan aluminum smelter in Kitimat (e.g., Tannant & Morgenroth, 2020).

General causes of landslides include low ground surface friction caused by heavy rainfall on slopes of $10^{\circ}$ or more (Lin, 2015). The Kitimat Arm fjord's complex dynamics, encompassing steep topography, high precipitation, rapid sedimentation, seismicity, glacially over-deepened bathymetry, tidal stress, gas release or migration, excessive pore water pressure, and human activities, collectively present potential triggers for slope failures (Lintern et al., 2019). Geological mapping indicates steep subaerial terrain in Hartley Bay, with the submarine fjord wall characterized by steep (~40°) and narrow terrain with minimal marine sediment accumulation (Stacey et al., 2020). Subaerial slope gradients typically range from 30° to 45°, while several areas of the fjord have slopes of 45°to 60° (Lintern et al., 2019). Similar conditions of extreme subaerial slopes with minimal sediment accumulation on submarine fjord walls are observed in other parts of Douglas Channel, such as Gardner Canal, Giltoyees Inlet, and Miskatla Inlet (Figure 3.1) (Stacey et al., 2020).

Stacey et al. (2020) proposed a categorization system for failure mechanism and morphology in Douglas Channel (Figure 3.2). Multiple landslide types in the channel can cause tsunamis, with small, shallow-seated translational slides being the most common type that has occurred throughout much of the Holocene (Lintern et al., 2019; Stacey et al., 2020). Debris flows are widespread in the area (Stacey et al., 2020), with steep slope angles on the western fjord walls in Douglas Channel, suggesting that only a small amount of additional loading from recent deposition would be required to cause slope failure (Lintern et al., 2019). Despite their smaller size, these slides have the potential to generate tsunamis due to the high velocity at which the entire slide volume enters the water (Fine et al., 2003). Fifty-two slide deposits linked to the subaerial environment are associated with fjord walls having high slope gradients. These slides are typically smaller than the submarine slides occurring on fjord walls with lower slopes, which permit higher sediment accumulation and cause larger slides with volumes exceeding $10^6$ $m^3$ (Stacey et al., 2020).

Local landslides are deemed more likely to cause significant tsunamis in Douglas Channel than offshore earthquake activity, based on tsunami modelling (Thomson et al., 2012; Kirby et al., 2016; Stacey et al., 2020). The highest probability of experiencing a damaging tsunami is near the landslide source, owing to the rapid decay of tsunami height with distance along the fjord (Thomson et al., 2012; Kirby et al., 2016; Stacey et al., 2020).

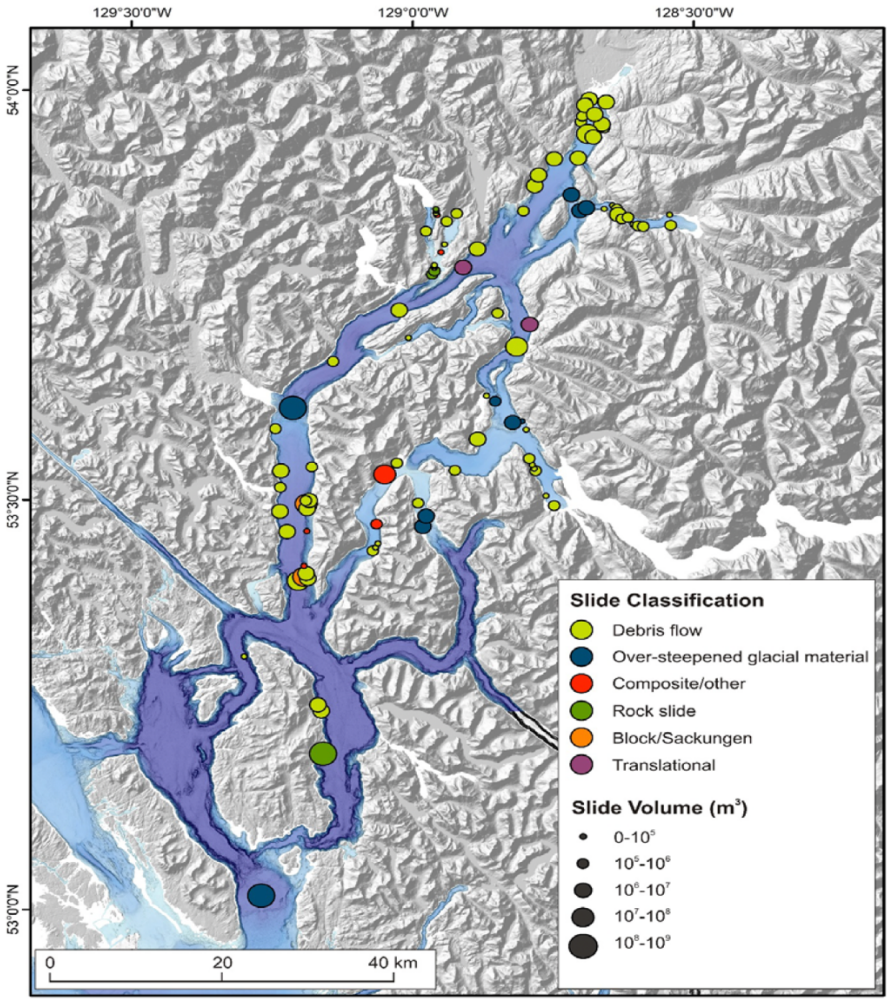


Figure 3.2 Distribution and characteristics of submarine slide classes and volumes in Douglas Channel. Various slide classes are dispersed across the channel, with the most significant deposits correlated with over steepened material. Debris flow accumulations are predominantly found at the heads of fjords. Figure from Stacey et al. (2020).

The biggest slope failures in Douglas Channel occurred during deglaciation, within Devastation Channel (Stacey et al., 2020). As a result of associations with large headwalls and possible subaerial contributions, the larger Holocene events in Kitimat Arm primarily occurred on slopes with lower gradients and thick sediment accumulation (Stacey et al., 2020). This increases the potential height of tsunamis when these events occur in shallow water (Fine et al., 2003; Thomson et al., 2012; Kirby et al., 2016).

The active Kitimat Delta, with its thick sediments, complex sinuous bed forms and uneven topography, has the capacity to enhance the shaking amplification effects of seismic waves reflected within the subsurface or those originating from landslides in the region (Brillon et al., 2018; Stacey et al., 2020). Numerous studies on the association between landslides and tsunamis

in fjord environments have documented large-scale natural slope failures in the Kitimat Delta predating human industrial activity (Lintern et al., 2019). Historical incidents at this and similar sites, including the 1958 Alaskan Lituya Bay event and the 1974 and 1975 landslide-generated tsunamis in Kitimat Arm, underscore the destructive potential of these occurrences (Miller, 1960; Murty & Brown, 1979; Rabinovich et al., 2003).

Two submarine landslides dating to early mid-Holocene time (i.e., 5000 to 10000 years before present), were detected on fjord walls across from the Gitga'at settlement of Hartley Bay in Douglas Channel (Conway et al., 2012; Lintern et al., 2019). Radiocarbon dating suggests a consistent rate of sedimentation in this region for at least 10,000 years, indicating slope stability and a lack of future large-scale submarine collapses (Conway & Barrie, 2015). However, many parts of the system remain susceptible to subaerial failures.

In the context of this study, the research detailed in this chapter attempts to establish a proof of concept for a landslide and tsunami detection system, providing the framework for a possible early tsunami warning system. The historical occurrence of a submarine landslide at Kitimat Arm at the northern end of Douglas Channel, BC, in 1975, which caused damaging tsunami waves, emphasizes the importance of this research. Through the application of complex signal processing methods to seismic, hydroacoustic, and pressure sensor data, the goal is to develop a comprehensive methodology that can identify the location and timing of landslides as well as detect changes in water level that may result from tsunami waves. By highlighting the significance of proactive detection systems for coastal locations vulnerable to subaerial and/or submarine landslides and related tsunamigenesis, this research adds to the larger field of disaster mitigation.

In the following sections, this chapter delves into the methodology (Section 3.2) employed in this study, drawing insights from various studies to justify the selection of specific methods tailored to the objectives of the research. This encompasses a comprehensive exploration of seismological, passive acoustic, and sea level monitoring techniques, strategically chosen to address identified limitations and contribute to filling critical knowledge gaps. Section 3.3 introduces the study area and instrument network. Section 3.4 describes the application of the methods introduced in Section 3.2 to the available instrumental data within our study area. Section 3.5 details an investigation of the validity of these techniques by testing if they can successfully detect previously documented landslides in the study area. Finally, Section 3.6 concludes the chapter, summarizing the key findings and paving the way for future research endeavors.

## 3.2 Methodology

### 3.2.1 Previous studies for the detection of submarine landslides and volcanic activity

Monitoring landslides and submarine volcanism activity is challenging due to the often remote locations and unexpected occurrences. The limited availability of geophysical sensors in the oceans and sparse land-based instruments on isolated islands exacerbates these challenges, resulting in a significant number of unreported incidents (Clare et al., 2024).

The use of global hydroacoustic networks for detecting and monitoring submarine volcanic eruptions dates to the 1940s and 1950s, exemplified by works of Dietz and Sheehy (1954) and Ewing et al. (1946). A comprehensive approach involving moored hydrophones and terrestrial seismic networks is crucial for monitoring earthquakes, tremor, volcanoes, and landslides (Shan et al., 2022). Technological progress and an improved understanding of submarine eruption signals have validated the practicality of these networks (Tepp & Dziak, 2021). For example, the timing of submarine landslides has been determined from signals detected by submerged hydrophones and geophones, as well as land-based seismic monitoring systems (Clare et al., 2024). Therefore, observational passive monitoring datasets can provide new insights into the timing and frequency of submarine landslides, starting to fill a key knowledge gap. Despite these advancements, the rapid identification of submarine landslides using seismic or hydroacoustic data remains an unresolved challenge (Tepp & Dziak, 2021), as evidenced by the recent January 15$^{th}$, 2022 Tonga volcanic eruption and tsunami. The event highlighted the complexities involved in quickly detecting and characterizing submarine landslides triggered by volcanic activity, underscoring the ongoing need for improved detection methods and monitoring systems (Hu et al., 2023).

Around half of the geophysical detections of past submarine eruptions were made possible by seismic stations or hydrophones located more than 500 km away, showcasing the significance of long-distance monitoring (Tepp et al., 2019). Hydroacoustic signals exploit the sound-fixing and ranging (SOFAR) channel, a low-velocity zone in the ocean facilitating signal propagation across ocean basins, with detections of submarine eruptions at distances exceeding 14,000 km (Bryan et al., 1963; Dziak & Fox, 2002; Metz et al., 2016; Chadwick et al., 2019). The waveguide's depth varies with latitude, enabling extensive signal travel (e.g., Bryan et al., 1963; Dziak & Fox, 2002; Metz et al., 2016; Chadwick et al., 2019). If the depth of the waveguide were unchanging with latitude, the propagation of sound waves would be less directed and confined. Without the gradient in acoustic properties created by varying depths, sound waves would disperse more quickly into the surrounding water column, leading to shorter propagation distances and potentially reduced signal strength over long distances. Seismo-acoustic signals, which include hydroacoustic, atmospheric/acoustic, and seismic waves, appear in different Earth domains and

can convert and spread across boundaries (Tepp & Dziak, 2021). For example, earthquake seismic waves can, under certain circumstances, transform into hydroacoustic or atmospheric waves (Tolstoy & Ewing, 1950; Talandier & Okal, 1998; Arrowsmith et al., 2010). Due to varying winds and atmospheric conditions (e.g., de Groot-Hedlin et al., 2010), atmospheric signals, especially those at infrasonic frequencies (<20 Hz), can spread thousands of kilometers in the atmosphere (Garcés et al., 1998; Fee & Matoza, 2013). To detect and monitor submarine eruptions and landslides, each wave category has unique benefits and constraints. The transmission effectiveness of seismic waves is limited due to their higher attenuation as compared to hydroacoustic and atmospheric signals. Because of waveguide effects, weak seismicity frequently escapes detection beyond 100–200 km, while hydroacoustic and atmospheric signals benefit from longer detection ranges (Tepp & Dziak, 2021).

The unique propagation characteristics of hydroacoustic waves, specifically "T-phases", enable their efficient travel through the SOFAR channel, exhibiting slower energy reduction compared to seismic body waves (Tepp et al., 2019). T-phases are special types of underwater sound waves that travel long distances and loss energy relatively slowly compared to seismic body waves, making them important for detecting and monitoring underwater events. The optimization of detection thresholds and location accuracy in submarine eruption monitoring is facilitated by the efficient propagation of converted hydroacoustic waves, emphasizing the role of regional hydrophone arrays (Tepp & Dziak, 2021).

Tepp & Dziak (2021) and Matsumoto et al. (2023) review the historical development of remote monitoring for submarine volcanoes through global seismo-acoustic networks including the Sound Surveillance System (SOSUS), the Polynesian Seismic Network (PSN) for T-wave detection, and the Comprehensive Nuclear-Test-Ban Treaty (CTBT) International Monitoring System (IMS) hydroacoustic network. Green et al. (2013), Tepp et al. (2019), and Talandier et al. (2020) investigated submarine eruptions, emphasizing the comparison of hydroacoustic and seismic data. The first seismo-acoustically detected eruption, recorded in 1939 at Kick ’em Jenny in the Lesser Antilles, showcased T-phase detections beyond 500-km distances (Tepp & Dziak, 2021). Utilizing ocean-bottom seismometers (OBSs) becomes essential for detecting weak seismic signals from seamounts located too far from land-based seismic stations (Tepp & Dziak, 2021). The IMS hydroacoustic network, incorporating T-phase-optimized seismic stations on land and cabled hydrophone arrays in the ocean, plays a pivotal role in detecting submarine eruptions (Tepp & Dziak, 2021).

Tepp and Dziak's (2021) investigation centers on hydroacoustic landslide detection, utilizing instruments including a high-rate hydrophone within the Hawaii Undersea Geo-Observatory (HUGO) (50 km from the source) and the Eastern Pacific hydrophone array managed by the Pacific Marine Environmental Laboratory (PMEL) (located >5000 km from Kilauea). The HUGO system deployment at Lo’ihi Seamount in 1997 highlights a noteworthy experiment package with

hydrophone, seismometer, and pressure sensor components (Caplan-Auerbach & Duennebier, 2001; Matsumoto et al., 2023).

Hydrophone deployments have successfully detected submarine landslides; examples include the detection of dozens of small landslides occurring on the submarine flank of Kilauea volcano in 1998 using hydrophones placed on the summit of Lo'ihi volcano, detection of a major landslide at the NW Rota-1 volcano summit in the Mariana arc ~100 km north of Guam, detection of landslides in the vicinity of the West Mata and Northern Mata volcanoes in Lau Basin from December 2009 to May 2010, which were triggered by material loading during active lava flows into the ocean, and detection of the 1998 earthquake-induced landslide in Papua New Guinea that in turn triggered devastating tsunami waves (Caplan-Auerbach et al., 2001; Chadwick et al., 2012; Caplan-Auerbach et al., 2014; Clare et al., 2024). Notably, hydroacoustic recordings dating back to the 1952 submarine volcanic eruption of Myojin-sho in Japan demonstrate widespread detections at both local and global distances (Tepp & Dziak, 2021). The utilization of global hydrophone networks, initially developed for military purposes, significantly enhances the global recognition of hydroacoustic signals, contributing to our understanding of underwater seismic activity (Tepp & Dziak, 2021).

The seismic detection of low-magnitude volcanic earthquakes (M<3), typically limited to mid-regional ranges (around a few hundred kilometers), necessitates alternative approaches such as the use of local instruments like Ocean Bottom Seismometers (OBSs), exemplified during a 1996 earthquake swarm at Lo'ihi Seamount, Hawaii, where a local OBS outperformed nearby land-based seismic networks (Tepp & Dziak, 2021) by detecting weak signals. Hydroacoustic signals, converted from seismic waves, offer another solution, lowering earthquake detection thresholds in remote ocean areas (Bohnenstiehl et al., 2002; Fox et al., 1994), but this only works for earthquakes and landslides that generate detectable hydroacoustic phases.

Where hydroacoustic data are unavailable, seismic data can help identify large events: T-phases generated by a large landslide and eruptive activity on Monowai volcano in the Kermadec arc were recorded by seismometers throughout Polynesia (Chadwick et al., 2008; Wright et al., 2008). In 1998 the previously-mentioned earthquake-induced landslide in Papua New Guinea was recorded by both hydrophones and seismometers in the Pacific region (Okal, 2003). The signals allowed researchers to identify the slide and explain how a relatively small earthquake generated a massive and deadly tsunami. On land, seismic data were of critical importance in quantifying and characterizing the slope failure of Mount St. Helens during its 1980 eruption (Caplan-Auerbach et al., 2014). Landslides generate hydroacoustic signals that can be detected either by hydrophones or, if the signal couples into the ground, by seismometers.

Recording the time series of hydrostatic bottom pressure within the water column above pressure sensor instruments, known as Offshore-Bottom Pressure Gauges (OBPGs) or, in shallow water, Bottom Pressure Sensors (BPSs), facilitates precise measurements of sea level variations. BPS is a general term for any device that senses pressure in the water. In this chapter, it refers to

measuring pressure in shallow water, whereas an OBPG specifically describes an instrument made for long-term monitoring of pressure changes on the sea/ocean floor; these instruments are often focused on tasks like detecting tsunamis in the deep sea. BPSs play a crucial role in accurately measuring sea levels, offering the capability to identify sudden changes, which is particularly valuable for early tsunami wave detection (Chierici et al., 2017, Kurkin et al., 2016).

The comprehensive approach of integrating multiple instrument types for diverse seismo-acoustic waves has been increasingly widespread, with examples including Japan's Dense Ocean floor Network system for Earthquakes and Tsunamis (DONET) providing real time data from seismometers and OBPGs for precise tsunami early warning (Igarashi et al., 2016; Kaneda et al., 2009) and a similar system developed by Ocean Networks Canada offshore Vancouver Island (Heesemann et al., 2014).

These sensors can detect all possible tsunamis in fjords or lakes, e.g., providing a means of detecting waves due to failure of unstable rock slopes (Harbitz et al., 2014). Due to distinct source processes and shorter tsunami travel durations from rockslide locations to areas at risk, the seismic signal and deep-water pressure sensor technique, which is frequently employed in oceanic earthquake tsunami warning systems, is inadequate for fjords or lakes (Harbitz et al., 2014).

Deep-ocean tsunami observations, particularly those from Deep-Ocean Assessment and Reporting of Tsunamis (DART) instruments, offer valuable insights into tsunami characteristics, enhancing global research and warning systems. Despite substantial progress with approximately 60 DARTs installed worldwide, their spatial resolution remains constrained, with distances between neighboring DARTs ranging from 400 to 4000 km (Heidarzadeh & Gusman, 2018). In contrast, dense observations from OBPGs provide higher spatial resolution, enabling the study of spatial variations in tsunamis (Heidarzadeh & Gusman, 2018).

In the pursuit of improved tsunami early warning, Wang et al. (2020) introduced an advanced tsunami early warning system designed for Crete in the Eastern Mediterranean Basin. This system leverages OBPGs to monitor sea surface elevation, assimilating real time offshore observations for prompt and effective regional tsunami status estimation. The strategic deployment of twelve OBPGs around Crete Island adheres to specific criteria, ensuring large azimuthal coverage, optimal distance from the coast (at least 50 km to allow enough lead time for tsunami early warning), and strategic placement in areas characterized by energetic dynamics (Wang et al., 2020). Empirical Orthogonal Function (EOF) analysis was used to validate the chosen OBPG locations, incorporating insights from three scenarios inspired by past tsunami events (Wang et al., 2020). Wang et al.'s (2020) warning system showcases high forecasting accuracy for both seismically-generated and landslide tsunamis, achieving an impressive 87.3% accuracy for hypothetical landslide tsunamis. The system's retrospective examination of a tsunami that occurred in May 2020 underscores its efficacy in predicting near-field tsunamis, offering a remarkable warning lead time of 10 minutes. The deployment of OBPGs, as advocated by the

study, is not only recommended for Crete Island but extends its relevance to other tsunamigenic zones in the Eastern Mediterranean Basin and beyond.

Based on a review of previous studies described above, the deployment of integrated onshore and offshore networks equipped with broadband seismometers, hydrophones, and underwater pressure-monitoring sensors has emerged as a potential solution for the detection of landslides and landslide-generated tsunamis (Brillon et al., 2018; Clare et al., 2024). This comprehensive monitoring strategy has the potential to improve early warning systems by identifying probable tsunamis caused by submarine/subaerial landslides and measuring subsequent wave dynamics.

Seismic and hydro-acoustic signals provide essential information regarding event magnitude and propagation dynamics, making landslides easier to identify, localize, and characterize (different forms of mass movements produce unique signals) (Allstadt et al., 2018). However, in this developing field, the detection, categorization, and extraction of quantitative information from the seismic and audio signals generated by landslides remain difficult problems (Allstadt et al., 2018).

### 3.2.2 Seismic signal analysis techniques for landslide detection

Dynamic seismic sources such as landslides, debris flows, rockfalls, and snow avalanches induce ground vibrations as material moves downward due to gravity (Suriñach et al., 2005; Kao et al., 2012). Waveform analysis has been shown to be useful for detecting seismic signals linked to these occurrences in real time or almost in real time (Suriñach et al., 2005).

Galitzin (1915), Jeffreys (1923), Norris (1994), and Uhira et al. (1994) were among the first to conduct investigations of landslide signals recorded by seismometers. A thorough investigation on the signals produced by different kinds of landslides, such as mudslides and debris flows, was conducted by Brodsky et al. (2003). Later, Kao et al. (2012) demonstrated that the long-period wave source associated with landslides may be theoretically explained by a single force or a shallow horizontal fault.

Broadband seismic data are recorded by land-based seismologic networks to capture very long period seismic signals (20-50 seconds) linked to elastic rebound (as the overlying landslide mass collapses and moves downslope, the newly exposed levels experience elastic rebound), and large amplitude high-frequency signals (1-10 Hz) from terrestrial landslide impact (Lin, 2015). Seismic data recordings have enabled successful detection of events such as the Hsiaolin hillslope landslide during Typhoon Morakot in Taiwan (Lin, 2015). Land-based seismic monitoring in the Gulf of Mexico identified 85 otherwise unknown submarine landslides, providing vital information for risk assessments and resilient infrastructure development (Fan et al., 2020; Chaytor et al., 2020). Similarly, 14 submarine landslides were detected in the Kaoping Canyon, offshore Taiwan, using terrestrial broadband seismic networks (Lin et al., 2010; Huhn et al., 2019). This highlights the potential of broadband seismic networks for rapid detection and location of landslides both onshore and offshore, hence improving tsunami warning systems (Clare et al., 2024).

As opposed to conventional earthquake monitoring, landslide detection is based on identifying non-impulsive, tremor-like seismic waves that exhibit sporadic high-amplitude bursts, lack defined phases like P and S waves, and continue for tens of seconds with a low frequency range (lower than 10 Hz) (Suriñach et al., 2005; Kao et al., 2012). Although these unique features make it possible to identify landslide waveforms, pinpointing the exact moment of the landslide occurrence and its seismic phase can still be challenging (Tsai & Wu, 1997). Furthermore, if the power of these tremor-like signals is low due to the magnitude of landslides (of all kinds), it will be more difficult to determine the wave signals from background seismic noise.

To overcome this problem, the design of an algorithm to identify the detailed seismic signature of landslides becomes critical, particularly for real time seismic data analysis (Kao et al., 2012). An improved understanding of landslide seismic and geologic properties, enabled by seismic analysis, not only enables early public warnings but also supports other risk mitigation activities (Suriñach et al., 2005).

In this study, I employ seismic data processing techniques, including Empirical Mode Decomposition (EMD) (Feng, 2011), the Hilbert-Huang Transform (HHT) (Huang et al., 1998), and seismicity-scanning based on navigated automatic phase-picking[1] (SSNAP) (Tan et al., 2020) integrated with the Earthquake Transformer (EQT) neural networks Artificial Intelligence (AI) and Deep-Learning (DL) model (Mousavi et al., 2020). The SSNAP-EQT technique, which is novel in landslide detection, in conjunction with EMD and HHT, facilitates comprehensive seismic analysis, automatically detecting and picking seismic phases. These combined techniques enhance the effective identification and characterization of earthquake and landslide events in the study area.

#### 3.2.2.1 Empirical mode decomposition and Hilbert-Huang transform

In this project, given the absence of ready-to-use automatic landslide detection models, I opted to adapt the SSNAP model, originally designed for earthquake detection. The necessary adjustments for utilizing it in landslide detection are explained in detail below.

The SSNAP-EQT model estimates P wave arrival times, facilitating precise identification of seismic events in terms of location and time. The model requires P wave velocity as a key input for accurate event detection in the study area.

The intricate nature of landslide waveforms poses challenges in determining seismic wave arrival times for velocity computation. Since there were no prior studies to estimate the P wave velocity of the shallow crust in the complex coastal study area, it was necessary to estimate the velocity in this study. To address this, I initially employed the Empirical Mode Decomposition (EMD) approach, distinguishing weak surface-wave signals, producing distinctive waveforms,

[1] Phase-picking refers to the process of identifying specific seismic phases, which represent distinct arrivals of seismic energy at a seismometer or seismic array. These phases can include primary (P), secondary (S), and surface waves, among others.

establishing arrival times, and calculating landslide P and surface-wave velocities (Feng, 2011). However, only the P wave velocity is required for the SSNAP-EQT model.

Employing EMD, the data-driven methodology decomposes seismic signals into intrinsic mode functions (IMFs), enabling a detailed analysis of earthquake or landslide signals (Feng, 2011; Feng et al., 2021). In this technique, seismic signals are effectively segmented into numerous low-frequency residual IMFs; the subsequent application of HHT to each IMF provides a comprehensive time-frequency representation, identifying seismic patterns at various time scales (Feng, 2011; Feng et al., 2021). Utilizing the Z component of waveform data from the first or second IMF obtained through EMD, P-wave and surface-wave velocities are computed (Feng, 2011). Data from more than one station are needed to compute velocities.

The HHT is employed for EMD spectra frequency transform to determine the frequency content of the signals and IMFs, returning instantaneous phase, frequency, and amplitude. HHT technique, known for adaptability and efficiency in analyzing nonlinear and nonstationary signals, have also been successfully implemented in various other geophysical fields (Huang & Wu, 2008; Crockett et al., 2010). The combination of HHT and Fast Fourier Transform (FFT) is used to produce time-frequency spectra and power versus frequency ratio of landslide signals, determining seismic parameters (Feng, 2011). In seismic wave analysis, the FFT stands out as a widely used signal processing technique. This transformation converts time-domain signals into frequency-domain signals, a crucial step for analyzing the spectral content of seismic waves. In earthquake early warning systems, the FFT aids in filtering out noise and unwanted signals from seismic data, elevating the precision of earthquake detection and analysis (Abdalzaher et al., 2023).

To determine the P- and surface-wave velocity in the study area, I followed the techniques outlined in Figure 3.3; Section 3.4.1.1 will provide more detail.

#### 3.2.2.2 Seismicity-Scanning based on Navigated Automatic Phase-picking (SSNAP) with incorporation of the Earthquake Transformer (EQT) (SSNAP-EQT)

Accurate seismic source phase picking are crucial aspects of seismology. Traditional methods face challenges in minimizing travel time residuals due to errors in phase picking, requiring a precise velocity model. Phase-picking errors, especially in low signal-to-noise ratio scenarios, complicate onset identification, especially for closely-spaced events. To improve algorithmic accuracy and efficiency, advancements are needed for fully automatic seismic source location processes without human intervention.

Automatic techniques, such as those using short-term-average and long-term-average ratio (STA/LTA)[2] or kurtosis, aim to overcome limitations in manual picking methods. The STA/LTA approach is highly flexible in detecting impulsive arrivals but may fail for events with amplitude

[2] STA refers to the short-term average of seismic signal amplitudes over a short time window, while LTA refers to the long-term average of seismic signal amplitudes over a longer time window.

near the noise level and closely spaced in time such that their arrivals overlap. Characteristic functions based on higher order statistics of the waveforms, such as skewness and kurtosis, have been shown to improve on STA/LTA for low signal-to-noise ratio and intense seismic activity (Baillard et al., 2014; Grigoli et al., 2016; Poiata et al., 2016).

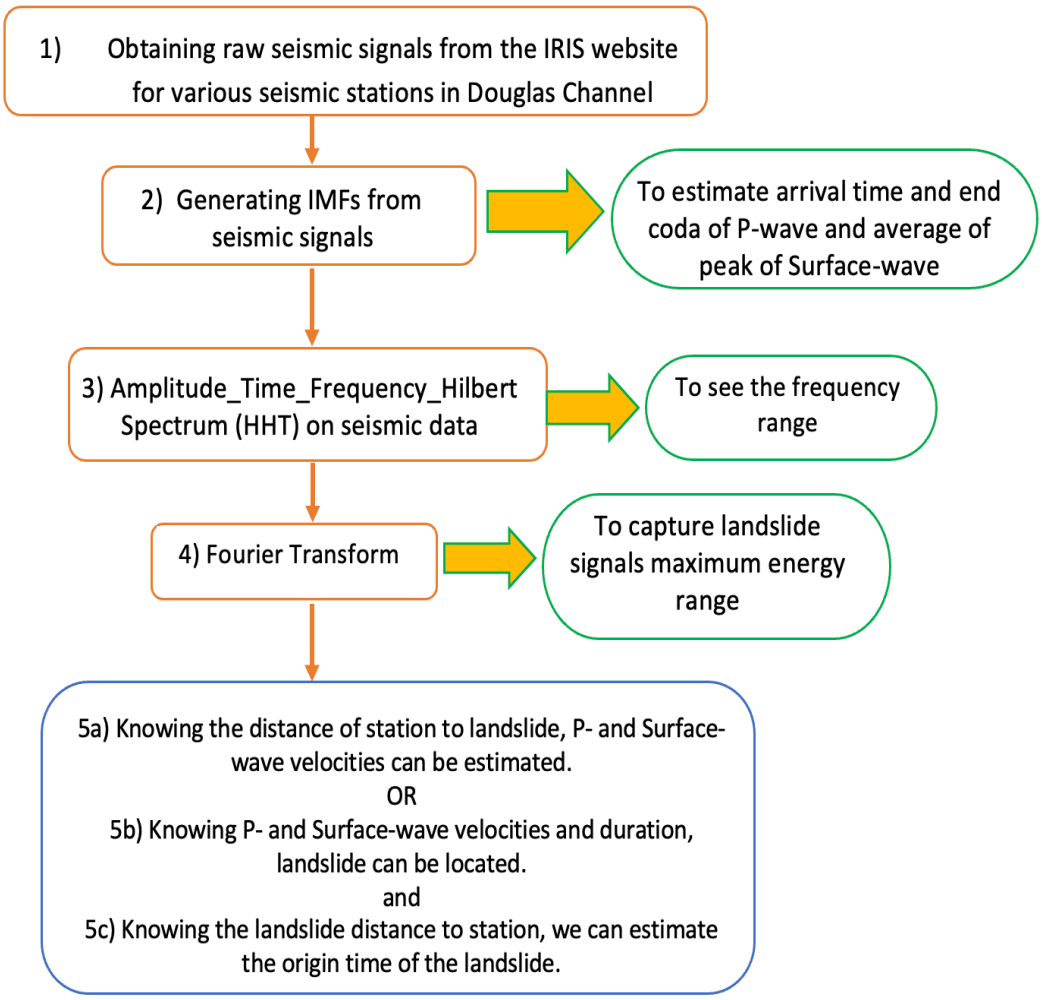


Figure 3.3. EMD and HHT analysis steps.

In the initial steps of this study, a simplified version of Baillard et al.'s (2014) kurtosis-based phase picker is employed as the first phase-picking attempt for landslides. Seismic phase arrival timings are determined by detecting sudden spikes in signal strength linked to these phases (Tan et al., 2020). Despite the cutting-edge nature of kurtosis in earthquake localization, surpassing established methods like the STA/LTA algorithm (Allen, 1982, 1978), this approach proved unsuitable for determining landslide arrival times. Consequently, a robust technique integrating a global AI and DL model, named Earthquake Transformer (EQT) (Mousavi et al., 2020), is implemented within the SSNAP model, for simultaneous event detection and phase picking (Dokht et al., 2019; Wang et al., 2019; Zhu & Beroza, 2019; Mousavi et al., 2020; Zhang et al.,

2021a). The EQT model, extensively used in various experiments, exhibits accuracy on par with human analysts' manual picks (Gong & Fan, 2022; Chuang et al., 2023; Shiddiqi et al., 2023). Its effectiveness will be demonstrated in a later section, with increased sensitivity and accuracy, especially in reducing erroneous arrival time detections caused by complex landslide waveforms. Moreover, the EQT model has outperformed previous deep learning and traditional algorithms in both phase picking and detection. Its success lies in efficiently combining information from seismic phases and full waveforms through a hierarchical attention mechanism.

The EQT model was trained on the STanford EArthquake Dataset (STEAD), comprising globally labeled earthquakes and noise signals (Mousavi et al., 2019). During this phase, approximately 1 million earthquakes and 300,000 noise waveforms recorded at stations within an epicentral distance of up to 300 km were employed, representing around 450,000 events. Notably, most events within STEAD have a magnitude lower than 2.5 and are recorded at epicentral distances within 100 km. The EQT transformer demonstrated a precision of 99% while picking for P and S waves and had a recall of 99% and 96% for P and S waves respectively. The training traces for the EQT model extended for 1 minute with a sampling rate of 100 Hz and underwent bandpass filtering in the range of 1–45 Hz.

While the EQT transformer was originally designed for earthquake phase picking, it is trained for lower magnitude earthquakes in the frequency range of 1-45 Hz, based on noise signals as well, and has a sampling rate of 100 Hz. Therefore, it appears reasonable to use it for landslide detection. The waveforms used for landslide detection maintain the same sampling rate of 100 Hz, with an equivalent earthquake magnitude ranging from 1 to 3, depending on the size of landslides, and lower frequency ranges, generally below 10 Hz. Consequently, the filtered traces from the trained EQT model enhance its suitability for landslide and microseismic detection.

The workflow of the SSNAP-EQT model closely mirrors that of the original SSNAP code, initially designed for earthquake detection (more detail in Tan et al., 2020). However, adjustments were necessary to apply SSNAP to landslide and microearthquake detection in the study area. These modifications address the challenges of identifying P phases for small seismic sources with noisy and intricate waveforms.

The SSNAP-EQT workflow comprises four fundamental processes. The first step involves source scanning, utilizing the Source-Scanning Algorithm (SSA) to analyze seismic data across a grid of nodes, identifying potential energy sources and generating brightness functions. The larger the value of the brightness function, the more the energy source is seismic rather than noise. Since landslide waveforms have longer durations, the original SSA can only estimate location roughly. To improve the accuracy of source location, I stacked the probabilities of P phases calculated by the EQT model using a 4-second time window with a 1-second increment. Subsequently, peaks with maximum brightness values are recognized as prospective events and advance to the next step. Grid nodes with brightness below the established threshold (0.4) are deemed too weak or noisy for further processing. Additionally, a minimum event interval of 5 seconds is imposed

between consecutive seismic events to prevent the algorithm from detecting closely-spaced events (e.g., multiple pulses of one landslide) as separate occurrences.

The second process associates the detected sources with EQT P phases according to the theoretical arrival times. A minimum probability threshold of 0.3 is assigned to seismic phases, designating phases below this threshold as less reliable and potentially negligible in event characterization. To be considered valid, an event must exhibit a minimum of 4 seismic phases, ensuring the removal of events lacking an adequate number of associated seismic phases. The integration of this method into the SSNAP model shows superior precision and sensitivity in detecting and characterizing seismic events including both earthquakes and landslides at the same time.

The third process in the SSNAP-EQT workflow focuses on location determination. It first uses equal-differential-time (EDT) layers among station pairs to locate the event and then refine the location with finer grids according to the travel time residual. The fourth and final step is the determination of an equivalent earthquake magnitude; the calculated size of the event (equivalent to local magnitude, ML, of an earthquake) based on recorded seismic wave amplitudes within 2 minutes of the P phase arrival.

The processing time of the SSNAP-EQT workflow is determined by various parameters, including the size of the research area, the number of stations, the scanning grid spacing, the computational hardware, and the number of events. Analysis of shorter waveform segments can significantly minimize processing time. In this study, processing of 1-hour waveform segments for 5 to 6 seismic stations will take 2-3 minutes. The distance a landslide-generated tsunami can travel in 3 minutes depends on various factors such as the initial energy of the landslide, the bathymetry of the ocean floor, and the coastal topography. In shallow water regions like the Douglas Channel, the speed of a tsunami wave decreases due to the shallower water depth. If a typical water depth for the Douglas Channel is assumed around 200 meters (although the actual depth may vary), in 3 minutes, a tsunami wave could travel approximately 7.97 km.

It's crucial to emphasize that real time deployment of SSNAP-EQT would entail processing shorter waveform segments. This approach would demand considerably less processing time, thereby extending the potential warning times.

## 3.2.3 Hydrophone data analysis

### 3.2.3.1 Previous studies and background information

Hydrophones, equipped with transducers that convert underwater sound waves into electrical impulses, play a crucial role in real time data analysis and the generation of calibrated waveform data (Madhusudhana et al., 2022). These underwater microphones record audio files capturing a broad spectrum of frequencies. Marine acoustic technology is pivotal for exploring the submarine environment and capturing signals from diverse geophysical phenomena, supporting marine

mammal observation, vessel monitoring, and soundscape analysis (Allstadt et al., 2018; Talandier et al., 2020; Shan et al., 2022; Abdalzaher et al., 2023). Beyond these traditional applications, hydrophones are essential in environmental monitoring, underwater communication research, and seismic detection (Biffard et al., 2022).

Hydrophone data are a crucial resource in the study of landslides, revealing distinctive spectral banding and signal duration throughout different stages of landslides (Caplan-Auerbach et al., 2014; Chierici et al., 2017). Recognizing ground motions and acoustic emissions due to friction during landslide deformation enhances the effectiveness of these devices in detecting and mitigating potential hazards, including tsunamis (Chierici et al., 2017).

#### 3.2.3.2 Data availability

In our study, the objective of incorporating hydrophones into the landslide detection network is to improve detection accuracy and to aid in the verification of events detected by the SSNAP-EQT model. The hydrophone data are also analyzed to determine whether landslides display a characteristic spectral signature that could further aid in landslide detection.

Ocean Networks Canada (ONC)'s hydrophone data archive includes 169 hydrophones, comprising 11 different types. Most common in the archive by both number and by data stored is the Ocean Sonics icListen High-Frequency (HF) instrument. The icListen HF is a broadband digital hydrophone, sampling at up to 512 kHz and capable of being deployed at ONC's deepest locations (up to 2660 m depth) (Biffard et al., 2022). Detailed information about the five hydrophones already deployed by Ocean Networks Canada in the NCBC region is shown in Table 3.1.

Table 3.1. Hydrophones operated by ONC in the North Coast of British Columbia region.

| Location Code | Location | Lat. (°N) | Lon. (°E) | Depth (m) | Data Coverage |
|---|---|---|---|---|---|
| **DIIP** | Digby Island | 54.259 | -130.431 | 27.5 | 2016-03-30 to Current (not continuous) |
| **HAK1A** | Queen Charlotte Sound | 51.712 | -128.236 | 79.0 | 06-Jul-2016 to 27-Jun-2017 |
| **HBIP** | Hartley Bay | 53.422 | -129.246 | 93.7 | 20-Oct-2020 to Current (not continuous; lacks data for the 2022-2023 events analyzed in this study) |
| **HEC1B.H1** | Hecate Strait | 52.821 | -129.846 | 82.0 | 30-Jun-2014 to 22-Jun-2015 |
| **KVIP (HYD1 in our study)** | Kitamaat Village | 53.975 | -128.657 | 46.1 | 29-Mar-2016 to 03-Dec-2023 (not continuous) |

Ocean Networks Canada processes all hydrophone data in a standardized setting: the information is structured into blocks of 4096 samples for broadband (BB) hydrophones and 512 samples for low-frequency (LF) hydrophones, featuring a 50% overlap (Ragland et al., 2022). Subsequently, the Welch mean, and median power spectral density (PSD) estimates are computed using a Hann window, employing 4096 FFT points for BB data and 512 FFT points for LF data (Ragland et al., 2022). Additionally, the datasets are reduced to a maximum frequency of 2 kHz to facilitate comparison. Spectrogram image files (PDF/PNG) are accessible for all individual hydrophones and hydrophone arrays (https://wiki.oceannetworks.ca/display/DP/45).

For this study, only one of the ONC stations was both optimally located and had data covering the periods of interest. I specifically investigated the hydroacoustic data recorded by the water-column-suspended hydrophone of the HYD1 hydroacoustic station 10 km south of Kitimat (KVIP in Table 3.1); the instrument is an Ocean Sonics icListen-HF smart hydrophone. The HYD1 hydrophone was installed for use in environmental monitoring and for ambient noise measurement in the study area, to monitor marine renewable energy devices, marine mammals, ocean noise, and for pipeline leak detection. It has a potential frequency range between 10 and 200 kHz (+/- 6 dB bandwidth) and is depth rated to 200 m. The HYD1 hydrophone is configured to capture data within high-frequency ranges, specifically spanning from 10 to 35 kHz. The location of the hydrophone is shown in Figure 3.4.

The hydrophone deployed at Kitamaat Village (HYD1) recorded data spanning from March 29, 2016, to December 3, 2023, capturing high-frequency ranges from 10 to 35 kHz with sampling rates reaching up to 64 kHz. Despite intermittent gaps in the data recording process throughout this specified timeframe, our study benefited from the identification of available hydroacoustic data pertinent to our targeted duration, facilitating the validation of landslides detected through the SSNAP-EQT model.

As mentioned previously, the first process typically followed by ONC personnel following data collection involves reading the data, calculating the Fast Fourier Transform (FFT), Welch mean, and median power spectral density (PSD), and applying a Hann window to the PSD to increase the number of degrees of freedom and smooth the spectra, thereby increasing the reliability of specific peaks. This methodology underscores the significance of careful processing to enhance the accuracy of hydrophone data interpretation, but it is not totally suitable for detecting landslide signals in lower frequency ranges.

Given that the HYD1 hydrophone in the study area records high-frequency data and is not explicitly engineered or calibrated for landslide detection and considering the necessity to discern signals associated with landslides occurring in lower frequency ranges (1-20 Hz), a systematic approach was employed, described in Sections 3.2.3.3-3.2.3.5 and 3.4.2. This involved customization of a Python code to address the inadequacy of the default ONC setup for processing hydrophone data for landslide detection.

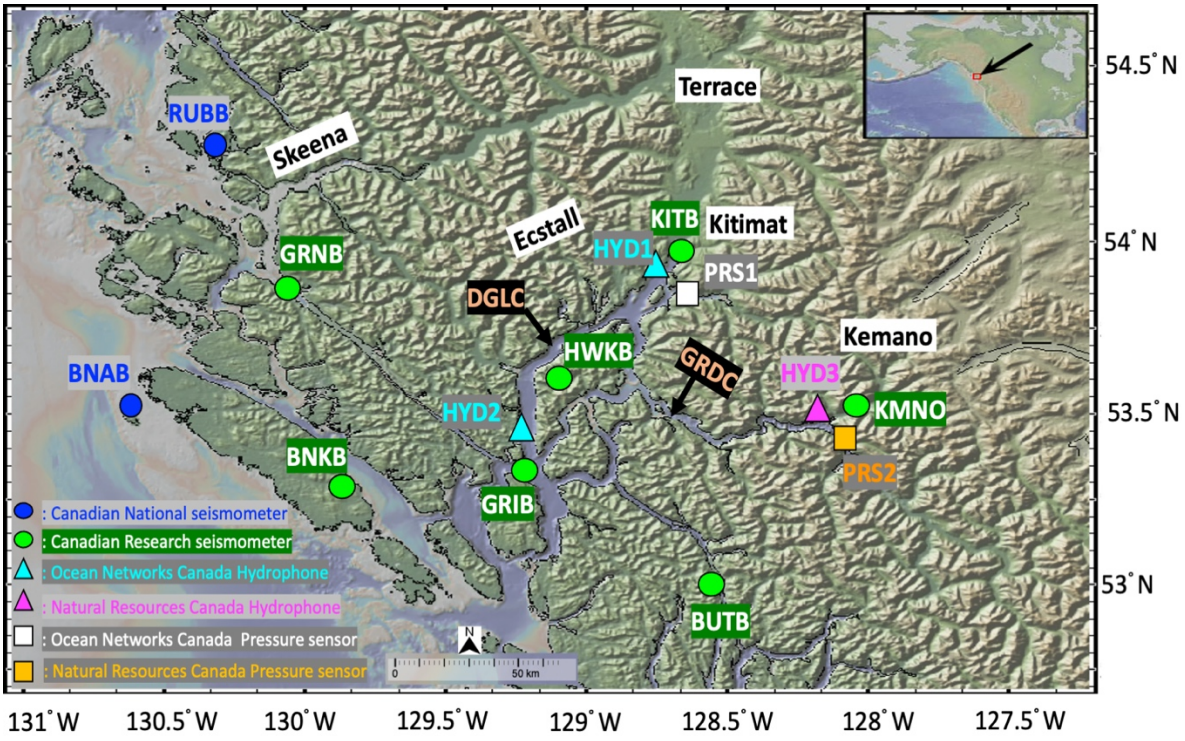


Figure 3.4. Instrument locations in the Douglas Channel (DGLC) and Gardner Canal (GRDC) region. Circle symbols denote research seismometers (C8) and national seismometers (CN), square symbols pressure sensors, and triangle symbols hydrophones.

### 3.2.3.3 Sensitivity Calibration

In this study, we incorporate crucial information from the hydrophone calibration sensitivities, specifically obtained for the HYD1 hydrophone. The data outline the sensitivity calibration for each frequency bin. The calibration covers a frequency range spanning from 10 to 4440 Hz. This information is paramount for the acoustic data interpretation, as it enables us to understand the hydrophone's sensitivity in decibels (dB) relative ($re$) to a reference level, considering the squared counts of the recorded signal per micro-Pascal ($\mu Pa$) squared at various frequencies, expressed in $dB\ re\ Counts^2/\mu Pa^2$. Here, “Counts” represents the digital units or measurements obtained from the hydrophone and is a measure of the hydrophone's response to the received signal. The amplitude or pressure level of the acoustic signal has units of $\mu Pa$. The calibration data are effective from 29-March-2016 onward, and their integration enhances the accuracy and reliability of the analyses by accounting for the hydrophone’s unique response characteristics across different frequency bands. In this study, I interpolate the calibration on the frequency bins. Only the bins that are within the range of calibration are selected.

#### 3.2.3.4 Bandpass filtering

Employing hydrophones for landslide detection from PSD plots requires specific configurations, including a 50% overlap, bandpass filtering within the 1-30 Hz frequency range and 64,000 FFT points for broadband (BB) data, following the setup of the PMEL hydrophone array (Caplan-Auerbach & Duennebier, 2001b). This arrangement played a crucial role in identifying landslides at the Kilauea Ocean entry (the location where lava flows enter the ocean), detecting between four and ten events daily during the active period of HUGO (Caplan-Auerbach & Duennebier, 2001b). The characteristic low-frequency component of the landslide signals serves as a vital indicator of their source, in this case often associated with the collapse and movement of large blocks due to massive lava outcrops. Notably, these landslide signals resemble earthquake T-phases, featuring emergent profiles with durations lasting several minutes (Chadwick et al., 2012).

In this study, a low pass filter (30 Hz) or high pass filter (10 Hz) is applied, data are excluded outside of the cut-off frequencies. The filtered data are then plotted showcasing the amplitude of the filtered signal over time. The output demonstrates the application of a bandpass filter to hydroacoustic data and provides a visual representation of the filtered signal's amplitude.

#### 3.2.3.5 Power Spectral Density (PSD)

Power Spectral Density (PSD) is a mathematical function that characterizes how the power of a signal is distributed across different frequencies, providing a measure of the signal's power at each frequency component over a given time period. PSD assume that the time series is stationary over the period used. The PSD is visually represented in a series of spectrograms, showcasing the time-varying frequency content of hydrophone data. This condensed overview of hydrophone spectral data aids in detailed audio analysis, allowing users to identify sources and characteristics of sounds. For instance, wave spectra from passing ships appear as hyperbolic curves, while whales generate distinctive chirps and resonances. Visual analysis of spectrogram data proves more efficient than relying solely on auditory perception.

In this study, two types of statistical analyses were performed for comparison: FFT and wavelet analysis.

**I) FFT method**

In this study, I compute the spectrogram of the audio data using a specified window length within 1 hour, 10 minutes, or 5 minutes depending on the event, an overlap factor of 50%, and a Hann window function. Calibration is applied using sensitivity information obtained from a calibration file, where sensitivity data are interpolated to match the frequency bins. I define high and low pass cut-off frequencies and apply interpolation to align sensitivity data with the spectrogram's frequency range. Using the windowed data matrix and the FFT technique, the

power spectral density (PSD) is calculated while taking windowing and calibration effects into account. The PSD for Hanning noise power bandwidth is then scaled. I then correct the spectral response by applying the sensitivity calibration. In order to account for windowing, the maximum Hann window PSD is found and subtracted from the final PSD. The technique yields a calibrated PSD, enabling precise measurement of the signal strength in the hydrophone audio recordings at various frequencies and times.

**II) Wavelet method**

The other type of spectral analysis, wavelet analysis, was performed using the Python wavelet package. The term "wavelet function" encompasses both orthogonal and non-orthogonal wavelets, whereas "wavelet basis" specifically denotes an orthogonal set of functions. Utilizing an orthogonal basis implies employing the discrete wavelet transform, while a non-orthogonal wavelet function can be applied with either the discrete or continuous wavelet transform (Farge, 1992).

Wavelet analysis reveals the frequency-time content of landslide waveforms and shows changes in signal amplitudes over time as the landslide moves. For wavelet analysis, the continuous wavelet transform (CWT) is used (Heidarzadeh & Satake, 2015). For the purposes of this study, only the continuous transform is utilized.

### 3.2.4 Bottom Pressure Sensor (BPS) data analysis

The use of BPS technology, employed since the 1990s in deep-sea environments, has proven instrumental in discerning tectonic deformation and exploring dynamics in submerged volcanic regions (Chadwick et al., 2006; Ballu et al., 2009; Chierici et al., 2016). However, challenges arise in near-surface measurements (less than 200–300 m depth), leading to noisy records that present difficulties in interpretation (Chierici et al., 2016). In addition, the detection of tsunamis in shallower regions is challenging due to coastal effects like harbor resonance, nonlinear effects, refractions, and scattering (Heidarzadeh & Gusman, 2018; Nemati et al., 2019, 2023). In this context, Chierici et al. (2017) applied techniques such as tidal component extraction, real time de-tiding through band-pass filtering, and spectral analysis to mitigate noise in bottom pressure time series. Processing like this makes it easier to identify tsunami signals that cross a certain threshold. Utilizing information from abyssal observatories in the Western Ionian Sea and the Gulf of Cadiz, as well as data from Haida Gwaii in 2012, the algorithm has shown promise (Chierici et al., 2017).

For this study, I specifically investigated the water level data recorded by the PRS1, 10 km south of Kitimat (KVIP in Table 3.2) which had data covering some of the periods of interest. PRS1 is a CTD (Conductivity, Temperature, and Depth) instrument deployed by ONC in 2017-2018 in the vicinity of Kitamaat Village. In November 2022, as part of the present study in collaboration with Natural Resources Canada (NRCan), a pressure sensor (PRS2 in Table 3.2) was installed near

Kemano; unfortunately the instrument was destroyed during a storm soon afterwards, and no data were retrieved.

Table 3.2. Pressure sensors in the study region.

| Item | Station Code | Location | Lat. (°N) | Lon. (°E) | Depth (m) | Data Coverage |
|---|---|---|---|---|---|---|
| **1** | KVIP.C1 (PRS1 in our study) | Kitamaat Village | 53.975 | -128.657 | 40 | 06-Apr-2017 to 23-Oct-2018 (not continuous) |
| **2** | PRS2 | Kemano | 53.48 | -128.125 | 10 | Destroyed because of storm |

Three phases comprise our BPS algorithm for tsunami detection in this study. This procedure, based on the work of Chierici et al. (2017), helps to achieve more precise, fast, and reliable tsunami detection. In the first stage, a set of procedures for combining and creating metadata from raw pressure data from PRS1 at Kitamaat Village is performed. The combination of raw CTD data and metadata yields a full dataset for our study.

Tidal analysis of acquired pressure data is conducted in the second stage. The tidal analysis provides information on tidal fits, residuals, and their relation to pressure variations, allowing for a thorough comprehension of tidal impacts on recorded pressure data. I analyze pressure sensor data to calculate and remove tidal aspects of the sea level time series to identify potential tsunami waves that exceed a specified threshold (Chierici et al., 2017). The process begins by importing processed data from the previous step and involves calculating tidal coefficients using the UT-solve approach (Codiga, 2011) for forecasting the tidal signal. The UTide toolbox simplifies tidal analyses, including constituent selection and confidence interval estimation for both two-dimensional (e.g., tidal currents) and one-dimensional cases (e.g., sea level); the UTide toolbox consists of two MATLAB functions: 1) ut_solv() for analysis, the results of which are passed to 2) ut_reconstr() for reconstructing a hind-cast or forecast/prediction, or “fit”, as needed. These functions accommodate uniformly or irregularly distributed time records and facilitate accurate nodal correction results. The reconstructed tidal signal and residuals (non-tidal pressure variations) are stored separately. The UT-solve method processes and resamples oceanographic data and solves for coefficients related to the first baroclinic mode based on time, pressure, and latitude. The UTide toolbox is widely used in oceanography and related fields to analyze tidal signals and extract information about tidal constituents from time series data (Torres & Nadal-Caraballo, 2021; Byun & Hart, 2019; Viola et al., 2021). It employs harmonic analysis techniques to decompose the data into a sum of sinusoidal components representing different tidal frequencies, which can then be subtracted from the data, leaving a residual time series. After that, amplitude will be significantly reduced up to two orders when the tidal components are eliminated from the dynamic change of amplitude in time series. According to Chierici et al.

(2017), this process aids in the achievement of more accurate, timely, and dependable tsunami detection.

The last step of the algorithm, which focuses on event identification, employs a moving average and a threshold of ±3 cm to identify possible events, demonstrating its applicability in the setting of our investigation. After that, the algorithm reads the tidal analysis results. By identifying abrupt variations in water level data suggestive of possible occurrences, it performs an event identification analysis. Once events are discovered, I conduct a detailed analysis. Various event characteristics, such as duration, wave amplitude, and start/end timings, are calculated. The findings acquired, including event details, are stored for further examination, and cross-checked against seismic waveforms and spectrograms of hydroacoustic data to determine if variations in water level may be tsunami waves triggered by landslides or earthquakes, or if they likely result from other causes.

## 3.3 Study area

The Douglas Channel study area, characterized by significant slopes exceeding 20°, experiences distinctive seasonal variations that markedly influence landslide occurrences, particularly during the wet season (Figure 3.5). The climatic pattern in the area is strongly influenced by its rugged topography. The region witnesses substantial rainfall in the fall (October to January), a total average precipitation of 270 mm over these four months, in contrast to the summer season (May to August), which experiences less precipitation at around 65 mm for the whole months of summer. This increased rainfall significantly contributes to the elevated frequency of landslides in this portion of BC (Guthrie et al., 2010; Sobie, 2020).

Environmental factors, such as high-intensity, short-duration precipitation, are recognized triggers for shallow landslides (Martelloni et al., 2012; Germain et al., 2022). Hence, given the factors that exist in regions like the Douglas Channel area in northwest BC, there is a high possibility of the occurrence of shallow landslides.

The study specifically focuses on the distinct regions of Kitimat, Hartley Bay, and Kemano in northwest BC, situated within the mountainous region of NCBC (Figures 3.1 and 3.4). Kitimat stands as the most populated area in Douglas Channel with 8,131 residents. The region experiences an oceanic climate with mild summers (average temperature: 12 °C) and cold, rainy winters (average temperature: -2 °C) amounting to an annual precipitation of approximately 164 mm (Figure 3.5). Hartley Bay, a First Nations settlement near the mouth of Douglas Channel, experiences an annual precipitation of about 4,500 mm. Accessible only by air and sea, it is the home of the Gitga'at First Nation with a population of 200. Kemano, located 75 km southeast of Kitimat, was established to support a hydroelectric power station for Alcan's aluminum smelter. The Kemano Generating Station, situated inside Mt Dubose, produces 896 MW from eight generators (Morgenroth, 2016).

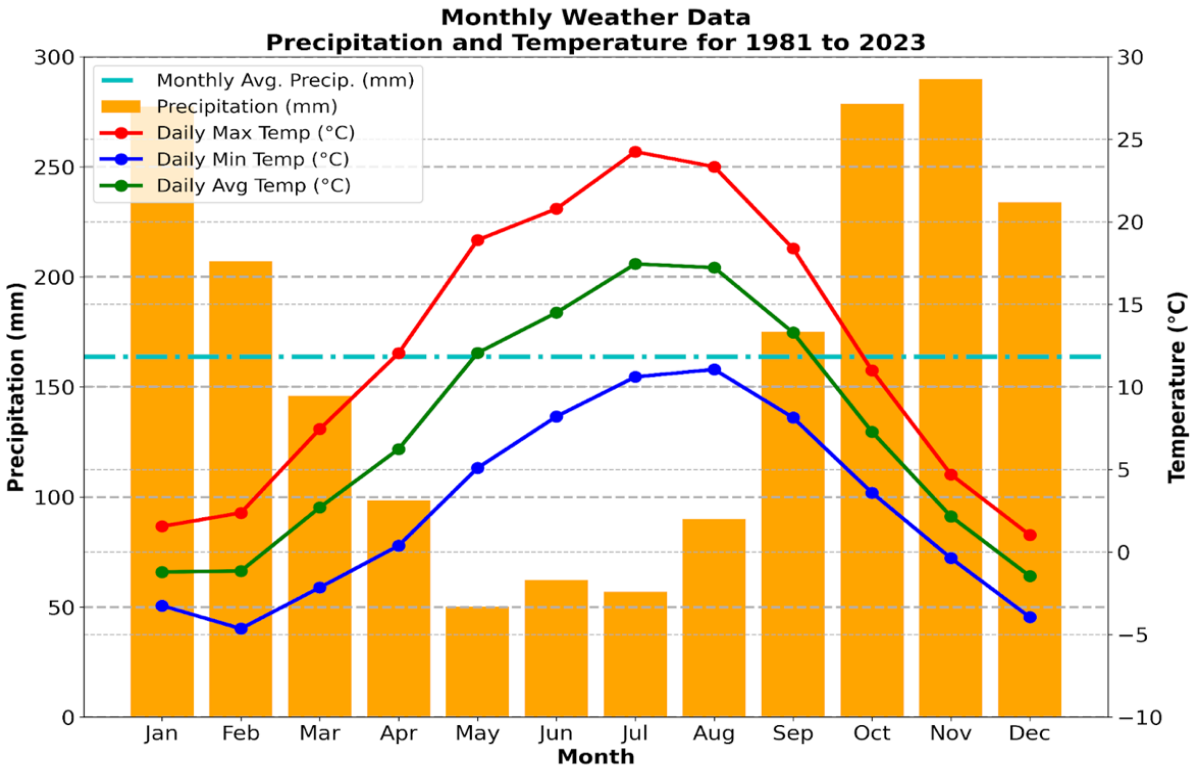


Figure 3.5. Monthly precipitation and temperature averaged over 1981-2023 at Kemano weather station, BC (Environment and Climate Change Canada, 2024). Total monthly average precipitation (mm) is represented by a cyan-colored dot-dash line, total average monthly precipitation (mm) shown as orange bars, and average daily maximum, minimum, and average temperatures (°C) depicted by red, blue, and green lines, respectively (Government of Canada, 2023).

The methods described in Section 3.2 are applied to development of an innovative landslide and tsunami detection system in the Douglas Channel area. This coastal region is marked by a history of landslide tsunamis which pose a substantial risk to population centers in Kitimat, Kitamaat Village, the traditional territory of the Haisla Nation, industry infrastructure, and maritime activities. The aim is to detect and locate potential landslides, both subaerial and submarine, as well as earthquakes, including microearthquakes (an earthquake with magnitude less than 2), and to detect and measure any triggered tsunami waves.

In 2017, a series of landslides occurred in the Douglas Channel region (Figure 3.6 and Table 3.3), likely triggered by heavy rainfall between September and October (Stan Hutchings, personal communication, 2018). Additionally, four landslide events near the Ecstall River were likely induced by intense rainfall from August 30$^{th}$ to September 1$^{st}$, 2022 (Figure 3.6 and Table 3.3). A significant rockslide event was recorded between Terrace and Kitimat on December 9$^{th}$, 2022, detected by north coast seismometers (Figure 3.6 and Table 3.3). The most recent landslide documented within the study region took place near the southwest of Kemano on May 9$^{th}$, 2023 (Figure 3.6 and Table 3.3). These events will be used to test the detection and location capabilities of the seismic-hydrophone network described in the following section.

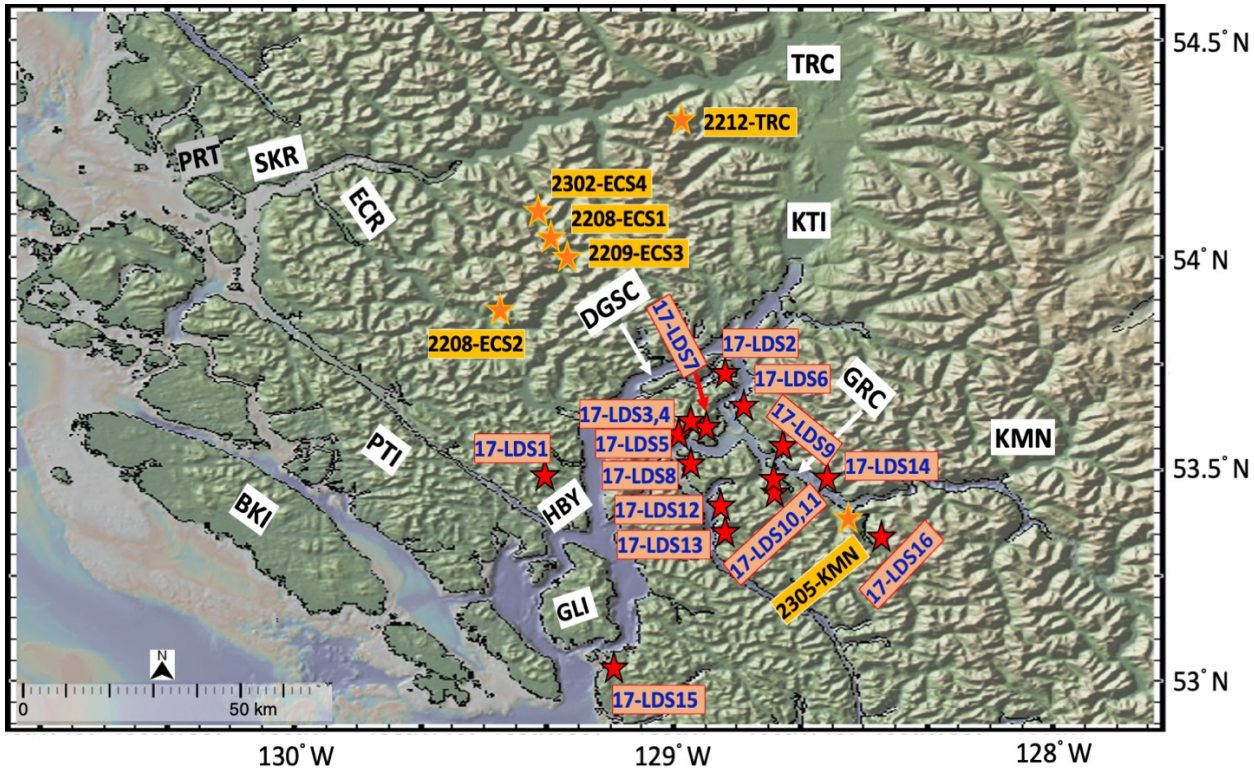


Figure 3.6. Locations of known landslides from the time periods analyzed in this study. Banks Island (BKI), Douglas Channel (DGSC), Ecstall River (ECR), Gardner Canal (GRC), Gil Island (GLI), Hartley Bay (HBY), Hawkesbury Island (HWBI), Kemano (KMN), Kitimat (KTI), Prince Rupert (PRT), Pitt Island (PTI), Skeena River (SKR), and Terrace (TRC) are also labelled. Red stars represent landslide events likely occurring in September and October 2017, while orange stars represent landslide events occurring between August 2022 and May 2023.

### 3.3.1 Instrument network

As highlighted in previous research, seismometers and hydrophones are valuable tools for detecting seismic sources, while BPSs are commonly used to identify abrupt changes in water level for tsunami detection. Establishing a network with these instruments allows for the identification and location of potential landslide events with tsunami-generating potential, forming a crucial part of an early warning system. Seismic stations provide a time series of acceleration in three spatial directions, hydrophones detect ocean sounds from all directions, and pressure sensors collect the time series of hydrostatic bottom pressure, enabling explicit measurements of sea level and tsunami waves. This combination of instruments enhances the detection and specification of seismic sources like submarine and subaerial landslides, and the use of multiple monitoring tools helps identify abnormal events, even when data from one of the instruments is unavailable.

In the Douglas Channel area, there are currently eight seismic stations, mostly installed since 2014; there are also hydrophones located at Hartley Bay and near Kitamaat Village (Figure 3.4 and Table 3.4). There is currently only one BPS in the area that can be used to detect tsunami

waves, located at Kitimat, with no current way to detect water level changes in Gardner Canal. The seismic network provides good coverage to the north, west, and south of the Douglas Channel system, but not to the east, making it a challenge to accurately locate landslides or microearthquakes.

Table 3.3. Geospatial and magnitude characteristics of landslide events in the Douglas Channel region.

| Landslide[3] | Lat. (°N) | Lon. (°E) | Event Location | SSNAP-EQT Mag. (ML) | Event Time |
|---|---|---|---|---|---|
| **17-LDS1** | 53.429 | -129.279 | Hartley Bay Lake | - | September / October 2017 (No information about the precise time) |
| **17-LDS2** | 53.639 | -128.881 | North Kitsaway Anchorage | - | |
| **17-LDS3** | 53.596 | -128.924 | Evelyn Creek | - | |
| **17-LDS4** | 53.599 | -128.924 | Evelyn Lake | - | |
| **17-LDS5** | 53.582 | -128.963 | Danube Bay | - | |
| **17-LDS6** | 53.611 | -128.817 | North of Crab River | - | |
| **17-LDS7** | 53.581 | -128.895 | South Kitsaway Anchorage | - | |
| **17-LDS8** | 53.535 | -128.961 | Moody Point | - | |
| **17-LDS9** | 53.540 | -128.7421 | Collins Bay | - | |
| **17-LDS10** | 53.498 | -128.770 | Ochwe Bay | - | |
| **17-LDS11** | 53.478 | -128.780 | Paril River tributary | - | |
| **17-LDS12** | 53.377 | -128.882 | North of Goat Harbour | - | |
| **17-LDS13** | 53.337 | -128.884 | South of Goat Harbour | - | |
| **17-LDS14** | 53.491 | -128.617 | West of Shearwater Point | - | |
| **17-LDS15** | 53.051 | -129.114 | Barnard Harbour | - | |
| **17-LDS16** | 53.380 | -128.486 | Kiltuish Inlet | - | |
| **2208_ECS1** | 54.017 | -129.305 | 44 km W of Kitimat | 2.1 | 2022-08-30 at 22:46:58 |
| **2208_ECS2** | 53.885 | -129.436 | 50 km W of Kitimat | 1.9 | 2022-08-31 at 03:36:02 |
| **2209-ECS3** | 53.982 | -129.300 | 50 km W of Kitimat | 2.8 | 2022-09-01 at 18:03:11 |
| **2302-ECS4** | 54.054 | -129.329 | 43 km W of Kitimat | 1.2 | 2023-02-17 at 04:45:12 |
| **2212-TRC** | 54.299 | -129.0024 | 34 km NW of Kitimat | 2.0 | 2022-12-09 at 15:03:38 |
| **2305-KMN** | 53.416 | -128.586 | 72 km S of Kitimat | 1.8 | 2023-05-09 at 03:46:06 |

In the project's initial phases, plans were made to install essential monitoring instruments in Kemano in November 2022 to address the eastern gap in the instrumental network, aiming to enhance event detection and location capabilities while facilitating measurements of water level changes in Gardner Canal. In this regard, the installation of a seismic station (PQ_KMNO in Figure 3.4 and Table 3.4), a moored hydrophone (HYD3 in Figure 3.4 and Table 3.4), and a BPS (PRS2 in

[3] Details of the 2017 events are from Stan Hutchings (personal communication, 2018); details of the 2022-2023 landslides are from C. Brillon (personal communication, 2023).

Figure 3.4 and Table 3.4) at Kemano in the Gardner Canal was performed. The selection of Kemano dock as our base provides accessibility by boat, AC power near the dock, and real time communications. The PQ_KMNO seismic station is positioned on land near Kemano dock.

Table 3.4. Locations and start dates of seismic (C∗), hydrophone (HYD∗), and pressure sensor (PRS∗) instruments in the study area.

| Instrument | Location | Lat. (°N) | Lon. (°E) | Elevation[4] (m) | Start |
|---|---|---|---|---|---|
| **CN_BNAB** | Bonilla | 53.4932 | -130.6368 | 19 | 1999-04-16 |
| **CN_RUBB** | Prince Rupert | 54.3262 | -130.2523 | 12 | 2001-07-17 |
| **C8_BNKB** | Banks Island | 53.33 | -129.908 | 421.0 | 2014-08-20 |
| **C8_BUTB** | Butedale | 53.063 | -128.4633 | 1094.0 | 2014-08-21 |
| **C8_GRIB** | Gribbell Island | 53.3385 | -129.1383 | 418.0 | 2017-08-30 |
| **C8_GRNB** | Granville Island | 53.85 | -129.96 | 461.0 | 2014-08-24 |
| **C8_HWKB** | Hawkesbury Island | 53.60 | -129.15 | 778.0 | 2014-08-21 |
| **C8_KITB** | Kitimat | 54.0779 | -128.6368 | 72.0 | 2014-03-20 |
| **PQ_KEMNO** | Kemano | 53.487 | -128.115 | - | 2022-11-07 |
| **HYD1** | Kitimat | 53.975 | -128.657 | 46.1 | 2016-Mar-26 |
| **HYD2** | Hartley Bay | 53.422 | -129.246 | 93.7 | 2020-Oct-17 |
| **HYD3**[5] | Kemano | 53.478 | -128.133 | ~20 | 2022-11-07 |
| **PRS1** | Kitimat | 53.975 | -128.657 | 40 | 2017-04-06 |
| **PRS2**[3] | Kemano | 53.479 | -128.123 | ~10 | 2022-11-07 |

Hydroacoustic signals, generated by landslides, may integrate into the ground, making them detectable by hydrophones or seismometers. Given the rigid nature of the seismometer's location, the installation of the HYD3 hydrophone would be valuable for improved landslide signal detection. Consequently, the HYD3 hydrophone and the "PRS2" pressure sensor were placed underwater, with the PRS2 BPS positioned near Kemano dock and the HYD3 hydrophone located ~330 m farther away from the dock, both connected to the shore for real time monitoring capabilities. The placement of HYD3 at a distance from the dock was chosen in order to minimize

[4] The values for the hydrophones and pressure sensors are depth below sea level.
[5] Kemano instruments that were destroyed in a storm soon after deployment.

noise interference and to avoid potential landslide paths, ensuring a cleaner acoustic database for this hydrophone and minimizing the risk of instrument loss or damage (Clare et al., 2020, 2021; Heerema et al., 2020).

Unfortunately, the HYD3 hydrophone recorded only three days of data due to a power outage at Kemano port caused by a severe storm. Additionally, the storm resulted in the destruction of the PRS2 BPS. As a result, there is only one BPS in the study region, PRS1 in the vicinity of Kitimat. Unfortunately, PRS1 did not have data for all targeted time periods of the study, specifically for the landslide events that occurred within the years 2022 and 2023 in the study region. Similarly, there is only one hydrophone in the region that recorded acoustic data during the chosen time window: the HYD1 hydrophone near Kitimat. Hence, a system was created to detect and locate landslides in the region using information from one hydrophone and nine seismic stations, some of which had incomplete data coverage. Two seismic stations are part of the Canadian National Seismic Network (CN) and seven are part of the Canadian Research Seismometer (C8) (Figure 3.4 and Table 3.4). Data from the single pressure sensor were also analyzed, to assess and quantify the occurrence of potential tsunami waves near Kitimat.

## 3.4 Application of methodology to the Douglas Channel study

### 3.4.1 Seismic signal analysis

This study delves into seismic signals linked to landslide dynamics, underscoring factors shaping ground motions and noise generation across various stages of landslide evolution. Landslide seismic signals markedly differ from earthquake-generated signals, showcasing a high-energy, low-frequency (0.1-10 Hz) signature, contrasting with the higher frequencies typical of seismic signals (Figure 3.7) (e.g., Clare et al., 2024).

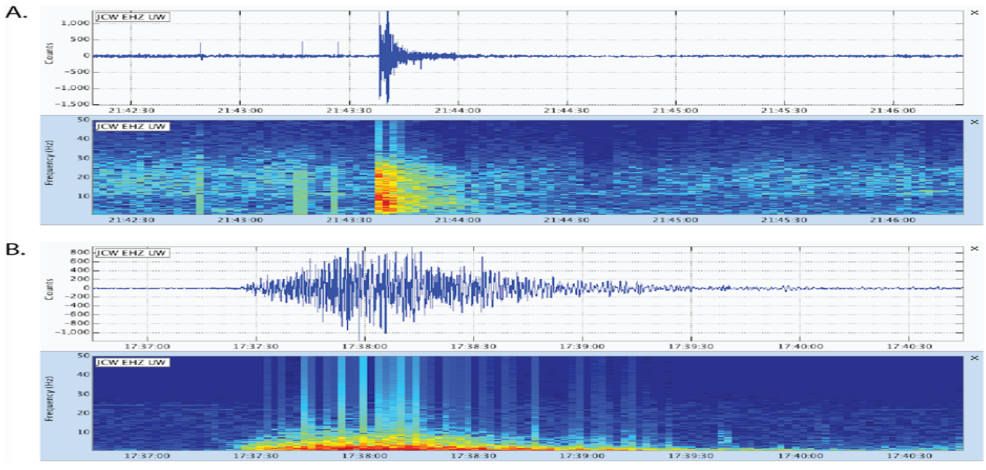


Figure 3.7. Comparison of (a) earthquake and (b) landslide seismic signatures (Allstadt et al., 2014).

#### 3.4.1.1 EMD and HHT approach for velocity estimation

In this chapter, I examine the seismic signals generated by landslides in 2017, 2022, and 2023 in the Douglas Channel region. The recordings were captured by broadband and short-period seismic stations located within a 34–260-km distance range from the source (Table 3.5). Table 3.5 provides information on the broadband seismic stations, including their azimuths to two landslides that occurred in 2022 (2212-TRC and 2209-ECS3, Table 3.3), to provide a clearer idea of the relative placement of the seismic stations. The low-frequency seismograms for all landslides reveal a complex time history in the release of seismic energy. Here, I specifically focus on the seismic wave properties of the 2022 Terrace rockslide as recorded at the seismic stations in the study area, utilizing the Empirical Mode Decomposition (EMD) approach to analyze signal properties and frequency spectra, as previously described in Section 3.2.2.1.

Table 3.5. Seismic monitoring network: station positions (distance, azimuth) relative to two landslides in 2022.

| **Station Name and Location** | **Distance (km)/ Azimuth (°)** | **Terrace Rockslide (2212-TRC) (-129.0024° E, 54.299° N)** | **Ecstall River landslide (2209-ECS3) (-129.300° E, 53.982° N)** |
|---|---|---|---|
| **C8_RUBB (-132.4767° E,53.2025° N)** | Distance (km) | 258.9 | 226.8 |
| | Azimuth (°) | 243.3 | 248.8 |
| **C8_GRNB (-129.9575° E,53.8468° N)** | **Distance (km)** | **80.1** | **45.6** |
| | Azimuth (°) | 231.5 | 251.0 |
| **CN_BNAB (-130.6368° E,53.4932° N)** | **Distance (km)** | **139.6** | **103.4** |
| | Azimuth (°) | 230.7 | 238.8 |
| **C8_KITB (-128.6368° E,54.0779° N)** | **Distance (km)** | **34.2** | **44.6** |
| | Azimuth (°) | 135.8 | 75.9 |
| **C8_HWKB (-129.1544° E,53.5984° N)** | **Distance (km)** | **78.5** | **43.7** |
| | Azimuth (°) | 187.3 | 167.3 |
| **C8_BNKB (-129.9017° E,53.3318° N)** | **Distance (km)** | **122.7** | **82.5** |
| | Azimuth (°) | 209.1 | 209 |
| **C8_GRIB (-129.1383° E,53.3385° N)** | **Distance (km)** | **107.2** | **72.3** |
| | Azimuth (°) | 184.8 | 171.5 |
| **C8_BUTB (-128.4633° E, 53.063° N)** | **Distance (km)** | **141.9** | **116.2** |
| | Azimuth (°) | 165.3 | 151.2 |

To showcase the effectiveness of the method, I chose a 10-minute continuous waveform dataset with distinct features. This dataset, representing the vertical component of the seismic

signal, was collected between 15:00 and 15:10 UTC on December 9th, 2022, during the Terrace rockslide event.

The Terrace rockslide occurred in the vicinity of C8_KITB, C8_HWKB, CN_RUBB, C8_GRIB, and CN_BNAB stations. Sample waveforms are provided in Figure 3.8 to demonstrate the general seismic characteristics of the landslide signals, such as the absence of distinct seismic phases and the presence of a tremor-like pattern with sporadic bursts of significant amplitudes. Larger seismic amplitudes were generated by stronger impacts, whereas small seismic amplitudes were generated by slowly moving landslides at an early stage, exhibiting low momentum, which increased as the landslide accelerated. Despite the presence of significant noise levels in the original data, the signals associated with the Terrace rockslide were still distinguishable at the C8_KITB, C8_HWKB, C8_GRIB, and CN_BNAB stations, as depicted in Figure 3.8. However, to obtain a clearer representation of the signals transmitted from the rockslide, minimize the impact of noise, and estimate the arrival time of P and surface-waves, I filtered the waveforms and applied the EMD method.

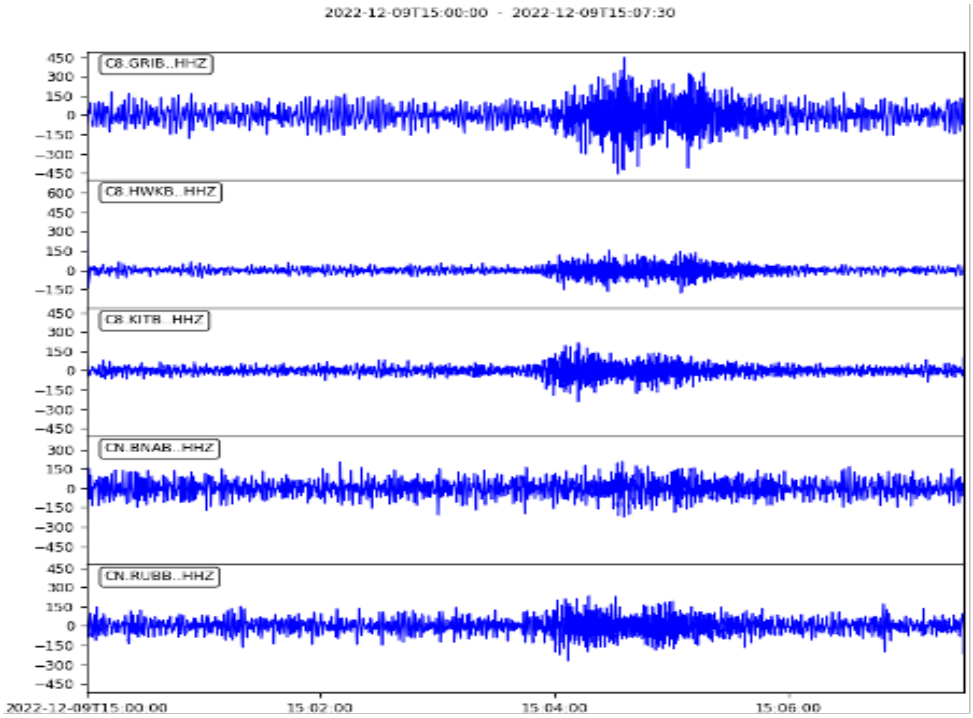


Figure 3.8. Signals from the 2022 Terrace rockslide recorded by different seismic stations. Units on the y-axis are counts.

The EMD technique allowed me to sift the signals from the noise into the IMF frequency ranges, which enabled me to visually identify the signals relevant to the landslide. I present the 7 IMFs obtained from the EMD processing in Figure 3.9. The analysis focused on examining the IMFs obtained from the broadband stations, specifically C8_HWKB and C8_GRIB.

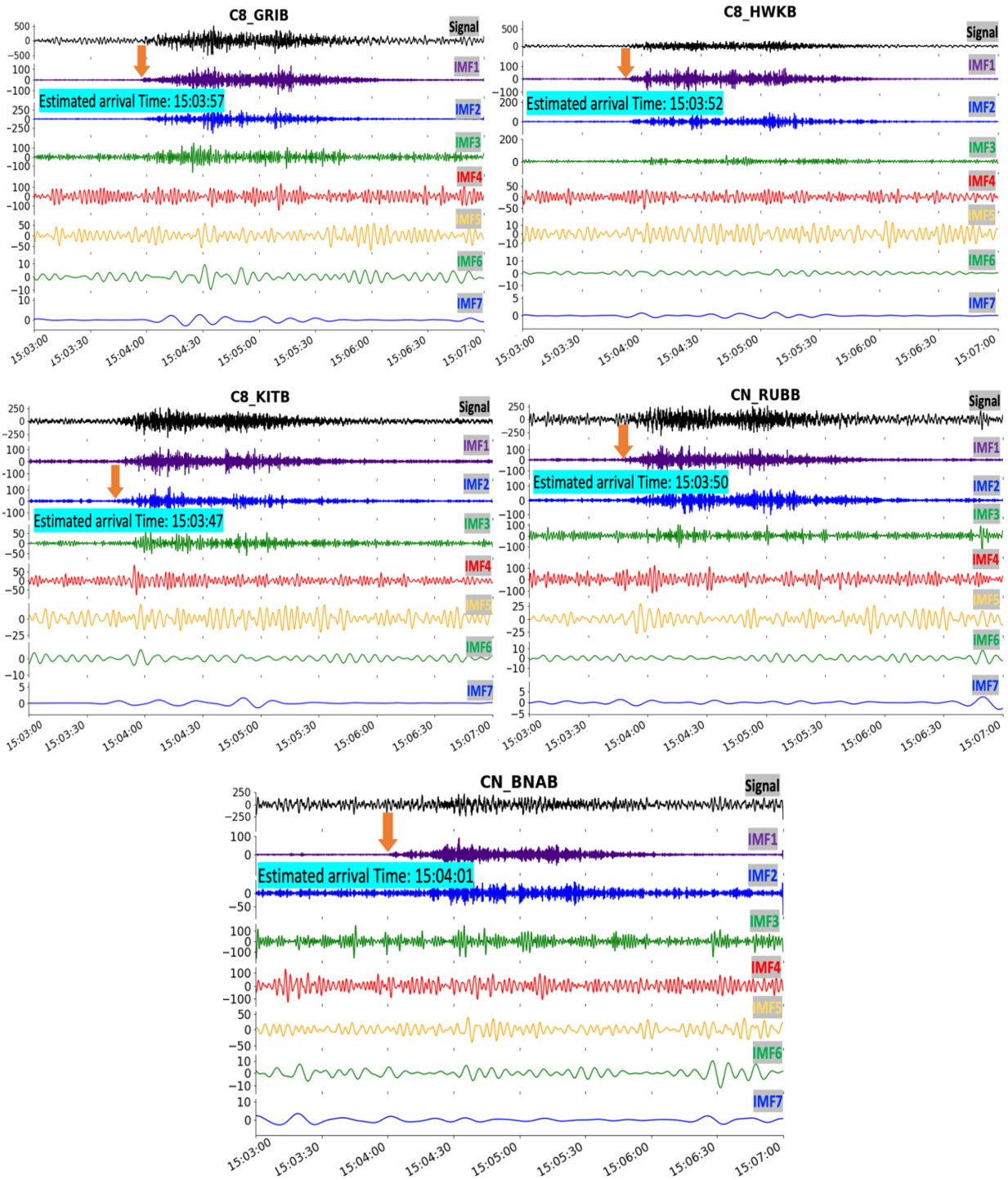


Figure 3.9. EMD of vertical component seismograms from C8_GRIB to CN_RUBB stations (the same stations shown in Figure 3.8): IMFs 1-7 with estimated arrival time shown with arrows.

A spectrogram, as shown for the same five stations in Figure 3.10, serves as a visual representation of the frequency content of a signal over time, offering a means to analyze how the frequency components evolve across different time intervals. In this representation, the x-

axis corresponds to time, the y-axis to frequency, and the color intensity or brightness denotes the magnitude or power of the signal at a specific time and frequency.

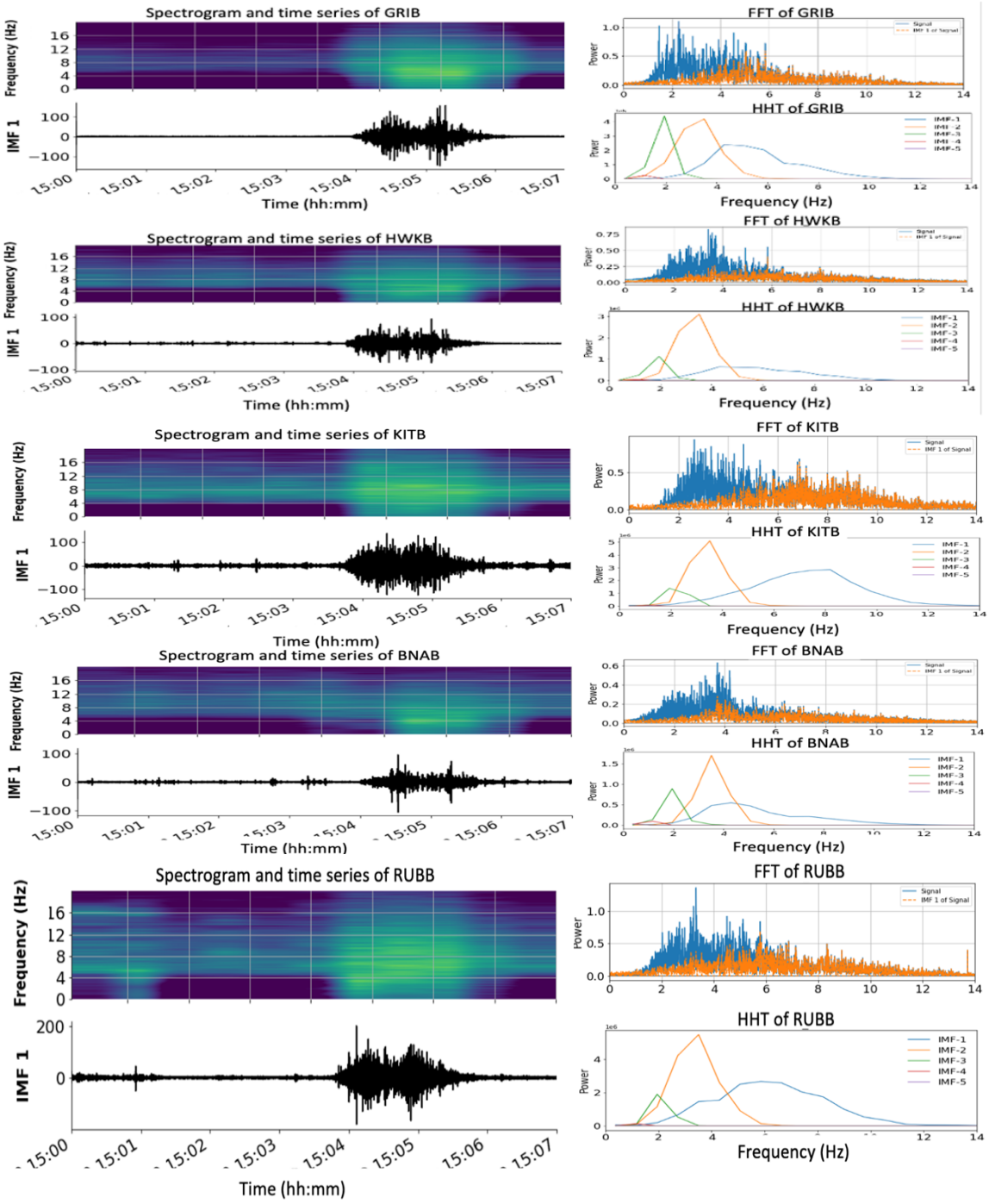


Figure 3.10. LHS: time frequency spectra (HHT) of IMF 1; RHS-Top: FFT of the signal (blue) and IMF 1 (orange) of the five seismic stations (the same stations shown in Figure 3.8); RHS-Bottom: HHT of different IMFs of the signal for the five seismic stations.

Previous seismic research on landslides, as demonstrated by Suriñach et al. (2005), has affirmed that surface mass movements contribute to observable increases in frequencies and amplitudes on spectrograms over time. The Suriñach et al. (2005) study further highlighted that capturing the seismic signal from a moving source at a sensor aligned with its propagation direction results in a distinctive change in the spectrogram representation. Our research aligns with these established findings, revealing a consistent change pattern in the spectrogram that strengthens its efficacy in landslide detection.

Figure 3.10 (left-hand side, LHS) illustrates IMF 1 and the corresponding amplitude-time-frequency Hilbert (HHT) spectrograms for all five stations. These spectrograms reveal temporal changes in the landslide's frequency content, ranging from 1 to 14 Hz, with intermittent bursts of seismic energy. Notably, the coherent signal behavior in the spectrograms aids in the recognition of onset of the landslide signal, which becomes evident at 15:03:57 at GRIB station. The gradual increase in frequency content and amplitudes of the spectrogram and waveform over time is characteristic of a landslide signal. On the right-hand side (RHS) of Figure 3.10, the FFT and IMF 1 of the filtered signals showcase a frequency range from 0.1 to 14 Hz.

The case study results further demonstrate that the seismic amplitudes of high-frequency signals (2 to 12 Hz) initially increased before subsequently decreasing at stations surrounding Douglas Channel, as depicted in Figures 3.9 and 3.10. This pattern may represent the overall process of landslide movement (Lin, 2015) and has implications for the spectrogram of the signal. Specifically, when the distance between the source and sensor increases, a spectrogram of a signal will display a greater proportion of low-frequency energy. Conversely, shortening distance between the source and sensor will result in a higher amount of high-frequency energy, leading to an overall increase in signal amplitudes (Suriñach et al., 2005).

Previous research by Feng (2011) has indicated that high-energy IMFs may introduce noise, especially for stations located at a distance from the landslide, such as CN_BNAB and C8-GRIB (Figure 3.9). The CN_BNAB station, positioned 140 km from the Terrace rockslide, is much farther from the source than C8_KITB, C8_HWKB, and CN_RUBB. While the latter stations had sufficient energy for distinguishing landslide signals, frequency content proved to be a better diagnostic for more distant stations like C8_GRIB and CN_BNAB, as the frequencies generated by a landslide should remain relatively constant, only slightly altered by wave propagation (Figure 3.10).

The propagation of high-frequency signals (2 to 12 Hz) is known to be susceptible to attenuation, which can be caused by a range of factors, including absorption, scattering, and diffraction. Examining the IMF 1 of CN_BNAB, it is observed that the landslide signals lasted 130 seconds longer than the 119 seconds recorded at the C8_KITB site, located closer to the landslide. This discrepancy is attributed to wave propagation dispersion, wherein waves travel at varying speeds based on their frequency (Deparis et al., 2008).

For instance, C8_KITB, positioned at the closest proximity to the Terrace rockslide at 34.2 km (Figure 3.4 and Table 3.5), demonstrated the highest wave amplitude for IMF 1, ranging from

approximately -120 to 120, accompanied by a greater amount of high-frequency energy between 2 and 12 Hz (Figures 3.9 and 3.10). In contrast, CN_BNAB, situated 140 km from the source, exhibited the lowest IMF 1 wave amplitude, ranging from approximately -60 to 60, and minimal frequency energy varying between 2 and 8 Hz (Figures 3.9 and 3.10). These observations indicate that signals from CN_BNAB attenuated more, mainly due to the greater distance travelled by the seismic waves compared to the other stations (Fang, 2011).

To assess P wave and surface-wave velocities, I estimated the seismic signals' arrival time at stations. P wave velocity is a crucial input for the modified SSNAP-EQT model used in landslide detection. Surface-wave velocity is not utilized in the SSNAP-EQT model and is calculated solely to provide additional information about landslide velocity within the study region. The selection of stations for signal processing was contingent on data availability.

Assuming that the geological configuration of the study area is relatively homogeneous, I took advantage of the approximately linear arrangement between the location of the Terrace rockslide and stations C8_HWKB and C8_GRIB. The azimuths of the rockslide to HWKB and GRIB were 187° and 184°, respectively, as provided in Table 3.5, and the signals originating from the rockslide were readily identifiable at both stations. By processing the IMF 1 and IMF 2 signals obtained from these stations, I was able to estimate the seismic wave velocities and use them to calculate the origin time of the rockslide.

The vertical component of the signal first reached C8_HWKB at 15:03:52, and the coda persisted until 15:05:59, indicating a signal duration of approximately 78 seconds. At 15:03:57, the vertical component of the seismic signal was first detected by C8_GRIB. The coda phase ended at 15:06:03, after a duration of approximately 107 seconds. In Figure 3.9, the solid arrows represent the estimated first-arrival times of the compressive P waves. These waves took approximately 5 seconds to travel from C8_HWKB to C8_GRIB. Based on the distance of 28.6 km between the two stations, the average P wave propagation velocity was calculated to be 5.73 km/s, assuming a straight-line travel path.

To approximate the surface-wave velocity in our study area, the peak amplitudes in the IMF 2 time series of the C8_HWKB and C8_GRIB stations were selected. The average start times of these six to seven surface-wave peaks were 15:04:34 and 15:04:43 for C8_HWKB and C8_GRIB, respectively. As shown in Figure 3.9, determining the average time of these surface-wave peaks from the original signals of the C8_HWKB and C8_GRIB stations are not as straightforward as it is from their IMF 2 time series. The surface wave traveled between C8_HWKB and C8_GRIB in approximately 9 seconds. Based on the distance of 28.6 km between the two stations, the propagation velocity of the surface wave was calculated to be approximately 3.2 km/s. These average velocities of 5.7 km/s and 3.2 km/s for P and surface waves, respectively, are appropriate for their propagation through the sedimentary layers of the Douglas Channel region over a relatively shallow crustal route. The landslide signals detected at C8_GRIB persisted for approximately 29 seconds longer than those recorded at C8_HWKB. This difference in duration is

attributed to the phenomenon of wave propagation dispersion, where waves of varying frequencies travel at different speeds (e.g., Nemati et al., 2023).

Given the distance of 78.5 km between the Terrace rockslide and the C8_HWKB station, the P waves generated by the landslide were expected to have taken roughly 13.6 seconds to travel through the shallow subsurface. Based on this calculation, the event time of the Terrace rockslide is predicted to be 15:03:38 on December 9$^{th}$, 2022; this origin time matches the time of the same event in the NRCan Earthquake Catalog (Table 3.3).

Lin (2015) used a comparable methodology for estimating P wave velocity. Lin (2015) observed high-frequency seismic signals with a propagation velocity of approximately 5 km/s, detected only at nearby stations within less than 100 km. These signals are likely associated with P waves that propagated through the crust and decayed significantly with increasing distance. Lin (2015) also observed signals with exceptionally long periods that propagated at a speed of approximately 3.4 km/s, which is typical for earth surface (Rayleigh) waves. Hence, the calculated velocities align with Lin (2015)'s study and the NRCEC (Table 3.3).

#### 3.4.1.2 SSNAP-EQT model

Using the limited number of seismic stations in the study area, I conducted a thorough investigation to identify the most effective technique to accurately detect and locate landslides, testing the method using the known locations and exact or approximately known timing of 22 landslides (Table 3.3). Various methods were explored to achieve optimal results. Initially, I exclusively tried to stack absolute values of the filtered waveforms for seismic phase picking in the SSNAP model. Subsequently, I implemented the EMD approach and kurtosis methods in a separate attempt, which provide to be less accurate in event detection. Ultimately, the best results were attained by leveraging the neural networks EQT AI-model and applying machine learning techniques to the original SSNAP code. Finally, the best results were achieved by integrating the EQT model into the SSNAP model and stacking the P phase probability series output by EQT.

To illustrate the efficacy of the technique, I applied it to a set of nine seismic signals (depending on availability during the target time period) and presented the results alongside waveform data from all landslides. The detected events were evaluated by comparing the estimated location and time with those in the NRCan Earthquake Catalog (NRCEC) (Earthquakes Canada, 2021). However, it should be noted that the event locations recorded in the NRCEC are also subject to uncertainty (Mahani et al., 2016). According to Mahani et al. (2016), the positional error in areas well-covered by seismic stations is generally under 3 km in both the east-west and north-south components, but in regions with limited regional network coverage, location uncertainties may reach 10 km in the eastward component. However, Brillon (personal communication, 2024) suggests that NRCEC uncertainties vary from ±5 km in well-monitored areas (southwest BC) to approximately ±20 km

in northern BC. Ideally, ground-truthed observations (e.g., satellite image or field observations of landslides) are necessary to properly assess the location accuracy of the SSNAP-EQT model.

As shown in following sections, the SSNAP-EQT model not only excels in detecting landslides within the study area, but it also demonstrates the capability to identify small earthquakes occurring within the specified target timeframe.

Accuracy in detecting events in both space and time is influenced by factors such as the configuration and quantity of seismic stations near a landslide site, the size and type of the landslide events (e.g., rigid rockslide versus debris flow), and the distance of the seismometers from the event location. Challenges arise for SSNAP-EQT when the network lacks a seismometer on any side of the landslide, impacting the accurate determination of the event's location. Additionally, the magnitude of landslide events plays a role in detection precision, as larger events generate less noisy waveforms, facilitating better picking of arrival times and, consequently, more accurate location estimates. Landslides of different types also vary in their typical signal to noise ratio. For instance, rigid rockslides provide stronger seismic signals in comparison to debris flows.

### 3.4.2 Hydroacoustic signal analysis

In a study area, a hydrophone network plays a crucial role in estimating the position and timing of events, particularly when seismic stations are unable to capture signals from small landslides. In this research, since there is only one hydrophone, the exclusive hydroacoustic dataset from the HYD1 hydrophone serves as a valuable resource, confirming and validating the results obtained from the SSNAP-EQT model.

All the 2022 and 2023 landslides detected by the SSNAP-EQT model were also detected by the HYD1 hydrophone data analysis. Not only do the onset times coincide, but the duration of the signals can also be correlated between the seismic stations and the HYD1 hydrophone (more details in Sections 3.5.1 to 3.5.6). Since the HYD1 recordings are bandpass filtered between 10 and 30 Hz, only the low frequency portion of the signal is considered for the interpretation. The hydroacoustic data from HYD1, representing events in higher frequency ranges, are also plotted without filtering. The methods rely on the duration, shape, and frequency content of the signals. The range of seismic and acoustic signal characteristics from different event types is demonstrated in Sections 3.5.1 to 3.5.6.

### 3.4.3 Bottom pressure sensor analysis

I apply the technique described in Section 3.2.4 to BPS data collected in 2017 at Kitamaat Village in Douglas Channel and discover that it can detect changes in water level above a ±3 cm threshold. Figure 3.11 shows a series of filters and processes like those utilized in our code. The processing includes the removal of tide effects, spike removal, and bandpass filtering to extract noise, to enable identification of tsunami signals above a defined threshold (Chierici et al., 2017).

In this study, the spike removal step was not necessarily since there were no spikes in the time series of data analyzed.

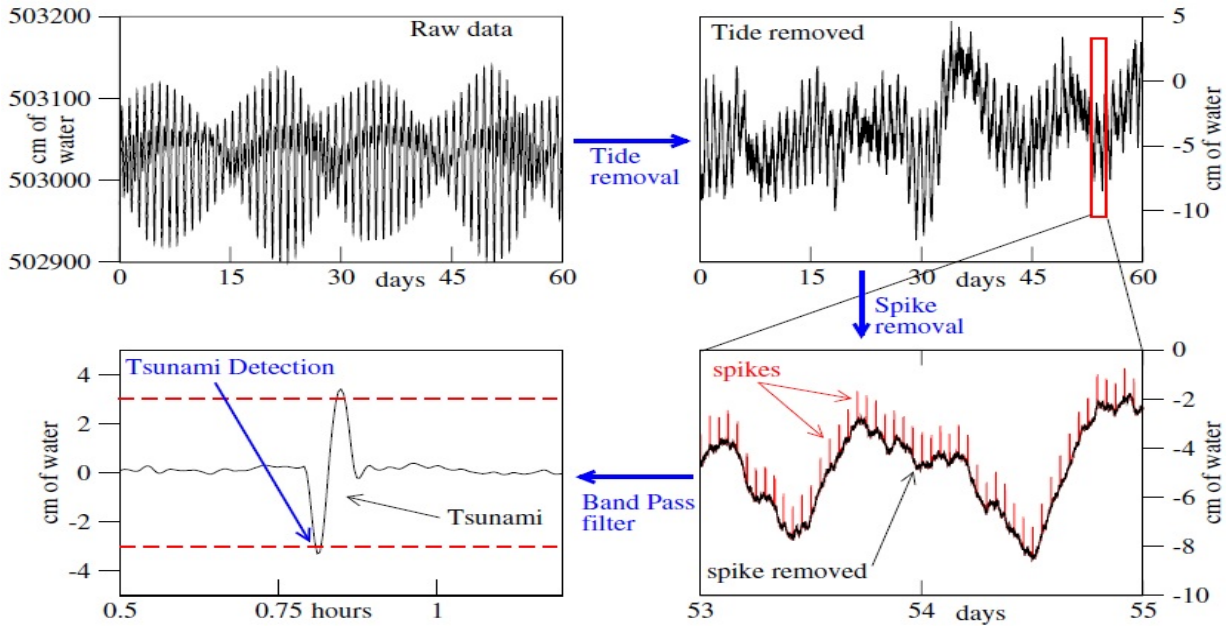


Figure 3.11. BPS algorithm data processing for monitoring water level changes exceeding ±3 cm. Figure from Chierici et al. (2017).

The algorithm introduced for analyzing BPS data successfully detected the 2012 Haida Gwaii earthquake-triggered tsunami using a pressure sensor situated approximately 600 km south of the earthquake epicenter. Figure 3.12 serves as a notable example of pressure sensors indirectly detecting seismic events through the propagation of tsunami waves in the water column.

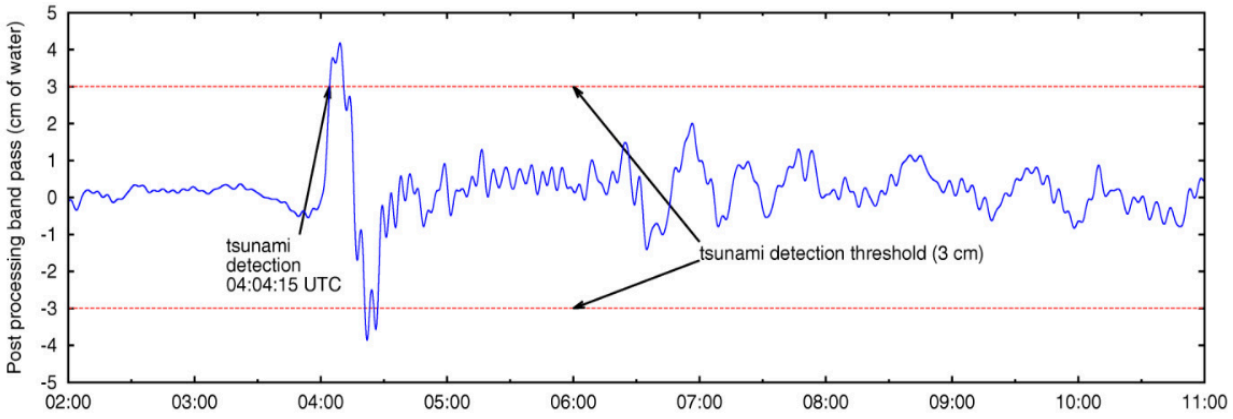


Figure 3.12 Recording of the 2012 Haida Gwaii tsunami at a BPS offshore Vancouver Island (ONC ODP 889), 590 km south of the 28 October 2012 M7.8 earthquake epicenter (Chierici et al., 2017). The tide-removed data were bandpass filtered to highlight the tsunami wave features.

## 3.5 Instrumental results for the historical events in the study area

In Sections 3.5.1 through 3.5.6, I will focus on landslides that were recorded in 2022 and 2023. On each of the dates of these occurrences, I will examine 24-hour seismic and hydrophone data to see if these events could be detected and quantified. Unfortunately, there are no BPS data available for the relevant time period. In Section 3.5.7, two months of data from September and October 2017 will be analyzed in an effort to identify and pinpoint a number of landslides that probably occurred during that time. In addition, over these two months, the BPS data will be examined for any possible correlations with changes in water levels. Finally, I will draw conclusions based on the instrumental data analysis in Section 3.6.

### 3.5.1 2208_ECS1 Landslide event with Mw= 2.1

#### 3.5.1.1 Seismic results from SSNAP-EQT model

On August 30th, 2022, at 22:46:58, the 2208_ECS1 event occurred about 44 km west of Kitimat, near Ecstall River (coordinates 54.017°N, -129.305°E) (Table 3.3). This event was preceded by three days of continuous rainfall, as shown in Figure 3.13. To examine the seismic activity during this event, waveforms were acquired from the IRIS database (IRIS, 2023) for five specific stations: CN_RUBB, CN_BNAB, C8_KITB, C8_HWKB, and C8_GRIB for the entire day of August 30th, 2022. Seismic data were not available for the other stations in the study area.

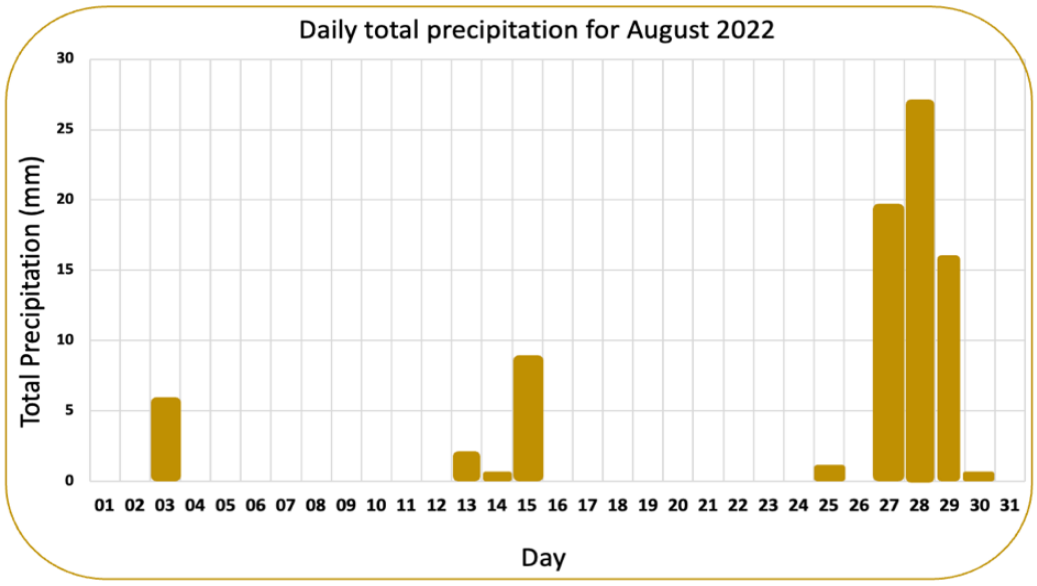


Figure 3.13. Daily total precipitation in August 2022 at Kemano weather station, B.C (Environment and Climate Change Canada, 2024).

Upon subjecting seismic signals from the aforementioned stations to the SSNAP-EQT model, the analysis not only confirmed the detection of the 2208_ECS1 event but also identified two additional events documented in the NRCEC (https://earthquakescanada.nrcan.gc.ca/stndon/NEDB-BNDS/bulletin-en.php). All three events are reported as earthquakes in the NRCEC. However, through personal communication with NRCan (C. Brillon, March 2023), the 2208-ECS1 event was recognized as a landslide.

Figure 3.14 depicts the waveforms and brightness maps of the two three detected events. The brightness map, a key output of the SSNAP-EQT model, serves as a visual representation, facilitating a comprehensive understanding of the spatiotemporal characteristics of an event. The brightness map vividly illustrates the locations and times of these three distinct events (Figure 3.14). The brightness map also illustrates the distribution of seismic stations in four primary directions (north, west, east, and south) around the events. To enhance clarity, the timesteps on top of the brightness maps should be converted to minutes and seconds. If the SSNAP-EQT model detects any events, it will produce a brightness map for each event. Upon examining these plots, we will see a timestep that accurately indicates the time of event occurrence within that hour. To accurately calculate the time of occurrence and knowing that each timestep represents 1 second, the reported time at the top of the brightness map, which is 2816 seconds for the landslide event, can be converted to 46 minutes and 56 seconds for the 22:00-23:00 one-hour plot.

Comprehensive details of both the detected and NRCEC events are presented in Table 3.6 for reference. As previously mentioned, the SSNAP-EQT model currently lacks the ability to automatically categorize detected events as earthquakes or landslides. Consequently, differentiating between these events requires a comprehensive examination of associated waveforms and of spectrograms of hydroacoustic data (explained in the following sections), offering valuable insights into the SSNAP-EQT model's accuracy and reliability in seismic event detection and location estimation.

Analyzing the waveform patterns of the detected events unveiled distinct characteristics. Events detected at 06:26:08 and 20:05:06 exhibit features typical of earthquakes, characterized by impulsive and well-defined P and S waves, and an overall signal lasting approximately 25 seconds. In contrast, the event detected at 22:46:56 displays a waveform pattern consistent with a landslide event. This pattern lacks distinct P or S waves, presenting non-impulsive, tremor-like seismic waves, with sporadic high-amplitude bursts. These characteristics persist for tens of seconds, here 80 seconds, in lower frequency ranges. Notably, the detected landslide event is positioned within 2.3 km spatial deviation and exhibits a time differential of 2 seconds compared to the event recorded in the NRCEC (Figure 3.15 and Table 3.6).

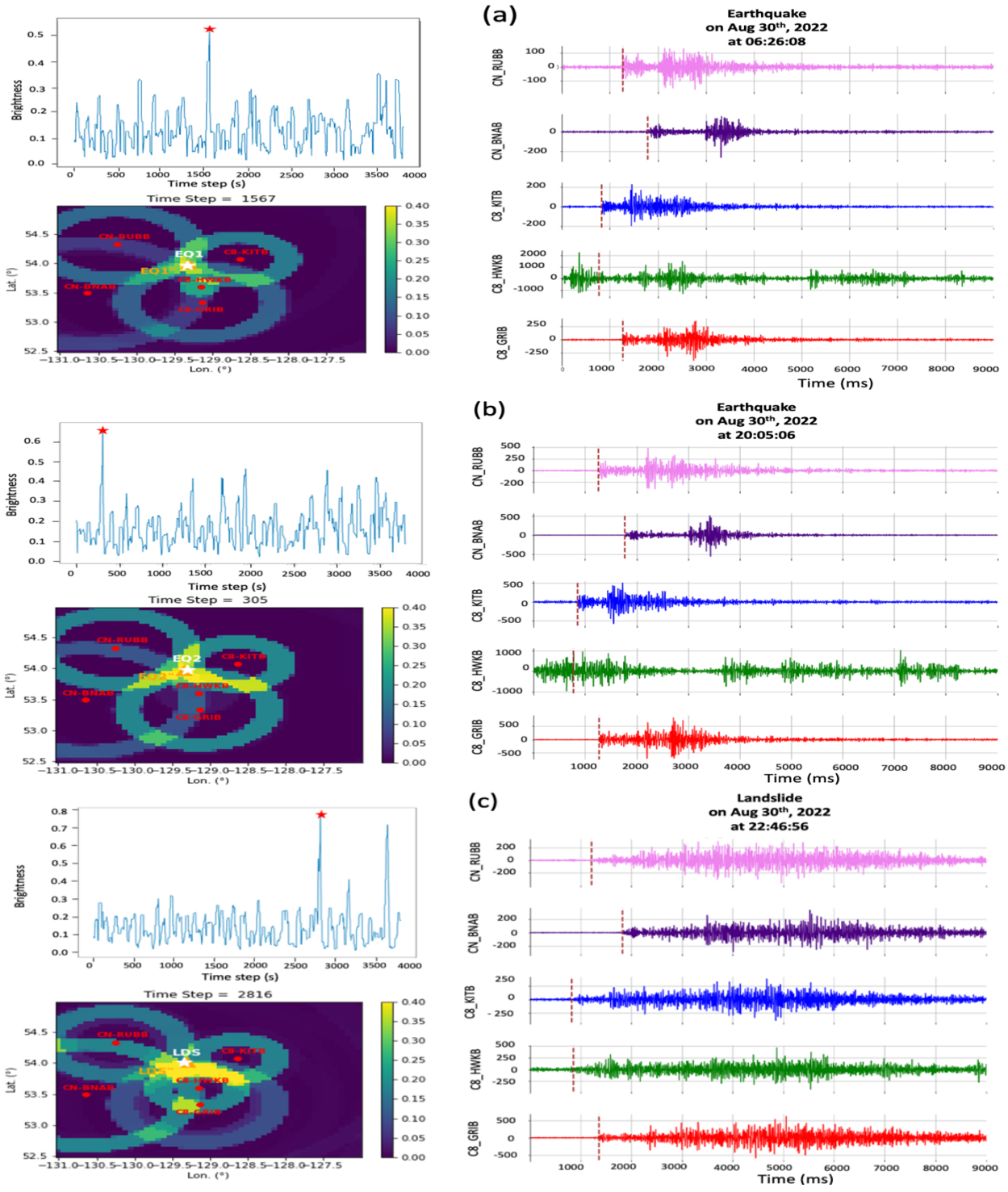


Figure 3.14. Events detected on August 30th, 2022, including (a) earthquake no. 1, (b) earthquake no. 2, and (c) landslide. For each of (a)-(c), upper left shows a brightness vs. time plot over a 1-hour time period, where the red star indicates a time step where brightness exceeds the 0.4 threshold. Lower left: brightness map at the indicated time step. The white star indicates the location based on NRCEC, while the yellow triangle represents the detected location. RHS: the x-axis in the waveform plot represents the time in milliseconds. The dashed red line on each waveform - event signal onset as detected by SSNAP-EQT.

Table 3.6. Events detected on August 30th, 2022, by SSNAP-EQT model.

| Event | NRCEC Event Location (°E,°N) | NRCEC Event Time (hh:mm:ss) | NRCEC Mag. (ML) | Detected Location (°E, °N) | Detected Time (hh:mm:ss) | SSNAP -EQT Mag. (ML) | Detection Distance offset (km) | Detection Time Offset (s) |
|---|---|---|---|---|---|---|---|---|
| **44 km W of Kitimat Earthquake** | (-129.311, 53.99) | 06:26:09 | 1.7 | (-129.332, 53.9744) | 06:26:08 | 1.6 | 2.21 | 1 |
| **43 km W of Kitimat Earthquake** | (-129.297, 53.983) | 20:05:07 | 2.5 | (-129.343, 53.9716) | 20:05:06 | 2.2 | 3.29 | 1 |
| **Ecstall River landslide (no.1)** | (-129.305, 54.017) | 22:46:58 | 2.1 | (-129.339, 54.0221) | 22:46:56 | 2.02 | 2.3 | 2 |

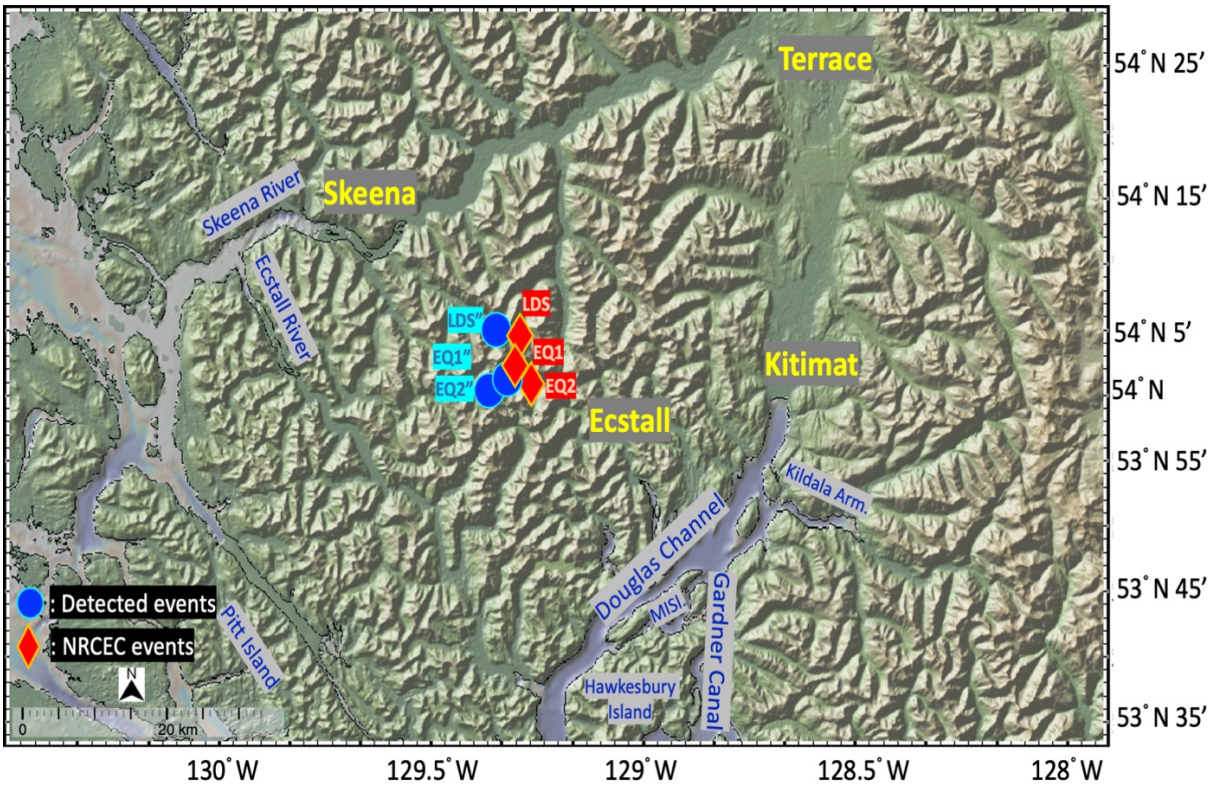


Figure 3.15. Location of one landslide (2208-ECS1) and two earthquakes on Aug 30th, 2022, as located using SSNAP-EQT (blue) versus the NRCEC locations (red).

### 3.5.1.2 Hydroacoustic analysis results

Figures 3.16 and 3.17 display spectrograms representing hydrophone data from HYD1 near Kitimat on August 30th, 2022. Time is depicted on the x-axis, while frequency is on the y-axis in kilohertz (kHz). Each pixel in the spectrogram corresponds to the power spectral density (PSD) of

the audio signal at a specific time and frequency. The color of each pixel in Figure 3.16 is based on dB and for Figure 3.17 is indicative of the log-scaled PSD value, as represented by the color bar at the bottom of the figure. Decibels, a logarithmic unit measuring signal intensity or power relative to a reference level, are used in the color bar to denote PSD values in dB relative (re) to the reference level of $1\mu Pa^2/Hz$. To summarize, the spectrogram visually illustrates the time-varying frequency content of the hydrophone data, with color intensity reflecting signal strength at various frequencies over time.

Figure 3.16 displays three one-hour spectrograms of hydroacoustic data obtained from the HYD1 hydrophone during the three August 30 events detected using the SSNAP-EQT seismic analysis described in the previous section. The data in Figure 3.16 are presented without bandpass filtering or sensitivity calibration, utilizing the Fast Fourier Transform (FFT) for Power Spectral Density (PSD) calculation.

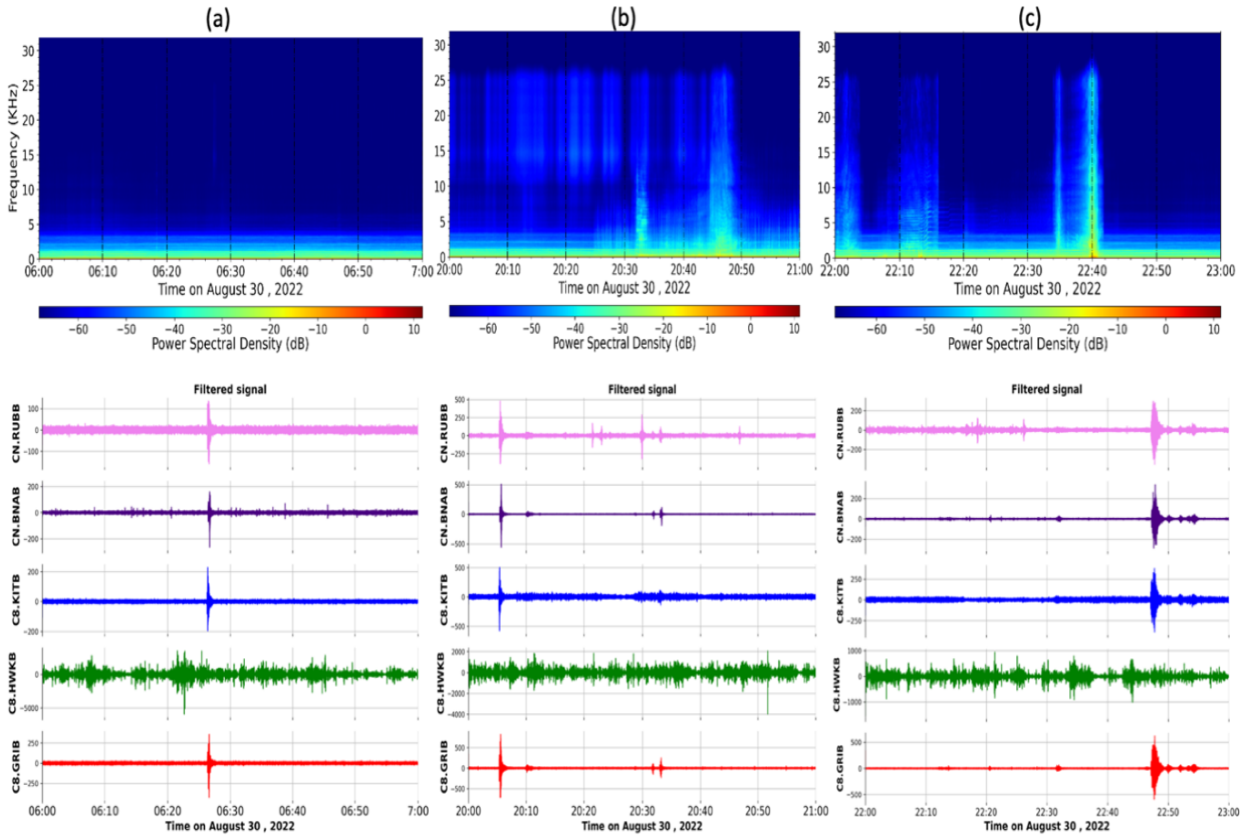


Figure 3.16. Top: One-hour spectrograms of high-frequency hydroacoustic data from HYD1 covering the times of the earthquake no.1 (a), the earthquake no.2 (b), and the landslide (2208-ECS1) (c) detected in seismic data near Ecstall River on August 30th, 2022. Spectrograms are without bandpass filtering or sensitivity calibration; Bottom: one-hour filtered waveforms from the same time periods recorded at seismic stations.

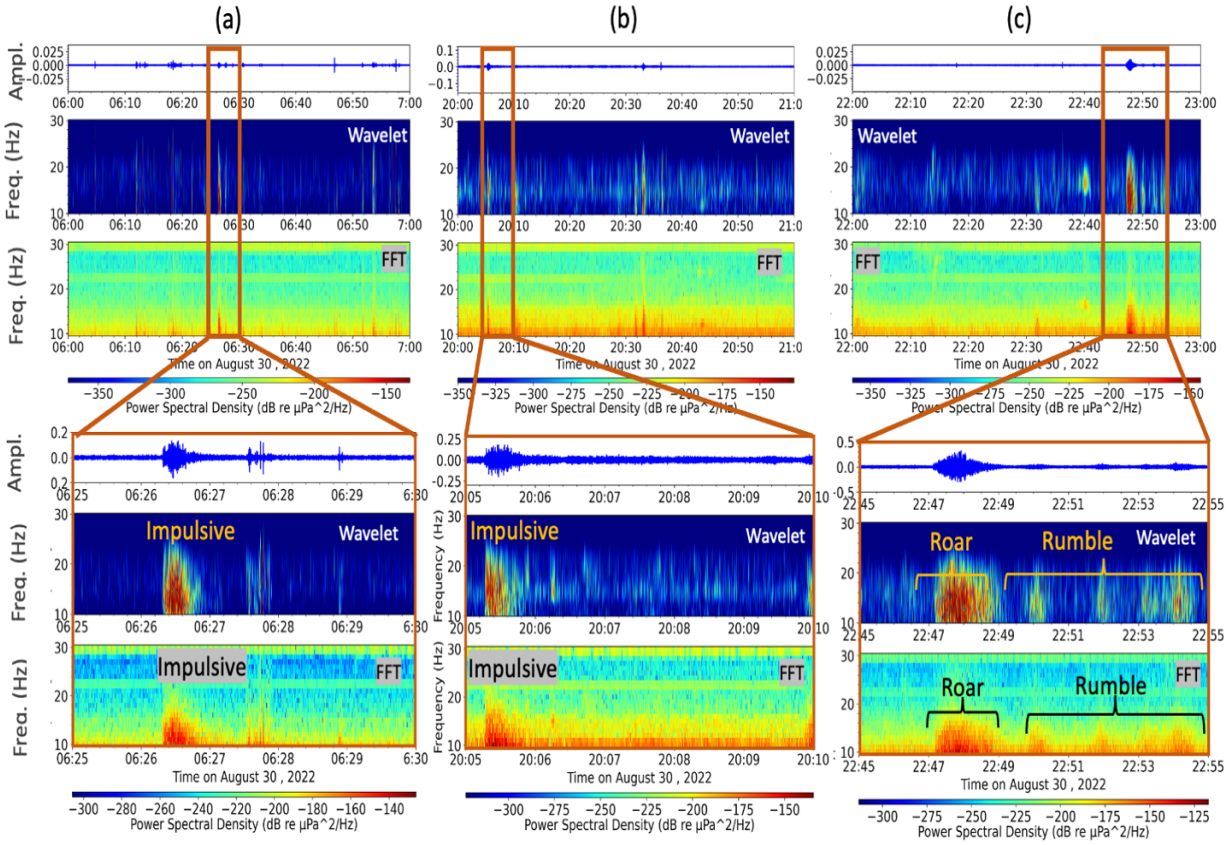


Figure 3.17. Top: Three one-hour time series and spectrograms of HYD1 hydroacoustic data for August 30th, 2022 with bandpass filtering and sensitivity calibration; Bottom: detailed time series and spectrograms of the above row.

In contrast, Figure 3.17 showcases PSD calculated based on FFT and wavelet analysis of bandpass-filtered data obtained from the HYD1 hydrophone that emphasizes frequency ranges of 10 to 30 Hz for PSD, following the methodology described by Matsumoto et al. (2023). These figures include sensitivity calibration, as elaborated in Section 3.2.3.3, providing insights into the PSD calculation technique. The hydroacoustic signal associated with the earthquake events commenced abruptly at 06:26 and 20:05 UTC and persisted for ~40 seconds for both earthquakes detected on August 30th, 2022. Subsequently, the signal stopped, exhibiting no further activity following the earthquake initiation. The time series pattern of hydroacoustic data corresponding to the earthquake events also displays distinct P and S wave characteristics. The hydroacoustic signal associated with the landslide event becomes prominent around 22:47 UTC, as depicted in Figure 3.17 (c). The spectrogram reveals prolonged roaring noises consistent with landsliding. The low-frequency phase of the event recorded in Figure 3.17(c) has the highest amplitudes lasting for 2 minutes (labelled “Roar”); this is followed by ~6 minutes of lower-amplitude intermittent “rumbling”. These observations suggest that two of the events are earthquakes, while the third

is identified as a landslide, consistent with patterns observed in seismic waveforms and with other studies (e.g., Chadwick et al. 2012).

The broadband rumble observed is a promising hydroacoustic characteristic for landslide monitoring. These signals exhibit a distinct pattern, initiating with an extended broadband coda accompanied by a low-frequency rumble, lasting from tens of seconds to minutes (Caplan-Auerbach et al., 2001; Chadwick et al., 2012). Hydroacoustic landslide signals typically lack a sharp onset, gradually increasing due to the momentum and size of surficial mass movements (Allstadt et al., 2018). The frequency range with maximum amplitudes remains below 20 Hz (Bohnenstiehl et al., 2013; Okal, 2003; Matsumoto et al., 2023). Hydroacoustic data time series for landslide events mirrors seismic data for the same events, lacking distinct P or S waves, featuring tremor-like bursts of sporadic amplitudes, and lasting longer than earthquake events (Caplan-Auerbach et al., 2001). Landslide events exhibit common spectral characteristics, differentiating them from earthquake-generated seismic T-phases, whale vocalizations, and man-made acoustic sources. Most landslides commence with a low-frequency rumble (<20 Hz). Landslide durations vary from 1-2 minutes to several hours.

Unlike the prolonged and non-impulsive hydroacoustic signals generated by landslides, hydroacoustic T-waves resulting from local and shallow earthquakes exhibit distinctive characteristics such as impulsive onsets, short durations (around 30 seconds), rapid signal decay rates, and higher frequency content (approximately <30 Hz) (Matsumoto et al., 2023). Hydroacoustic data time series for earthquake events mirrors seismic data for earthquakes, displaying distinct P and S waves, impulsive characteristics, and shorter durations compared to landslide events, aligning with interpretations provided by Chadwick et al. (2008).

The most noticeable similarity lies in the duration of T-phases on the hydrophone versus the seismic recording (see Figures 3.14 and 3.17). In this context, the hydrophone data spectrogram proves valuable for estimating the arrival time of seismic events, as established by previous studies (Caplan-Auerbach et al., 2001).

## 3.5.2 2208-ECS2 Landslide event with Mw= 1.9

### 3.5.2.1 Seismic results from SSNAP-EQT model

On August 31$^{st}$, 2022, at 03:36:02 UTC, the landslide event labeled 2208-ECS2 occurred ~50 km west of Terrace near Ecstall River (coordinates 53.885°N, -129.4365°E) (Table 3.3), following a continuous three-day rainfall (Figure 3.13). Based on data from CN_RUBB, CN_BNAB, C8_KITB, C8_HWKB, and C8_GRIB stations, SSNAP-EQT model identified three events on the same day, all of which were documented in the NRCEC as earthquake events. Table 3.7 provides details on the detected and recorded events, while Figure 3.18 illustrates the brightness map, brightness timesteps plot, and related waveform plots. Upon waveform examination, it became evident that the event occurring at 03:36:02 UTC is a landslide, while the other two events are earthquakes.

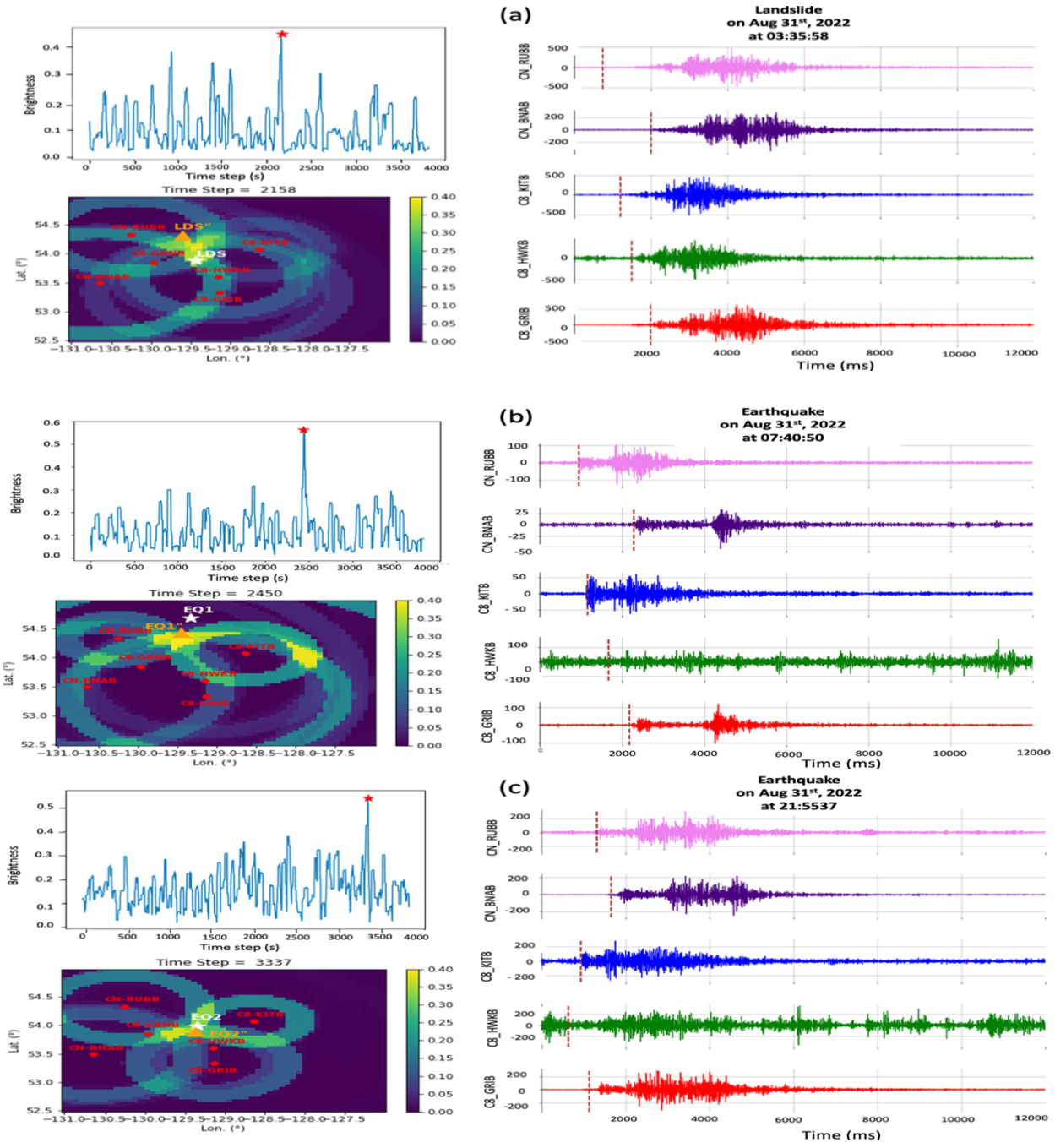


Figure 3.18. Events detected on August 31st, 2022, including (a) a landslide, (b) earthquake no. 1, (c) earthquake no. 2. For each of (a)-(c), upper left shows a brightness vs. time plot over a 1-hour time period, where the red star indicates a time step where brightness exceeds the 0.4 threshold. Lower left: brightness map at the indicated time step. The white star indicates the location based on NRCEC, while the yellow triangle represents the detected location. RHS: the x-axis in the waveform plot represents the time in milliseconds. The dashed red line on each waveform - event signal onset as detected by SSNAP-EQT.

It is noteworthy that the detected landslide event is positioned ~50 km away from the NRCEC event location, with a source time differential of 4 seconds compared to the NRCEC event (Figure 3.19 and Table 3.7). This implies a significantly lower precision of event detection for 2208-ECS2 compared to 2208-ECS1, possibly due to the lower magnitude of the seismic event (1.9 for 2208-ECS2 compared to 2.1 for 2208-ECS1). The type and volume of the landslide can result in weaker and noisier waveforms, impacting the precision of phase picking and, consequently, influencing event location and time detection. It is also worth noting that the NRCEC detection carries its own uncertainty, which is also larger for a lower magnitude event. It would be necessary to physically groundtruth the event location in order to accurately estimate the precision of the location detection.

The EQT model is designed for earthquake phase picking. Although, it can be worked for landslides but sometimes it lacks to detected arrival time as precisely as it should be. As shown in Figure 3.18, the detected arrival time for CN_RUBB is a little bit off which may cause to inaccuracy of the location estimation. At this stage, we can improve it by manual picking after the automatic process.

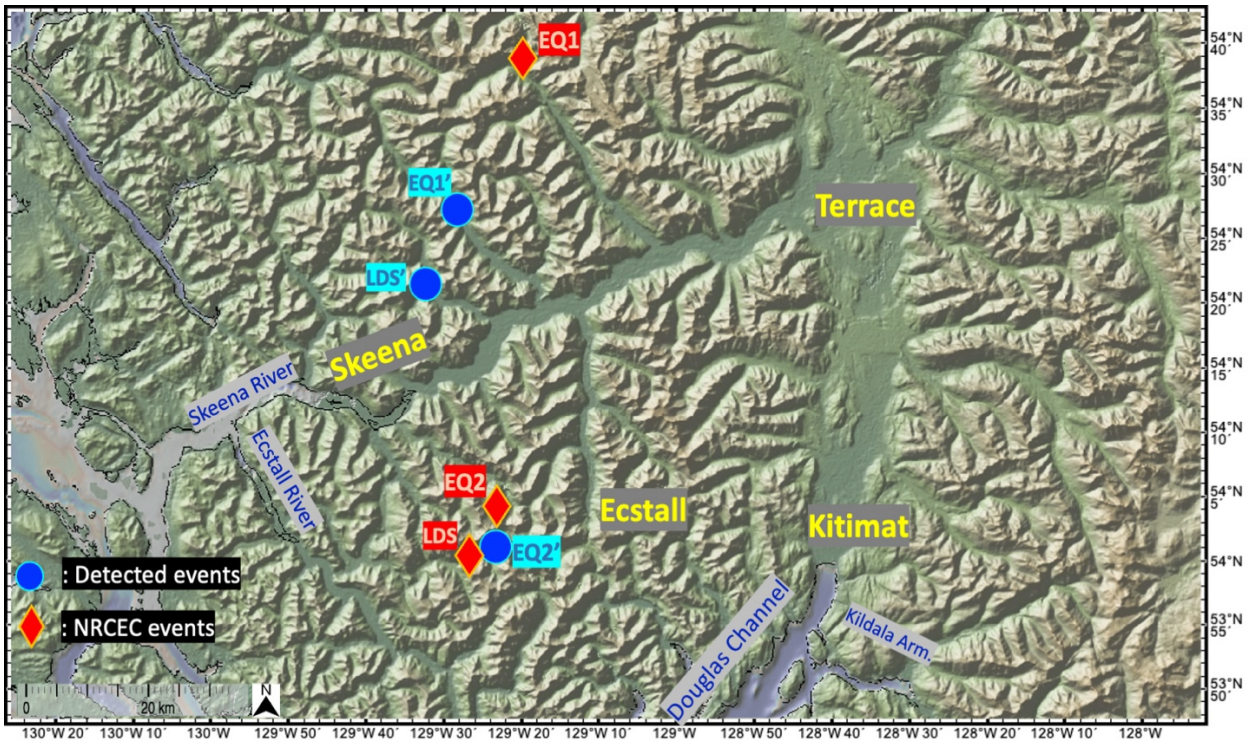


Figure 3.19. Location of one landslide (2208-ECS2) and two earthquakes on Aug 31st, 2022, as located using SSNAP-EQT (blue) versus the NRCEC locations (red).

Table 3.7. Events detected on August 31st, 2022, by SSNAP-EQT model.

| Event | NRCEC Event Location (°E, °N) | Event Time (hh:mm:ss) | NRCEC Mag. (ML) | Detected Location (°E, °N) | Detected Time (hh:mm:ss) | SSNAP-EQT Mag. (ML) | Detection Distance offset (km) | Detection Time Offset (s) |
|---|---|---|---|---|---|---|---|---|
| **Ecstall River landslide (no.2)** | (-129.436, 53.885) | 03:36:02 | 1.9 | (-129.601, 54.319) | 03:35:58 | 1.9 | 49.53 | 4 |
| **50 km W of Terrace Earthquake** | (-129.335, 54.690) | 07:40:48 | 1.7 | (-129.453, 54.432) | 07:40:50 | 1.4 | 29.7 | 2 |
| **46 km W of Kitimat Earthquake** | (-129.350, 53.990) | 21:55:39 | 2.0 | (-129.380, 53.892) | 21:55:37 | 1.6 | 11 | 12 |

#### 3.5.2.2 Hydroacoustic analysis results

Figures 3.20 and 3.21 each present three spectrograms covering the time intervals from 03:00 to 04:00 UTC, 07:00 to 08:00 UTC, and 21:00 to 22:00 UTC on August 31$^{st}$, 2022, as recorded by the HYD1 hydrophone near Kitimat. On this date, the SSNAP-EQT model successfully pinpointed three events, corroborated by the simultaneous detection of recorded signals by nearby seismometers. Examination of the seismic waveforms, time series of hydroacoustic data, and the spectrogram of the PSD facilitated the categorization of the first detected event as a landslide and the other two events as earthquakes.

Figure 3.20 illustrates the FFT of the PSD for unfiltered and un-sensitivity-calibrated acoustic data from the HYD1 hydrophone, presented in a one-hour spectrogram plot. Meanwhile, Figure 3.21 displays PSD calculated based on FFT and wavelet analysis of bandpass-filtered data and sensitivity-calibrated data.

Figure 3.20 illustrates signals in higher frequency ranges at 03:00 to 04:00 UTC and 21:00 to 22:00 UTC. However, these signals do not align with events detected by the SSNAP-EQT model or with waveforms in the one-hour plot. Given their higher frequency (more than 5 kHz) and short duration, these signals may be attributed to ice, animal calls, human activity, or passing vessels (e.g., Blondel et al., 2020).

In contrast to the extended (60 seconds) and non-impulsive hydroacoustic signals produced by the 2208-ECS2 landslide (in Figure 3.21 (a)), the hydroacoustic signals related to the two earthquakes exhibit abrupt onsets and short durations (less than 1 minute) (in Figure 3.21 (b)). Analyzing the frequency content and magnitude, we can conclude that these two earthquake events may be associated with T-waves originating from local and shallow earthquakes. The time series of hydroacoustic data during these two earthquake events closely resembles earthquake

seismic data, featuring discernible P and S waves, impulsive characteristics, and shorter durations in comparison to landslide events which does not have distinct P and S waves (Figure 3.21(a)).

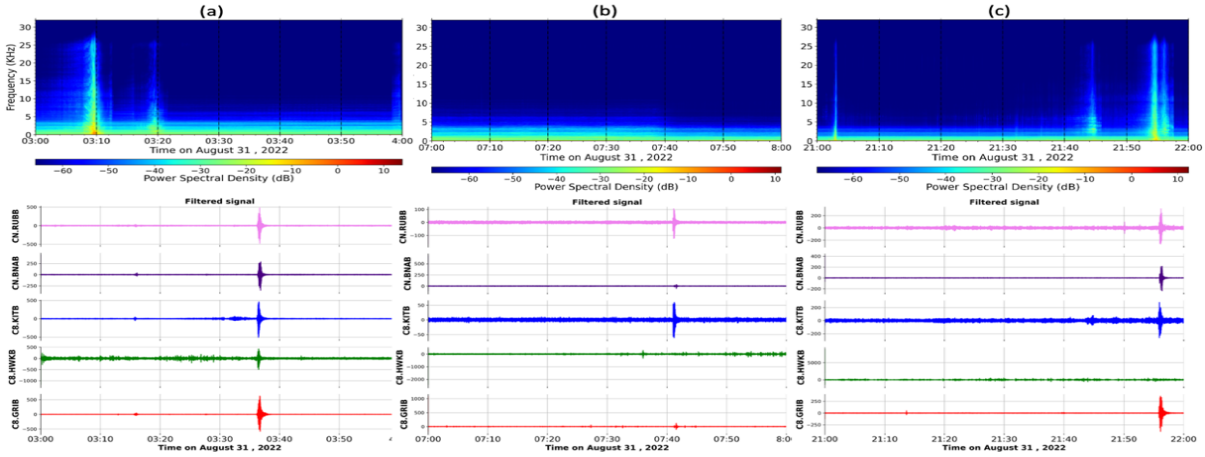


Figure 3.20. Top: One-hour spectrograms of high-frequency hydroacoustic data from HYD1 covering the times of the landslide (2208-ECS2) (a), earthquake no. 1 (b), earthquake no. 2 (c) detected in seismic data near Ecstall River on August 31st, 2022. Spectrograms are without bandpass filtering or sensitivity calibration; Bottom: one-hour filtered waveforms from the same time periods recorded at seismic stations.

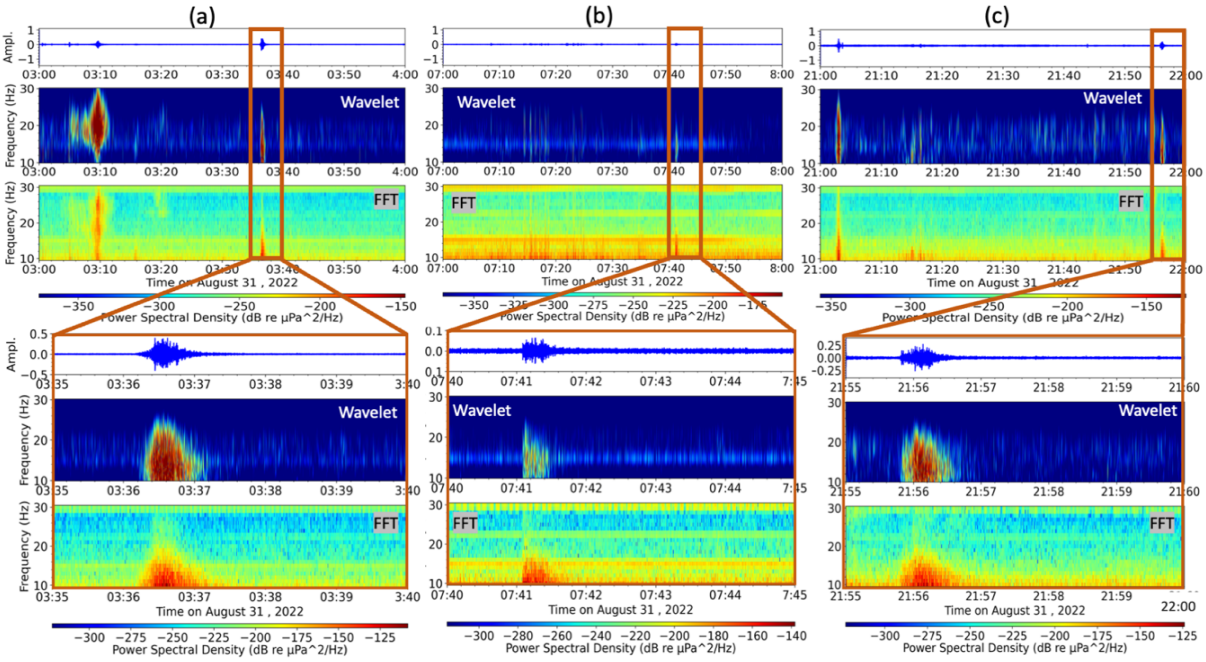


Figure 3.21. Top: Three one-hour time series and spectrograms of HYD1 hydroacoustic data for August 31st, 2022 with bandpass filtering and sensitivity calibration; Bottom: detailed time series and spectrograms of the above row.

## 3.5.3 2209_ECS3 Landslide event with Mw= 2.8

### 3.5.3.1 Seismic results from SSNAP-EQT model

On September 1st, 2022, at 18:03:11 UTC, the landslide event labeled 2209_ECS3 happened approximately 50 km W of Kitimat near Ecstall River (coordinates 53.982°N, -129.300°E) (Table 3.3), following a continuous three-day period of rainfall and previous landslide and earthquake events in the area as documented in Sections 3.5.1 and 3.5.2.

After applying the SSNAP-EQT model to seismic signals from various stations, I successfully identified the 2209_ECS3 event and discovered an additional nine landslide events within the study area. Detailed information on these events is provided in Tables 3.8 and 3.9, and their locations are visualized on the map in Figure 3.22. While the events in Table 3.8 are documented in the NRCEC, those listed in Table 3.9 are not recorded in the catalog. Notably, the event at 18:03:11 UTC (the largest magnitude event on this date) is classified as a landslide in the NRCEC, while the others in Table 3.9 are categorized as earthquakes.

Figure 3.23 shows a 1-hour brightness time series starting at 18:00 UTC and a number of brightness maps at different timesteps; associated waveform plots for all detected events are displayed in Figure 3.24.

Table 3.8. Event detected on September 1st, 2022, that are also reported in the NRCEC.

| Event | NRCEC Event Location (°E, °N) | Event Time (hh:mm:ss) | NRCEC Mag. (ML) | Detected Location (°E, °N) | Detected Time (hh:mm:ss) | SSNAP-EQT Mag. (ML) | Detection Distance offset (km) | Detection Time Offset (s) |
|---|---|---|---|---|---|---|---|---|
| **1) Ecstall River Landslide (no.3)** | (-129.300, 53.982) | 18:03:11 | 3.4 | (-129.306, 53.994) | 18:03:10 | 2.8 | 1.4 | 1 |
| **2) 50 km W of Kitimat Landslide** | (-129.398, 53.980) | 18:29:21 | 2.1 | (-129.404, 53.940) | 18:29:20 | 2.1 | 4.42 | 1 |
| **3) 65 km SW of Kitimat Landslide** | (-129.563, 53.831) | 18:39:05 | 1.4 | (-129.453, 53.927) | 18:39:04 | 1.4 | 12.81 | 1 |
| **4) 59 km SW of Kitimat Landslide** | (-129.466, 53.846) | 18:49:42 | 2.4 | (-129.343, 54.005) | 18:49:38 | 2.3 | 19.44 | 4 |

Table 3.9. Detected events on September 1st, 2022, by SSNAP-EQT model and not reported in the NRCEC.

| Event | SSNAP-EQT Detected Location (°E, °N) | SSNAP-EQT Detected Time (hh:mm:ss) | SSNAP-EQT Mag. (ML) |
|---|---|---|---|
| **5) Landslide at 11 km SW of 2209_ECS3** | (-129.392, 53.901) | 18:10:45 | 1.33 |
| **6) Landslide at 33.4 km N of 2209_ECS3** | (-129.416, 54.274) | 18:21:01 | 1.15 |
| **7) Landslide at 10 km E of 2209_ECS3** | (-129.196, 54.045) | 18:27:29 | 1.77 |
| **8) Landslide at 29 km NW of 2209_ECS3** | (-129.712, 54.078) | 18:32:11 | 0.8 |
| **9) Landslide at 7 km N of 2209_ECS3** | (-129.398, 53.960) | 19:30:29 | 1.9 |
| **10) Landslide at 23 km SW of 2209_ECS3** | (-129.583, 53.854) | 19:41:35 | 1.2 |

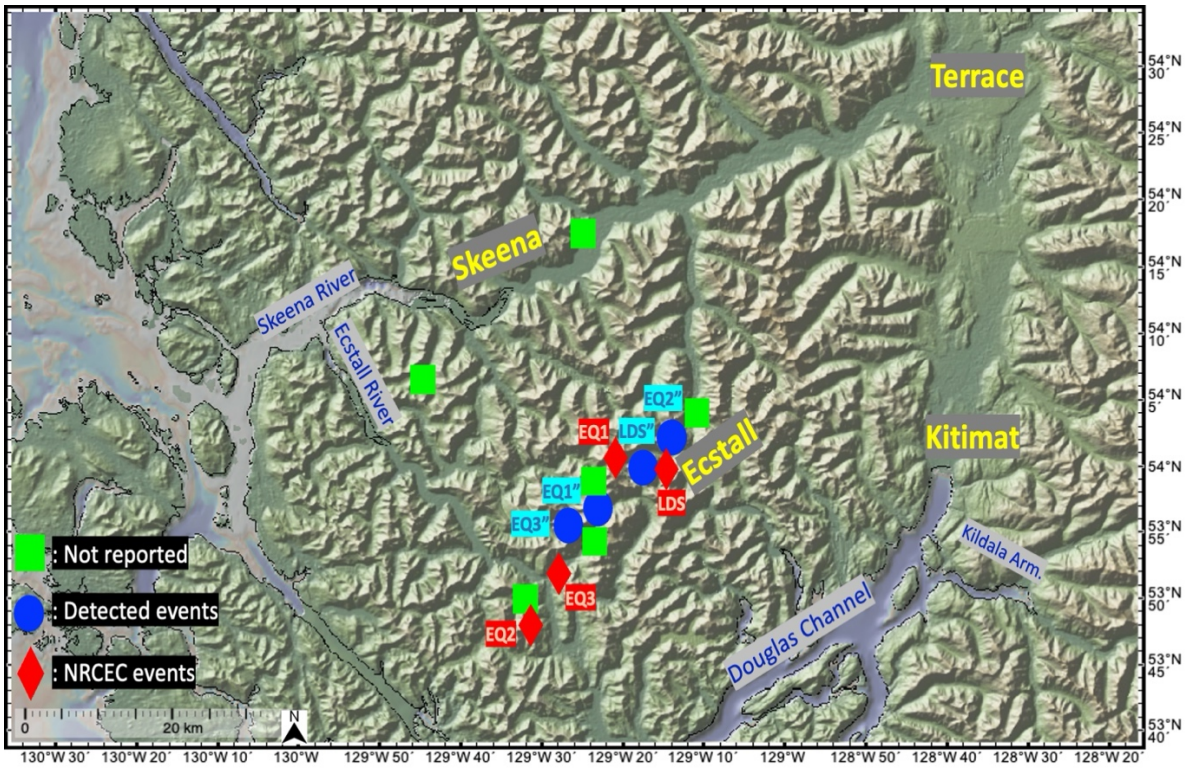


Figure 3.22. Locations of detected events between 18:00 and 20:00 UTC Sep 1st, 2022. Four events detected by SSNAP-EQT (blue symbols) are also documented in the NRCEC (red symbols). Green symbols show an additional six events detected by SSNAP-EQT that were not reported in the NRCEC.

For the detected events that are also recorded in the NRCEC, the location differences range from ~3-22 km, with onset time differentials of 1-4 seconds (Table 3.8). Based on this comparison, the precision of event detection for 2209_ECS3 exceeds that of 2208_ECS2, likely attributed to the higher magnitude of the event (2.8 for 2209_ECS3 compared to 1.9 for 2208_ECS2).

Examination of the seismic waveforms, time series of hydroacoustic data, and the spectrogram of the PSD facilitated the categorization of all of the detected events in Tables 3.8 and 3.9 as

landslides. The analysis of waveforms and spectrogram PSD of acoustic data indicates these detected events as landslides. Further discussion on events not documented in the NRCEC is elaborated in the subsequent section.

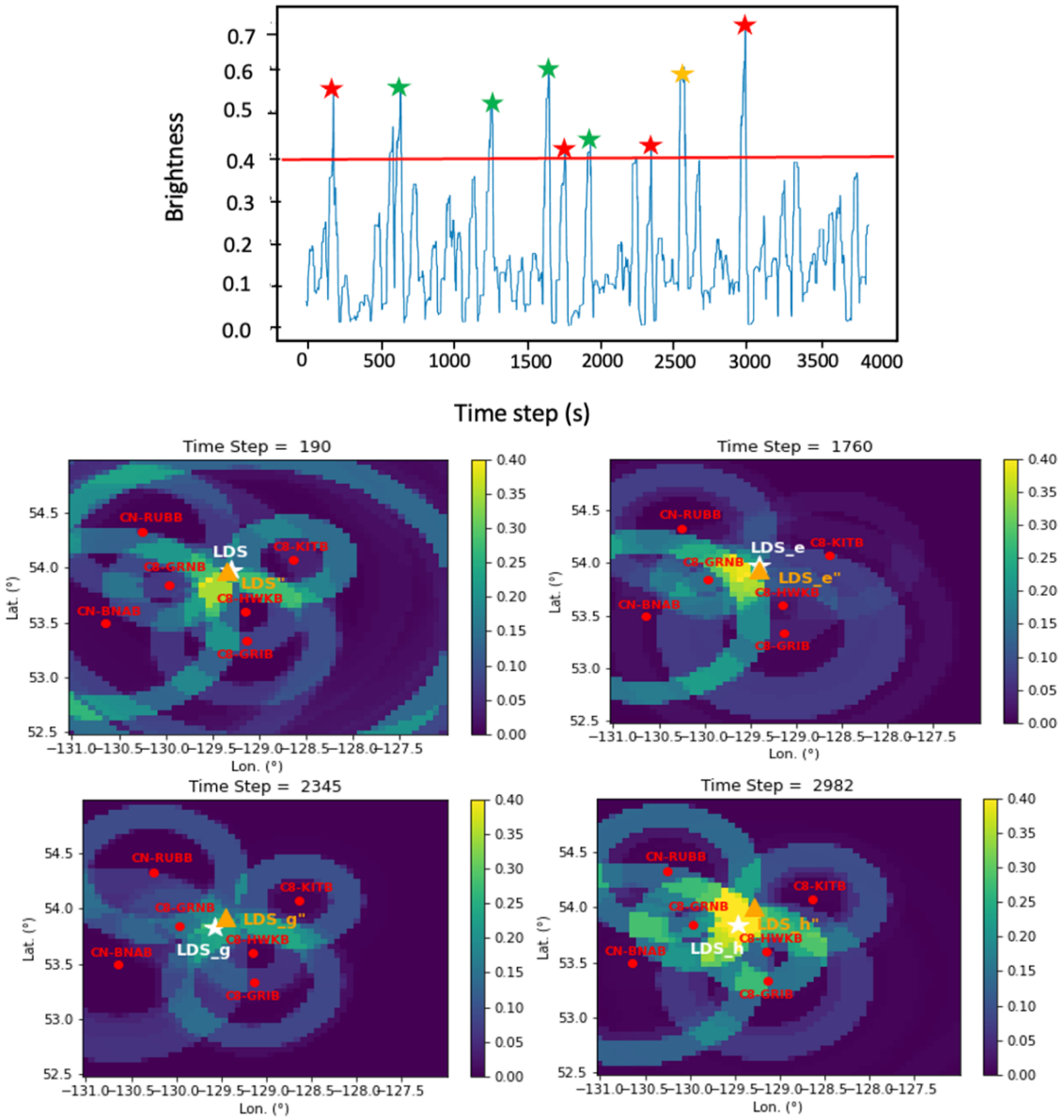


Figure 3.23. Landslide events detected on September 1st, 2022 including (a) 2209_ECS3 landslide no. 1, (b) landslide no. 2, (c) landslide no. 3, (d) landslide no. 4. Top: brightness vs. time plot over a 1-hour time period plot from 18:00 to 19:00 UTC, where the colored stars indicate time steps where brightness exceeds the 0.4 threshold within that hour. Red stars represent events detected by SSNAP-EQT, each of which has a corresponding match in the NRCEC catalog. Green stars denote events detected by the SSNAP-EQT model only. A yellow star indicates brightness exceeding 0.4 but is not recognized as an event by SSNAP-EQT or the NRCEC catalog. Right: brightness map at the indicated time steps related to the red stars. In each case (a)-(d), a white star represents the NRCEC location, while a yellow triangle denotes the SSNAP-EQT detected location.

**(a)**

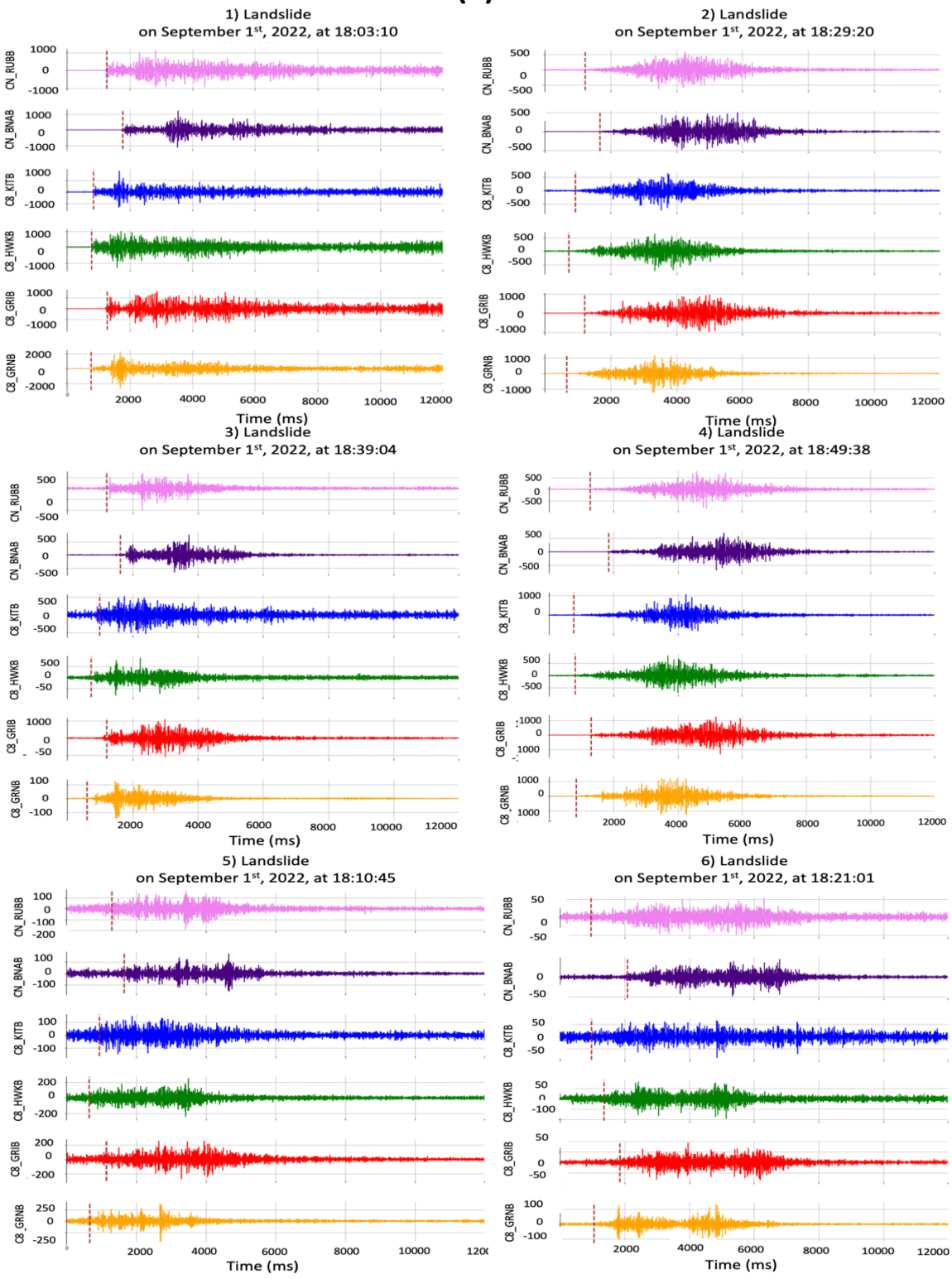
1) Landslide
on September 1st, 2022, at 18:03:10
2) Landslide
on September 1st, 2022, at 18:29:20
3) Landslide
on September 1st, 2022, at 18:39:04
4) Landslide
on September 1st, 2022, at 18:49:38
5) Landslide
on September 1st, 2022, at 18:10:45
6) Landslide
on September 1st, 2022, at 18:21:01
CN_RUBB
CN_BNAB
C8_KITB
C8_HWKB
C8_GRIB
C8_GRNB
Time (ms)

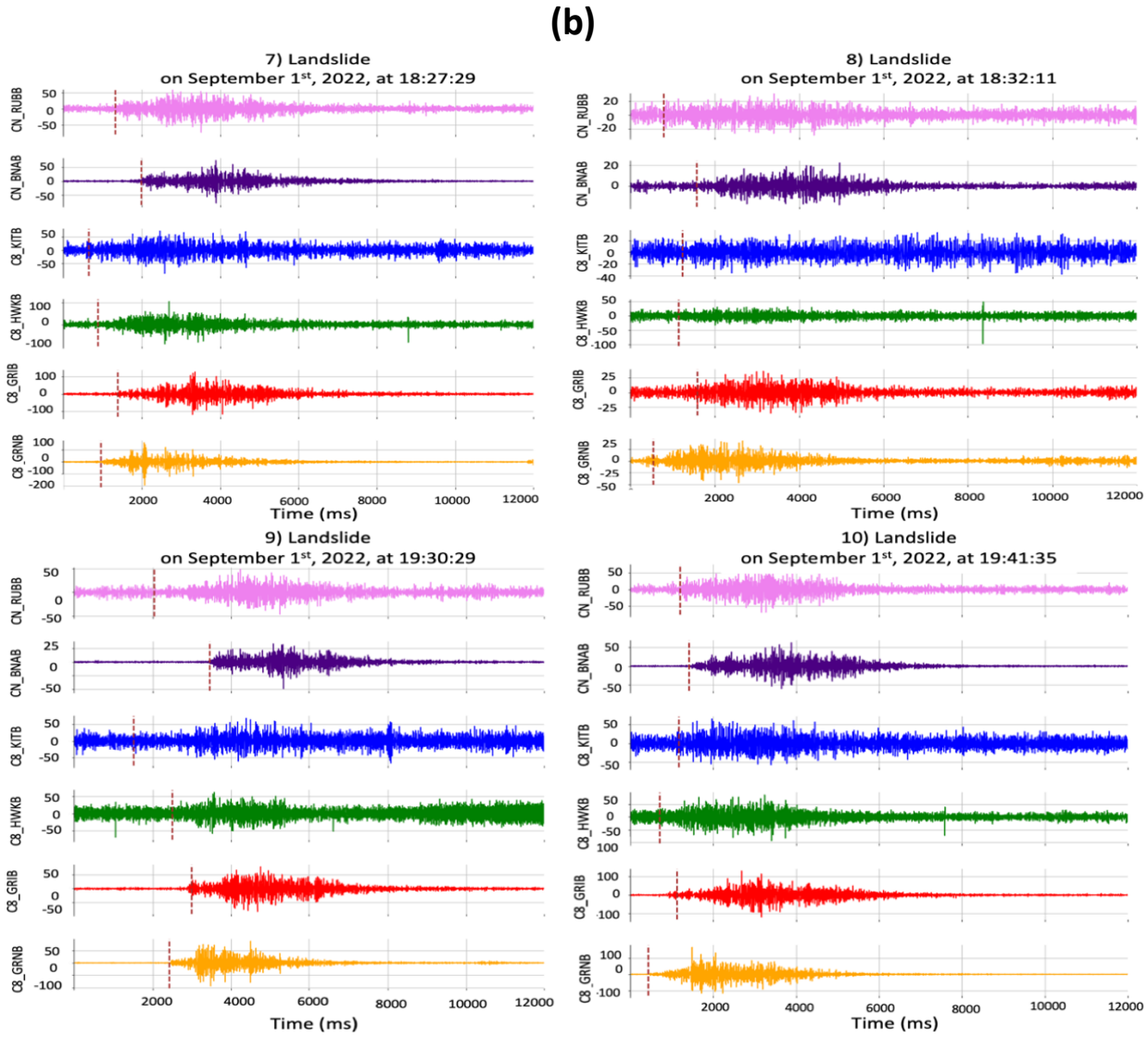


Figure 3.24. (a, b) Events detected on September 1st, 2022 based on the SSNAP-EQT model. The x-axis on the waveform plots represents the time in milliseconds. The dashed red line on each waveform marks the event signal onset as detected by SSNAP-EQT.

### 3.5.3.2 Hydroacoustic analysis results

Figures 3.25, 3.26, and 3.27 show 1-hour spectrograms covering the time interval from 18:00 to 20:00 UTC, on September 1st, 2022, as recorded by the HYD1 hydrophone near Kitimat. Figure 3.24 illustrates the FFT of the PSD for unfiltered and un-calibrated acoustic data; Figures 3.26 and 3.27 display PSD calculated based on FFT and wavelet analysis of bandpass-filtered data and sensitivity-calibrated data.

The spectrograms in Figure 3.25 illustrate signals in higher frequency ranges. However, these signals do not align with events detected by the SSNAP-EQT model or with seismic waveforms.

The signal at higher frequencies (more than 25 kHz) and with short durations may be attributed to ice, biophotonics (animal calls), human activity, or passaging vessels (e.g., Blondel et al., 2020).

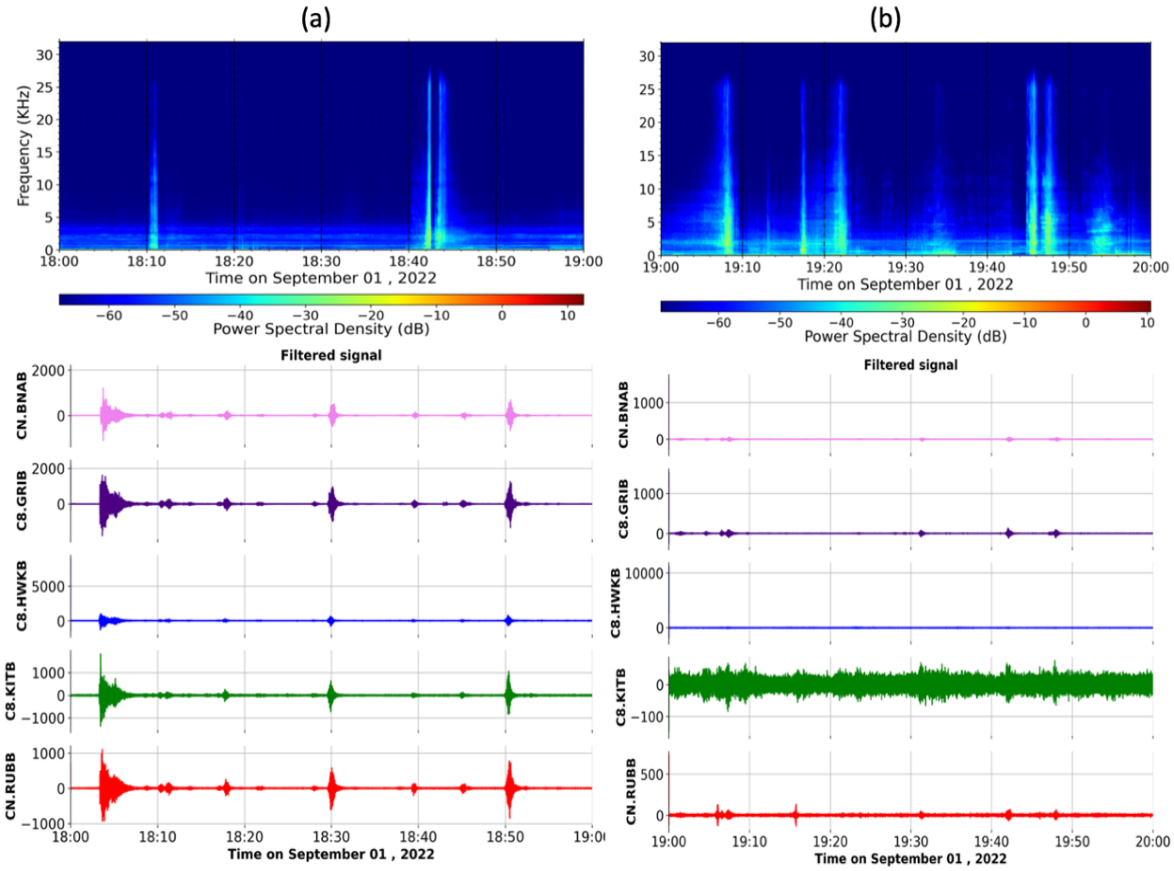


Figure 3.25. Top: One-hour spectrograms of high-frequency hydroacoustic data from HYD1 covering the times of the landslide 2209-ECS3 and six other landslides detected in seismic data near Ecstall River on September 1st, 2022. Spectrograms are without bandpass filtering or sensitivity calibration; Bottom: one-hour filtered waveforms from the same time periods recorded at seismic stations.

The hydroacoustic signal associated with the landslide event (the largest signal) becomes notably pronounced around 18:03 UTC (Figure 3.26-1). In contrast to the 2208-ECS events, this spectrogram reveals prolonged roaring noises. The persistent broadband hiss observed may indicate the downslope motion of debris or rocks following the initial low-frequency signal, representing the failure of large blocks (Chadwick et al., 2012). The largest landslide event on September 1st, known as 2209-ECS3, exhibits an impulsive onset in the spectrogram, followed by multiple pulses; the long overall signal duration (20 min) indicates that the 2209-ECS3 landslide likely involved an extended sequence of failures (Matsumoto et al., 2023) (Figure 3.26-1). It is common for landslides to occur as multiple failures over time instead of single large events (Okal & Synolakis, 2004; Masson et al., 2006). Similarly, the events listed in Table 3.8 may not be singular independent landslide occurrences, but rather part of a related sequence of failures on September 1st, 2022.

The confirmation of the event detections by SSNAP-EQT supports this assertion, as all hydrophone-detected events closely align with the timing of SSNAP-EQT-detected events listed in Tables 3.7 and 3.8.

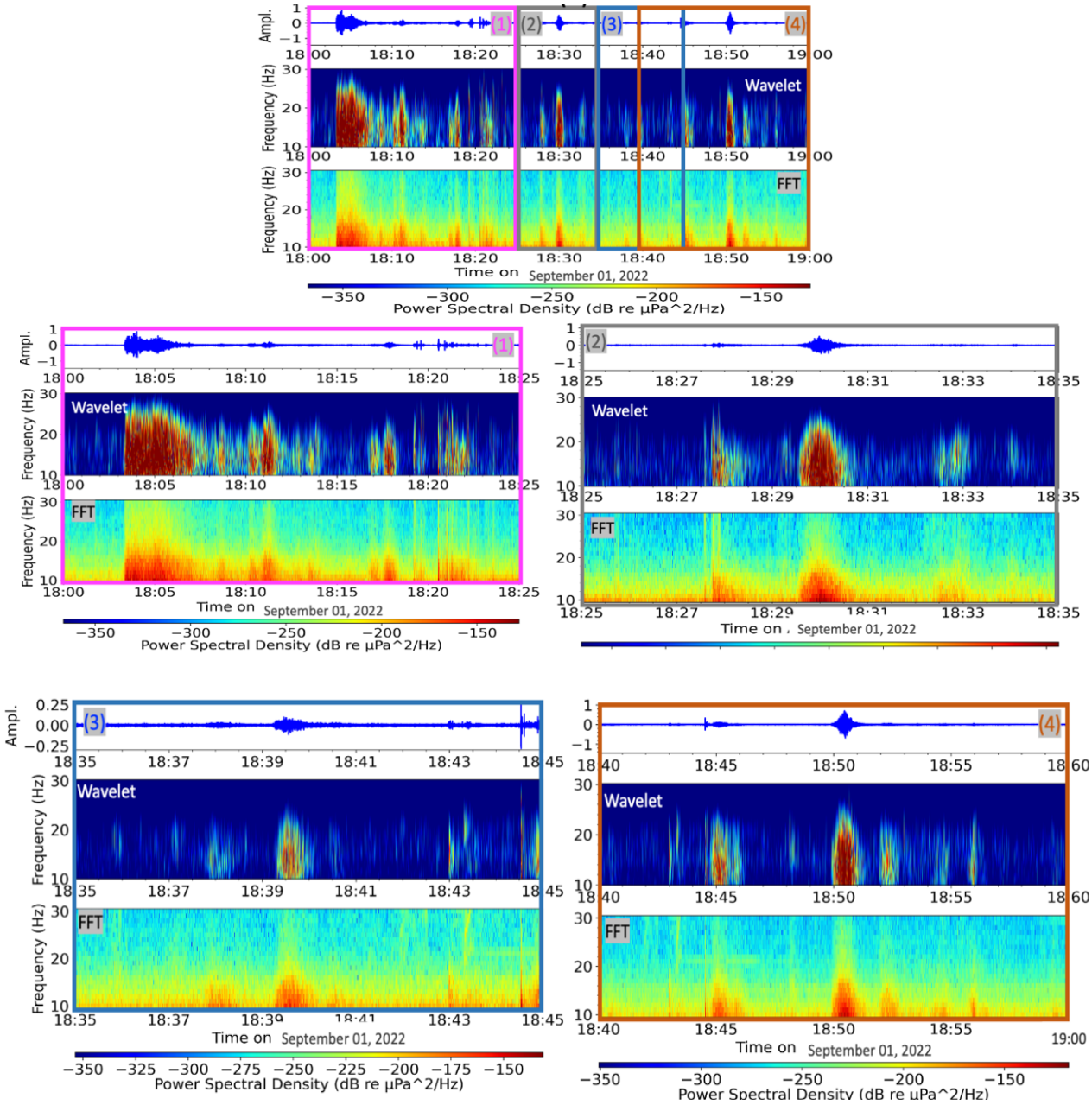


Figure 3.26. Top: Three one-hour time series and spectrograms of HYD1 hydroacoustic data for September 1st, 2022 with bandpass filtering and sensitivity calibration; Bottom: detailed time series and spectrograms of the above row.

Conversely, other events depicted in Figure 3.26 (labelled-2,3,4) and Figure 3.27 (labelled-1,2) commence with a non-impulsive signal, featuring an extended broadband coda accompanied by a low-frequency rumble. The frequency range with maximum amplitudes remains below 20 Hz.

Figures 3.26 (2 to 4) and 3.27 (1,2) show the signals of five landslides occurring approximately 10 minutes apart, each with similar duration and interference patterns, suggesting a spatial proximity. The hydroacoustic similarity observed aligns with the common occurrence of landslides in clusters with short temporal intervals (Tepp and Dziak, 2021).

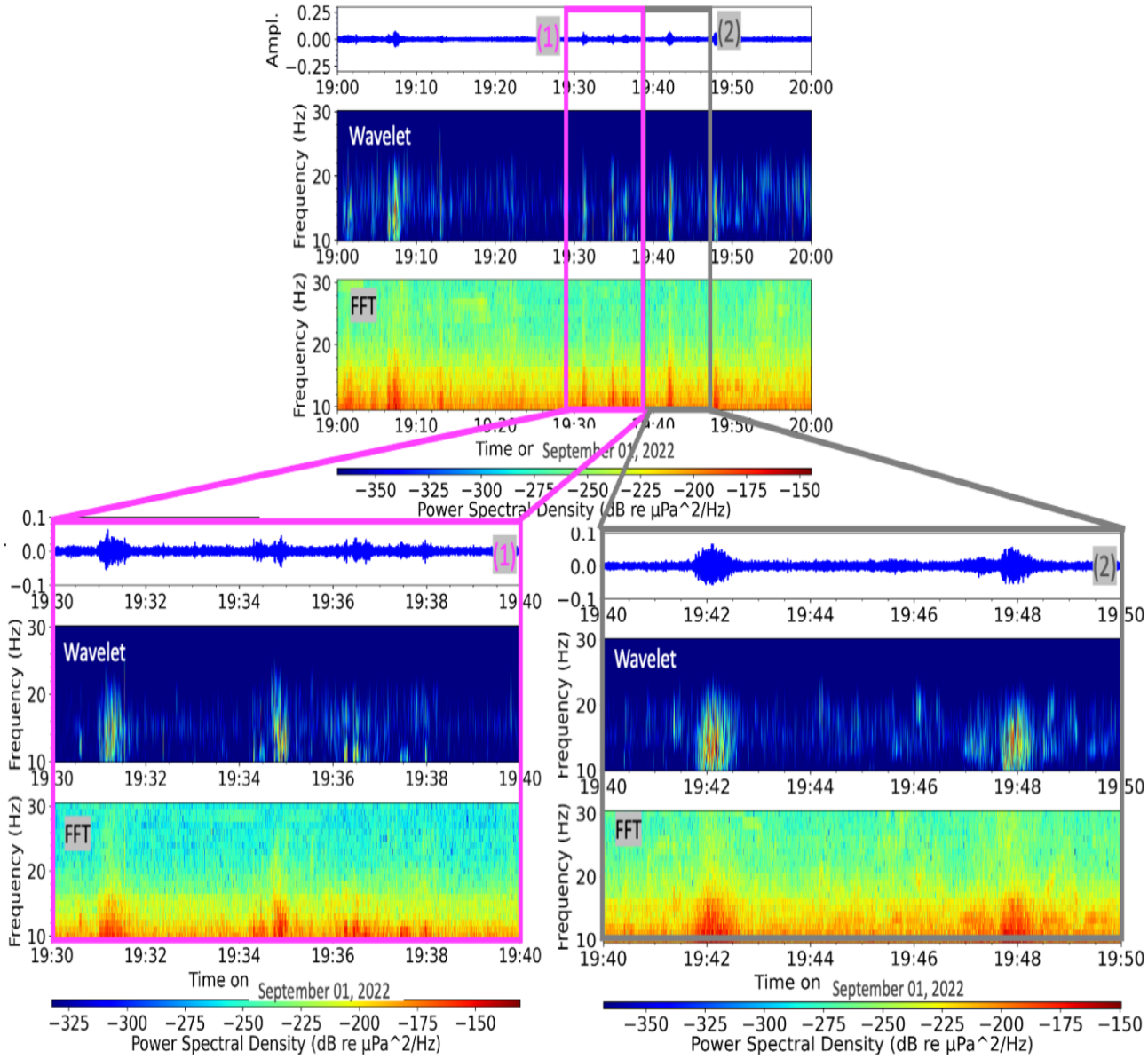


Figure 3.27. Top: Three one-hour time series and spectrograms of HYD1 hydroacoustic data for September 1st, 2022 with bandpass filtering and sensitivity calibration; Bottom: detailed time series and spectrograms of the above row.

### 3.5.3.3 Comparison with ground-truthing information for the Ecstall River landslide (2209_ECS3):

On September 1st, 2022, an ice/rock avalanche occurred in the northern region of Kitimat, specifically near the Ecstall River, resulting in significant impact. The event was initially recognized based on seismic data; examination of satellite imagery revealed further details (Petley, 2022). Initial observations suggest that the incident commenced as a near-vertical rock failure, transitioning into a rock/ice avalanche. The avalanche moved downward into a nearby lake, triggering a downstream flood similar to the Elliot Creek event (Petley, 2022). Satellite images from the day of the failure show that debris was then carried southward down the valley (Petley, 2022). Analysis of InSAR data by Blenman (Examining the Feasibility of Sentinel-1 InSAR data for landslide monitoring and failure forecasting in western Canada, 2023) shows that the steep rock slope south of the lake exhibited some precursory movement prior to the failure.

As shown in Figure 3.26, the seismic signal of the event exhibited an impulsive onset, indicative of an initial impact from a near-vertical rockslide. Its prolonged duration, characterized by multiple pulses, aligns with the interpreted sequence of events, wherein a rockslide transitioned into a rock/ice avalanche with a long run-out. The trajectory of the avalanche was predominantly southward, potentially involving multiple impacts at bends in the valley.

The estimated source location of the landslide from the SSNAP-EQT model 53.994°N, -129.306°E, whereas the NRCEC location is 53.982°E, -129.300°N (Figure 3.28). In this case, it is possible to use ground-truthing data to evaluate the accuracy of the SSNAP-EQT and NRCEC locations.

Figure 3.28 illustrates the seismic events detected on September 1st, 2022, between 18:00 and 20:00 UTC, in relation to the groundtruthed landslide location. Figure 3.28(c) provides a visualization of the rockslide event's early trajectory, with an approximate location of maximum impact marked with a white star at (53.977°N, -129.306°E) within the yellow polygon. By referencing this estimated event location on Google Maps, we can assess the precision of the detection as follows detailed in Table 3.10.

Table 3.10. Comparison of the detected locations of 2209_ECS3 no. 1 by different studies.

| | **Distance to 2209_ECS3 no. 1 (53.977°N, -129.306°E)** |
|---|---|
| SSNAP-EQT (53.994°N, -129.306°E) | 1.9 km |
| NRCEC (53.982°E, -129.300°N) | 0.7 km |

Based on ground-truthed location, both the SSNAP-EQT and NRCEC locations are pretty accurate, within 2 km of the true location (Table 3.10).

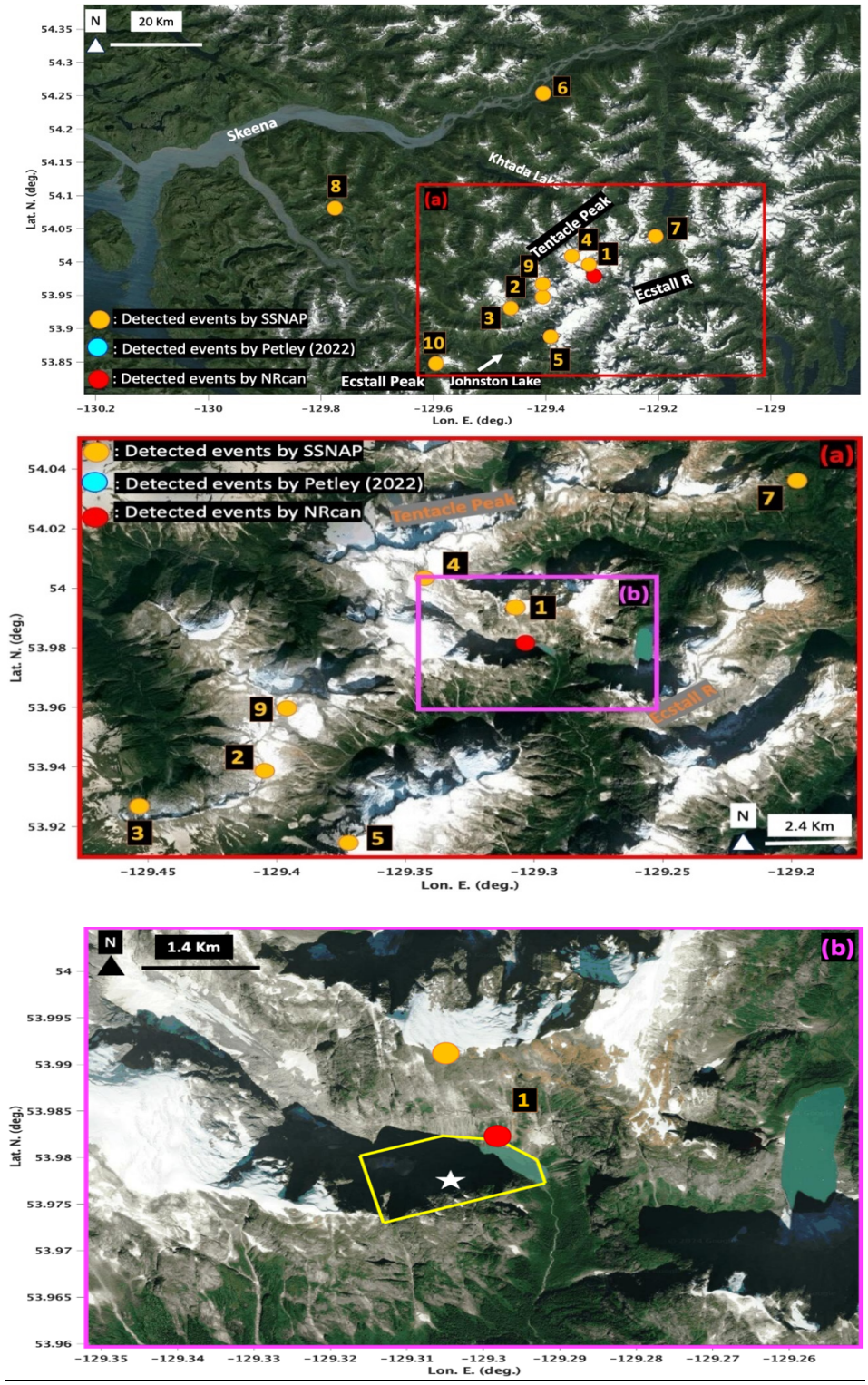


Figure 3.28 Map of detected landslides on September 1st, 2022 between 18:00 and 20:00 UTC. (a) Map of detected landslide locations near Ecstall R; (b) zoomed-in map of SSNAP-EQT and NRCEC events close to the main landslide. The yellow polygon shows the approximate main trace land proof the rockslide (2209_ECS3 no. 1 in this study).

## 3.5.4 2302-ECS4 Landslide event with Mw= 1.2

### 3.5.4.1 Seismic results from SSNAP-EQT model

On February 17th, 2023, at 04:45:12 UTC, the landslide event labeled 2302-ECS4 happened ~43 km west of Kitimat near Ecstall River (coordinates 54.054°N, -129.329°E) (Table 3.3), following a continuous sixteen-day rainfall in February 2023 (Figure 3.29). The SSNAP-EQT model detected one event, which is documented in the NRCEC as an earthquake event (details in Table 3.11). Figure 3.30 includes a brightness time series and map, and related waveform plots. Upon examination of the waveform and the spectrogram of hydroacoustic data, it became evident that the event occurring at 04:45:11 UTC is a landslide, having a waveform pattern that is in line with landslide occurrences. This pattern exhibits non-impulsive, tremor-like seismic waves with intermittent high-amplitude bursts instead of discrete P or S waves. At lower frequencies, these features hold for ~40 seconds (Figure 3.30).

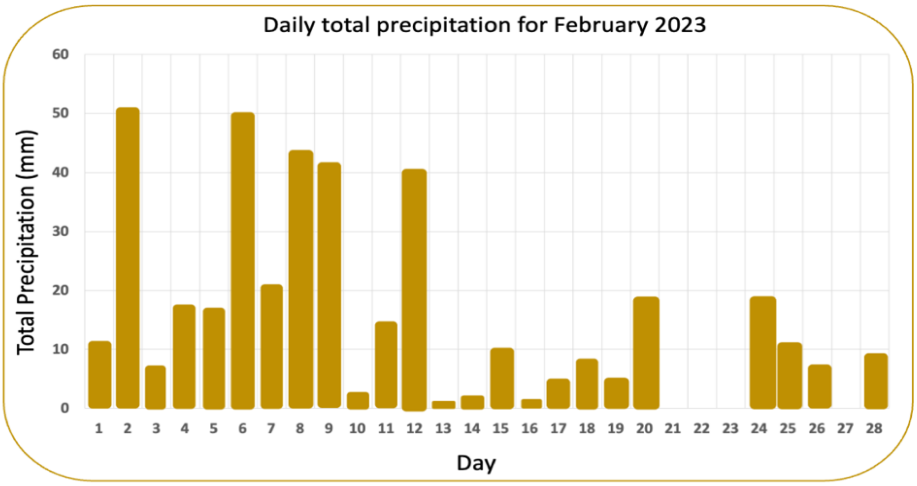


Figure 3.29. Daily total precipitation in February 2023, at Kemano Station, BC (Environment and Climate Change Canada, 2024).

Table 3.11. Event detected on February 17th, 2023, by SSNAP-EQT model.

| Event | NRCEC Event Location (°E,°N) | NRCEC Event Time (hh:mm:ss) | NRCEC Mag. (ML) | Detected Location (°E, °N) | Detected Time (hh:mm:ss) | SSNAP-EQT Mag. (ML) | Detection Distance offset (km) | Detection Time Offset (s) |
|---|---|---|---|---|---|---|---|---|
| **Ecstall River Landslide (no.4)** | (-129.329, 54.054) | 04:45:10 | 1.5 | (-129.403, 53.928) | 04:45:11 | 1.23 | 14.8 | 1 |

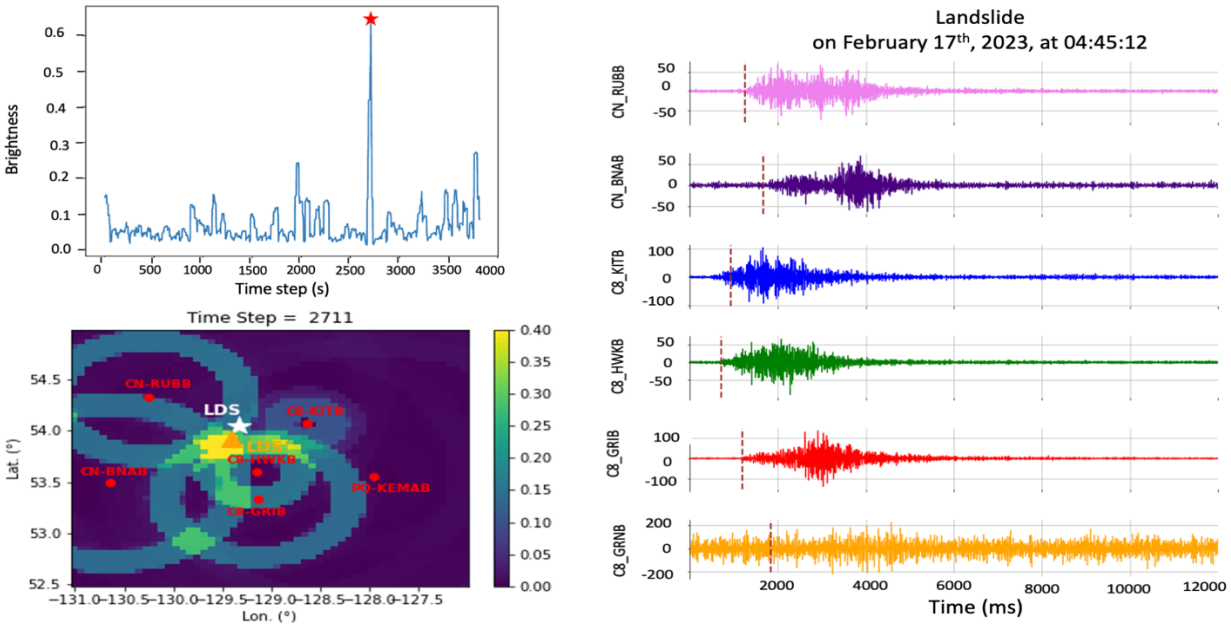


Figure 3.30. The event detected on February 17th, 2022, as a landslide. Upper left shows a brightness vs. time plot over a 1-hour time period from 04:00 to 05:00 UTC, where the red star indicates a time step where brightness exceeds the 0.4 threshold. Lower left: brightness map at the indicated time step. The white star indicates the NRCEC location, while the yellow triangle represents the SSNAP-EQT detected location. RHS: the x-axis on the waveform plots represents the time in milliseconds. The dashed red line on each waveform marks the event signal onset as detected by SSNAP-EQT.

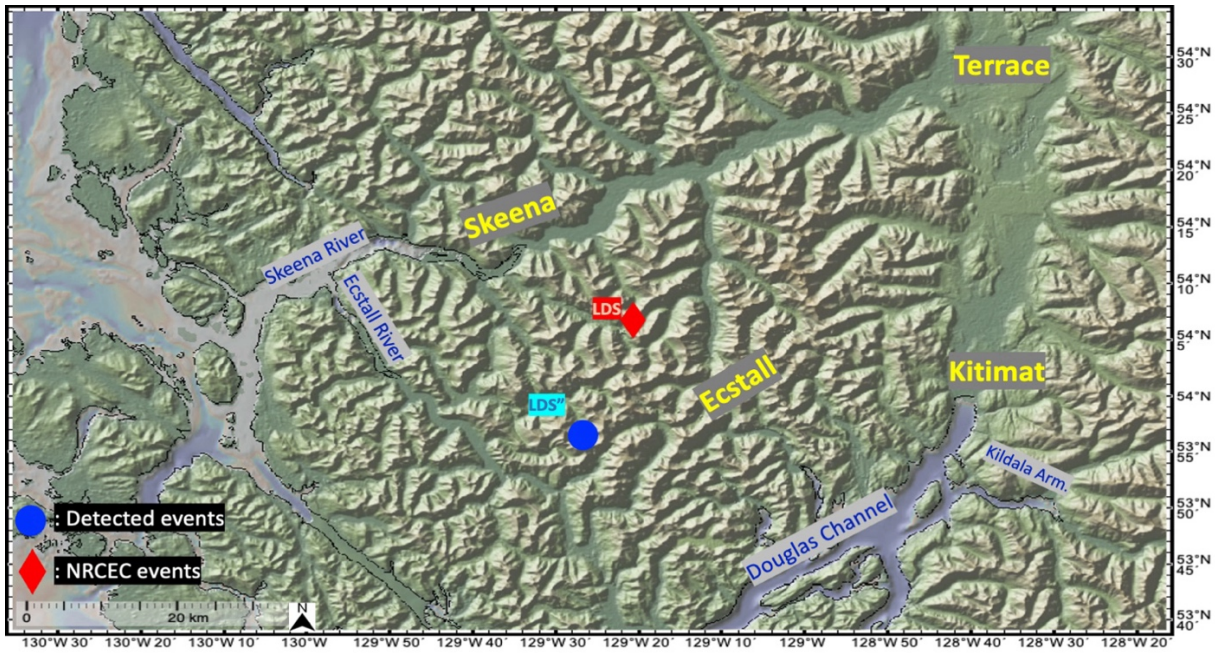


Figure 3.31. Location of landslide 2302-ECS4 on Feb 17th, 2023, as located using SSNAP-EQT (blue) versus the NRCEC location (red).

The detected landslide location is ~15 km away from the NRCEC location, with a time differential of less than 2 seconds (Figure 3.30 and Table 3.11). These differences are greater than for 2208_ECS1 and 2209-ECS3, possibly due to the lower magnitude of the seismic event (1.5 for 2302-ECS4 compared to 2.1 for 22008_ECS1 and 2.8 for 2209_ECS3). The type and volume of the landslide can result in weaker and noisier waveforms, impacting the precision of phase picking and, consequently, influencing event location and time detection, for both SSNAP-EQT and NRCan detection processes.

### 3.5.4.2 Hydroacoustic analysis results

Figures 3.32 and 3.33 each show a 1-hour spectrogram covering the time interval from 04:00 to 05:00 UTC on February 17th, 2023, as recorded by the HYD1 hydrophone near Kitimat. Figure 3.32 illustrates the FFT of the PSD for unfiltered and un-calibrated acoustic data from the HYD1 hydrophone, presented in a one-hour spectrogram plot; Figure 3.33 displays PSD calculated based on FFT and wavelet analysis of bandpass-filtered data and sensitivity-calibrated data.

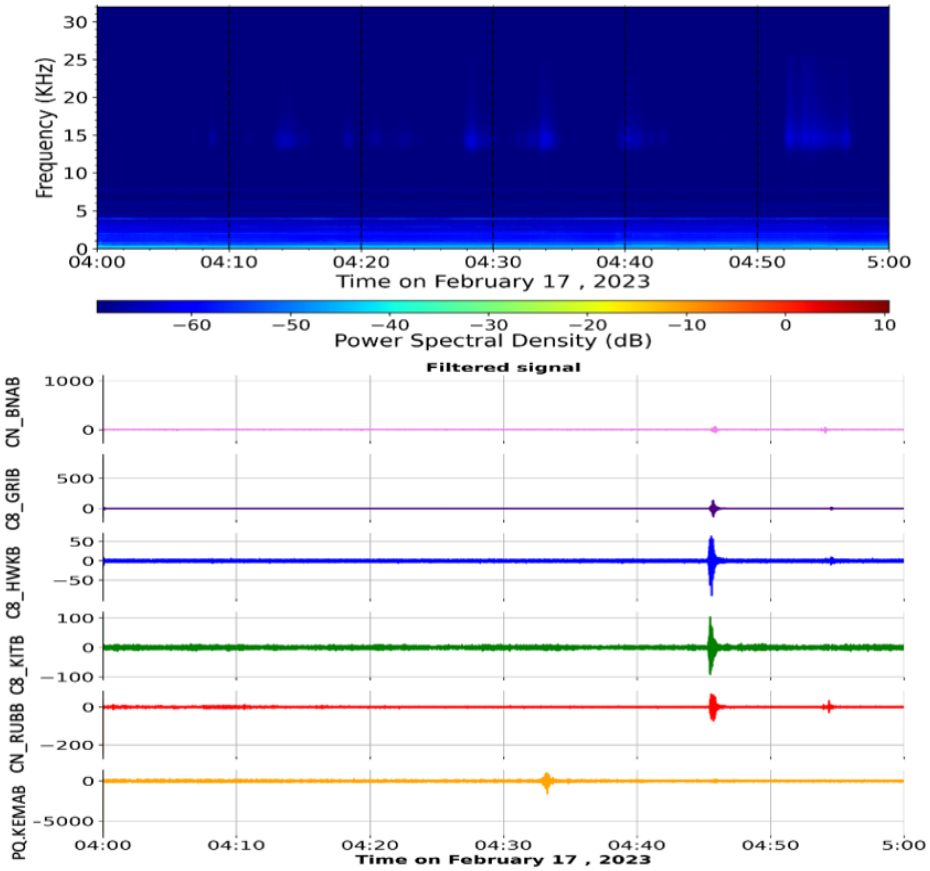


Figure 3.32. Top: One-hour spectrogram of high-frequency hydroacoustic data from HYD1 covering the time of landslide 2302-ECS4 detected in seismic data near Ecstall River on February 17th, 2023. The spectrogram is without bandpass filtering or sensitivity calibration; Bottom: one-hour filtered waveforms from the same time periods recorded at seismic stations.

Figure 3.32 illustrates signals in higher frequency ranges. However, these signals do not align with events detected by the SSNAP-EQT model or with waveforms in the one-hour plot. Given their higher frequency but lower than 5 kHz and continuous in time, these signals may be attributed to wind in the study area.

The hydroacoustic signal associated with the landslide event becomes prominent around 04:45 UTC, as depicted in Figure 3.33. The spectrogram reveals prolonged roaring noises consistent with landsliding. These signals exhibit a distinct pattern, initiating with an extended broadband coda accompanied by a low-frequency rumble, lasting from ~60 minutes. The frequency range with maximum amplitudes remains below 20 Hz. The time series of hydroacoustic data exhibits a similar pattern to that of a landslide seismic waveform, lacking P or S waves, gradually increasing in amplitude, and lasting for ~60 seconds (Figure 3.33).

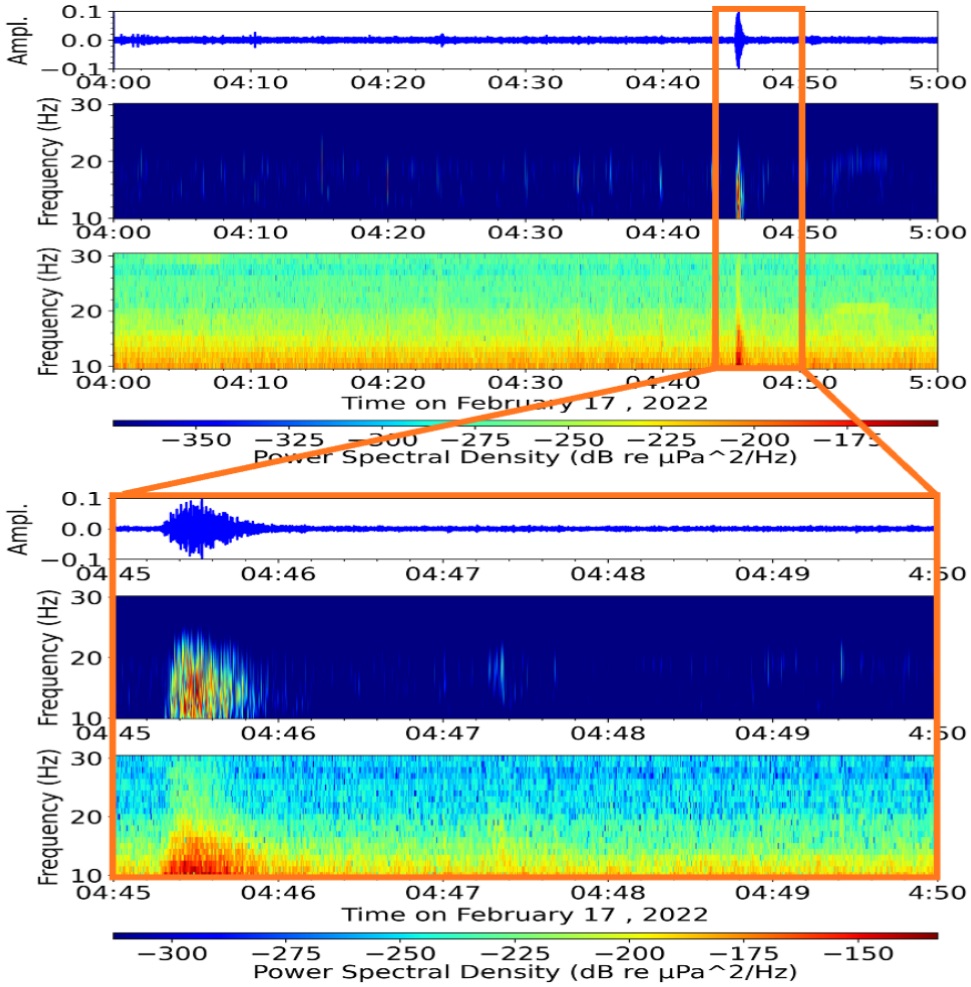


Figure 3.33. Top: Three one-hour time series and spectrograms of HYD1 hydroacoustic data for February 17th, 2023 with bandpass filtering and sensitivity calibration; Bottom: detailed time series and spectrograms of the above row.

## 3.5.5 2212-TRC Landslide event with Mw= 2.0

### 3.5.5.1 Seismic results from SSNAP-EQT model

December 9th, 2022, at 15:03:38, the landslide event labeled 2212-TRC happened approximately 34 km NW of Kitimat near Terrace, at (coordinates 54.299° N, -129.0024° E) (Table 3.3), following a continuous few days of rainfall in December 2022 (Figure 3.34). Upon subjecting the recorded seismic signals to the SSNAP-EQT model, the detection of the 2212-TRC event is revealed. This event is categorized as an earthquake in the NRCan database, but analysis of the event waveform and spectrogram shows the event to be a landslide due to having a non-impulsive, tremor-like signal, and a lack of distinct P or S waves. Figure 3.35 illustrates the brightness time series and map, and related waveform plots. Table 3.12 provides details on the detected and recorded events for reference, while their locations are visualized on the map in Figure 3.36. The difference between the SSNAP-EQT and NRCEC locations is ~25 km, with a time differential of ~2 seconds (Figure 3.36 and Table 3.12).

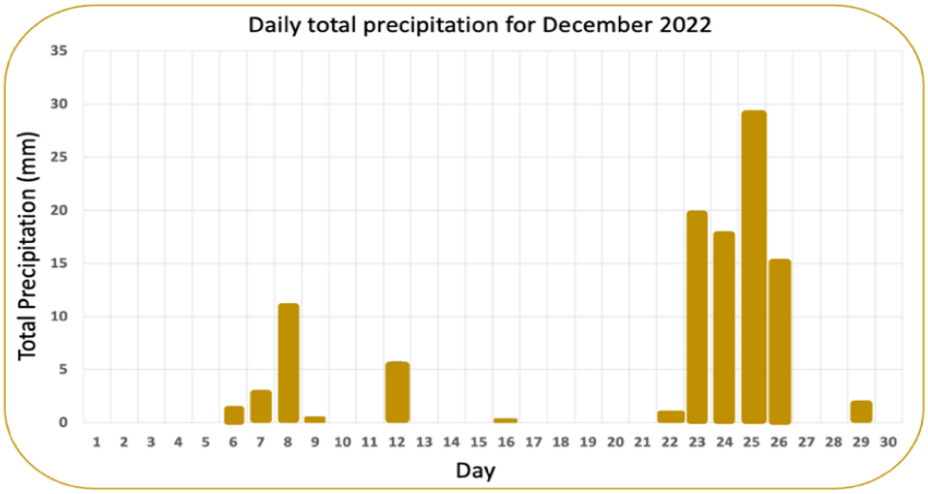


Figure 3.34. Daily total precipitation in December 2022 at Kemano weather station, B.C (Environment and Climate Change Canada, 2024).

Table 3.12. Event detected on December 9th, 2022, by SSNAP-EQT model.

| Event | NRCEC Event Location (°E, °N) | Event Time (hh:mm:ss) | NRCEC Mag. (ML) | Detected Location (°E, °N) | Detected Time (hh:mm:ss) | SSNAP-EQT Mag. (ML) | Detection Distance offset (km) | Detection Time Offset (s) |
|---|---|---|---|---|---|---|---|---|
| **Terrace rockslide** | (-129.0024, 54.299) | 15:03:38 | 2.0 | (-129.345, 54.409) | 15:03:36 | 2.0 | 25.4 | 2 |

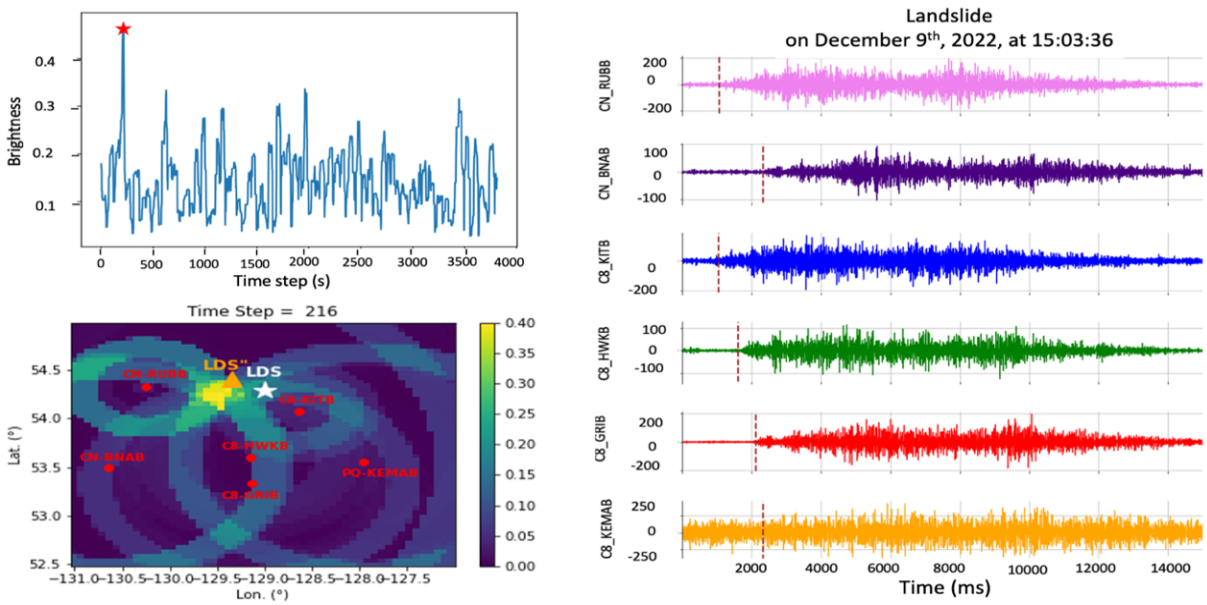


Figure 3.35. The event detected on December 9th, 2022 as a landslide. Upper left shows a brightness vs. time plot over a 1-hour time period, where the red star indicates a time step where brightness exceeds the 0.4 threshold. Lower left: brightness map at the indicated time step. The white star indicates the location based on NRCEC, while the yellow triangle represents the detected location. RHS: the x-axis in the waveform plot represents the time in milliseconds. The dashed red line on each waveform - event signal onset as detected by SSNAP-EQT.

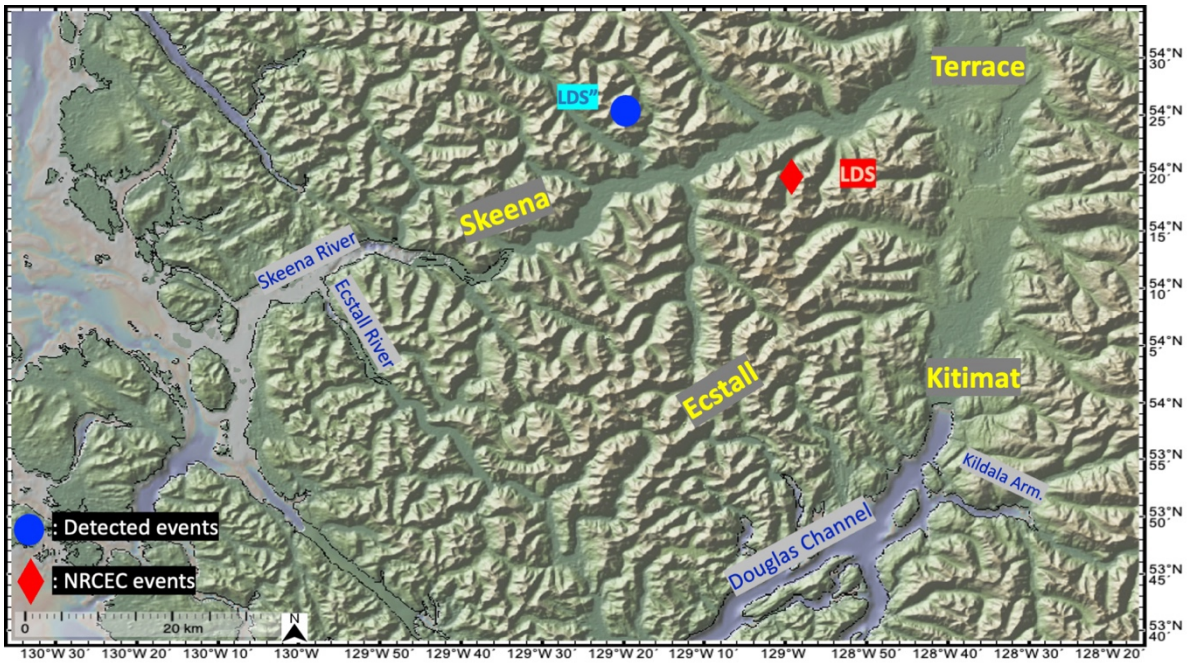


Figure 3.36. Location of landslide (2212-TRC) on Dec 12th, 2022, as located using SSNAP-EQT (blue) versus the NRCEC location (red).

### 3.5.5.2 Hydroacoustic analysis results

Figures 3.37 and 3.38 show a 1-hour spectrogram covering the time interval from 15:00 to 16:00 UTC on December 9th, 2022, as recorded by the HYD1 hydrophone near Kitimat.

Figure 3.37 illustrates the FFT of the PSD for unfiltered and un-calibrated acoustic data from the HYD1 hydrophone, presented in a one-hour spectrogram plot. Meanwhile, Figure 3.38 displays PSD calculated based on FFT and wavelet of filtered and sensitivity-calibrated data.

Figure 3.37 illustrates signals in higher frequency ranges. However, these signals do not align with events detected by the SSNAP-EQT model or with waveforms in the one-hour plot. Given their higher frequency but lower than 15 kHz and short duration, these signals may be attributed to animal calls or vessel transit.

The hydroacoustic signal associated with the landslide event becomes prominent around 15:03:46 UTC, as depicted in Figure 3.38. The spectrogram reveals prolonged roaring noises over a duration of 120 seconds. These features in the spectrogram, as well as the pattern of time series hydroacoustic data, demonstrate that the event is a landslide.

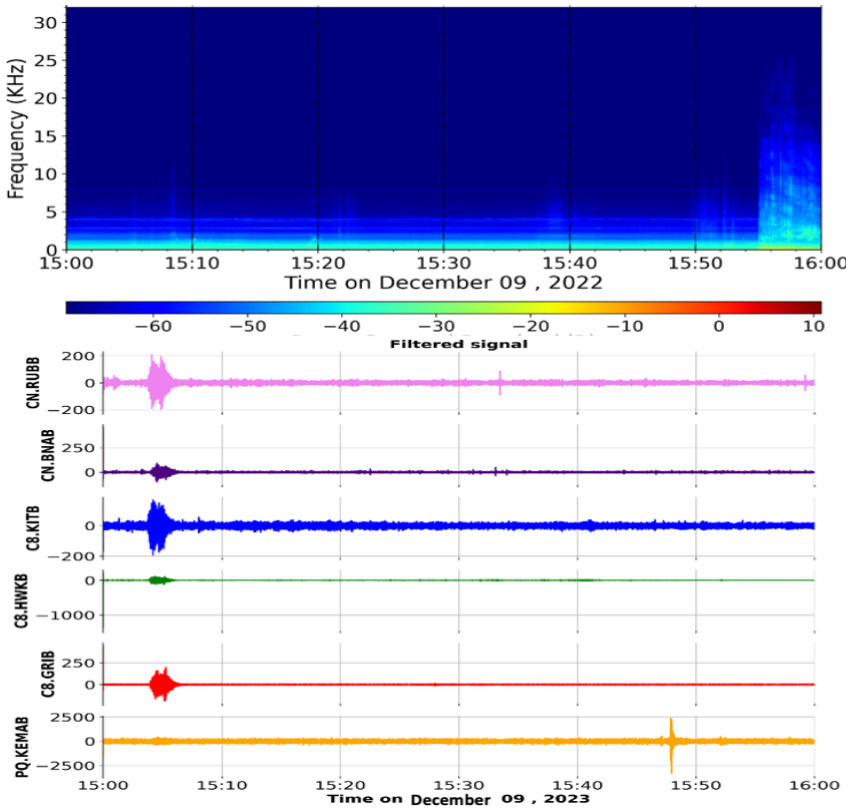


Figure 3.37. Top: One-hour spectrogram of high-frequency hydroacoustic data from HYD1 covering the time of the landslide (2212-TRC) detected in seismic data near Ecstall River on December 9th, 2022. Spectrogram is without bandpass filtering or sensitivity calibration; Bottom: one-hour filtered waveforms from the same time period recorded at seismic stations.

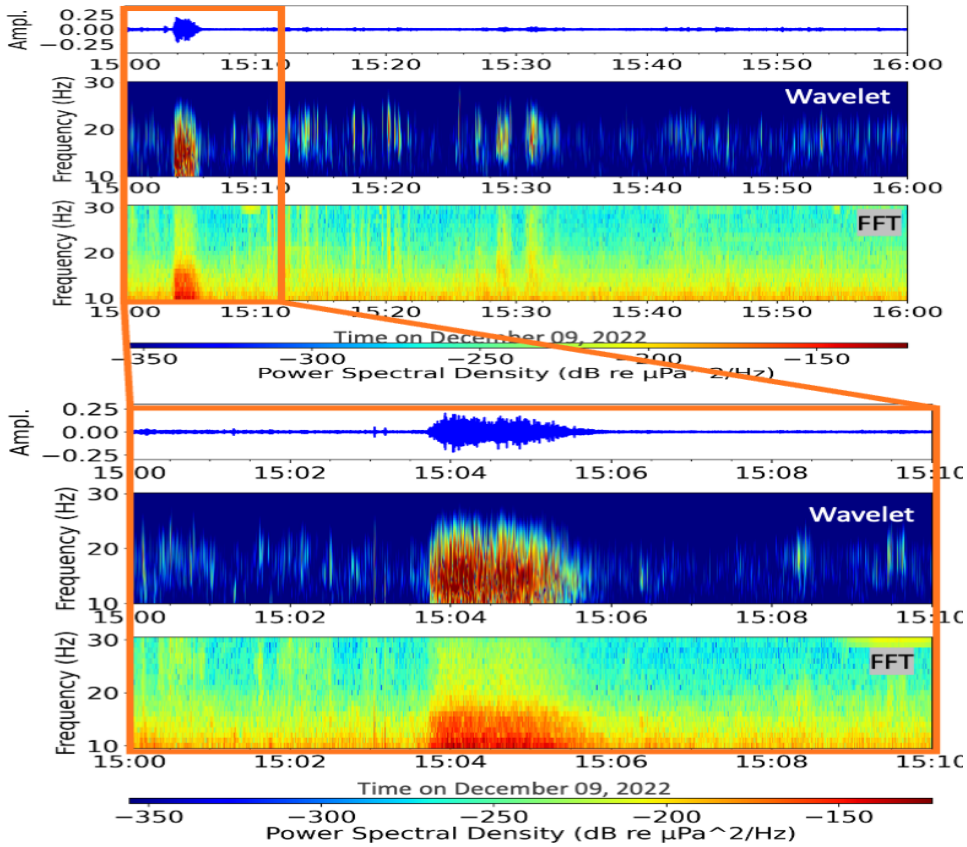


Figure 3.38. Top: One-hour spectrogram of HYD1 hydroacoustic data for on December 9th, 2022, with bandpass filtration and sensitivity calibration; Bottom: detailed spectrogram of the above row.

## 3.5.6 2305-KMN Landslide event with Mw= 1.5

### 3.5.6.1 seismic results from SSNAP-EQT model

May 9th, 2023, at 03:46:06, the landslide event labeled 2305-KMN happened approximately 72 km S of Kitimat near Kemano (coordinates 53.416°N, -128.586°E) (Table 3.3), following a continuous few days of rainfall in May 2022 (Figure 3.39). To conduct a detailed analysis of the seismic activity during this event, waveforms from five specific stations, namely CN_RUBB, CN_BNAB, C8_HWKB, and C8_GRIB, PQ_KEMAB were obtained from the IRIS database for the entire day of May 9th, 2023.

Upon subjecting the seismic signals from these stations to the SSNAP-EQT model, the 2305-KMN event at 03:46:06 was detected. This event is categorized as an earthquake in the NRCEC, but the waveform and spectrogram of the events show it to be a landslide.

The details of the events are noted in Table 3.13. The detected event location is ~60 km away from the NRCEC event location, with a time differential of ~12 seconds. These differences are larger than for 2208_ECS1 and 2, which might be attributed to the lower magnitude of the event

(1.5 for 2305-KMN). The difference between the 2 locations could be partly due to the uncertainty of the NRCan location.

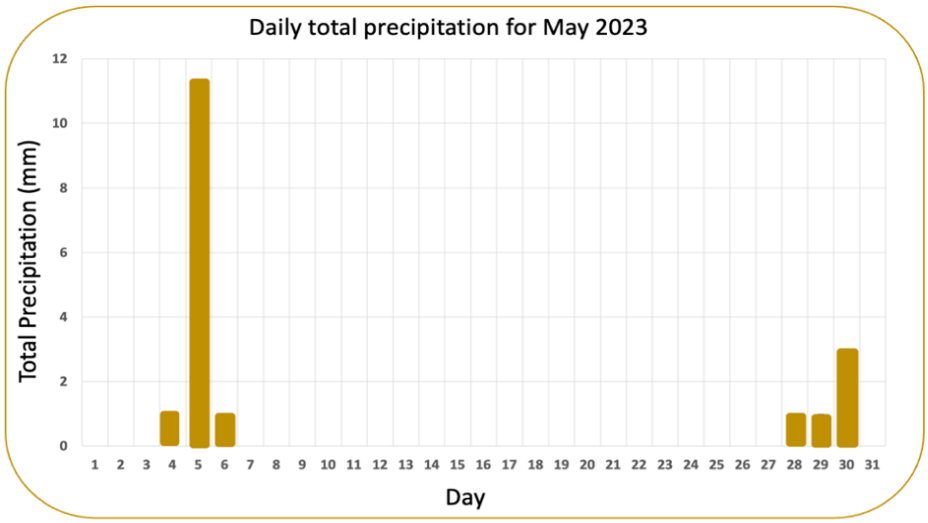


Figure 3.39. Daily total precipitation in May 2023 at Kemano weather station, B.C (Environment and Climate Change Canada, 2024).

Table 3.13. Event detected on May 9th, 2023, by SSNAP-EQT model.

| Event | NRCEC Event Location (°E, °N) | Event Time (hh:mm:ss) | NRCEC Mag. (ML) | Detected Location (°E, °N) | Detected Time (hh:mm:ss) | SSNAP-EQT Mag. (ML) | Detection Distance offset (km) | Detection Time Offset (s) |
|---|---|---|---|---|---|---|---|---|
| **Kemano Landslide** | (-128.586, 53.416) | 03:46:06 | 1.5 | (-127.714, 53.589) | 03:45:56 | 1.8 | 60.97 | 12 |

Figure 3.40 shows the brightness time series and map, and the recorded waveforms; the event locations are visualized on the map in Figure 3.41. Given the absence of hydroacoustic data from the HYD1 hydrophone during the event in question, I sought additional confirmation of its nature as either a landslide or an earthquake. I focused on spectrograms of the seismic data, which have characteristics consistent with a landslide event. The maximum power of the FFT plot is within 1 to 12 Hz-a range associated with lower frequencies typical of landslides (Figure 3.42). Furthermore, the waveform pattern was found to be non-impulsive, with tremor-like seismic waves that exhibit sporadic high-amplitude bursts. The signal lacks definite P and S wave phases and is characterized by a long (40 second) duration and a low frequency. Based on these features, it can be concluded that the event detected by the SSNAP-EQT model on May 9th, 2023, at 03:36 UTC is a landslide.

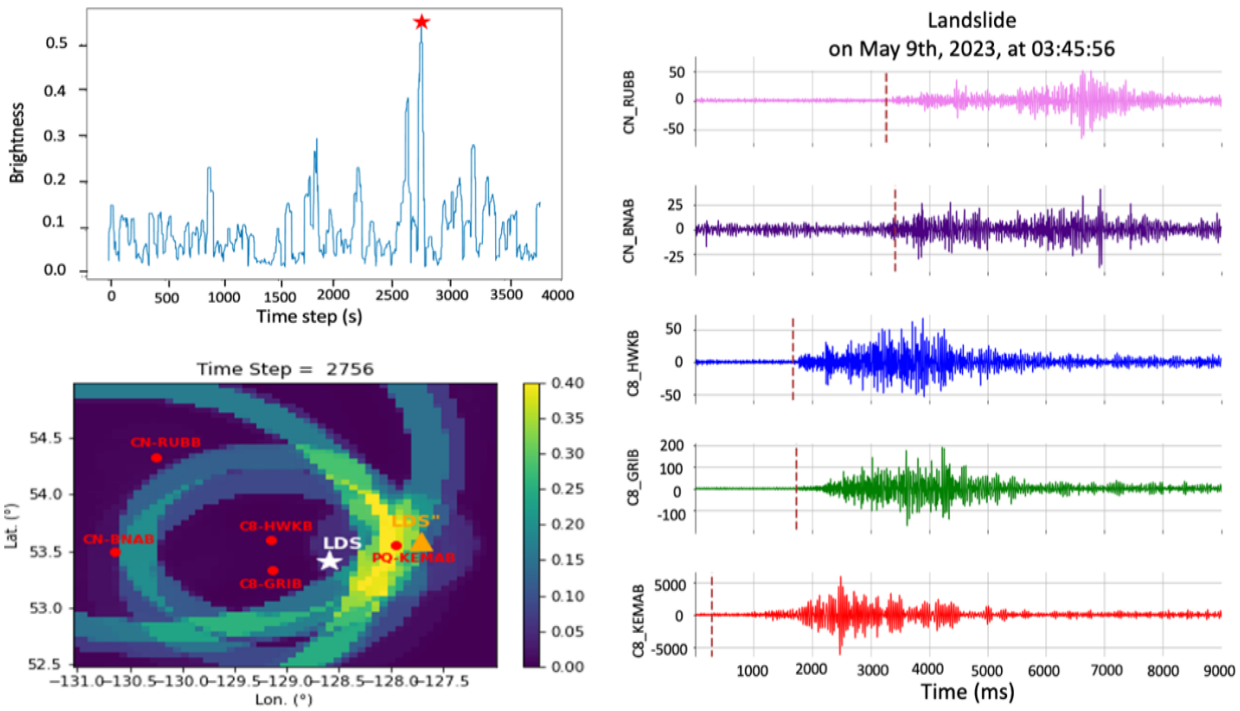


Figure 3.40. Event detected on May 9th, 2023 as a landslide. Upper left shows a brightness vs. time plot over a 1-hour time period, where the red star indicates a time step where brightness exceeds the 0.4 threshold. Lower left: brightness map at the indicated time step. The white star indicates the location based on NRCEC, while the yellow triangle represents the detected location. RHS: the x-axis in the waveform plot represents the time in milliseconds. The dashed red line on each waveform - event signal onset as detected by SSNAP-EQT.

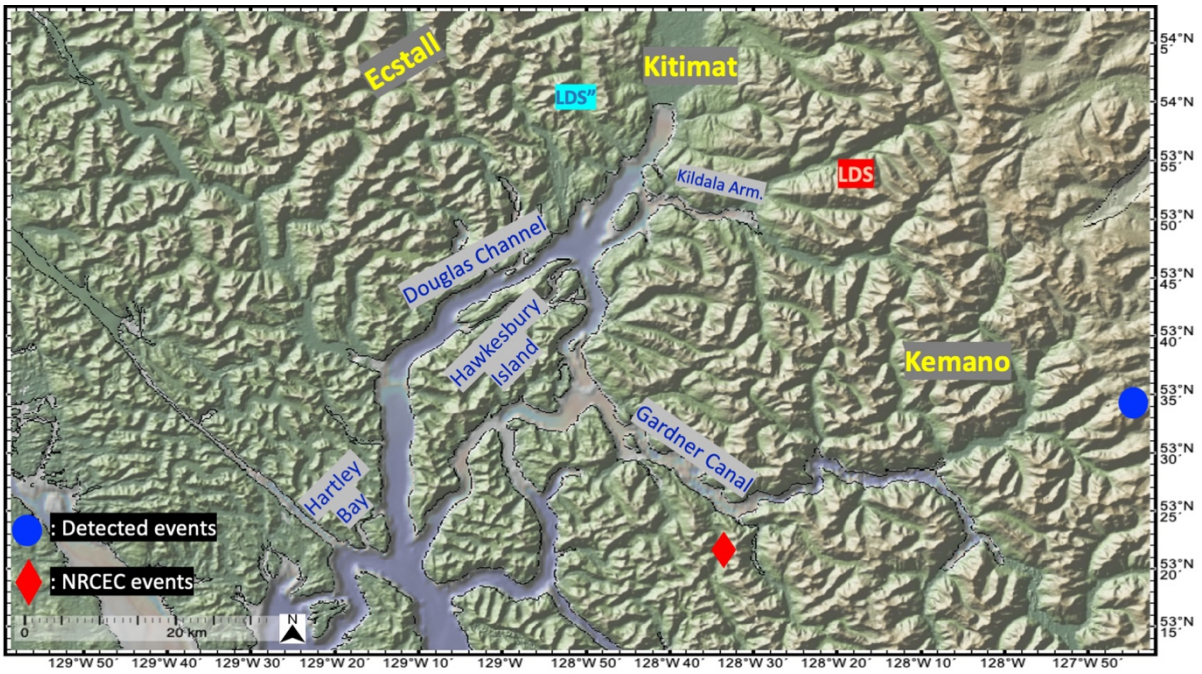


Figure 3.41. Location of landslide (2305-KMN) on May 9th, 2023, as located using SSNAP-EQT (blue) versus the NRCEC locations (red).

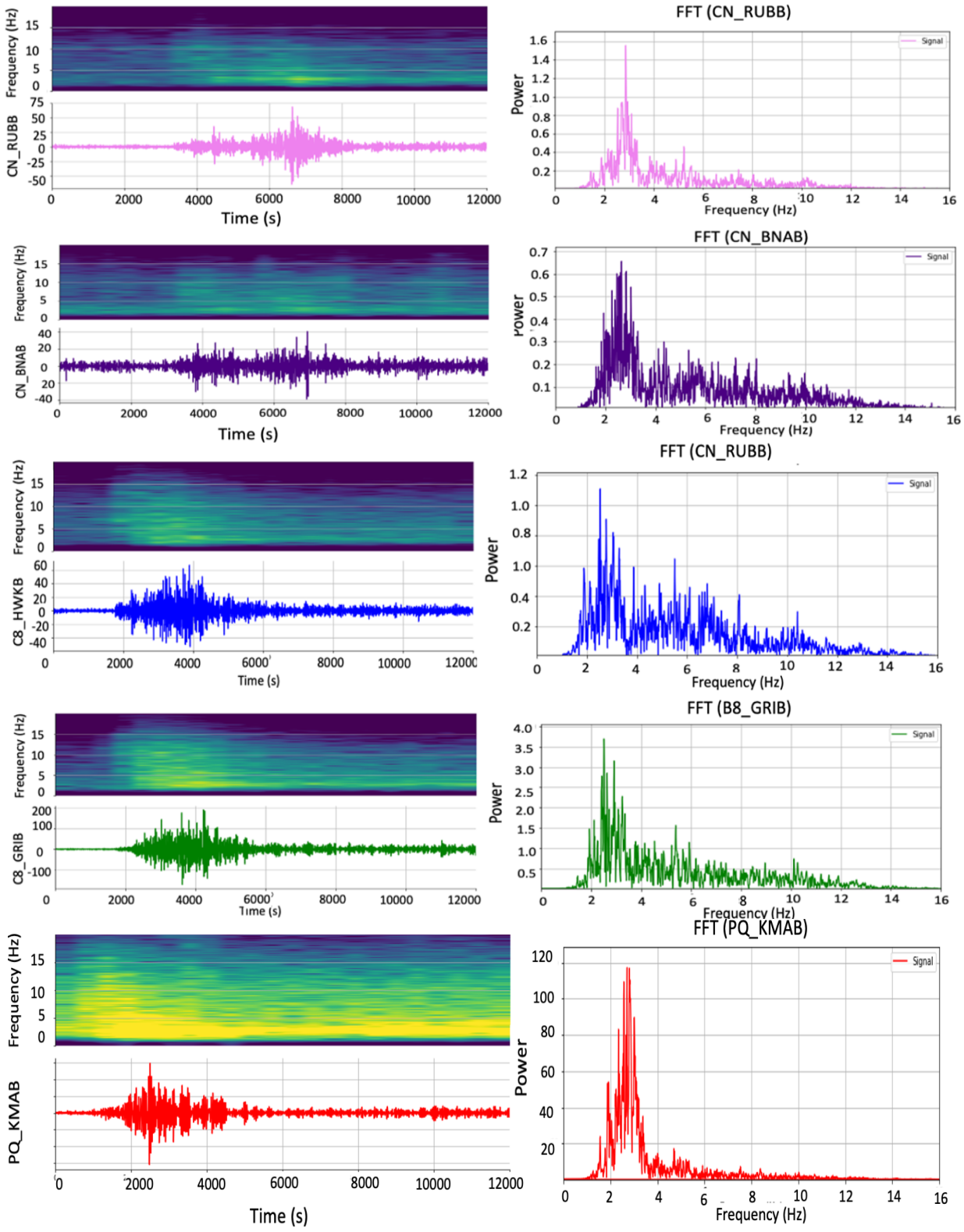


Figure 3.42. Spectrogram, waveform and FFT plots of seismic data for 2305-KMN event.

### 3.5.7 Can landslides of known location but unknown exact timing be detected within September-October 2017?

The geographical locations of landslides occurred in September and/or October 2017 are depicted in Figure 3.43 and summarized in Table 3.3. Figure 3.43 displays photographs of 11 out of the 16 landslide events that likely occurred during this period (Stan Hutchings, personal communication, 2018), offering potential insights into their type and scale. However, the precise volume, magnitude, and exact timing of these landslides remain unknown, and only the approximate locations of these sixteen events are available. As observed in Figure 3.43, the landslides exhibit relatively small sizes, showing similarities in their downslope movement towards Douglas Channel and Gardner Canal, resembling debris flows.

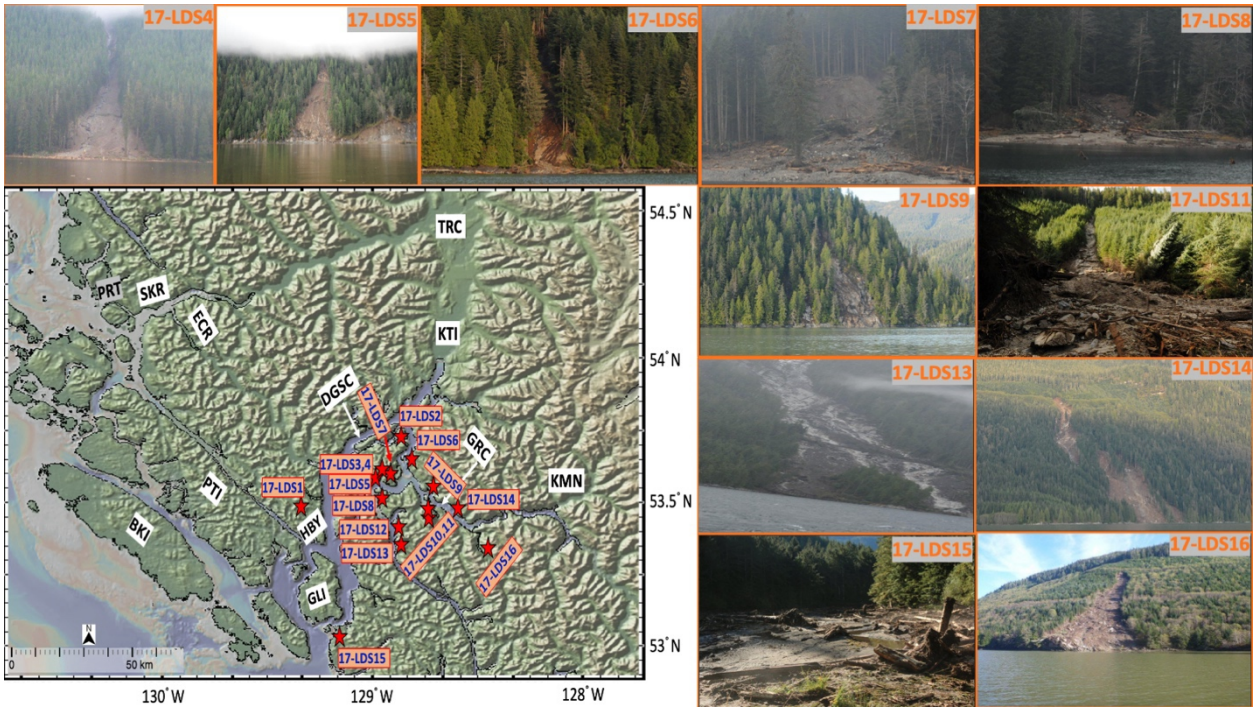


Figure 3.43. The locations of landslides that likely occurred in September/ October 2017, with photos taken by Stan Hutchings.

As a landslide disinteglarates, it may switch from a plastically deforming mass of sediment to a dense slurry dominated by grain-to-grain collisions, or a more dilute flow that is characterized by sediment suspended primarily by turbulence (e.g., Talling et al., 2007; Sumner & Paull, 2014; Clare et al., 2024). Each of these modes will likely generate different signals. Where the moving mass generates a sudden physical impact and comes to rest, such as at breaks in slope (ten Brink et al., 2006), following a sudden height drop, or where it meets pronounced topographic barriers, strong, high frequency signals should be anticipated (Clare et al., 2024). Finally, the indirect effects

of the landslide may also generate a seismic signal, such as where displacement of the overlying water mass generates a tsunami (Clare et al., 2024).

Given their size and debris flow type, seismic signals generated by the 16 events are expected to be weak and might not be readily recorded by seismic stations. However, the utilization of hydrophones or pressure sensors within the study area could enhance the likelihood of recording any potential landslides or associated tsunami waves during this timeframe.

### 3.5.7.1 Seismic results from SSNAP-EQT model

The SSNAP-EQT model was run on seismic data from the stations in the network for the 2-month period from September 1 to October 31, 2017. The model detected some events that it located within the study area; however, based on events in the NRCEC, these events likely occurred outside of the study region (Figure 3.44). The SSNAP-EQT model detects events outside the study area but tries to locate them inside the computational domain. As shown in Figure 3.44, most events that are detected are earthquakes near the plate boundary in the Haida Gwaii region.

The SSNAP-EQT model effectively detected seven seismic events not catalogued in the NRCEC database and their waveform patterns are consistent with landslide waveform, prompting an investigation into potential connections with the 2017 landslide events.

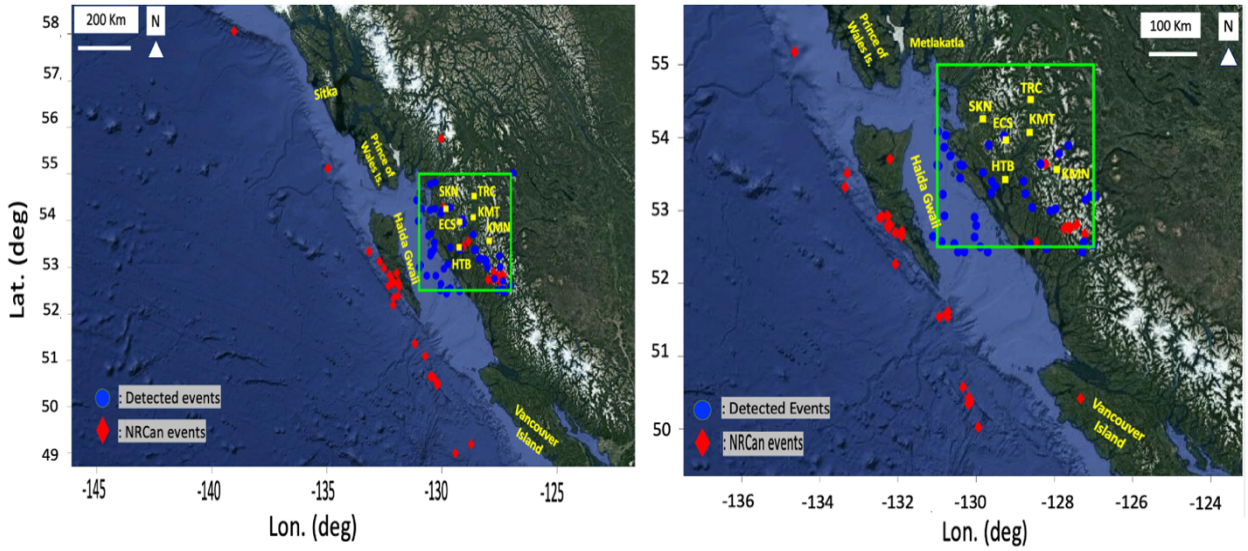


Figure 3.44. Detected and NRCEC event locations in September 2017 (left) and October 2017 (right). The green box shows the study area.

To test this question, the study involved a multi-step analysis. Firstly, the geographical proximity of the newly detected events to the known 2017 landslides was examined; three events occurred in September 2017 (Table 3.14 and Figure 3.45) and four occurred in October 2017 (Table 3.15 and Figure 3.46). Subsequently, waveform analysis was conducted to scrutinize the distinctive patterns of the detected events (Figures 3.47 and 3.48). The investigation also utilized

spectrograms calculated through FFT of seismic data, plots generated to provide insights into the frequency characteristics of the events (Figure 3.49). Sections 3.5.7.2 and 3.5.7.3 delve into the analysis of hydroacoustic and pressure sensor data to determine whether the devised algorithm can identify any signals linked to these events occurring in September and October 2017. In a comprehensive analysis, the determination of event type relies on observing consistent patterns across seismic, acoustic, and water level change datasets if all instruments are suitably located in the study area.

Table 3.14. SSNAP-EQT detected events in September 2017 and proximity (km) to the 16 landslide events.

| **17-LDS No.** | **Sep 5th, 2017 (-128.938°E, 53.511°N) at 17:05:04** | **Sep 14th, 2017 (-127.9813°E, 54.163°N) at 19:01:17** | **Sep 23rd, 2017 (-129.546°E, 53.778°N) at 03:10:06** |
|---|---|---|---|
| **1** | 24.39 Km | 42.50 | 42.65 |
| **2** | 14.75 Km | 10.90 | 46.54 |
| **3** | 9.51 Km | 15.71 | 45.80 |
| **4** | 9.84 Km | 15.38 | 45.65 |
| **5** | 8.07 Km | 17.71 | 44.25 |
| **6** | 13.73 Km | 14.95 | 51.60 |
| **7** | 8.31 Km | 17.29 | 48.26 |
| **8** | 3.06 Km | 22.79 | 47.17 |
| **9** | 13.42 Km | 24.17 | 59.36 |
| **10** | 11.27 Km | 27.85 | 60.03 |
| **11** | 11.14 Km | 29.80 | 60.67 |
| **12** | 15.38 Km | 40.01 | 62.64 |
| **13** | 19.70 Km | 44.46 | 65.81 |
| **14** | 21.45 Km | 33.05 | 69.24 |
| **15** | 52.52 Km | 77.62 | 85.83 |
| **16** | 33.41 Km | 48.16 | 82.99 |

The three events detected in September 2017 that are not documented in the NRCEC have waveforms that can be associated with landslides to some extent (Figure 3.47), and occur in proximity to some of the known landslides (Table 3.14 and Figure 3.45). The events include: i) occurring on September 5th, 2017, at 17:05:04 UTC, located at 53.511°N, -128.938°E, south of Hawkesbury Island and ~3 km from 17-LDS8; ii) occurring on September 14th, 2017, at 19:01:17 UTC at 54.163°N, -127.9813°E, positioned 46 km northeast of Kitimat; and iii) unfolding on September 23rd, 2017, at 03:10:06 UTC located at 53.778°N, -129.546°E, 44 km northwest of Hartley Bay and in close proximity to 17-LDS1. Among the three events identified as potentially associated with landslides, the occurrence on September 5th was in close proximity to one of the known landslides. However, the events on September 5th, 2017, did not occur after a few days of

heavy precipitation, which is one of the primary factors triggering landslides (Figure 3.50). Conversely, the events on September 14th and 23rd happened after a few days of precipitation, but was detected far from the 16 landslide events (Figures 3.45 and 3.50).

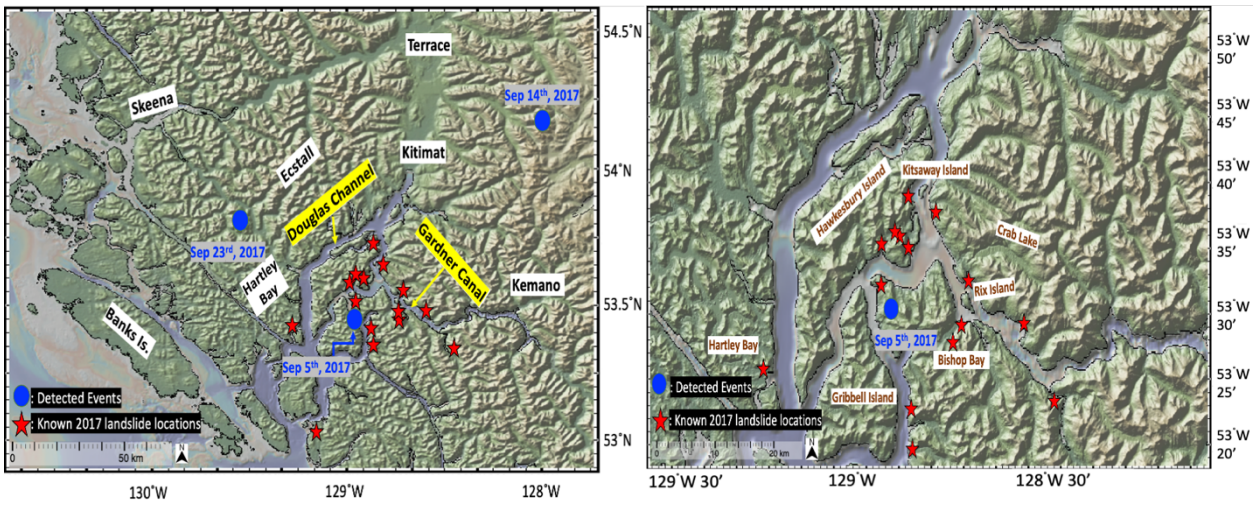


Figure 3.45 Map showing the locations of events detected in September 2017, and the 16 known landslide locations.

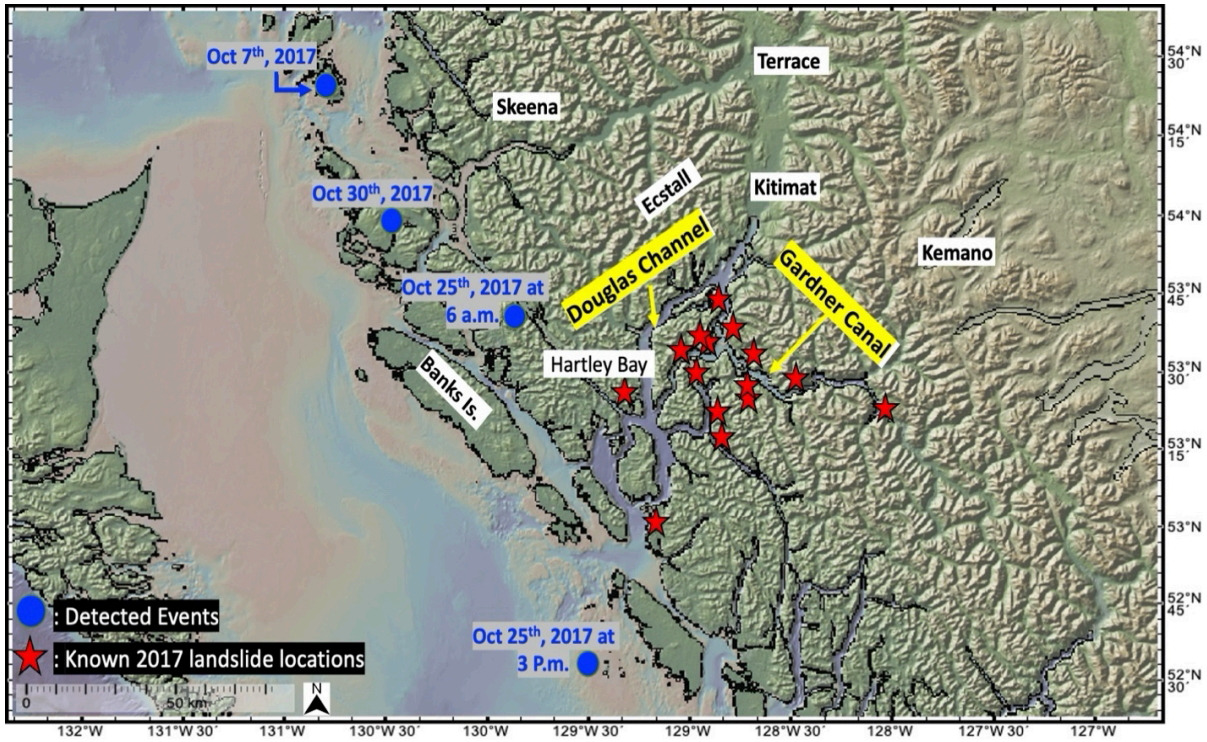


Figure 3.46. Map of events detected in October 2017, and the 16 locations.

On the other hand, no detected events were identified near the 16 landslide locations during the application of the SSNAP-EQT model for October 2017. However, four notable seismic events with distinctive waveforms, potentially related to landslide occurrences, were observed. These events, detailed in Table 3.15 and Figure 3.46 include: i) an event on October 7th, 2017, at 20:34:55 UTC, at 54.387°N, -130.779°E, approximately 32 km northwest of Prince Rupert; ii) an event on October 25th, 2017, at 06:55:16 UTC, located at 53.713°N, -129.896°E, 55 km northwest of Hartley Bay; iii) an event on October 25th, 2017, at 15:08:14 UTC, located at 52.433°N, -129.7058°E, 75 km southwest of Gil Island; and iv) an event on October 30th, 2017, at 14:13:25 UTC, located at 53.93224°N, -130.3558°E, approximately 35 km west of Ecstall River. All these events occurred following a few days of precipitation (Figure 3.50).

Table 3.15. SSNAP-EQT detected events in October 2017 and proximity (km) to the 16 landslide events.

| **LDS No.** | **Oct 7th, 2022 (-130.779°E, 54.387°N) at 20:34:55** | **Oct 25th, 2022 (-129.896°E, 53.713°N) at 06:55:16** | **Oct 25th, 2022 (-129.7058°E, 52.433° N) at 15:08:14** | **Oct 30th, 2022 (-130.3558°E, 53.93224°N) at 14:13:25** |
|---|---|---|---|---|
| **1** | 62.00 | 51.66 | 21.68 | 68.61 |
| **2** | 50.45 | 67.55 | 54.74 | 92.98 |
| **3** | 52.51 | 65.55 | 50.01 | 89.96 |
| **4** | 52.24 | 65.48 | 50.16 | 89.96 |
| **5** | 52.40 | 63.38 | 47.01 | 87.37 |
| **6** | 55.58 | 72.20 | 57.14 | 97.07 |
| **7** | 54.98 | 67.78 | 51.07 | 91.88 |
| **8** | 56.99 | 64.94 | 45.14 | 87.68 |
| **9** | 64.80 | 78.71 | 59.17 | 102.14 |
| **10** | 67.32 | 78.26 | 56.31 | 100.65 |
| **11** | 68.74 | 78.36 | 55.27 | 100.24 |
| **12** | 75.03 | 76.90 | 47.90 | 95.62 |
| **13** | 79.01 | 79.08 | 48.22 | 96.68 |
| **14** | 74.38 | 88.18 | 66.19 | 110.83 |
| **15** | 105.20 | 90.20 | 50.55 | 97.50 |
| **16** | 89.40 | 100.52 | 74.22 | 121.27 |

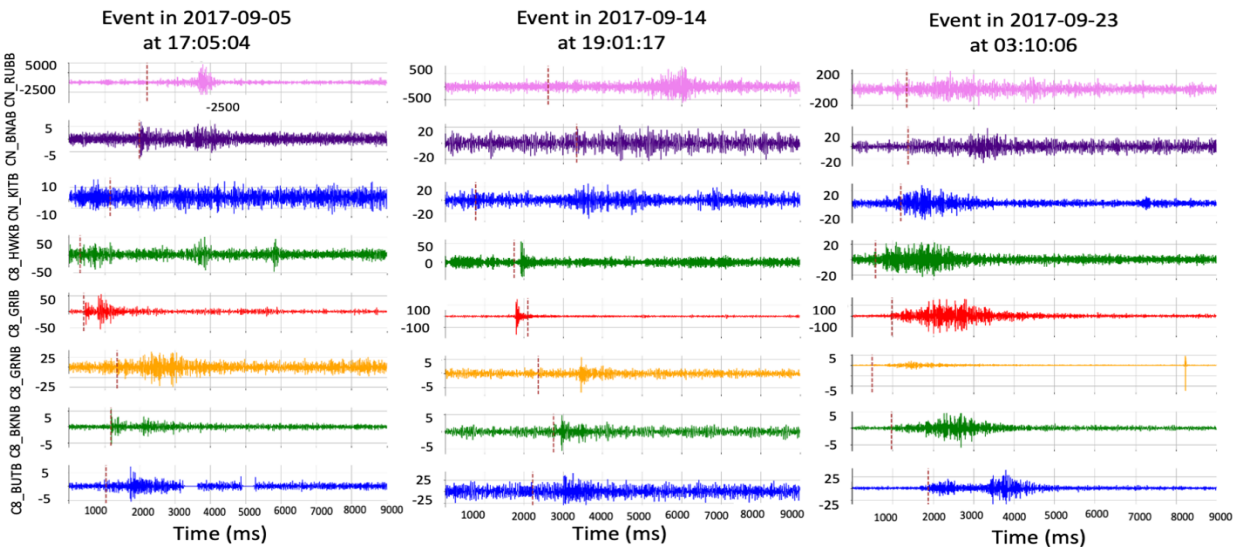


Figure 3.47. Waveforms of potential landslide events during September 2017. The dashed red line on each waveform - event signal onset as detected by SSNAP-EQT.

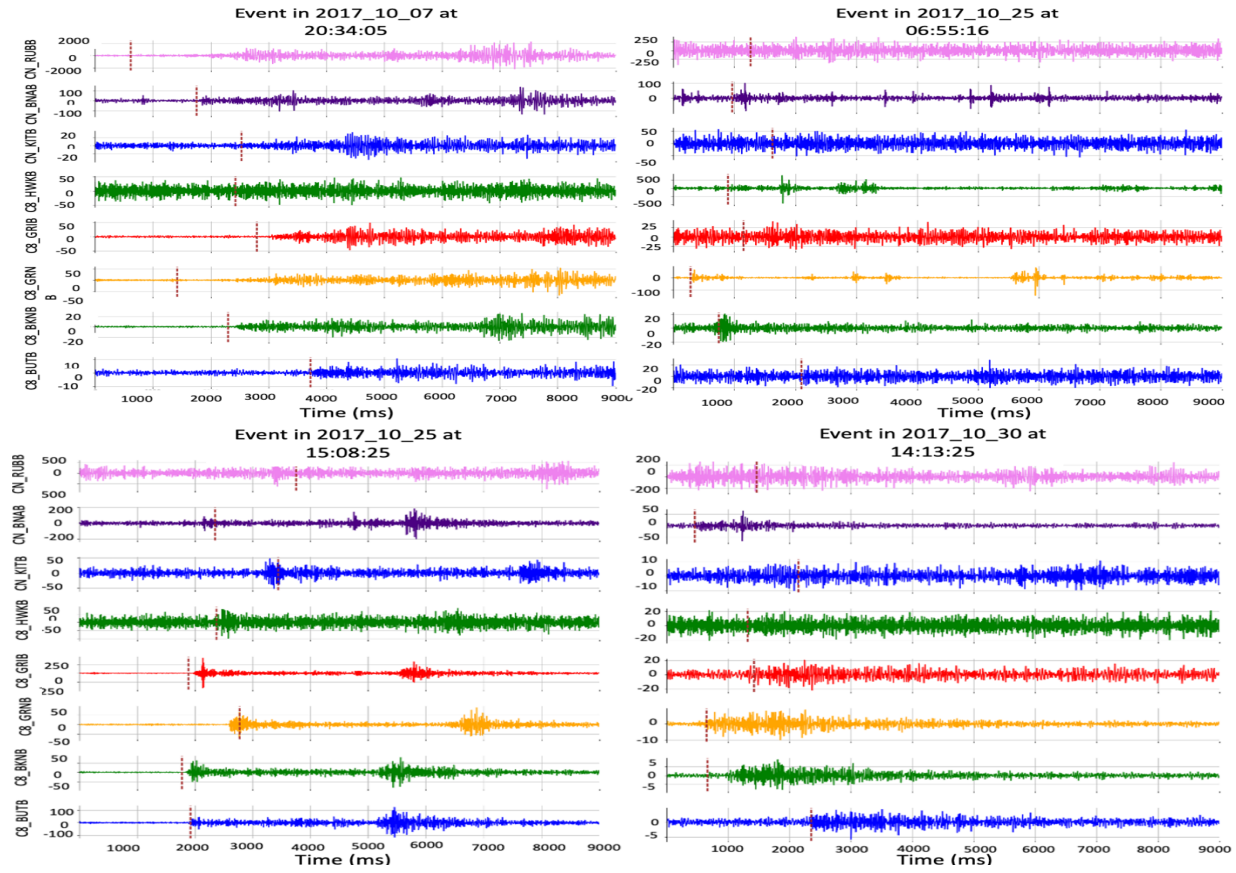


Figure 3.48. Waveforms of potential landslide events during October 2017. The dashed red line on each waveform - event signal onset as detected by SSNAP-EQT.

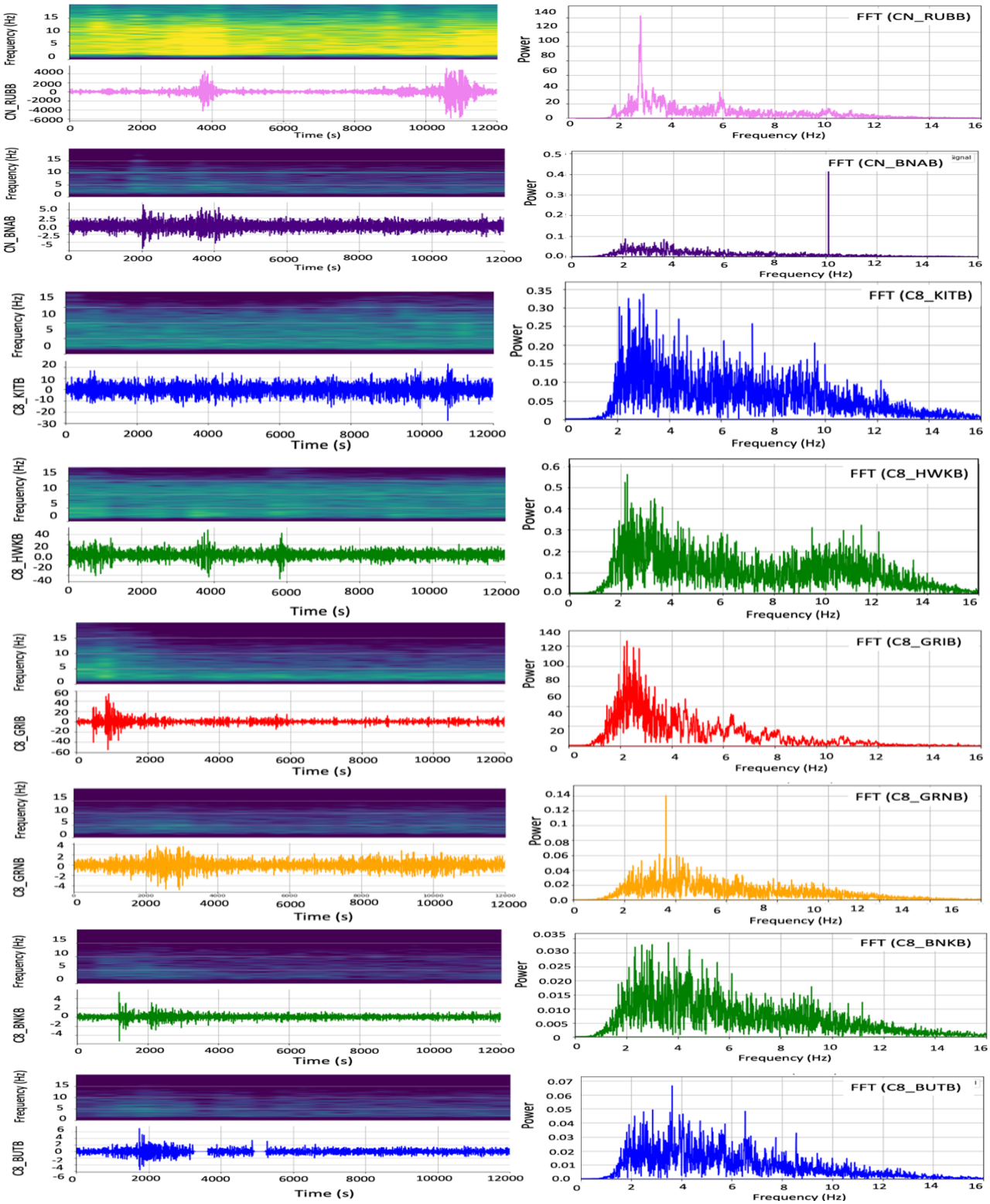


Figure 3.49. Spectrogram, waveform and FFT plots of seismic data for September 5th, 2017 event.

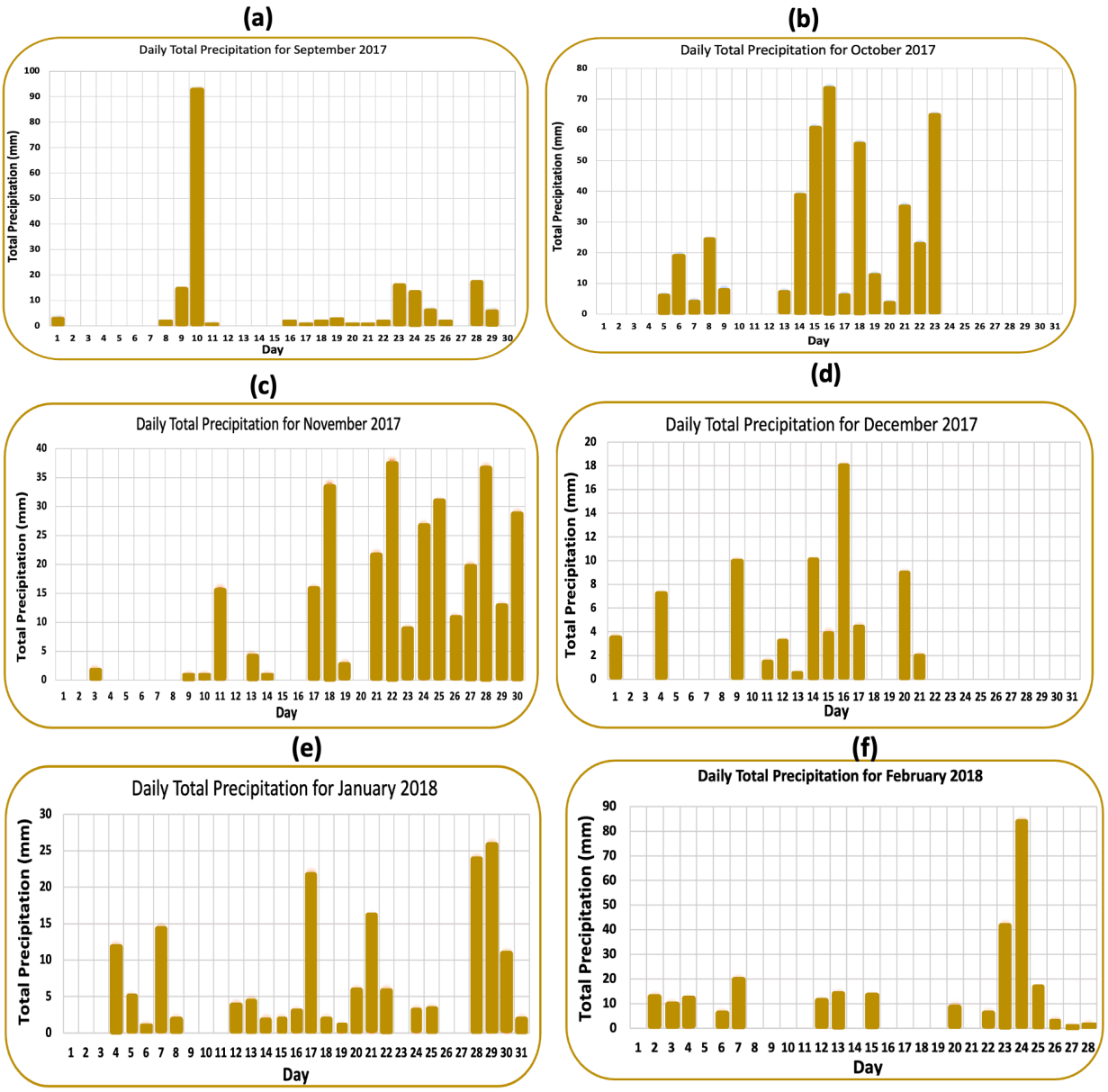


Figure 3.50. Total precipitation within September 2017 to February 2018 at Kemano weather station, B.C (Environment and Climate Change Canada, 2024). Note: different scale for each graph.

In the subsequent analysis, I scrutinized the waveforms corresponding to the detected candidate events for potential association with the 2017 landslide occurrences. As depicted in Figures 3.47 and 3.48, these waveforms exhibit a less distinct signal profile compared to the previously mentioned events indicative of landslides (Sections 3.5.1.1, 3.5.2.1, 3.5.3.1, 3.5.4.1, 3.5.5.1, and 3.5.6.1), despite undergoing signal filtering within the frequency range of 2 to 12 Hz. Notably, the waveforms exhibit a significant level of noise; however, their patterns bear a closer resemblance to the typical characteristics of landslide events than to earthquakes.

Evaluating the waveform of seismic signals can be challenging when attempting to distinguish between a landslide and an earthquake source. This complexity arises because for events that originate beneath the ocean or in continental crustal regions where the signal traverses subfloor the ocean, and/or continental crust paths, the waveforms often exhibit seismic signal patterns resembling a landslide event, even if the seismic source was an earthquake (C. Brillon, personal communication, 2023). To address this challenge, examining the spectrograms may provide valuable insights into the frequency ranges associated with the event. However, both landslides and microseismic earthquakes typically fall within low-frequency ranges, approximately 1 to 12 Hz. Hence, only relying on the spectrogram may not be sufficient to differentiate microseismic earthquakes from landslides.

As a third step of investigation of these detected events, I examine spectrograms and FFT plots for the identified candidate events (Figure 3.49). The analysis indicates that the event's frequency ranges mainly fall within 1 to 12 Hz, supporting the assumption that it could be either a landslide or a microseismic earthquake at this point.

#### 3.5.7.2 Hydroacoustic analysis results

Figures 3.51 and 3.52 display the spectrograms of SPD data in high and low frequency derived from hydrophone data from HYD1 near Kitimat, showcasing the detected candidate events in September 2017.

Figure 3.51 presents the unfiltered data of Fast Fourier Transform (FFT) for the acoustic waveform data during the event on September 5$^{th}$, 2017; a continuous signal is evident in the frequency range below 6 kHz between 17:00 and 17:10 UTC. The cause of the signal between 17:00 and 17:10 is challenging to ascertain and is out of scope of this research, but it may be associated with weather conditions or a vessel passage, based on the extended duration of the signal. Another short-lived signal appears at 17:30 UTC in higher frequency range which cannot be related to landslide events. This signal around 17:30 UTC is likely related to animal vocalizations, which typically have frequencies between 100 Hz and 100 kHz. As mentioned in earlier sections, the time series data from the hydrophone exhibit a similar pattern to the waveform of seismic data. If it could be related to the landslide event, particularly in the lower frequency range of the spectrogram, we should observe a corresponding signal at the detected time (Figure 3.52), as seen with other events occurring in 2022 and 2023.

Figure 3.53 presents the unfiltered data of FFT for the acoustic data waveform during the event on September 14$^{th}$, 2017; two signals are evident in the frequency range below 30 kHz at 19:06 and 19:14 UTC. As mentioned for the previous detected event, the cause of the signals at 19:06 and 19:14 is challenging to ascertain, but they may be associated with animal vocalizations, typically occurring in high frequency and short in duration.

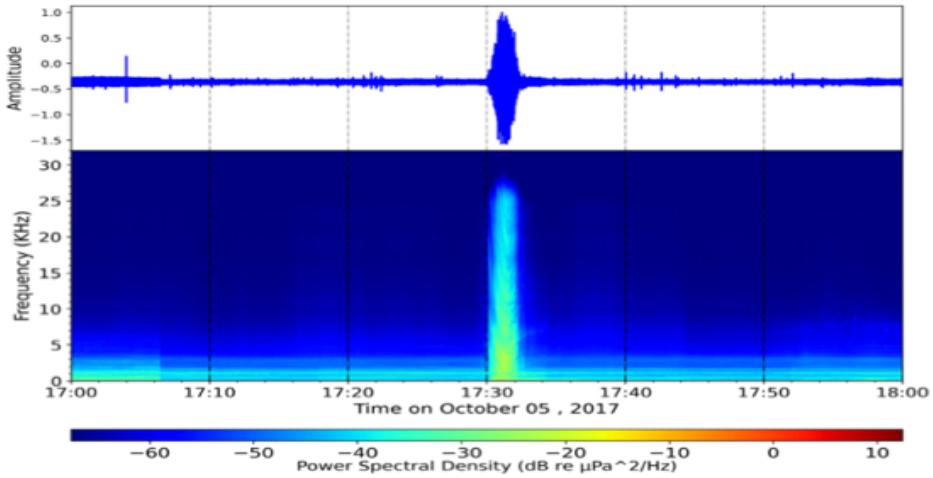


Figure 3.51. One-hour spectrogram plot of HYD1 data in high frequency without filtering, covering time period of September 5th, 2017 event detected by SSNAP-EQT.

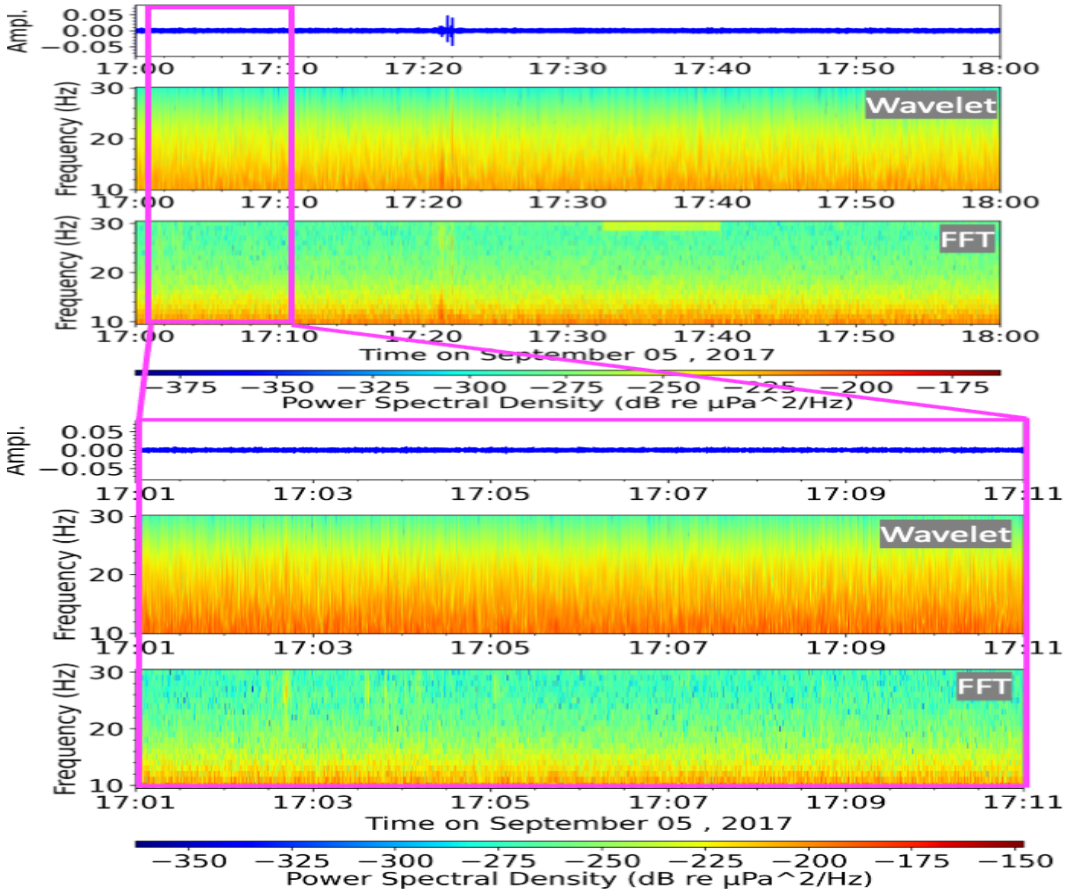


Figure 3.52. Low frequency spectrogram plots covering time period of September 5th, 2017 event detected by SSNAP-EQT. Top: 1-hour filtered time series of hydroacoustic data; middle: 1-hour spectrogram plot of HYD1 data calculated with wavelet and FFT methods; bottom: zoom-in of spectrogram after filtering, calculated with wavelet and FFT methods.

Examining the detailed, lower frequency ranges of acoustic data on September 14th, 2017, did not reveal any signals consistent with landslide events (Figure 3.54). The background noise in the data could be attributed to wind or weather conditions. So, it can be concluded that the detected signal cannot be associated with these 16 landslides or with any events detected by SSNAP-EQT.

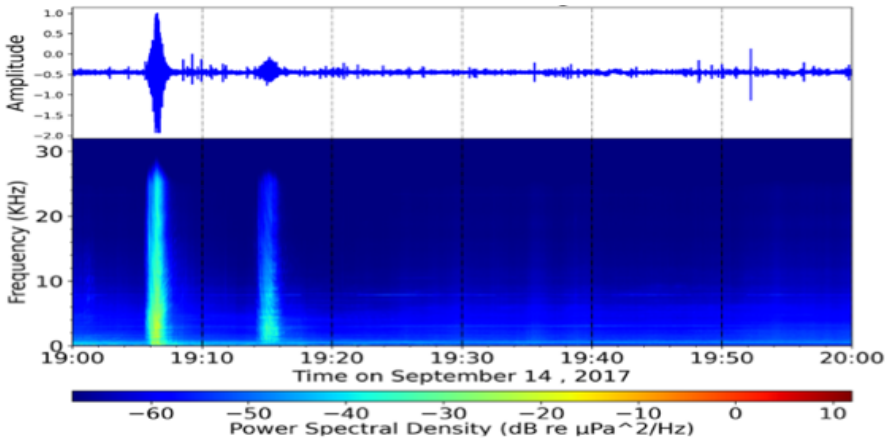


Figure 3.53. One-hour spectrogram plot of HYD1 data in high frequency without filtering, covering time period of September 14th, 2017 event detected by SSNAP-EQT.

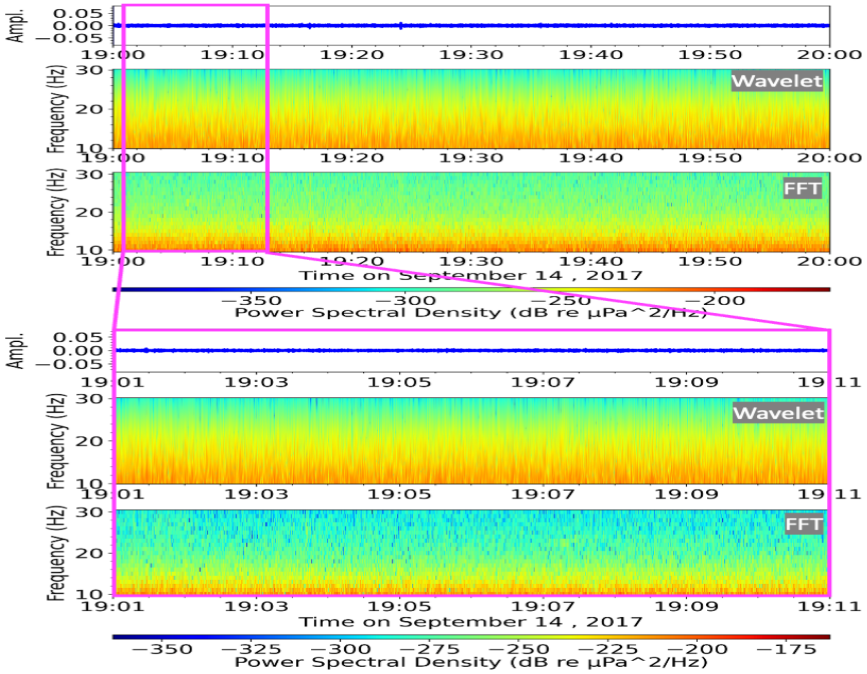


Figure 3.54. Low frequency spectrogram plots covering time period of September 14th, 2017 event detected by SSNAP-EQT. Top: 1-hour filtered time series of hydroacoustic data; middle: 1-hour spectrogram plot of HYD1 data calculated with wavelet and FFT methods; bottom: zoom-in of spectrogram filtering, calculated with wavelet and FFT methods.

Figure 3.55 illustrates the unfiltered FFT of the acoustic data waveform during the September 23rd, 2017 event, with a continuous signal in the frequency range below 10 kHz between 03:00 and 04:00 UTC, although not entirely clear in the higher frequency range spectrogram plot. The origin of this signal during the specified time frame is challenging to ascertain, but since this signal is present through the 1-hour spectrogram, it may be linked to weather conditions such as rain. Upon detailed examination of the lower frequency ranges of the acoustic data for September 23rd, 2017, no signals consistent with landslide events were identified (Figure 3.56). The background noise in the data could be attributed to rain, as mentioned earlier. Consequently, it can be inferred that the detected signal is not associated with any of the 16 known landslides.

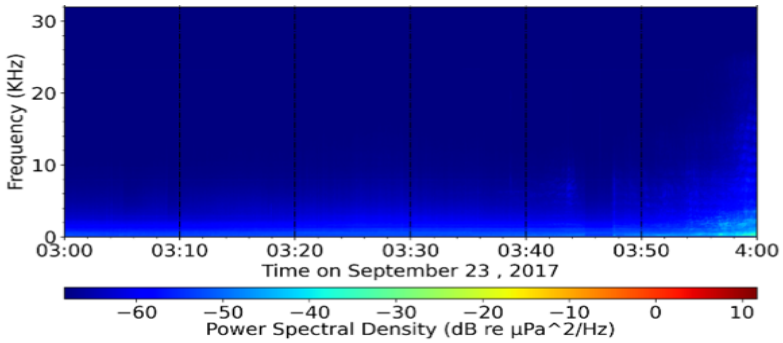


Figure 3.55. One-hour spectrogram plot of HYD1 data in high frequency without filtering, covering time period of September 23rd, 2017 event detected by SSNAP-EQT.

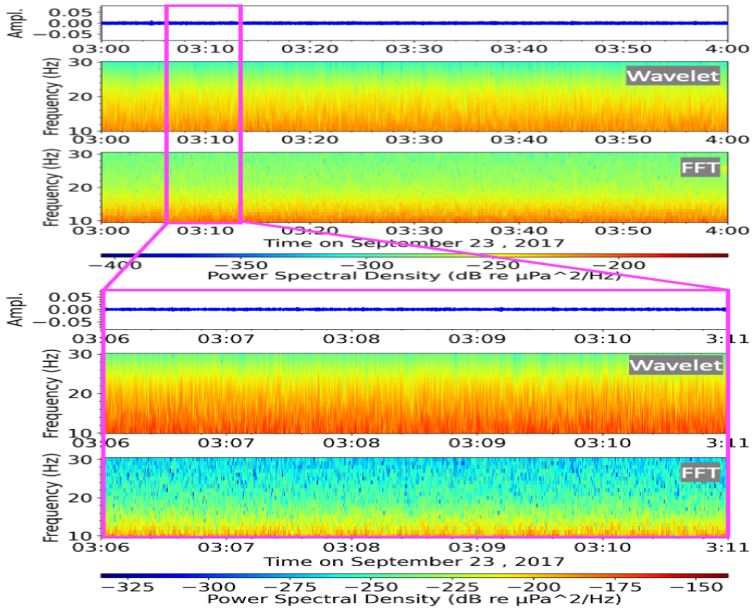


Figure 3.56. Low frequency spectrogram plots covering time period of September 23rd, 2017 event detected by SSNAP-EQT. Top: 1-hour spectrogram plot of HYD1 data calculated with wavelet and FFT methods; Bottom: zoom-in of spectrogram after filtering, calculated with wavelet and FFT methods.

Figure 3.57, the unfiltered FFT of the acoustic data waveform during the October 7th, 2017 event, reveals a continuous signal in the frequency range below 28 kHz between 20:00 and 21:00 UTC, and also multiple short signals in higher frequency ranges. The origin of this signal during the specified time frame is challenging to specify, but since this signal is present throughout the 1-hour spectrogram, it may be linked to weather conditions such as wind. The multiple short signals at higher frequency may reflect animal calls, or vessel transit.

Upon detailed examination of the lower frequency ranges of the acoustic data for October 7th, 2017, no signals consistent with landslide events were identified (Figure 3.58). The background noise in the data could be attributed to wind, as mentioned earlier. Consequently, it can be inferred that the detected signal is not associated with one of the 16 known landslides.

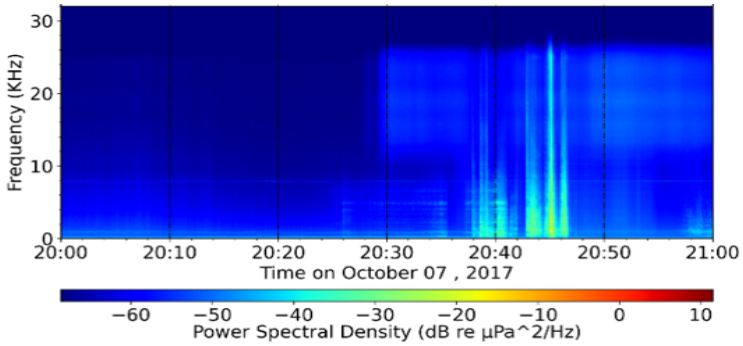


Figure 3.57. One-hour spectrogram plot of HYD1 data in high frequency without filtering covering time period of October 7th, 2017 event detected by SSNAP-EQT.

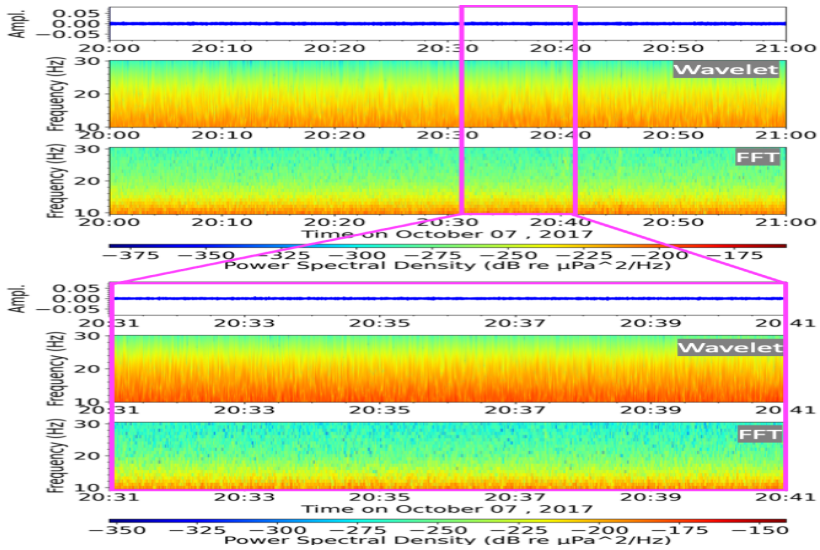


Figure 3.58. Low frequency spectrogram plots covering time period of October 7th, 2017 event detected by SSNAP-EQT. Top: 1-hour filtered time series of hydroacoustic data; middle: 1-hour spectrogram plot of HYD1 data calculated with wavelet and FFT methods; bottom: zoom-in of spectrogram after filtering, calculated with wavelet and FFT methods.

Figure 3.59, the unfiltered FFTs of the acoustic data waveform during the two October 25th, 2017, SSNAP-EQT events, reveals a continuous signal in the frequency range below 28 kHz between 06:00 and 07:00 UTC, and between 15:00 to 16:00 UTC. The origin of these signals during the specified time frames is difficult to determine, but since this signal is present throughout the 1-hour spectrograms, it may be linked to weather conditions such as wind for the continuous signals in the background. The multiple short signals at higher frequency may reflect animal calls, or vessel transit.

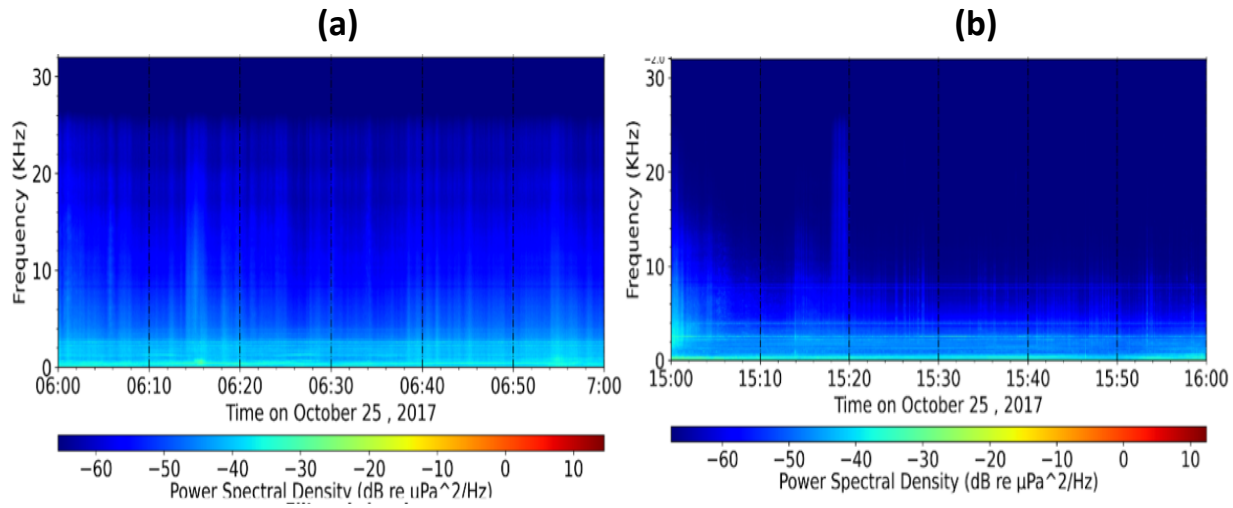


Figure 3.59. One-hour spectrogram plot of HYD1 data in high frequency without filtering, covering time period of two October 25th, 2017 event detected by SSNAP-EQT; (a) within time 06:00 to 07:00 UTC, (b) at time 15:00 to 16:00 UTC.

Upon detailed examination of the lower frequency ranges of the acoustic data for October 25th, 2017, no clear signals consistent with landslide events were identified (Figure 3.60). The background noise in the data could be attributed to wind, as mentioned earlier. Consequently, it can be inferred that the detected signals are not associated with any of the 16 known landslides.

In Figure 3.61, the unfiltered FFT of the acoustic data waveform covering the time of the October 30th, 2017 event reveals multiple signals below 28 kHz between 14:00 and 15:00 UTC. Identifying the origin of these signals during the specified time frame is challenging. The first two signals within the 14:00 to 14:30 time frame, based on the spectrogram shape and higher frequency range, may be associated with the movement of a ship or catamaran in the Douglas Channel. The two other short signals could be linked to animal vocalizations.

Upon detailed examination of the lower frequency ranges of the acoustic data for October 30th, 2017, no clear signals consistent with landslide events were identified (Figure 3.62). The background noise in the data could be attributed to wind. Consequently, it can be inferred that the detected signal is not associated with one of the 16 known landslides.

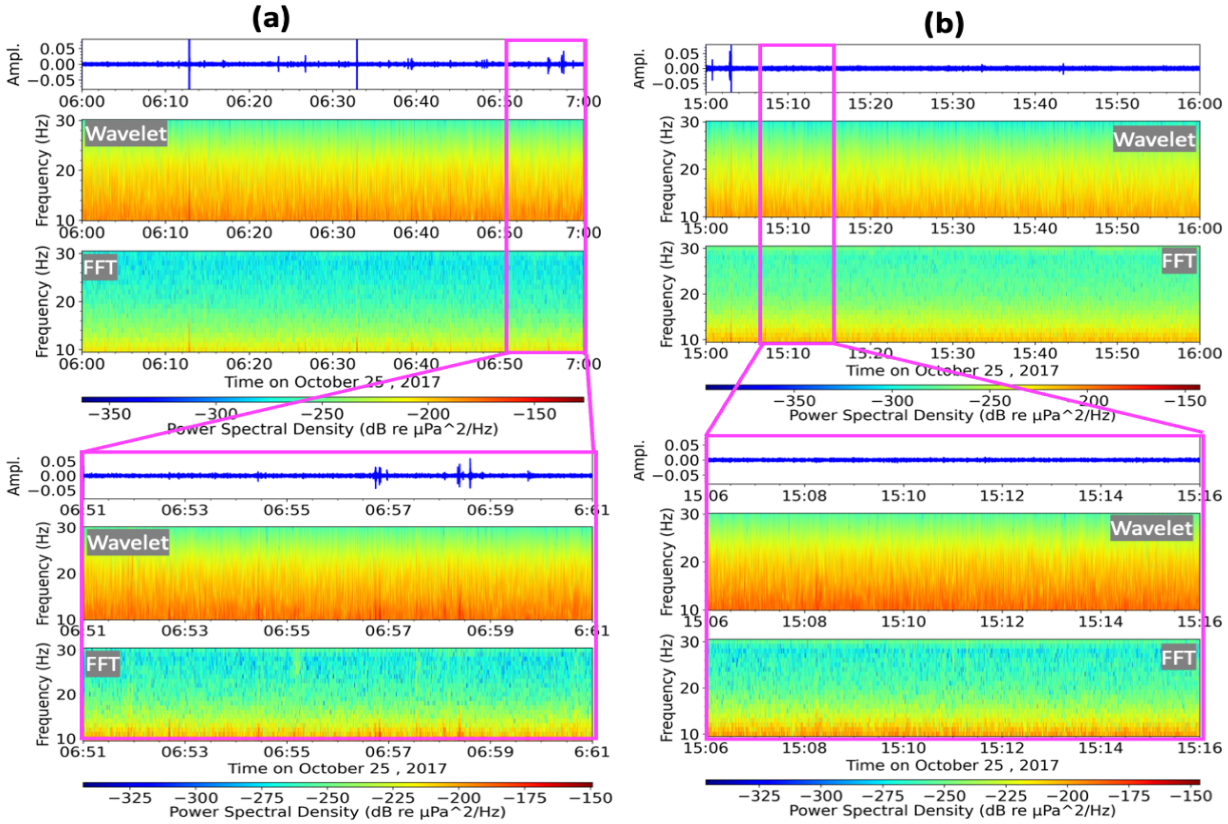


Figure 3.60. Low frequency spectrogram plots covering time period of October 25th, 2017 event detected by SSNAP-EQT. Top-left: 1-hour spectrogram plot of HYD1 data calculated with wavelet and FFT methods within time 06:00-07:00 UTC; Bottom-left: zoom-in of spectrogram after filtering, calculated with wavelet and FFT methods within time 15:00-16:00 UTC. Top-right: 1-hour spectrogram plot of HYD1 data calculated with wavelet and FFT methods within time 15:00-16:00 UTC; Bottom-right: zoom-in of spectrogram after filtering, calculated with wavelet and FFT methods.

In summary, examining seismic and hydroacoustic data from the period between September 1 and October 31, 2017, when it was deemed likely that the 16 known landslides had occurred, the analysis suggests that it is more likely that these events did not occur during these months. There is a possibility that these landslides occurred in November or December 2017, when higher levels of precipitation occurred (Figure 3.50). However, it is also possible that the landslides did occur within the September-October timeframe, but evaded detection by the SSNAP-EQT model. As mentioned previously, the 16 observed landslides appear small, mostly debris flow events. These types of landslides and other mass flow events generate weak seismic signals that may not be clearly captured by seismometers. These smaller landslides may be detectable only locally, if at all, posing difficulties for the SSNAP-EQT.

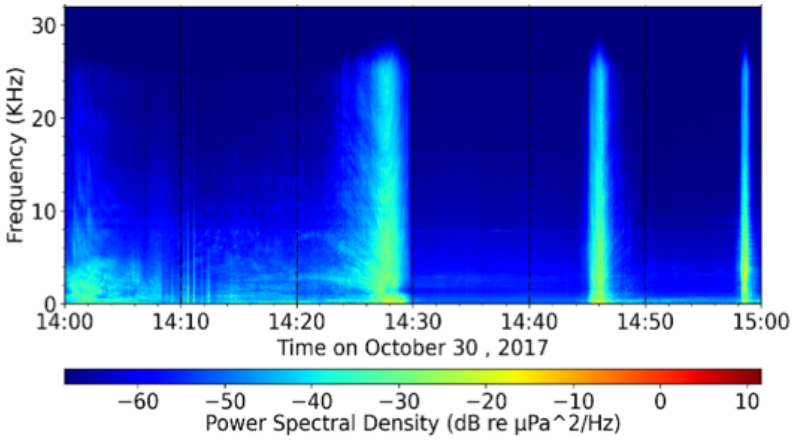


Figure 3.61. One-hour spectrogram plot of HYD1 data in high frequency without filtering, covering time period of two October 30th, 2017 SSNAP-EQT events.

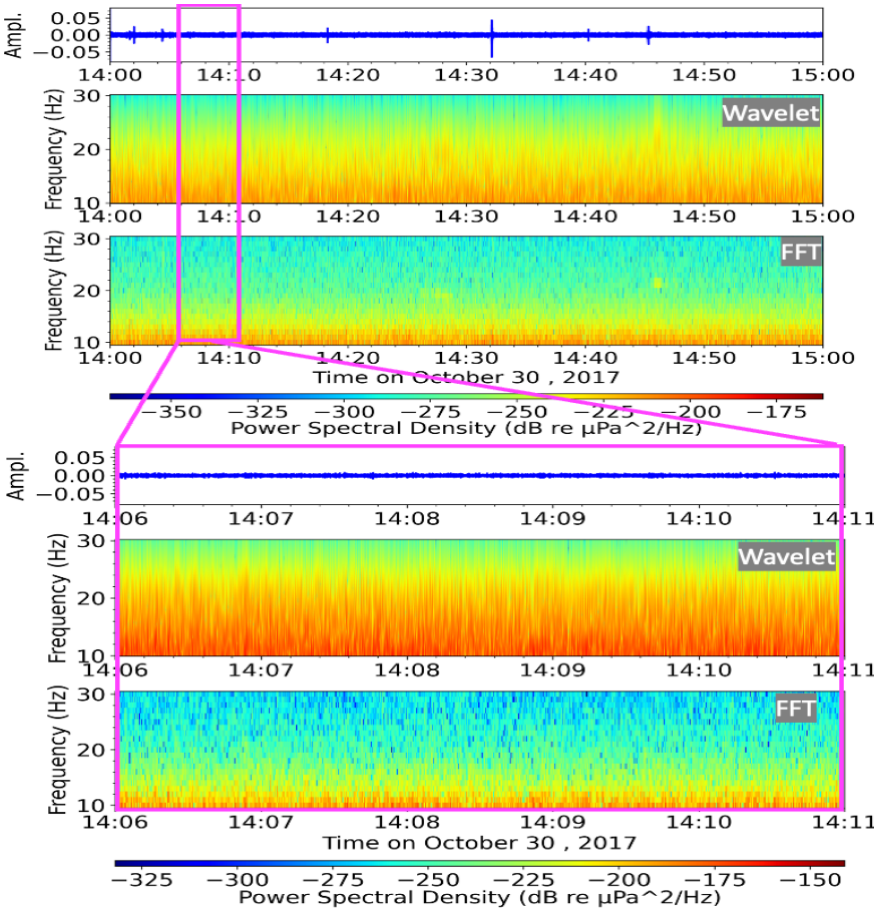


Figure 3.62. Low frequency spectrogram plots covering time period of October 30th, 2017 SSNAP-EQT event. Top: 1-hour filtered time series of hydroacoustic data; middle: 1-hour spectrogram plot of HYD1 data calculated with wavelet and FFT methods; bottom: zoom-in of spectrogram after filtering, calculated with wavelet and FFT methods.

#### 3.5.7.3 Pressure sensor output

Data for the September 1st, 2017 to February 28, 2018 timeframe from the bottom pressure sensor located near Kitamaat Village (PRS1, Table 3.4) were processed using the method outlined in Section 3.4.3.

The implementation algorithm is designed for water level monitoring and ultimately for tsunami detection, as illustrated in Figure 3.63. The procedure begins with obtaining raw pressure data from PRS1; Figure 3.63(a) shows the six-month time series. The next step involves eliminating the tidal signal, illustrated in Figure 3.63(b). Tidal removal significantly reduces the range of water level changes from thousands of centimeters to tens of centimeters. Tidal analysis is the process of evaluating periodic fluctuations in sea level (tides) throughout time. It entails analyzing tidal data obtained by the sensor in order to identify and interpret the components of the tidal signal. More specifically, in our study, pressure data with associated times are resampled every 10 minutes. The tidal coefficients are then calculated using the "ut-solv" function, which takes the resampled time and pressure data, as well as the latitude of the data collection point (Tables 3.2 and **Error! Reference source not found.**). Tidal coefficients are very useful for many coastal and m arine projects and are essential for comprehending tidal patterns in various locations. These coefficients, which are obtained via harmonic analysis of tidal data, are a measure of the amplitudes of the tidal components in relation to a standard reference level. The tidal signal is then predicted for each data point. Tidal reconstruction is calculated using the "ut_reconstr" function and the derived tidal coefficient. This approach enables the prediction of tidal behavior at specified sites and times, even in the absence of continuous tide gauge data. Tidal reconstruction has several uses, including navigation, coastal engineering, and environmental monitoring. Figure 3.63(b) illustrates residual water pressure data following removal of tidal signals. Figure 3.63(c) provides a closer look at the residual water pressure data which are converted to the water-level in cm. Tsunami detection relies on the residual signal with 5 minutes moving average; it is deemed significant when a water-level change surpasses the predetermined threshold, set at $\pm$3 cm in this study.

Given the suspected occurrence of 16 coastal landslides in the region sometime in September or October 2017 (Figure 3.6), it is possible that some of these events caused displacement water waves, at least locally. A thorough examination of the pressure sensor data including this time period was conducted to discern any anomalous water level changes. Notably, a total of eight discernible waves were identified within these two months near Kitamaat Village, surpassing the specified threshold of 3 cm (Figures 3.64, 3.65, and Table 3.16).

The analysis was then extended to cover four additional months from November 2017 to February 2018, inclusive; during this period, a total of five events were successfully detected as detailed in Figures 3.64, 3.65, and Table 3.16. As documented in the previous section, the seismic data were analyzed with SSNAP-EQT only for the months of September and October 2017, and also for five other days between November 2917 and February 2018 without any detection.

However, the NRCan earthquake catalog also does not include events in the region that are close in time to the water level events during the September 2017 to February 2018 period.

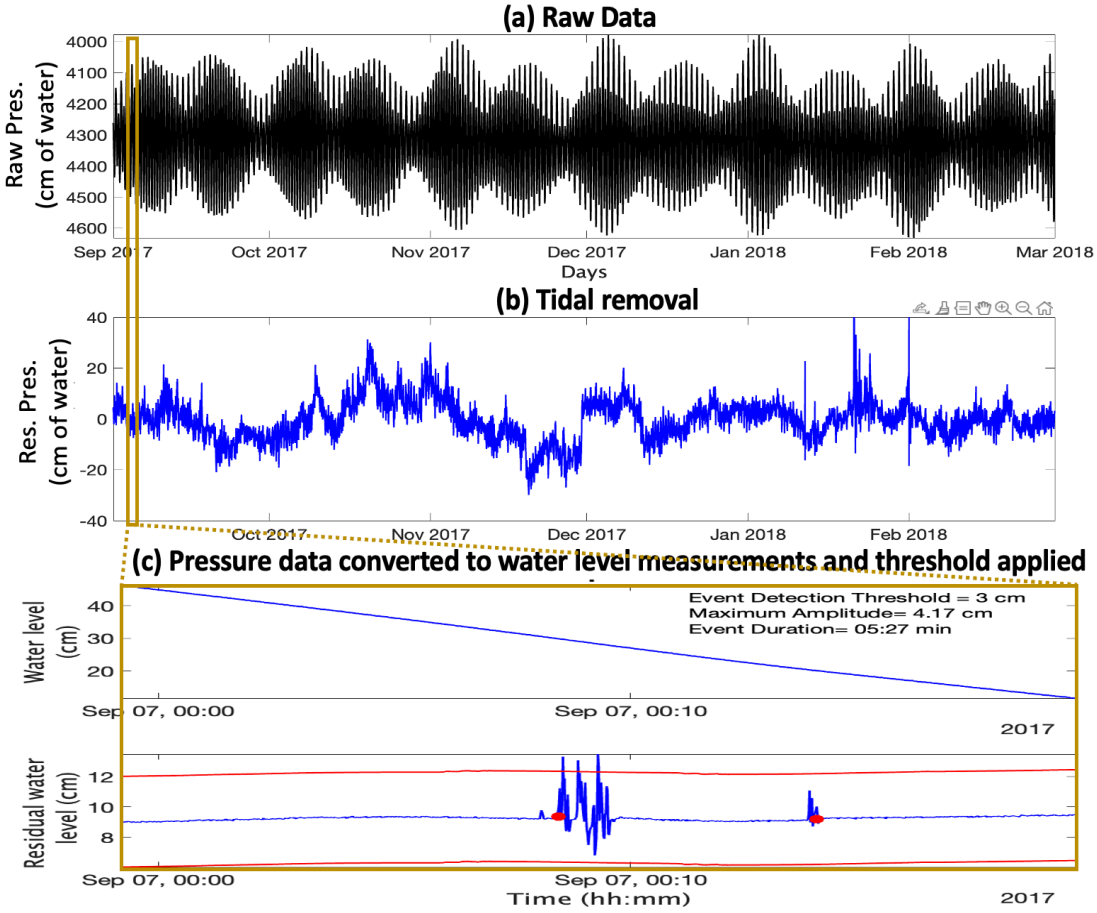


Figure 3.63. Processing of data from the PRS1 bottom pressure sensor near Kitamaat Village for the September 2017-February 2018 time period. (a) The dynamic range of raw pressure data over the 6-month time series; (b) the 6-month residual pressure time series following removal of tidal signals due to astronomical factors, such as the gravitational interactions between the Earth, Moon, and Sun; (c) example of a 20 sec residual time series for water level (blue line) monitoring exceeding the assigned threshold ( $\pm$3 cm) (red lines). Red bullets show the start and end of the detected water level changes surpassing the assigned thresholds.

To investigate the cause of these observed water level changes, I examined the spectrogram of the hydrophone data (both in high frequency (HF) and low frequency (LF)) and seismic data (Figures 3.66 and 3.67).

As illustrated in Figures 3.66 and 3.67, the LF spectrograms across all events do not exhibit any indications of signals that can clearly be attributable to landslides or microseismic earthquakes. Moreover, upon examining all waveforms and HF spectrograms of the PRS1 detected events, discernible signals emerge at specific times preceding wave detections at PRS1 (Table 3.16): September 6$^{th}$, 2017 at 23:43 UTC (preceding the 4.2 cm amplitude PRS1 event on September 7$^{th}$,

2017 at 00:08 UTC); September 12th, 2017 between 14:00 and 14:32 UTC; September 21st, 2017 at 21:08 UTC; January 31st, 2018 at 23:32 UTC; and February 13th, 2018 at 20:36 UTC.

Table 3.16. Detected events in pressure sensor data.

| Date | Detected time (hh:mm:ss) | Amplitude (cm) | Duration (mm:ss) |
|---|---|---|---|
| 2017-09-05 | 07:49:26 | 3.25 | 07:33 |
| 2017-09-07 | 00:08:53 | 4.17 | 05:27 |
| 2017-09-12 | 14:42:08 | 6.19 | 01:57 |
| 2017-09-12 | 23:35:04 | 4.88 | 00:04 |
| 2017-09-14 | 09:39:32 | 5.62 | 00:49 |
| 2017-09-21 | 05:11:11 | 5.33 | 01:08 |
| 2017-09-21 | 21:25:35 | 7.37 | 04:20 |
| 2017-10-23 | 19:17:56 | 6.76 | 08:13 |
| 2018-01-11 | 23:47:43 | 31.11 | 01:16 |
| 2018-01-13 | 21:05:54 | 15.35 | 00:44 |
| 2018-01-31 | 23:38:36 | 41.14 | 05:07 |
| 2018-02-13 | 20:59:19 | 10.97 | 08:06 |
| 2018-02-27 | 16:20:41 | 3.56 | 09:31 |

On average, the duration of water level changes for these events is ~5 minutes with highest wave amplitude as 41.14 cm on January 31st, 2018 and the lowest one on September 6th, 2017 (Figure 3.65 and Table 3.16). Given that none of these events were detected by the SSNAP-EQT codes nor reported in NRCEC, coupled with the lack of observed tremors at seismic stations and duration of the events, it can be inferred that vessel passage or weather condition may result in these water level changes.

Some additional events detected at PRS1 on September 12th, 14th, and 21st, 2017, as well as January 11th and 13th, 2018, with very short durations averaging approximately 48 seconds (Figure 3.65 and Table 3.16), may be attributed to other factors including marine animal movement in the water (like fish swimming up and down in the water).

Examining the events observed on October 23rd, 2017, and February 27th, 2018, characterized by respective durations of ~8.25 and 9.5 minutes and an respective amplitudes of about 6.8 cm and 3.6 cm (Figure 3.65 and Table 3.16), along with the presence of a continuous signal in the high-frequency spectrogram of hydroacoustic data, suggests a potential association with weather conditions such as wind or rain (Figure 3.50).

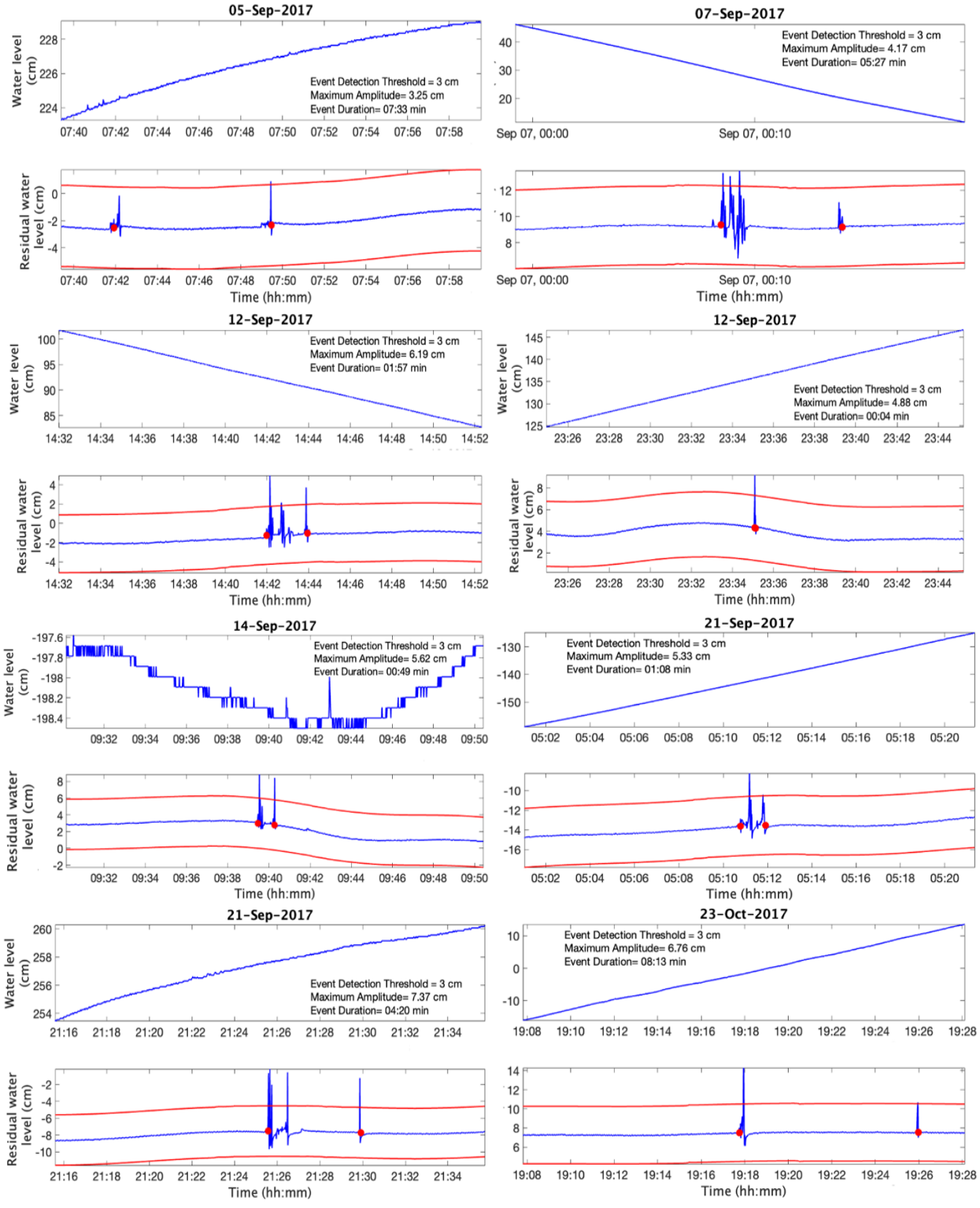


Figure 3.64. Raw and residual water level changes for events detected in Sept-Oct 2017 at the PRS1 pressure sensor near Kitamaat Village.

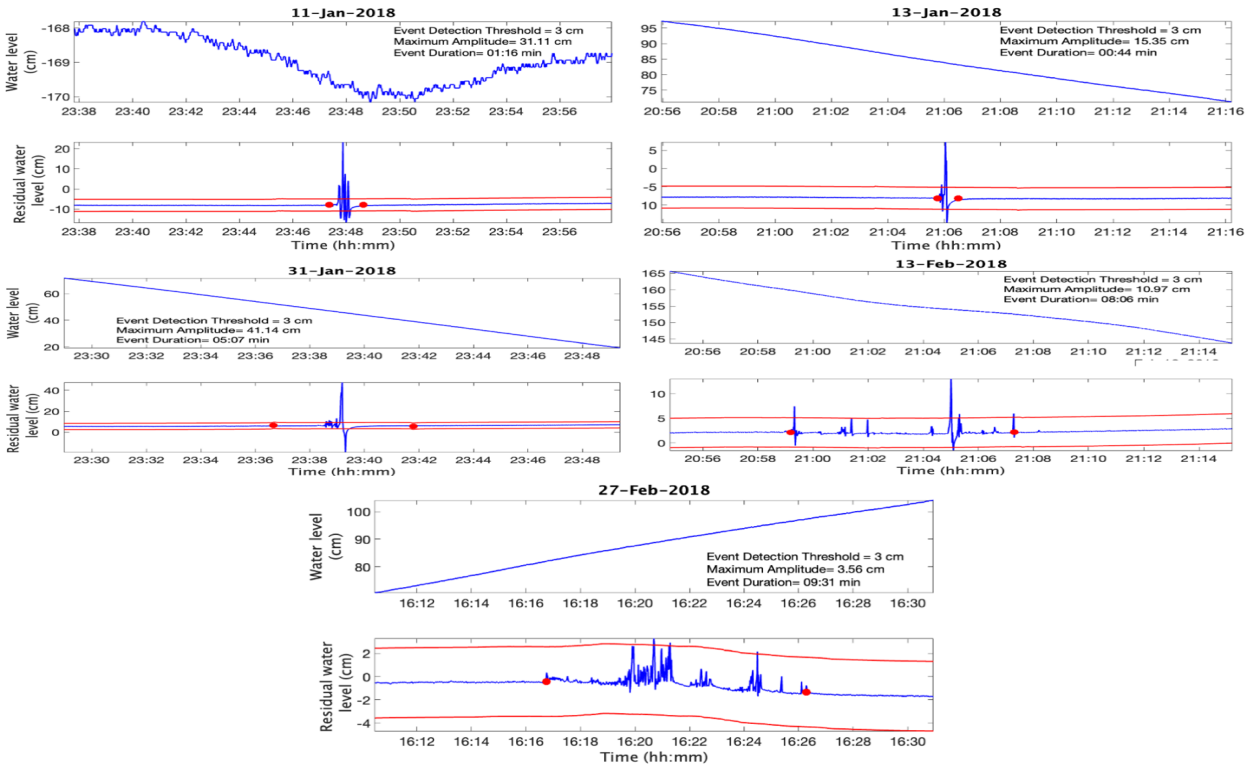


Figure 3.65. Raw and residual water level changes for events detected in Jan-Feb 2018 at the PRS1 pressure sensor near Kitamaat Village.

Two other events, detected on September 5th and 12th, 2017, exhibited amplitudes of 3.3 and 4.9 cm, respectively over respective durations of ~7.5 minutes and 4 seconds (Figure 3.65 and Table 3.16). Notably, no signals were detected in the LF spectrograms. However, for the times of both events a seismic signal similar to a landslide seismic signal was observed at nearby seismic station C8-KITB in Kitimat. The absence of signal in the hydrophone data and most of the seismic stations, coupled with no detection by the SSNAP-EQT model and no reports in the NRCEC, interpreting this event and pinpointing the source of the water level changes proved to be challenging.

Based on the analysis of the pressure sensor data, it appears that there are no corresponding events in the other instrumental datasets that align with the waves detected near Kitamaat Village. One possible explanation is that some of the detected events might be small tsunamis generated by landslides too small to capture on the seismic networks or hydrophone. Alternatively, these events may be too minor or distant from the Kitimat hydrophone to capture the signal effectively. Although some of the events detected in September and October 2017 could coincide with the timing of the 16 reported landslides, PRS1 is situated far from the locations of these landslides. So, it is also plausible that the landslides, being distant from Kitimaat Village, may not have generated waves large enough to be detected over a minimum distance of at least 32 km, considering the expected attenuation of the waves over such distances such that

any triggered waves may have dissipated below the 3-cm threshold before reaching the sensor. Alternatively, the detected waves could have originated from other local causes, such as boat activity, animal movements, or weather conditions.

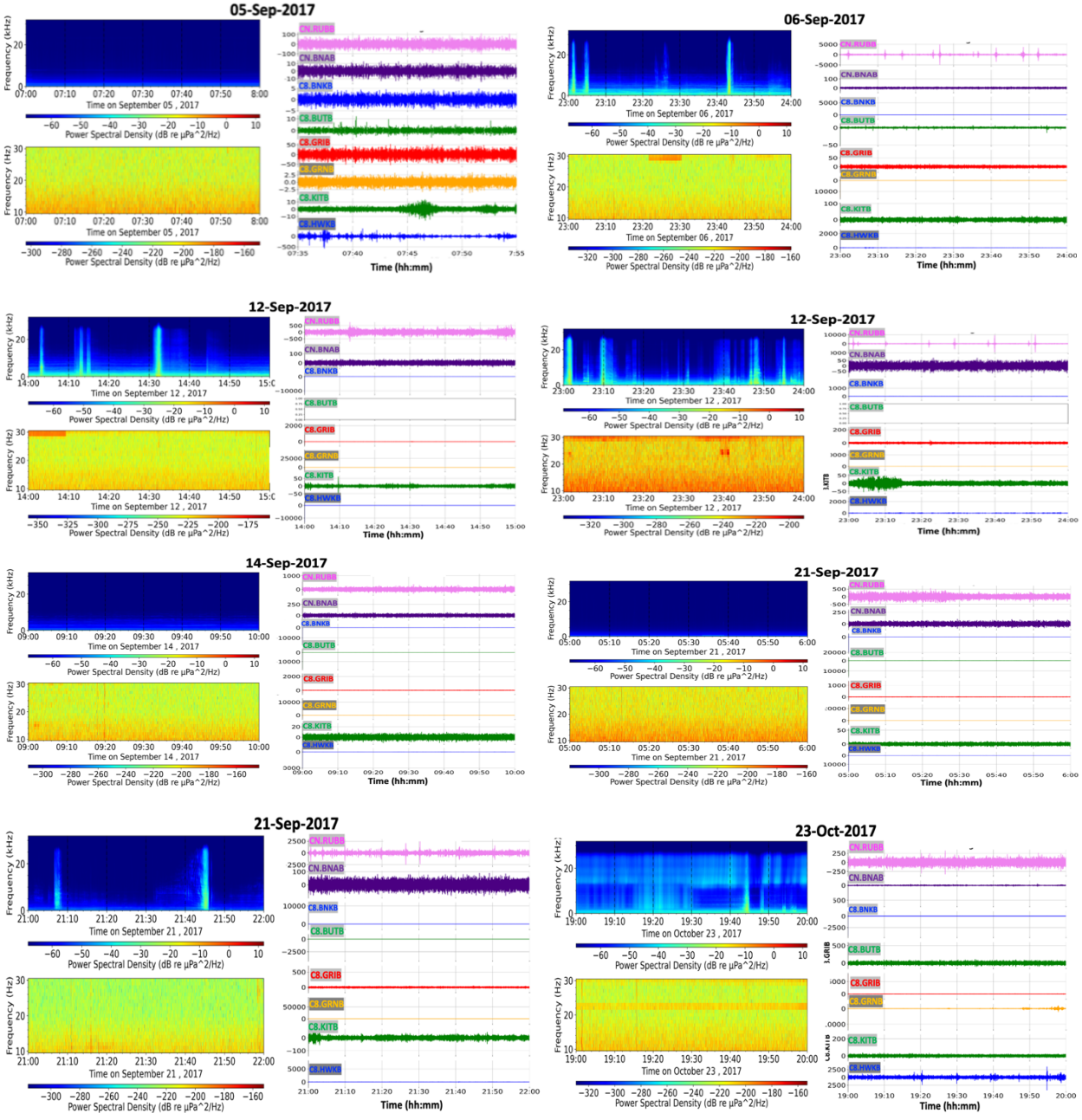


Figure 3.66. For each of 8 time periods in Sept-Oct 2017: (Top left) HF spectrogram of hydrophone data; (Bottom left) LF spectrogram of hydrophone data; (Right) waveform of seismic data for the same time periods, matching the timing of events detected in PRS1 pressure sensor data.

Based on the results obtained from the pressure sensor data, it is evident that the algorithm designed for monitoring water level changes, specifically for tsunami detection in the study area, is also somewhat sensitive to seismic activity or weather conditions in the vicinity. It is crucial to emphasize that the events detected by this algorithm do not inherently imply the occurrence of a tsunami in the study area.

In the initial phase of designing a tsunami detection and warning system, it is advisable to prioritize the analysis of events detected by pressure sensors. This approach ensures that these detected events can effectively serve as early warning notification – given the adequate instrumental coverage. To confirm whether the unusual waves detected in the study area are indeed tsunamis, additional verification through cross-referencing with other instrumental data is imperative. This includes checking seismic data and hydroacoustic data obtained from hydrophones.

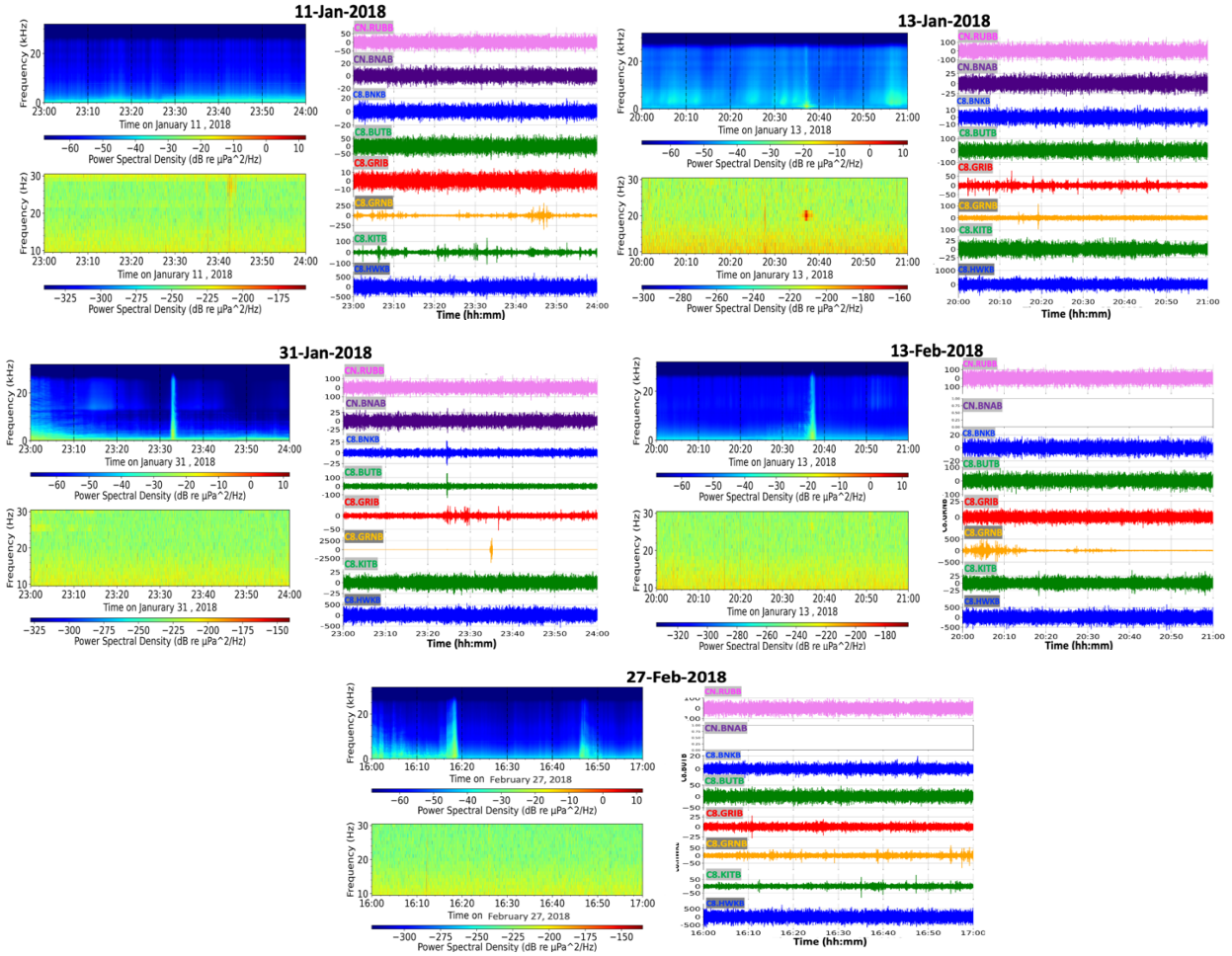


Figure 3.67. For each of 5 time periods in Jan-Feb 2018: (Top left) HF spectrogram of hydrophone data; (Bottom left) LF spectrogram of hydrophone data; (Right) waveform of seismic data for the same time periods, matching the timing of events detected in PRS1 pressure sensor data.

## 3.6 Conclusion

The study presented in this chapter delves into different types of instrumental data, encompassing seismic, hydroacoustic, and hydrostatic pressure data, with the aim of determining an optimal method for landslide and tsunami detection, providing a proof-of-concept with potential future application in tsunami early warning within the Douglas Channel study area.

In this study, I present a foundation for advancing understanding and knowledge in landslide signal detection through the integration of seismic and acoustic instrumental data. I also demonstrate the application of potential tsunami wave detection using bottom pressure data. The main findings from analysis of each data type are discussed in sections 3.6.1-3.6.3. Section 3.6.4 provides a brief discussion on landslide triggers in the study area. This is followed by suggestions for future work in section 3.6.5.

### 3.6.1 Seismic data analysis for detection and location of landslide signals

The capability to pinpoint when and where landslides occur, utilizing an onshore seismological network, has been significantly enhanced by integrating a Deep-Learning AI model known as EQT with the SSNAP model to form the SSNAP-EQT model. This advancement presents a transformative opportunity to address limitations in existing landslide catalogs and landslide hazard assessments. An improved understanding of landslide and associated tsunami hazards is crucial for the robust design of offshore and coastal engineering projects (such as oil and gas, renewables, and subsea cables), and to enable hazard mitigation for coastal communities, e.g., providing essential information for early tsunami warning and guiding civil response planning.

The application of the SSNAP-EQT model represents a novel methodology, combining the SSNAP and EQT models initially designed for earthquake detection (Tan et al., 2020; Mousavi et al., 2020). The integrated model has been adapted here for landslide detection, given the absence of readily available automated models for this purpose.

The outcomes derived from employing the SSNAP-EQT model demonstrate its effectiveness in detecting landslides and even microseismic earthquakes within computational grids. These results offer a valuable contribution to enhancing the NRCEC, which currently lacks the capability to distinguish between events as earthquakes or landslides. The proposed approach in this study facilitates the categorization of detected events based on their nature, such as landslides or earthquakes.

At this stage, it can be deduced that the algorithm applied to instrumental data exhibits a capability to identify substantial events, resulting in a comprehensive catalog of landslides and microseismic earthquakes. However, its efficacy is more pronounced in detecting landslides that generate significant seismic energy (with equivalent earthquake magnitude greater than 2), while it may exhibit limitations in capturing events that do not produce discernible seismic energy. Consequently, phenomena characterized by slow movement, such as creep-like activity, debris

flows, or small-scale landslides, may be less likely to trigger detections. This is exemplified by the 2017 landslide series, where the algorithm appears to have missed detecting 16 landslide events that were assumed to have occurred in the region in September or October 2017. However, there are a number of possible explanations including (1) the failures did not release sufficient seismic energy to be detected by the seismic network, or (2) the failures occurred later than October 2017. It is possible that a future systematic analysis of the seismic data from November 2017 to January 2018 could lead to detections of some of the documented landslides.

The limitations of the SSNAP-EQT model become evident due to the absence of a well-distributed seismic network, particularly on the east and north side of the study area. This lack of coverage poses challenges in accurately determining the timing and location of seismic events. The distance between the seismometer and an event location significantly impacts the precision of event detection in both space and time. Additionally, incomplete data availability from existing seismic stations adds another layer of complexity. Furthermore, the suitability of seismometers to capture T-phase events, essential for landslide detection, is a critical factor. Hence, the current seismic networks in the study area are not optimized for landslide detection. In conclusion, a comprehensive seismic station network with abundant data availability is crucial for enhancing the SSNAP-EQT model's capability to detect even minor events.

### 3.6.2 Hydroacoustic data analysis for the detection and characterization of landslide signals

The identification of signals over considerable distances highlights the potential efficacy of hydroacoustic methods in detecting landslides. An expanded hydrophone network could greatly enhance landslide and tsunami monitoring and early warning initiatives. The incorporation of hydroacoustic data into the analysis of data from an extensive seismic network offers promising prospects for enhancing hazard assessment and monitoring.

The single hydrophone employed in this study served as a validation tool for the outcomes obtained from SSNAP-EQT, ensuring the authenticity of the detected events within the study area. Landslides generate distinct acoustic signals that differ from those of earthquake events. Additionally, various sizes of landslide events produce diverse acoustic signatures, as detailed in Section 3.5. Consequently, analyzing spectrograms of the acoustic data provides insights into the size and type of landslide events.

Landslides generate T seismic waves, and hydrophones are better suited to recording this type of seismic wave compared to traditional seismic stations. Using the spectrogram of hydrophone data allows us to estimate the arrival time of seismic waves. Additionally, signals that exhibit consistent durations with similar interference patterns may reflect the occurrence of multiple landslides in close proximity. It's not uncommon for landslides to occur minutes apart during cluster events, or for one landslide to occur in phases. With an increased number of hydrophones, we could calculate the velocity and trajectory of a landslide by considering the time duration of

the hydroacoustic signal and the total predicted distance traveled by the landslide. A network of instruments could also be used to locate events, independently of (or in conjunction with) seismic instruments.

The alignment of detected events by the SSNAP-EQT model with spectrograms of hydroacoustic signals aids in classifying these events. Combining seismic and hydroacoustic data, analyzing seismic waveforms, reviewing hydrophone data spectrograms, and examining FFT plots for the frequency range of an event collectively assist in categorizing detected events as either earthquakes or landslides.

### 3.6.3 Pressure sensor data analysis for the detection of potential tsunami waves

The results from the pressure sensor data highlight the effectiveness of the algorithm designed to monitor changes in water levels, especially for detecting tsunamis in the study area. Although no tsunami waves occurred during the analyzed time period, several waves exceeding the 3-cm threshold were detected that likely resulted from passing boats or weather-related activity.

In the case of a tsunami, pressure sensor detections and measurements could provide critical early warning, particularly with a larger network of BPS instruments. To validate if the detected unusual waves in the study area correspond to an actual tsunami triggered by a landslide or earthquake, thorough cross-referencing with other instrumental datasets becomes essential. This entails scrutinizing seismic and hydroacoustic data.

### 3.6.4 Landslide triggers in the Douglas Channel region

Determining the triggers of mass failure events was not a primary objective of this study, but an understanding of triggering processes is essential to evaluating and mitigating the hazard of landslides and associated waves.

Upon investigating the landslides that occurred in the years 2022 and 2023, it becomes evident that precipitation plays a pivotal role as a triggering factor for landslides in the study area, as has been noted by previous studies. Consequently, following an intense rainfall event or a prolonged period of precipitation in the study region, a significant increase in the likelihood of landslide occurrences can be assumed.

Climate change is expected to lead to an increase in landslide occurrence in the region. Glacial retreat contributes both to increased ground saturation (and increased pore pressure) via meltwater, and to the destabilizing effect of de-buttressing on steep slopes. These factors may have played a role in the Sept 1$^{st}$, 2022 Ecstall River event discussed in section 3.5.3.

Proximity to major tectonic plate boundary faults means that strong ground shaking during periodic large earthquakes is another likely landslide trigger in the region, as implied by a significant increase in the number and area of mass failures in Haida Gwaii during and following the nearby 2012 M7.8 earthquake (Barth et al., 2020).

As assessment of the stability of submarine sediments requires an examination of the effects of low tides and pore pressure conditions, two elements that are critical in inducing potentially-tsunamigenic submarine mass failures. Variations in pore pressure weaken sediment layers, and low tides can increase instability by decreasing hydrostatic pressure. The destabilization of the slope by low tides and high pore pressures most likely contributed to the 1975 tsunamigeneic submarine failure in Kitimat.

### 3.6.5 Suggestions for future work

As shown in this study, seismometers and hydrophones demonstrate robust capabilities that can contribute to the development of comprehensive hazard catalogs. Given that tsunamigenic landslides tend to be large and to move relatively fast, generating more significant signals than most of the events detected during this study, the method provides a very promising step forward in landslide and tsunami detection across the study area, and will only be strengthened as broadband seismic, hydrophone, and pressure sensor networks are expanded and strategically distributed in Douglas Channel and Gardner Canal. The potential for future research and the development of an operational early landslide tsunami warning system in this area, and in other disparate geographic regions, lies in the expansion of instrumental networks and datasets. Additionally, the exploration of emerging techniques, such as fiber-optic sensing, holds promise for addressing crucial knowledge gaps associated with these significant phenomena.

Although we obtained promising results in detecting landslides that occurred in 2022 and 2023, it is imperative to further validate and refine these findings through complementary approaches, such as satellite imagery analysis or on-site field surveys. This validation process is essential for accurately documenting the method's true efficacy and identifying the specific types of landslides that can be consistently and reliably detected and characterized.

In conclusion, the detection of landslides and the establishment of potential early warning systems, similar to other advanced systems, hinge upon the application of sophisticated signal processing methodologies and specific parameters tailored to the real time detection and analysis of seismic and seismo-acoustic waves. A crucial aspect in achieving this objective is the development of algorithms, emphasizing the assessment of instrumental data to produce optimal results.

In future, it is possible that the SSNAP-EQT model could be further trained using the landslide waveforms from this and other studies, to enable automatic identification of events as landslides. The addition of hydroacoustic data, and associated training, could further improve the process.

# Chapter 4 Conclusions

This Ph.D. dissertation shares my findings from two studies focused on improving the understanding and mitigation of the hazard of landslide-generated tsunamis in coastal British Columbia. The region has a history of landslide tsunamis, and much of the coast is at risk of damage in future events, which remain poorly constrained. My PhD research has two main objectives: (1) to demonstrate the hazard of tsunami waves triggered by a large potential subaerial landslide in the Strait of Georgia, via numerical modeling, and (2) to develop a proof-of-concept landslide and tsunami detection system using a network of seismic, hydroacoustic, and bottom pressure instruments in the Douglas Channel region, towards a potential future early warning system. The main results and implications are summarized below.

## 4.1 Numerical modeling of landslide-generated tsunami waves in the Strait of Georgia

Chapter 2 presents a numerical analysis of the impacts of a potential subaerial landslide in the Strait of Georgia. The study uses dispersive numerical tsunami models (NHWAVE and FUNWAVE-TVD) to simulate tsunami waves generated by a large potential subaerial landslide on the steep NE coast of Orcas Island, Washington State, just south of the US/Canada border. The occurrence of large landslides in the past is evidenced by landslide deposits on the adjacent seafloor; such events could be triggered by strong ground shaking during large (M~7) earthquakes on the nearby Skipjack Island fault zone.

The simulations show that the subaerial landslide would generate tsunami waves with peak amplitudes of 15-20 meters, current speeds of up to 9 m/s, and wave periods of about 6.6-8 minutes. The modeled waves experience many reflections and significant dispersion due to their short wavelengths and the complex coastline and bathymetry in the Strait of Georgia. The most powerful waves and currents would occur at the shorelines adjacent to the failure on Orcas Island and opposite to it, near Lummi Bay. The modeling shows that Clark Island, which hosts a marine state park and campground, could be completely overwhelmed by massive waves within 2.5 minutes of the landslide.

Wave amplitudes rapidly attenuate with distance from the source due to the dispersion effect, geometric spreading, and transfer of tsunami energy in semi-enclosed areas. The simulated waves reach Lummi Bay in 8.5 minutes, the entrance of Boundary Bay in less than 12 minutes and arrive at Semiahmoo Bay, British Columbia, in less than 15 minutes. High runups and strong currents would affect Semiahmoo Bay, Birch Bay, and Neptune Beach at the southern end of the Boundary Bay region. In contrast, Point Roberts, Boundary Bay, and White Rock would experience lesser wave effects, with a maximum runup of up to 3.5 meters. However, such waves could still cause significant damage; studies have shown that coastal damage is possible even for tsunami

amplitudes as low as 0.5 meters, with more severe damage and inundation occurring for amplitudes or runup exceeding 1.5 meters (e.g., Whitmore et al., 2008).

The modeling findings underscore the potential for significant coastal impacts resulting from landslide-generated waves in the Strait of Georgia. Such waves would arrive with little to no warning, highlighting the need to incorporate their potential into tsunami hazard assessment and mitigation strategies in the region.

## 4.2 Landslide and tsunami detection in the Douglas Channel region

Chapter 3 investigates the use of instrumental data, including seismic, hydroacoustic, and hydrostatic pressure data, to determine an optimal method for landslide detection in the Douglas Channel region, with potential future application in a system to provide early warning of landslide-generated tsunami waves. The integration of seismic and acoustic instrumental data is presented as a foundation for advancing our understanding and knowledge in landslide signal detection.

A new landslide detection method was developed, by integrating a Deep-Learning AI model known as EQT with the pre-existing SSNAP earthquake detection model to form the SSNAP-EQT model. The model was tested using seismic waveform data from a network of up to 8 broadband seismic stations to determine if it could detect and locate a number of landslides that had been documented in the region in 2017, 2022 and 2023. The results from the SSNAP-EQT model demonstrate its effectiveness in detecting landslides and even microseismic earthquakes within computational grids. However, its efficacy is more pronounced in detecting landslides that generate significant seismic energy (with equivalent earthquake magnitude greater than 2), while it may exhibit limitations in capturing events that do not produce discernible seismic noise. This suggests that phenomena characterized by slow movement, such as creep-like activity, debris flows, or small-scale landslides, may be less likely to trigger detections. However, given that tsunamigenic landslides tend to be relatively large and fast-moving, the method demonstrates considerable promise.

Limitations of the SSNAP-EQT model largely result from the absence of a well-distributed seismic network, particularly on the east side of the study area. This lack of coverage poses challenges in accurately determining the timing and location of seismic events. The distance between the seismometers and an event location significantly impacts the precision of event detection in both space and time. Additionally, incomplete data availability from existing seismic stations adds another layer of complexity. The suitability of seismometers to capture T-phase events, essential for landslide detection, is another critical factor. Unfortunately, the current seismic networks in the study area are not optimized for landslide detection.

This study also investigated the potential use of hydrophone instruments in a landslide detection network, which could greatly enhance tsunami monitoring and modeling initiatives. Previous studies have highlighted the potential for hydroacoustic landslide signals to be identified

over considerable distances. Landslides generate distinct signals that differ from those of earthquake events. Only a limited amount of hydroacoustic data was available for this study, and from only one instrument, located near Kitimat. For this study, analysis of the hydrophone data served as a validation tool for the outcomes obtained from SSNAP-EQT, ensuring the authenticity of the detected events within the study area. Analysis of the spectrogram of the acoustic data provided insights into the size and duration of landslide events, and shows great potential in providing additional information to characterize the type and trajectory of mass failures. The study highlights that to optimize hydrophone use in landslide detection, it is necessary to obtain extensive data at high sample rates.

Limited data from one bottom pressure sensor deployed near Kitamaat Village were used to demonstrate an effective method to detect and measure potential tsunami waves. Although no tsunami waves occurred during the analyzed time period, several waves exceeding the 3-cm threshold were detected that may have resulted from passing boats or weather-related activity. Events detected by a pressure sensor can act as preliminary warnings, but a potential tsunami source should be validated through cross-referencing with other instrumental datasets. In this case, the single sensor was located at Kitimaat Village, near to the largest population centres in the region, such that wave detection would occur only as a tsunami was already impacting shorelines. To be useful in an early warning context, a larger network of bottom pressure sensors should be deployed such that potentially damaging waves could be detected minutes to tens of minutes before impacting populated regions.

While a series of along-channel BPSs can provide valuable data for detecting tsunamis, relying solely on them for a warning system may not be sufficient for several reasons: 1) Limited warning time for landslides: Unlike seismic and hydroacoustic signals, which can provide early indications of landslide activity, BPSs may only detect the resulting tsunami waves after they have been generated. Incorporating other detection methods can help capture the initial signs of landslide movements, enabling more timely warnings; 2) Installation and maintenance costs: Establishing and maintaining an along-channel array of BPSs can be expensive, requiring significant financial investment for equipment procurement, deployment, and ongoing maintenance. This cost factor may pose challenges, especially for regions with limited resources or funding constraints. 3) limited coverage: BPSs are typically deployed at specific locations, which means they have limited spatial coverage. This limitation can result in gaps in monitoring, making it difficult to detect tsunamis occurring outside the range of these sensors; 4) Detection delay: This method may result in a delay in detection, as it relies on the wave reaching the sensor location before being detected. This delay could impact the timeliness of warnings issued to coastal communities. 5) Incomplete information: While BPSs can provide information about the amplitude and timing of tsunami waves, they may not capture other important characteristics, such as location of source of tsunamis, which can be crucial for assessing the impact on specific coastal areas. 6) Redundancy and reliability: A comprehensive warning system typically incorporates multiple

detection methods to enhance redundancy and reliability. By relying solely on BPRs, the system may be more vulnerable to failures or malfunctions in individual sensors, leading to gaps in monitoring and potential false alarms or missed events.

The methods presented here provide a very promising step forward in landslide and tsunami detection across the study area. However, the study area, Douglas Channel, will face challenges in monitoring and detecting landslides and tsunami waves due to limited availability of submerged hydrophone and sparse land-based seismic instruments. Therefore, many small landslides, especially debris flows, will likely remain undetected. In the following, some suggestions for improving landslide and tsunami waves detections in the study area are provided:

1. Install seismometers in all directions of landslide-prone areas with a maximum spacing of approximately 100 km to enhance detection coverage.
2. Consider incorporating T-phase-optimized seismic stations on land to better capture the unique seismic and hydroacoustic wave characteristics typically associated with landslides.
3. While land-based seismometers are effective at detecting signals that travel through the ground, studies suggest that local Ocean-Bottom Seismometer (OBS) may outperform land-based networks by capturing weak seismic signals more efficiently. Therefore, integrating OBS could improve detection, particularly for debris flows, which often descend into water and produce small signals.
4. Given the lower attenuation of hydroacoustic signals compared to seismic signals, they can effectively capture landslide seismic events at far greater distances (up to ~500 km) compared to traditional seismic stations (~100 km). Furthermore, the hydrophone signal time series exhibit similarities waveforms recorded by seismometers, suggesting their potential utility in the SSNAP-EQT model. To enhance monitoring capabilities, I suggest prioritizing investment in additional hydrophones, particularly adding two more—one in Kemano and one south of Douglas Channel. Assuming continuous operation of the existing hydrophones in Kitimat and Hartley Bay, the larger network would ensure comprehensive detection of seismic sources, including relatively small landslides and debris flows.
5. Additionally, hydrophones in the study area should be strategically situated away from coastlines or docks to minimize noise interference, avoid potential landslide paths, and ensure a cleaner acoustic database, thereby reducing the risk of instrument loss or damage.
6. Seismic waves can also be converted into atmospheric waves. Atmospheric signals, especially those at infrasonic frequencies (<20 Hz), can propagate thousands of kilometers in the atmosphere (Garcés et al., 1998; Fee & Matoza, 2013). These types of signals have lower attenuation compared to hydroacoustic and especially seismic signals. Incorporating an instrument to capture atmospheric signals emphasizes the

feasibility of coordinated monitoring across varying distances and detection of different types of seismic sources.

7. Due to challenges in recording reliable signals with a single pressure sensor in shallower regions of the study area, compounded by noise from coastal effects such as harbor resonance, nonlinear effects, refractions, and scattering, bottom pressure sensors may not be reliable for detecting tsunamis in fjords due to picking up waves produced by other sources. The algorithm is proven to be sensitive to waves exceeding 3 cm. However, such waves may result from non-tsunami sources, necessitating cross-validation with other instrumental data. Installing pressure sensors in Kemano and at the entrance of the Douglas Channel is a secondary priority, aiding in the detection of landslide/earthquake-generated waves. The detection of water level changes due to tsunami sources can be enhanced if an along-channel array of bottom pressure sensors is installed. This will allow the detection of phase propagation, distinguishing between propagating waves and atmospherically induced events. Detection could be especially efficient if the sensors were moored mid-channel, with land-based fiber optic connections.
8. A large of landslide-generated tsunami scenarios should be modelled in advance, in order to improve early warning and enable timely decisions. Although instrumental detection of landslides and triggered waves could provide several minutes of warning before the arrival of waves to communities, the potential run-up, inundation, and impacts would be known without comparison to modelled scenarios (e.g., as demonstrated in Chapter 2).
9. There is potential to enhance the SSNAP-EQT model through the inclusion of landslide waveforms from various research endeavors, to enable automated event classification as landslides.
10. Additionally, by integrating hydroacoustic data with associated training, further improvements to this process could be realized.
11. Fiber optic sensing offers a promising avenue for enhancing landslide detection methodologies. By leveraging the unique properties of optical fibers, such as their ability to detect subtle changes in strain, temperature, and acoustic signals, fiber optic sensing systems can provide real time monitoring of ground conditions. This technology allows for the continuous surveillance of potential landslide-prone areas, enabling early warning systems to be deployed effectively. Additionally, fiber optic sensors can be deployed in challenging terrain and harsh environments, providing comprehensive coverage in remote or inaccessible regions. Integrating fiber optic sensing into landslide detection frameworks could significantly improve the accuracy and reliability of early warning systems (Murray et al., 2022).

The monitoring approach mentioned above has the potential to enhance early warning systems by identifying and detecting likely landslides and landslide-generated-tsunamis and tracking the ensuing wave dynamics.

# Bibliography


Abadie, S., Harris, J., Grilli, S., & Fabre, R. (2012). Numerical modeling of tsunami waves generated by the flank collapse of the Cumbre Vieja Volcano (La Palma, Canary Islands): Tsunami source and near field effects. Journal of Geophysical Research: Oceans, 117(C5), 66, https://doi.org/10.1029/2011JC007646.

Abadie, S., Morichon, D., Grilli, S., & Glockner, S. (2010). Numerical simulation of waves generated by landslides using a multiple-fluid Navier_Stokes model. Coastal Engineering, 57(9), 779–794, https://doi.org/10.1016/j.coastaleng.2010.03.003.

Abdalzaher, M., Krichen, M., Yiltas-Kaplan, D., Ben Dhaou, I., & Adoni, W. Y. (2023). Early detection of earthquakes using IoT and cloud infrastructure: a survey. Sustainability, 15 (15), 11713, https://doi.org/10.3390/su151511713.

Allen, R. (1978). Automatic earthquake recognition and timing from single traces. Bulletin of the Seismological Society of America, 68(5), 1521-1532.

Allen, R. (1982). Automatic phase pickers: Their present use and future prospects. Bulletin of the Seismological Society of America, 72(6B), S225-S242.

Allstadt, K., Malone, S., Vidale, J., Bodin, P., & Steele, B. (2014). Seismic signals generated by the Oso landslide. Pacific Northwest Seismic Network Summary, 26 March 2014. Available at: https://wa.water.usgs.gov/data/SeismicReport-OsoLandslide.pdf.

Allstadt, K., Matoza, R., B. Lockhart, A., Moran, S., Caplan-Auerbach, J., M. Haney, M., Thelen, W., & Malone, S. (2018). Seismic and acoustic signatures of surficial mass movements at volcano. Journal of Volcanology and Geothermal Research, 364(0377-0273), 76-106, https://doi.org/10.1016/j.jvolgeores.2018.09.007.

Altinok, Y., Alpar, B., Ersoy, S., & Yalciner, A. (1999). Tsunami generation of the Kocaeli Earthquake (August 17, 1999) inthe Izmit Bay, coastal observations, bathymetry and seismic data. Turkish Journal of Maritime and Marine Sciences, 5, 131–148.

Amante, C., Mullan, S., Love, M., Rankin, M., Carignan, K., Moore, T., Hastings, N., LeVeque, R., Amouzegar, R. Grivault, N., Moore, C., Garrison-Laney, C., & Titov, V. (2020). Canada-United States elevation mode collaboratio to improve tsunami inundation mapping. AGU 2020 Fall meeting, Abstract NH0140008.

Anderson, P. S., & Gow, G. (2004). Tsunamis and coastal communities in British Columbia: an assessment of the BC tsunami warning system and related risk reduction practices. Publication prepared for Public Safety an Emergency Preparedness Canada. Available at: https://epe.lac-bac.gc.ca/100/200/301/psepcsppcc assessment_bc_tsunami-e/ps4-13-2004e.pdf.

Aránguiz, R., Caama.o, D., Espinoza, M., G.mez, M., Maldonado, F., Sep.lveda, V., Rogel, I., Oyarzun, J., & Duhart P. (2023). Analysis of the cascading rainfall–landslide–tsunami event of June 29th, 2022, Todos los Santo Lake, Chile. Landslides, 20(4), 801–811, https://doi.org/10.1007/s10346-022-02015-1.

Arrowsmith, S., Johnson, J., Drob, D., & Hedlin, M. (2010). The seismoacoustic wavefield: a new paradigm in studying geophysical phenomena. Reviews of Geophysics, 48(4), https://doi.org/10.1029/2010rg000335.

Baillard, C., Crawford, W., Ballu, V., Hibert, C., & Mangeney, A. (2014). An automatic kurtosis-based P- and S-phase picker designed for local seismic networks. Bulletin of the Seismological Society of America, 104, 394–409, https://doi.org/10.1785/0120120347.

Ballu, V., Ammann, J., Pot, O., de Viron, O., Sasagawa, G. S., Reverdin, G., Bouin, M., Cannat, M., Deplus, Ch. Deroussi S., Maia, M., & Diament, M. (2009). A seafloor experiment to monitor vertical deformation at the Lucky Strike volcano, Mid-Atlantic Ridge. Journal of Geodesy, 83(2), 147–159.

Barrie, J., & Greene, H. (2018). The Devils mountain fault zone: an active Cascadia upper plate zone o deformation Pacific northwest of north America. Sedimentary Geology, 364, 228-241, https://doi.org/10.1016/j.sedgeo.2017.12.018.

Barth, S., Geertsema, M., Bevington, A., Bird, A., Clague, J., Millard, T., Bobrowsky, P., Hasler, A., & Liu, H. (2020) Landslide response to the 27 October 2012 earthquake (MW 7.8), southern Haida Gwaii, British Columbia Canada. Landslides, 17, 517–526, https://doi.org/10.1007/s10346-019-01292-7.

Baum, R., Coe, J., Godt, J., Harp, E. L., Reid, E., Savage, W. Z., Schulz, W., Brien, D.,Chleborad, A., McKenna, J., Michael, J. A. (2005). Regional landslide-hazard assessment for Seattle, Washington, USA. Landslides, 2, 266–279, https://doi.org/10.1007/s10346-005-0023-y.

Bernard, E. (1998). Program aims to reduce impact of tsunamis on Pacific states. Eos Transactions American Geophysical Union, 79(22), 262–263, https://doi.org/10.1029/98EO00191.

Biffard, B., Morgan, M., Muzi, L., Dakin, T., & Buren, P. V. (2022). An integrated hydrophone calibration system for ocean observing: ONC HydroCal. OCEANS 2022, Hampton Roads, Hampton Roads, VA, USA, 1-5, doi:10.1109/OCEANS47191.2022.9976955.

Blais-Stevens, A., & Septer, D. (2008). Historical accounts of landslides and flooding events along the sea to sky corridor, British Columbia, from 1855-2007. Geological Survey of Canada, Open File 5741, 117, https://doi.org/10.4095/224755.

Blais-Stevens, A., Behnia, P., & Castagner, A. (2018). Historical landslides that have resulted in fatalities in Canada (1771–2018). Geological Survey of Canada, Open File 8392, https://doi.org/10.4095/308393.

Blenman, P. (2023). Examining the feasibility of Sentinel-1 InSAR data for landslide monitoring and failure forecasting in western Canada. MSc thesis, University of Victoria, BC, 96p.

Blondel, P., Dell, B., & Suriyaprakasam, C. (2020). Acoustic signatures of shipping, weather and marine life: comparison of NE Pacific and Arctic Soundscapes. In Proceedings of Meetings on Acoustics, 40(1), 070011, https://doi.org/10.1121/2.0001312.

Bohnenstiehl, D., Tolstoy, M., Dziak, R., Fox, C., & Smith, D. (2002). Aftershock sequences in the mid-ocean ridge environment: An analysis using hydroacoustic data. Tectonophysics, 354(1-2), 49-70, https://doi.org/10.1016/S0040-1951(02)00289-5.

Bornhold, B., Harper, J., McLaren, D., & Thomson., R. (2007). Destruction of the First Nations village of Kwalate by a rock avalanche-generated tsunami. Atmosphere-Ocean, 45(2), 123–128, https://doi.org/doi:10.3137/ao.450205.

Bornhold, B., Rabinovich, A., Fine, I., Kulikov, E., & Thomson, R. (2004). Landslide-generated tsunamis and their risk in coastal areas. GéoQuébec 2004, 57th Canadian Geotechnical Conference 5th joint CGS/IAH-CNC Conference, Session 7G, 28-33.

Brillon, C., Cassidy, J. F., Nykolaishen, L., Allen, T. I., Bednarski, J. M., Greene, P., Bobrowsky, P., & Huntley, D. (2018). Assessment of seismic hazards in British Columbia's north coast region (2013-2018). Geological Survey of Canada, Open File 8461, 19, https://doi.org/10.4095/313286.

Brodsky, E., Gordeev, E., & Kanamori, H. (2003). Landslide basal friction as measured by seismic waves. Geophysical Research letters, 30, 2236, 1–5, doi:10.1029/2003GL0184852236.

Bryan, G., Truchan, M., & Ewing, J. (1963). Long-range SOFAR studies in the south Atlantic ocean. Journal of the Acoustical Society of America, 35, 273–278.

Byun, D., & Hart, D. (2019). On robust multi-year tidal prediction using T_tide. Ocean Science Journal, 54, 657–671, https://doi.org/10.1007/s12601-019-0036-4.

Canadian Hydrographic Service. (2022). Canadian tide and current tables, Volume 5: Juan de Fuca Strait and Strait of Georgia. Catalogue No Fs73-5/2022-PDF, ISBN 978-0-660-40395-3, 135.

Caplan-Auerbach, J., Fox, C., & Duennebier, F. (2001a). Hydroacoustic detection of submarine landslides on Kilauea volcano. Geophysical Research Letters, 28(9), 1811-1813.

Caplan-Auerbach, J., & Duennebier, F. (2001b). Seismic and acoustic signals detected at Loihi Seamount by the Hawaii UnderseaGeo-Observatory. Geochemistry Geophysics Geosystems, 2(1525-2027), p. 17, https://doi.org/10.1029/2000GC000113.

Caplan-Auerbach, J., Dziak, R., Bohnenstiehl, D., Chadwick, W., & Lau, T. (2014). Hydroacoustic investigation of submarine landslides at West Mata volcano, Lau Basin. Geophysical Research Letters, 41(16), 5927-5934.

Carignan, K., Mullan, S., Rankin, M., Douglas, K., Moore, T., Hastings, N., & Love, M. (2019). Cross-border DEM workshop collaboration for coastal flood hazard mitigation in the Salish Sea. AGU 2019 Fall Meeting, Abstract PA51E-0931.

Casalbore, D., Clare, M. A., Pope, E., Quartau, R., Bosman, A., Chiocci, F. L., & Santos, R. (2021). Bedforms on the submarine flanks of insular volcanoes: new insights gained from high resolution seafloor surveys. Sedimentology, 68, 1400–1438, https://doi.org/10.1111/sed.12725.

Casalbore, D., Passeri, F., Tommasi, P., Verrucci, L., Bosman, A., Romagnoli, C., & Chiocci, F. L. (2020). Small-scale slope instability on the submarine flanks of insular volcanoes: the case-study of the Sciara del Fuoco slope (Stromboli). International Journal of Earth Sciences (Geol. Rundsch), 109, 2643-2658, https://doi.org/10.1007/s00531-020-01853-5.

Caston, M. (2021). Tsunamigenic potential of crustal faults in the southern Strait of Georgia and Boundary Bay. MSc thesis, University of Victoria, BC, http://hdl.handle.net/1828/13351.

Chadwick, W. J., Dziak, R., Haxel, J., Embley, R., & Matsumoto, H. (2012). Submarine landslide triggered by volcanic eruption recorded by in situ hydrophone. Geology, 40(1), 51-54.

Chadwick, W. J., Nooner, S. L., Zumberge, M. A., Embley, R. W., & Fox, C. G. (2006). Vertical deformation monitoring at Axial Seamount since its 1998 eruption using deep-sea pressure sensors. Journal of Volcanology and Geothermal Research, 150(1), 313–327, https://doi.org/10.1016/j.jvolgeores.2005.07.006.

Chadwick, W. J., Rubin, K., Merle, S., Bobbitt, A., Kwasnitschka, T., & Embley, R. (2019). Recent eruptions between 2012 and 2018 discovered at West Mata submarine volcano (NE Lau Basin, SW Pacific) and characterized by new ship, AUV, and ROV data. Frontiers in Marine Science, 6, 495, https://doi.org/10.3389/fmars.2019.00495.

Chadwick, W. J., Wright, I., Schwarz-Schampera, U., Hyvernaud, O., Reymond, D., & de Ronde, C. (2008). Cyclic eruptions and sector collapses at Monowai submarine volcano, Kermadec arc: 1998-2007. Geochemistry, Geophysics, Geosystems, 9, https://doi.org/10.1029/2008GC002113.

Chaytor, J., Baldwin, W., Bentley, S., Damour, M., Jones, D., Maloney, J., Minor, M., Obelcz, J., & Xu, K. (2020). Short- and long-term movement of mudflows of the Mississippi River Delta Front and their known and potential impacts on oil and gas infrastructure. Geological Society, London, Special Publications, 500(1), 587-604.

Chen, Z., Zhang, B., Han, Y., Zuo, Z., & Zhang, X. (2014). Modeling accumulated volume of landslides using remote sensing and DTM data. Remote Sensing, 6(2), 1514–1537, https://doi.org/10.3390/rs6021514.

Cherniawsky, J., Titov, V., Wang, K., & Li, J. (2007). Numerical Simulations of tsunami waves and currents for southern Vancouver Island from a Cascadia megathrust earthquake. Pure and Applied Geophysics, 164, 465–492, https://doi.org/10.1007/s00024-006-0169-0.

Chierici, F., Embriaco, D., & Pignagnoli, L. (2017). A new real-time tsunami detection algorithm. Journal of Geophysical Research, Oceans, 122, 636–652. doi:10.1002/2016JC012170.

Chierici, F., Iannaccone, G., Pignagnoli, L., Guardato, S., Locritani, M., Embriaco, D., Donnarumma, G., odgers, M., Malservisi, R., & Beranzoli, L. (2016). A new method to assess long-term sea-bottom vertical displacement in shallow water using a bottom pressure sensor: application to Campi Flegrei, Southern Italy. Journal of Geophysical Research: Solid Earth, 121, 7775–7789, https://doi.org/10.1002/2016JB013459.

Chuang, L., Peng, Z., Lei, X., Wang, B., Liu, J., Zhai, Q., & Tu, H. (2023). Foreshocks of the 2010 Mw 6.7 Yushu, China earthquake occurred near an extensional step-over. Journal of Geophysical Research: Solid Earth, 128(1), e2022JB025176.

Clague, J. J. (2002). The earthquake threat in southwestern British Columbia: a geologic perspective. Natural Hazards, 26(1), 7–33, https://doi.org/10.1023/A:1015208408485.

Clague, J., & Orwin, J. (2005). Tsunami hazard to north and west Vancouver, British Columbia. Centre for Natural Hazards Research, Simon Fraser University, Burnaby, BC. Available at: http://www.nsemo.org/sites/default/files/files/NSEMOreport.pdf.

Clague, J., Bobrowsky, P., & Hutchinson, I. (2000). A review of geological records of large tsunamis at Vancouver Island, British Columbia, and implications for hazard. Quaternary Science Reviews, 19(9), 849-863, https://doi.org/10.1016/S0277-3791(99)00101-8.

Clague, J., Munro, A., & Murty, T. (2003). Tsunami hazard and risk in Canada. Natural Hazards, 28 (2-3), 435–463, https://doi.org/10.1023/A:1022994411319.

Clare, M.A., Lintern, G., Pope, E., Baker, M., Ruffell, S., Zulkifli, M.Z., Simmons, S., Urlaub, M., Belal, M. and Talling, P.J. (2024). Seismic and acoustic monitoring of submarine landslides. In Noisy Oceans (eds G. Bayrakci and F. Klingelhoefer), https://doi.org/10.1002/9781119750925.ch5.

Clarke, G., Jarosch, A., Anslow, F., Radić, V., & Menounos, B. (2015). Projected deglaciation of western Canada in the twenty-first century. Nature Geoscience, 8(5), 372–377, https://doi.org/10.1038/ngeo2407.

Codiga, D. (2011). Unified tidal analysis and prediction using the UTide Matlab functions. Technical Report 2011-01. Graduate School of Oceanography, University of Rhode Island, RI., 59. ftp://www.po.gso.uri.edu/ pub/downloads/codiga/pubs/2011Codiga-UTide-Report.pdf.

Comfort, L., Znati, T., Voortman, M., & Freitag, L. (2012). Early detection of near-field tsunamis using underwater sensor networks. Science of Tsunami Hazards, 31(4), 231-243.

Conway, K., & Barrie, J. (2015). Large submarine slope failures and asso-ciated Quaternary faults in Douglas Channel, British Columbia. Geological Survey of Canada, Current Research 2015-9, 12, https://doi.org/10.4095/297316.

Conway, K., Barrie, J., & Thomson, R. (2012). Submarine slope failures and tsunami hazard in coastal British Columbia: Douglas Channel and Kitimat Arm. Geological Survey of Canada, Current Research, 2012-10, 17, https://doi.org/10.4095/291732.

Crockett, R. G., Perrier, F., & Richon, P. (2010). Spectral-decomposition techniques for the identification of radon anomalies temporally associated with earthquakes occurring in the UK in 2002 and 2008. Natural Hazards Earth System Sciences, 10, 1079–1084, https://doi.org/10.5194/nhess-10-1079-2010.

Crone, T., & Bohnenstiehl, D. (2019). Acoustic evidence of a long-lived gas-driven submarine volcanic eruption in the Bismarck Sea. Geophysical Journal International, 217(1), 169–178, https://doi.org/10.1093/gji/ggy542.

de Groot-Hedlin, C., Hedlin, M., & Drob, D. (2010). Atmospheric variability and infrasound monitoring. In Infrasound Monitoring for Atmospheric Studies, Springer: Dordrecht, 475–507.

Deparis, J., Jongmans, D., Cotton, F., Baillet, L., Thouvenot, F., & Hantz, D. (2008). Analysis of rock-fall and rock-fall avalanche seismograms in the French Alps. Bulletin of the Seismological Society of America, 98(4), 1781-1796.

Di Roberto, A., Rosi, M., Bertagnini, A., Marani, M., & Gamberi, F. (2010). Distal turbidites and tsunamigenic landslides of Stromboli volcano (Aeolian Islands, Italy). In Submarine Mass Movements and Their Consequences. Springer, Dordrecht (pp. 719-731).

Dietz, R., & Sheehy, M. (1954). Transpacific detection of Myojin volcanic explosions by underwater sound. Geological Society of America Bulletin, 65(10), 941–956, https://doi.org/10.1130/0016-7606(1954)65[941:tdomve]2.0.co;2.

Dokht, R., Kao, H., Visser, R., & Smith, B. (2019). Seismic event and phase detection using time–frequency representation and convolutional neural networks. Seismological Research Letters, 90(2A), 481–490, https://doi.org/10.1785/0220180308.

Dunbar, D., & Harper, J. (2009). Numerical simulation of tsunamigenic submarine slope failure in the Fraser River delta, British Columbia. Marine Geodesy, 16(2), 101–108, https://doi.org/10.1080/15210609309379682.

Dunbar, P., & Weaver, C. (2015). U.S. states and territories national tsunami hazard assessment: historical record and sources for waves. Technical Report, pub. National Oceanic and Atmospheric Administration (NOAA), Federal Government Series, 38, http://pubs.er.usgs.gov/publication/70159744.

Dziak, R., & Fox, C. (2002). Evidence of harmonic tremor from a submarine volcano detected across the Pacific Ocean basin. Journal of Geophysical Research, 107(B5), ESE-1, https://doi.org/10.1029/2001jb000177.

Dziak, R., Bohnenstiehl, D., Baker, E., Matsumoto, H., Caplan-Auerbach, J., Embley, R. W., Merle, S., Walker, S., Lau. T., & Chadwick Jr, W. (2015). Long-term explosive degassing and debris flow activity at West Mata submarine volcano. Geophysical Research Letters, 42, 1480–1487, https://doi.org/10.1002/2014GL062603.

Earthquakes Canada. (2021). National Earthquake Database. Retrieved Mar 2023, from https://www.earthquakescanada.nrcan.gc.ca/stndon/NEDB-BNDS/bulletin-en.php.

Environment and Climate Change Canada. (2024). Daily total precipitation for August 2022. Retrieved Aug 01, 2023, from https://climate.weather.gc.ca/climate_data/generate_chart_e.html.

European Parliament and the Council of the European Union. (2008). Directive 2008/56/EC of the European Parliament and of the Council of 17 June 2008 establishing a framework for community action in the field of marine environmental policy (Marine Strategy Framework Directive). Official Journal of the European Union L 164, 25.6, 19–40, http://data.europa.eu/eli/dir/2008/56/oj.

Evans, S. (1989). The 1946 Mount Colonel Foster rock avalanche and associated displacement wave, Vancouver Island, British Columbia. Canadian Geotechnical Journal, 26(3), 447-452.

Evans, S., & Clague, J. (1994). Recent climatic change and catastrophic geomorphic processes in mountain environments. In Geomorphology and Natural Hazards, 10, 107-128, https://doi.org/10.1016/0169-555X(94)90011-6.

Ewing, M., Woollard, G., Vine, A., & and Worzel, J. (1946). Recent results in submarine geophysics. Geological Society of America Bulletin, 57(10), 909–934, https://doi.org/10.1130/0016-7606(1946)57[909:rrisg]2.0.co;2.

Eyles, N. (1987). Late Pleistocene debris-flow deposits in large glacial lakes in British Columbia and Alaska. Sedimentary Geology, 53(1-2), 33-71.

Fan, N., Nian, T., Jiao, H., Guo, X., & Zheng, D. (2020). Evaluation of the mass transfer flux at interfaces between submarine sliding soils and ambient water. Ocean Engineering, 216, 108069, https://doi.org/10.1016/j.oceaneng.2020.108069.

Farge, M. (1992). Wavelet transforms and their applications to turbulence. Annual Review of Fluid Mechanics, 24(1), 395-458.

Fee, D., & Matoza, R. (2013). An overview of volcano infrasound: from Hawaiian to Plinian, local to global. Journal of Volcanology and Geothermal Research, 249, 123–139, https://doi.org/10.1016/j.jvolgeores.2012.09.002.

Feng, Z. (2011). The seismic signatures of the 2009 Shiaolin landslide in Taiwan. Natural Hazards and Earth System Sciences, 11, 1559-1569, https://doi.org/10.5194/nhess-11-1559-2011.

Feng, Z., Shen, Z., & Zhuang, R. (2021). A Numerical investigation of the characteristics of seismic signals induced by rockfalls. Frontiers in Earth Science (9: 761455), 12, https://doi.org/10.3389/feart.2021.761455.

Fine, I., & Thomson, R. (2020). Numerical simulation of a Cascadia Subduction Zone tsunami with application to Boundary Bay in the southern Strait of Georgia. Report prepared for Defence Research and Development Canadas Centre for Security Science (DRDC CSS) Program (CSSP), Coastal flood mitigation Canada CSSP-2018-CP-2352, 34.

Fine, I., Cherniawsky, J., Rabinovich, A., & Stephenson, F. (2008). Numerical modeling and observations of tsunami waves in Alberni Inlet and Barkley Sound, British Columbia. Pure and Applied Geophysics, 165, 2019–2044, https://doi.org/10.1007/s00024-0080414-9.

Fine, I., Rabinovich, A., Thomson, R., & Kulikov, E. (2003). In A. Yalçiner, E. Pelinovsky, E. Okal, & C. Synolakis, Numerical modeling of tsunami generation by submarine and subaerial landslides. Submarine Landslides and Tsunamis. (Vol. 21, pp. 69-88). NATO Science Series, https://doi.org/10.1007/978-94-010-0205-9_9.

Fornaciai, A., Favalli, M., & Nannipieri, L. (2019). Numerical simulation of the tsunamis generated by the Sciara del Fuoco landslides (Stromboli Island, Italy). Science Report, 9, 18542, https://doi.org/10.1038/s41598-019-54949-7.

Fox, C., Dziak, R., Matsumoto, H., & Schreiner, A. (1994). Potential for monitoring low-level seismicity on the Juan de Fuca Ridge using fixed Hydrophone arrays. Marine Technology Society, 27(4), 22–30.

Friele, P., Millard, T., Mitchell, A., Allstadt, K., Menounos, B., Geertsema, M., & Clague, J. (2020). Observations on the May 2019 Joffre Peak landslides, British Columbia. Landslides, 17(4), 913–930, https://doi.org/10.1007/s10346-019-01332-2.

Fritz, H., Hager, W., & Minor, H. (2004). Near field characteristics of landslide generated impulse waves. Journal of Waterway, Port, Coastal, and Ocean Engineering, 130(6), 287-302, https://doi.org/10.1061/ (ASCE)0733-950X(2004)130:6(287).

Galitzin, P. (1915). Sur le tremblement de terre du 18 de février 1911. Comptes Rendus de l'Academie des Sciences de Paris, 160, 810–813.

Gao, D., Wang, K., Insua, T., Sypus, M., & Sun, T. (2018). Defining megathrust tsunami source scenarios for northernmost Cascadia,. Natural Hazards, 94, 445–469, https://doi.org/10.1007/s11069018-3397-6.

Garcés, M., Hansen, R., & Lindquist, K. (1998). Travel times for infrasonic waves propagating in a stratified atmosphere. Geophysical Journal International, 135(1), 255–263.

Gariano, S., & Guzzetti, F. (2016). Landslides in a changing climate. Earth science Reviews, 162, 227–252, https://doi.org/10.1016/j.earscirev.2016.08.011.

Gasperini, L., Zaniboni, F., Armigliato, A., Tinti, S., Pagnoni, G., Özeren, M., Ligi, M., Natali, F., & Polonia, A. (2022). Tsunami potential source in the eastern Sea of Marmara (NW Turkey), along the north Anatolian fault system. Landslides, 19(10), 2295-2310, https://doi.org/10.1007/s10346-022-01929-0.

Geertsema, M., Clague, J., Schwab, J., & Evans, S. (2006a). An overview of recent large catastrophic landslides in northern British Columbia, Canada. Engineering Geology, 83, 120-143, https://doi.org/10.1016/j.enggeo.2005.06.028.

Geertsema, M., Cruden, D., & Schwab, J. (2006b). A large rapid landslide in sensitive glaciomarine sediments at Mink Creek, northwestern, British Columbia, Canada. Engineering Geology, 83, 36-63, https://doi.org/10.1016/j.enggeo.2005.06.036.

Geertsema, M., Menounos, B., Bullard, G., Carrivick, J., Clague, J., Dai, C., Donati, D., Ekstrom, G., Jackson, J., Lynett, P., Pickier, M., Pon, A., Shugar, D., Stead, D., Del Bel Belluz, J., Friele, P., Giesbrecht, I., Heathfield, D., Millard, T., & Sharp, M. (2022). The 28 November 2020 landslide, tsunami, and outburst flood—A hazard cascade

associated with rapid deglaciation at Elliot Creek, British Columbia, Canada. Geophysical Research letters, 49, e2021GL096716, https://doi.org/10.1029/2021GL096716.

Germain, D., Roy, S., & Jose Teixera Guerra, A. (2022). Empirical rainfall thresholds for landslide occurrence in Serra do Mar, Angra dos Reis, Brazil. Landslides. IntechOpen, http://dx.doi.org/10.5772/intechopen.100244.

Glimsdal, S., L'Heureux, J., Harbitz, C., & Løvholt, F. (2016). The 29th January 2014 submarine landslide at Statland, Norway-landslide dynamics, tsunami generation, and run-up. Landslides, 13(6), 1435–1444, https://doi.org/10.1007/s10346-016-0758-7.

Goff, J. B., Huntley, D., Sawai, Y., & Tanagawa, K. (2020). Paleotsunamis along Canada's Pacific coast. Quaternary Science Reviews, 237, 106309, https://doi.org/10.1016/j.quascirev.2020.106309.

Gong, J., & Fan, W. (2022). Seismicity, fault architecture, and slip mode of the westernmost Gofar transform fault. Journal of Geophysical Research: Solid Earth, 127(11), 22, https://doi.org/10.1029/2022JB024918.

Government of Canada. (2023). Historical Climate Data - British Columbia. Environment and Climate Change Canada. Retrieved June 2023, from https://climate.weather.gc.ca/climate_data/daily_data_e.html?hlyRange=%7C&dlyRange=1951-08-01%7C2024-02-04&mlyRange=1951-01-01%7C2007-02-01&StationID=396&Prov=BC&urlExtension=_e.html&searchType=stnName&optLimit=yearRange&StartYear=1840&EndYear=2024&selRow.

Green, D., Evers, L., Fee, D., Matoza, R., Snellen, M., & Smets, P. e. (2013). Hydroacoustic, infrasonic and seismic monitoring of the submarine eruptive activity and sub-aerial plume generation at South Sarigan, May 2010. Journal of Volcanology and Geothermal Research, 257, 31-43.

Greene, H. (2019). Orcas Island landslide failures (image), In: Salish seafloor mapping identifies earthquake and tsunami risks. Seismological Society of America News Release, last access: 11 Jan 2022, https://www.eurekalert.org/news-releases/461113.

Greene, H., Barrie, J., & Todd, B. (2018). The Skipjack Island fault zone: an active transcurrent structure within the upper plate of the Cascadia subduction complex. Sedimentary Geology, 378, 61–79, https://doi.org/10.1016/j.sedgeo.2018.05.005.

Grigoli, F., Cesca, S., Krieger, L., Kriegerowski, M., Gammaldi, S., Horalek, J., Priolo, E., & Dahm, T. (2016). Automated microseismic event location using master-event waveform stacking. Scientific Reports, 6(1), 25744.

Grilli, S., & Watts, P. (1999). Modeling of waves generated by a moving submerged body: applications to underwater landslides, Engineering Analysis with Boundary Elements. 23(8), 645–656, https://doi.org/10.1016/S0955-7997(99)00021-1.

Grilli, S., & Watts, P. (2005). Tsunami generation by submarine mass failure. I: modeling, experimental validation, and sensitivity analyses. Journal of Waterway, Port, Coastal, and Ocean Engineering, 131(6), 283–297, https://doi.org/10.1061/(ASCE)0733950X(2005)131:6(283).

Grilli, S., Harris, J., Tajalli Bakhshi, T., Masterlark, T., Kyriakopoulos, C., Kirby, J., & Shi, F. (2013). Numerical simulation of the 2011 Tohoku tsunami based on a new transient fem co-seismic source: comparison to far-and near-field observations. Pure and Applied Geophysics, 170, 1333–1359, https://doi.org/10.1007/s00024-012-0528-y.

Grilli, S., O'Reilly, C., Harris, J., Tajalli Bakhsh, T., Tehranirad, B., Banihashemi, S., Kirby, J., Baxter, Ch., Eggeling, T., Ma, G., & Shi, F. (2015). Modeling of SMF tsunami hazard along the upper U.S. east coast: detailed impact around Ocean City, MD. Natural Hazards, 76(2), 705–746, https://doi.org/10.1007/s11069-014-15228.

Grilli, S., Shelby, M., Grilli, A., Guerin, C., Grosdidier, S., & Insua, T. (2016). Algorithms for tsunami detection by high frequency radar: development and case studies for tsunami impact in British Columbia, Canada, Proceedings of International Offshore and Polar Engineering Conference, 807-814.

Grilli, S., Tappin, D., Carey, S., Watt, S., Ward, S., Grilli, A., Engwell, S., Zhang, Ch., Kirby, J., Schambach, L., & Muin, M. (2019). Modelling of the tsunami from the December 22, 2018 lateral collapse of Anak Krakatau volcano in the Sunda Straits. Indonesia Science Report, 9(1), 11946, https://doi.org/10.1038/s41598-019-48327-6.

Guthrie, R. (2013). Socio-economic significance, Canadian technical guidelines and best practices related to landslides: a national initiative for loss reduction. Geological Survey of Canada, Open File 7311, 19, doi:10.4095/292241.

Guthrie, R., Friele, P., Allstadt, K., Roberts, N., Evans, S., Delaney, K., Roche, D., Clague, J., & Jakob, M. (2012). The 6 August 2010 Mount Meager rock slide-debris flow, Coast Mountains, British Columbia: characteristics,

dynamics, and implications for hazard and risk assessment. Natural Hazards and Earth System Sciences, 12(5), 1277-1294.

Guthrie, R., Mitchell, S., Lanquaye-Opoku, N., & Evans, S. (2010). Extreme weather and landslide initiation in coastal British Columbia. Quarterly Journal of Engineering Geology and Hydrogeology, 43(4), 417–428, doi: https://doi.org/10.1144/1470-9236/08-1.

Hamilton, T., & Wigen, S. (1987). The Foreslope Hills of the Fraser Delta: implications for tsunamis in Georgia Strait. Science of Tsunami Hazards, 5, 15–33.

Harbitz, C., Glimsdal, S., Løvholt, F., Kveldsvik, V., Pedersen, G., & Jensen, A. (2014). Rockslide tsunamis in complex fjords: from an unstable rock slope at Åkerneset to tsunami risk in western Norway. Coastal Engineering, 88, 101-122, http://dx.doi.org/10.1016/j.coastaleng.2014.02.003.

Heesemann, M., Insua, T., Scherwath, M., Juniper, K., & Moran, K. (2014). From geohazards research laboratories to smart ocean systems. Oceanography Society, 27(2), 151–153.

Heidarzadeh, M., & Gusman, A. (2018). Application of Dense Offshore Tsunami Observations from Ocean Bottom Pressure Gauges (OBPGs) for tsunami research and early warnings. In Geological Disaster Monitoring Based on Sensor Networks (Chap. 2, pp. 1–16). Singapore: Springer (https://doi.org/10.1007/978-981-13-0992-2_2).

Heidarzadeh, M., & Satake, K. (2015). Source properties of the 1998 July 17 Papua New Guinea tsunami based on tide gauge records. Geophysical Journal International, 202(1), 361–369, https://doi.org/10.1093/gji/ggv145.

Heller, V., & Hanger, W. (2010). Impulse product parameter in landslide generated impulse waves. Journal of Waterway, Port, Coastal, and Ocean Engineering, 136(3), 145, https://doi.org/10.1061/(ASCE)WW.1943-5460.0000037.

Hermanns, R., Sepu;veda, S., Lastras, G., Amblas, D.; Canals, M., Azpiroz, M., Bascunan, I., Calafat, A., Duhart, P., Frigola, J., Iglesias, O., Kemps, Ph., Lafuerza, S., Longva, O., Micallef, A., Oppikofer, Th., Rayo, Z., Vargas, G., Molina, F. (2014). Earthquake-triggered subaerial landslides that caused large scale fjord sediment deformation: combined subaerial and submarine studies of the 2007 Ays.n Fjord event, Chile. In G. Lollino, A. Manconi, J. Locat, Y. Huang, & M. Canals Artigas (Eds.), Engineering Geology for Society and Territory-Volume 4 (pp. 67-70). Cham: Springer.

Higman, B., Shugar, D., & Stark, C. (2018). The 2015 landslide and tsunami in Taan Fiord, Alaska. Science Report, 8, 12993, https://doi.org/10.1038/s41598-018-30475-w.

Hincks, T., Sparks, R., & Aspinall, W. P. (2011). Tsunami hazard and risk. Risk and Uncertaintity Assessment for Natural Hazards, 9781107006, 317–363, doi:10.1017/CBO9781139047562.011.

Hodgson, E. (1946). British Columbia earthquake, June 23, 1946. Journal of the Royal Astronomical Society of Canada, 40, 285-319.

Hu, G., Li, L., Ren, Z., & Zhang, K. (2023). The characteristics of the 2022 Tonga volcanic tsunami in the Pacific Ocean. Natural hazards and Earth System Sciences, 23(2), 675-691.

Huang, N., & Wu, Z. (2008). A review on Hilbert-Huang transform: Method and its applications to geophysical studies. Reviews of Geophysics, 46, 2,(1971), 1–23, https://doi.org/10.1029/2007RG000228.

Huang, N., Shen, Z., Long, S., Wu, M., Shih, H., Zheng, Q., Ye, N., Tung, C., & Liu, H. (1998). The empirical mode decomposition and the Hilbert spectrum for nonlinear and non-stationary time series analysis. Proceedings of the Royal Society A, 454, 903-999, https://doi.org/10.1098/rspa.1998.0193.

Huhn, K., Arroyo, M., Cattaneo, A., Clare, M. A., Gràcia, E., Harbitz, C., Krastel, S., Kopf, A., Løvholt, F., Rovere, M., Strasser, M., Talling, P., & Urgeles, R. (2019). Modern submarine landslide complexes: a short review. In K. Ogata, A. Festa, & G. Andrea Pini (Eds.), Submarine Landslides Subaqueous mass Transportation Deposits Outcrops Seismic Profiles 15, 181-200, https://doi.org/10.1002/9781119500513.ch12.

Hungr, O., Evans, S., Bovis, M., & Hutchinson, J. (2001). Review of the classification of landslides of the flow type. Environmental and Engineering Geoscience, VII (3), 221–238, doi: 10.2113/gseegeosci.7.3.221.

Huntley, D., Bobrowsky, P., Goff, J., Chagué, C., Stead, D., Donati, D., & and Mariampillai, D. (2018). Extending the terrestrial depositional record of marine geohazards in coastal NW British Columbia. Geological Society, London, Special Publications, 477.

Huntley, D., Rotheram, D., Bobrowsky, P., Lintern, G., MacLeod, R., & Brillon, C. (2020). InSAR investigation of sackung-like features and debris flows in the vicinity of Hawkesbury Island and Hartley Bay, British Columbia, Canada. In PM Dight (Ed.), Slope Stability 2020: Proceedings of the 2020 International Symposium

on Slope Stability in Open Pit Mining and Civil Engineering, Australian Centre for Geomechanics, Perth, 207-226, https://doi.org/10.36487/ACG_repo/2025_09.

Igarashi, Y., Hori, T., Murata, S., Sato, K., Baba, T., & Okada, M. (2016). Maximum tsunami height prediction using pressure gauge data by a Gaussian process at Owase in the Kii Peninsula, Japan. Marine Geophysical Research, 37, 361–370, https://doi.org/10.1007/s11001-016-9286-z.

Imamura, F., & Gica, E. (1996). Numerical model for tsunami generation subaqueous landslide along a coast. Science of Tsunami Hazards, 14(1), 13–28.

Imamura, F., Hashi, K., & Imteaz, M. (2001). Modeling for tsunamis generated by landsliding and debris flow. In Tsunami Research at the End of a Critical Decade, Springer, Dordrecht, 209-228, https://doi.org/10.1007/978-94-017-3618-3_15.

Insua, T., Moran, K., McLean, S., Moore, T., Heesemann, M., Pirenne, B., Gao, D., Hoeberechts, J., Salomomsson, P., Coady, Y., Leonard, L., & Wang, K. (2015). Advancing tsunami detection: the Ocean Networks Canada Tsunami Project. In Proceedings of the 11th Canadian Conference on Earthquake Engineering, 10.

Ioualalen, M., Asavanant, J., Kaewbanjak, N., Grilli, S., Kirby, J., & Watts, P. (2007). Modeling the 26 December 2004 Indian Ocean tsunami: case study of impact in Thailand. Journal of Geophysical Research: Ocean, https://doi.org/10.1029/2006JC003850, 112(C7).

IRIS. (2023). IRIS (Incorporated Research Institutions for Seismology), IRIS Data Services - DataSelect Web Service. Retrieved Mar 2023, from https://service.iris.edu/fdsnws/dataselect/1/.

Iwasaki, S., Furumoto, A., & and Honza, E. (1996). Can be a submarine landslide be considered as a tsunami source? Science of Tsunami Hazards, 14(2), 89–100.

Jackson, L. H., Jermyn, C., Conway, K., & Kung, R. (2008). Annotated images of submarine landslides and related features generated from swath multibeam bathymetry, Howe Sound, British Columbia. [online] Available from: http://geogratis.gc.ca/api/en/nrcan45 rncan/ess-sst/89e0f897-071f-564f-9fef-82ab5ac37019.html.

Jackson, L., Blais-Stevens, A., Hermanns, R., & Jermyn, C. (2014). Late glacial and Holocene sedimentation and investigation of fjord tsunami potential in lower Howe Sound, British Columbia. In: Lollino, G., Manconi, A., Locat, J., Huang, Y., Canals Artigas, M. (eds) Engineering Geology for Society and Territory – Volume 4. Springer, Cham, https://doi.org/10.1007/978-3-319-08660-6_12.

Jakob, M., & Lambert, S. (2009). Climate change effects on landslides along the southwest coast of British Columbia. Geomorphology (107(3-4)), 275-284.

Jakob, M., & Weatherly, H. (2003). A hydroclimatic threshold for landslide initiation on the North Shore Mountains of Vancouver, British Columbia. Geomorphology, 54(3-4), 137-156.

Jakob, M., Holm, K., Lange, O., & Schwab, J. (2006). Hydrometeorological thresholds for landslide initiation and forest operation shutdowns on the north coast of British Columbia. Landslides, 3, 228–238, https://doi.org/10.1007/s10346-006-0044-1.

Jeffreys, S. (1923). The Pamir earthquake of 18 February 1911, in relation to the depths of earthquake foci. Monthly Notices of the Royal Astronomical Society, Supplement 1, 22–31, https://doi.org/10.1111/j.1365-246X.1923.tb06566.x.

Johns, M., Prior, D., Bornhold, B. C., & Bryant, W. R. (1985). Geotechnical aspects of a submarine slope failure, Kitimat Fjord, British Columbia. Marine Geotechnology, 6 (3), 243–279, https://doi.org/10.1080/10641198609388190.

Johns, M., Prior, D., Bornhold, B., Coleman, J., & Bryant, W. (1986). Geotechnical aspects of a submarine slope failure, Kitimat Fjord, British Columbia. Marine Georesources & Geotechnology, 6(3), 243-279.

Johnson, S., Dadisman, S., Mosher, D., Blakely, R., & Childs, J. (2001). Active tectonics of the Devils Mountain fault and related structures, northern Puget Lowland and eastern Strait of Juan de Fuca region, Pacific Northwest, U.S. Geological Survey Professional Paper, 1643, 65 text, 2 tables, 38 figs., 2 plates.

Kaneda, Y., Kawaguchi, K., Araki, E., Matsumoto, H., Nakamura, T., Nakano, M., Kamiya, S., Ariyoshi, K., Baba, T., Ohori, M., Takahashi, N., & Hori, T. (2009). Dense Ocean Floor Network for Earthquakes and Tsunamis; DONET/ DONET2, Part2 Development and data application for the mega thrust earthquakes around the Nankai trough. AGU Fall Meeting Abstracts, 90.

Kao, H., Kan, C., Chen, R., Chang, C., Rosenberger, A., Shin, T., & Liang, W. (2012). Locating, monitoring, and characterizing typhoon-linduced landslides with real-time seismic signals. Landslides, 9, 557-563, https://doi.org/10.1007/s10346-012-0322-z.

Karlin, R., Holmes, M., Abella, S., & Sylwester, R. (2004). Holocene landslides and a 3500-year record of Pacific northwest earthquakes from sediments in Lake Washington. Geological Society of America Bulletin, 116(1-2), 94-108.

Kelsey, H., Sherrod, B., Blakely, R., & Haugerud, R. (2012). Holocene faulting in the Bellingham forearc basin: upper-plate deformation at the northern end of the Cascadia subduction zone. Journal of Geophysical Research, 17, B03409, doi:10.1029/2011JB008816.

Kirby, J., Shi, F., Nicolsky, D., & Misra, S. (2016). The 27 April 1975 Kitimat, British Columbia, submarine landslide tsunami: a comparison of modeling approaches. Landslides, 13, 1421-1434, https://doi.org/10.1007/s10346-016-0682-x.

Kirby, J., Shi, F., Tehranirad, B., Harris, J., & Grilli, S. (2013). Dispersive tsunami waves in the ocean: model equations and sensitivity to dispersion and Coriolis effects. Ocean Model, 62, 39–55, https://doi.org/10.1016/j.ocemod.2012.11.009.

Kirschbaum, D., Stanley, T., & Zhou, Y. (2015). Spatial and temporal analysis of a global landslide catalog. Geomorphology, 249, 4–15.

Koshimura, S., Mofjeld, H., & Moore, A. (2002). Modeling the 1100 bp paloetsunami in Puget Sound, Washington. Geophysical Research Letters, 29(20), 9, https://doi.org/10.1029/2002GL015170.

Kulikov, E., Rabinovich, A., Thomson, R., & Bornhold, B. D. (1996). The landslide tsunami of November 3, 1994, Skagway Harbor, Alaska. Journal of Geophysical Research, 101(C3), 6609–6615, https://doi.org/10.1029/95JC03562.

Kurkin, A., Belyakov, V., Makarov, V., Zeziulin, D., & Pelinovsky, E. (2016). Methods of tsunami detection and of post-tsunami surveys. Journal of Tsunami Society International, 35(2), 8755-6839.

Løvholt, F., Glimsdal, S., & Harbitz, C. (2020). On the landslide tsunami uncertainty and hazard. Landslides, 17, 2301–2315, https://doi.org/10.1007/s10346-020-01429-z.

Løvholt, F., Pedersen, G., Harbitz, C., Glimsdal, S., & Kim, J. (2015). On the characteristics of landslide tsunamis. Philosophical Transactions of the Royal Society, A373:20140376, https://doi.org/10.1098/rsta.2014.0376.

Leonard, L., Rogers, G., & Mazzotti, S. (2014). Tsunami hazard assessment of Canada. Natural Hazards, 70, 237–274, https://doi.org/10.1007/s11069-013-0809-5.

Lin, C. (2015). Insight into landslide kinematics from a broadband seismic network. Earth, Planets, and Space, 67, 8, https://doi.org/10.1186/s40623-014-0177-8.

Lin, C., Kumagai, H., Ando, M., & Shin, T. (2010). Detection of landslides and submarine slumps using broadband seismic networks. Geophysical Research letters. 37, L22309, https://doi.org/10.1029/2010GL044685.

Lin, C., Liu, S., Lee, S., & Liu, C. (2006). Impacts of the Chi-Chi earthquake on subsequent rainfall-induced landslides in central Taiwan. Engineering Geology, 86, 87–101, https://doi.org/10.1016/j.enggeo.2006.02.010.

Lintern, D., Rutherford, J., Hill, P., Campbell, C., & Normandeau, A. (2020). Towards a national-scale assessment of the subaqueous mass movement hazard in Canada. Geological Society, London, Special Publications, 500, 97–113, https://doi.org/10.1144/SP5002019-205.

Lintern, G., Blais-Stevens, A., Stacy, C., Shaw, J., Bobrowsky, P., Conway, K., Huntley, D., Mackillop, K., Overeem, I., & Scherwath, M. (2019). Providing multidisciplinary scientific advice for coastal planning in Kitimat Arm, British Columbia. In D. G. Lintern, D. C. Mosher, L. G. Moscardelli, P. T. Bobrowsky, C. Campbell, J. D. Chytor, Clague, J., Georgiopoulou, A., Lajeunesse, P., Normandeau, A., Piper, D., Scherwath, M., Stacy, C., & D. Turmel (Eds.), Subaqueous Mass Movements and their Consequences: Assessing Geohazards, Environmental Implications and Economic Significance of Subaqueous Landslides (Vol. 477, p. 477). The Geological Society of London, https://doi.org/10.1144/SP477.40.

Locat, J., Lee, H., ten Brink, U., Twichell, D., Geist, E., & Sansoucy, M. (2009). Geomorphology, stability and mobility of the Currituck slide. Marine Geology, 264(1), 28–40, https://doi.org/10.1016/j.margeo.

Ma, G., Shi, F., & Kirby, J. (2012). Shock-capturing non-hydrostatic model for fully dispersive surface wave processes. Ocean Modelling, 43, 22–35, https://doi.org/10.1016/j.ocemod.2011.12.002, 115.

Madhusudhana, S., Pavan, G., Miller, L., Gannon, W., Hawkins, A., Erbe, C., Hamel, J., & Thomas, J. (2022). Choosing equipment for animal bioacoustic research. Exploring Animal Behavior Through Sound: Volume, 37.

Madsen, P., Fuhrman, D., & Schaffer, H. (2008). On the solitary wave paradigm for tsunamis. Geophysical Research letters, 113, C12012, https://doi.org/10.1029/2008jc004932.

Maeda, T., Obara, K., Shinohara, M., Kanazawa, T., & Uehira, K. (2015). Successive estimation of a tsunami wavefield without earthquake source data: a data assimilation approach toward real-time tsunami forecasting. Geophysical Research letters, 42(19), 7923–7932.

Mahani, A., Kao, H., Walker, D., Johnson, J., & Salas, C. (2016). Performance evaluation of the regional seismograph network in northeast British Columbia, Canada, for monitoring of induced seismicity. Seismological Research Letters, 87(3), 648-660.

Martelloni, G., Segoni, S., Fanti, R., & Catani, F. (2012). Rainfall thresholds for the forecasting of landslide occurrence. Landslides, 9, 485-495.

Masson, D., Harbitz, C., Wynn, R., Pedersen, G., & Løvholt, F. (2006). Submarine landslides: processes, triggers and hazard prediction. Philosophical Transactions of the Royal Society A: Mathematical, Physical and Engineering Sciences, 364(1845), p.2009-2039.

Matsumoto, H., Zampolli, M., Haralabus, G., Stanley, J., Robertson, J., & Meral Özel, N. (2023). Hydroacoustic Signals originating from marine volcanic activity at Kadovar Island, Papua New Guinea, recorded by the comprehensive nuclear-test-ban treaty intnternational monitoring system. Pure and Applied Geophysics, 180(4), 1353–1373, https://doi.org/10.1007/s00024-022-03096-8.

Maynard, D., Weiland, I., Blais-Stevens, A., & Geertsema, M. (2017). Surficial geology, North Kitimat Arm, Douglas Channel area. Canadian Geoscience Map 300 (Preliminary Edition), Geological Survey of Canada, 1:25,000 scale map area, https://doi.org/10.4095/300850.

Melgar, D. (2021). Was the January 26th, 1700 Cascadia earthquake part of a rupture sequence? Journal of Geophysical Research: Solid Earth, 126(10), e2021JB021822, https://doi.org/10.1029/2021JB021822.

Metz, D., Watts, A., Grevemeyer, I., Rodgers, M., & Paulatto, M. (2016). Ultra-long-range hydroacoustic observations of submarine volcanic activity at Monowai, Kermadec Arc. Geophysical Research Letters, 43, 1529–1536, https://doi.org/10.1002/2015GL067.

Miller, D. (1960). The Alaska earthquake of July 10, 1958: giant wave in Lituya Bay. Bulletin of Seismological Society of America, 50 (2), 253-266, https://doi.org/10.1785/BSSA0500020253.

Minh Duc, D., Khang, D., Minh Duc, D., Minh Ngoc, D., Thi Quynh, D., Thi Thuy, D., Hoang Giang, N., Tien, P., & Huu Ha, N. (2020). Analysis and modeling of a landslide-induced tsunami-like wave across the Truong River in Quang Nam province, Vietnam. Landslides, 17(10), 2329–2341, https://doi.org/10.1007/s10346-020-01434-2.

Mofjeld, H., Gonzfilez, F., & Newman, J. (1999). Tsunami prediction in U.S. coastal regions, In Coastal Ocean Prediction, Coastal Estuarine Studies. Ser., vol. 56, edited by C. Mooers, chap. 14, pp. 353–375, AGU, Washington, D. C., doi:10.1029/CE056p0353.

Morgenroth, J. (2016). Elastic stress modelling and prediction of ground class using a Bayesian Belief Network at the Kemano tunnels. MSc Thesis, Civil engineering, University of British Columbia, Vancouver, BC, 212, http://hdl.handle.net/2429/58971.

Mosher, D., Monahan, P., Barrie, J., & Courtney, R. (2004). Coastal submarine failures in the Strait of Georgia, British Columbia: landslides of the 1946 Vancouver Island earthquake. Journal of Coastal Research, 201(1), 277–291, https://doi.org/10.2112/1551-5036(2004)20[277:CSFITS]2.0.CO;2.

Mousavi, S., Ellsworth, W., Zhu, W., Chuang, L., & Beroza, G. (2020). Earthquake transformer—an attentive deep-learning model for simultaneous earthquake detection and phase picking. Nature Communications, 11, 1-12, https://doi.org/10.1038/s41467-020-175.

Mousavi, S., Sheng, Y., Zhu, W., & Beroza, G. (2019). STanford EArthquake Dataset (STEAD): a global data set of seismic signals for AI. IEEE Access, 7, 179464-179476.

Mulligan, R., & Take, W. (2017). On the transfer of momentum from a granular landslide to a water wave. Coastal Engineering, 125, 16–22, https://doi.org/10.1016/j.coastaleng.2017.04.001.

Mulligan, R., Take, W., & Bulldard, G. (2018). Landslide generated tsunamis: new laboratory experiments and theoretical developments. Building Tomorrow's Society, 5.

Murray, C., Jalilian, E., Najeeb, A., Toms, S., & Hossain, T. (2022). High fidelity distributed fiber optic sensing for landslide detection. Proceedings of the 2022 14th International Pipeline Conference. Volume 3: Operations, Monitoring, and Maintenance; Materials and Joining. Calgary, Alberta, Canada. September 26–30, 2022. V003T04A017. ASME, https://doi.org/10.1115/IPC2022-87809.

Murty, T. (1979). Submarine slide-generated water waves in Kitimat Inlet, British Columbia. Journal of Geophysical Research, 84:2–4.

Murty, T., & Brown, R. (1979). The submarine slide of 27 April, 1975 in Kitimat Inlet and the water waves that accompanied the slide. Pacific Marine Science Report 79-11, Institute of Ocean Sciences, Sidney, British Columbia.

Natural Resources Canada. (2021). Canada West Coast Topo-Bathymetric Digital Elevation Model. Canadian Earthquake Database [Dataset]. Canadian Hazards, https://earthquakescanada.nrcan.gc.ca/stndon/NEDB-BNDS/bulletin-en.php.

Nemati, F., Grilli, S., Ioualalen, M., Boschetti, L., Larroque, C., & Trevisan, J. (2019). High-resolution coastal hazard assessment along the French Riviera from co-seismic tsunamis generated in the Ligurian fault system. Natural Hazards, 96, 553–586, https://doi.org/10.1007/s11069-018-3555-x.

Nemati, F., Leonard, L., Thomson, R., Lintern, G., & Kouhi, S. (2023). Numerical modeling of a potential landslide-generated tsunami in the southern Strait of Georgia. Natural Hazards, 117, 2029-2054, https://doi.org/10.1007/s11069-023-05854-w.

Norris, R. (1994). Seismicity of rockfalls and avalanches at three Cascade Range volcanoes; implications for seismic detection of hazardous mass movements. Bulletin of the Seismological Society of America, 84, 1925–1939, https://doi.org/10.1785/BSSA0840061925.

Okal, E. (2003). T waves from the 1998 Papua New Guinea earthquake and its aftershocks: timing the tsunamigenic slump. Pure and Applied Geophysics, 160, 1843–1863.

Okal, E., & Synolakis, C. (2004). Source discriminants for near-field tsunamis. Geophysical Journal International, 158(3), 899-912.

Petley, D. (2022). The landslide blog: The 1 Septemebr 2022 rock avalanche on the Ecstall River in British Columbia, Canada. Retrieved February 19, 2024, from https://blogs.agu.org/landslideblog/2022/09/21/ecstall-river-1/.

Poiata, N., Satriano, C., Vilotte, J., Bernard, P., & Obara, K. (2016). Multiband array detection and location of seismic sources recorded by dense seismic networks. Geophysical Journal International, 205(3), 1548-1573.

Preuss, J., & Hebenstreit, G. (1998). Integrated tsunami-hazard assessment for a coastal community, Grays Harbor, Washington. US Geological Survey professional paper 1560, 2, 517-536.

Rabinovich, A., Thomson, R., & Šepić, J. (2020). Historical tsunamis and other extreme longwave oscillations in the Strait of Georgia with focus on the Institute of Ocean Sciences (Patricia Bay) and Pacific Biological Station (Nanaimo) regions. Canadian Technical Report of Hydrography and Ocean Sciences, Fisheries and Oceans Canada, Institute of Ocean Sciences, Sidney.

Rabinovich, A., Thomson, R., & Hastings, N. (2023). Natural hazards in the Boundary Bay region of the Strait of Georgia: a compilation and summary of observations and numerical modeling studies. Canadian Technical Report Hydrography Ocean Sciences, 366, p44.

Rabinovich, A., Thomson, R., Bornhold, B. F., & Kulikov, E. (2003). Numerical modeling of tsunamis generated by hypothetical landslides in the Strait of Georgia, British Columbia. Pure and Applied Geophysics, 160(7), 1273- 1313, https://doi.org/10.1007/s000240300006.

Rabinovich, A., Thomson, R., Kulikov, E., Bornhold, B., & Fine, I. (1999). The landslide-generated tsunami of November 3, 1994 in Skagway Harbor, Alaska: a case study. Geophysical Research Letters, 26(19), 3009-3012.

Ragland, J., Schwock, F., Munson, M., & Abadi, S. (2022). An overview of ambient sound using Ocean Observatories Initiative hydrophones. The Journal of the Acoustical Society of America, 151(3), 2085-2100.

Rapatz, W., & Murty, T. (1987). Tsunami warning system for the Pacific coast of Canada. Marine Geodesy, 11:2-3, 213-220, https://doi.org/10.1080/15210608709379561.

Roberts, N., Clague, J., Brideau, M., & Ward, B. (2013). Impacts of the 2007 landslide- generated tsunami in Chehalis Lake, Canada. Conference: Second World Landslide Forum At: Rome, Italy, 6: Risk Assessment, Management and Mitigation, doi:10.1007/978-3-642-31319-6-19.

Romano, A., Lara, J., Barajas, G., Di Paolo, B., Bellotti, G., Di Risio, M., Losado, I., & De Girolamo, P. (2019). Numerical modelling of landslide-generated tsunamis with OpenFoam: a new approach. In Coastal Structures Conference 2019, Hannover, Germany, 30 September-2 October 2019, 11, https://doi.org/10.18451/9783-939230-64-9-049.

Ryan, W., Carbotte, S., Coplan, J., O'Hara, S., Melkonian, A., Arko, R., Weissel, R., Ferrini, V., Goodwillie, A., Nitsche, F., Bonczkowski, J., and Zemsky, R. (2009). Global multi-resolution topography synthesis, Geochemistry, Geophysics, Geosystems, 10, Q03014, doi:10.1029/2008GC002332.

Sarlin, W., Morize, C., Sauret, A., Sauret, A., & Gondret, P. (2021). Nonlinear regimes of tsunami waves generated by a granular collapse. Journal of Fluid Mechanics, https://doi.org/10.1017/ jfm.2021.400, 919:R6.

Sassa, S. (2023). Landslides and tsunamis: multi-geohazards. Landslides, 20, 1335–1341, https://doi.org/10.1007/s10346-023-02084-w.

Sassa, S., & Takagawa, T. (2019). Liquefied gravity flow-induced tsunami: first evidence and comparison from the 2018 Indonesia Sulawesi earthquake and tsunami disasters. Landslides, 16(1), 95–200, https://doi.org/10.1007/s10346-018-1114-x.

Schambach, L., Grilli, S., & Tappin, D. (2021). New high-resolution modeling of the 2018 Palu tsunami, based on supershear earthquake mechanisms and mapped coastal landslides, supports a dual source. Frontiers in Earth Science, Sec. Geohazards and Georisks, 8, 598839, https://doi.org/10.3389/feart.2020.598839.

Schambach, L., Grilli, S., Kirby, J., & Shi, F. (2019). Landslide tsunami hazard along the upper US east coast: effects of slide deformation, bottom friction, and frequency dispersion. Pure and Applied Geophysics, 176, 3059–3098, https://doi.org/10.1007/s00024-0181978-7.

Schambach, L., Grilli, S., Tappin, D., Gangemi, M., & Barbaro, G. (2020). New simulations and understanding of the 1908. Messina tsunami for a dual seismic and deep submarine mass failure source. Marine Geology, 421, 106093, https://doi.org/10.1016/j.margeo.2019.106093.

Schlesinger, A., Kukovica, J., Rosenberger, A., Heesemann, M., Pirenne, B., Robinson, J., & and Morley, M. (2021). An earthquake early warning system for southwestern British Columbia. Frontiers in Earth Science, 9:14.

Shan, Z., Wu, H., Ni, W., Sun, M., Wang, K., Zhao, L., Lou, Y., Liu, A., Wei, X., Zheng, X., Guo, X. (2022). Recent technological and methodological advances for the investigation of submarine landslides. Journal of Marine Science and Engineering, 10(11), 1728.

Shi, F., Kirby, J., Harris, J., & Grilli, S. (2012). A high order adaptive time-stepping TVD for Boussinesq modeling of breaking waves and coastal inundation. Ocean Model, 43, 36–51, https://doi.org/10.1016/j.ocemod 2011.12.004.

Shiddiqi, H. A., Ottemöller, L., Rondenay, S., Custódio, S., Halpaap, F., & Gahalaut, V. K. (2023). Comparison of earthquake clusters in a stable continental region: a case study from Nordland, northern Norway. Seismological Research Letters, 94 (3), 1627.

Skvortsov, A., & Bornhold, B. (2007). Numerical simulation of the landslide-generated tsunami in Kitimat Arm, British Columbia, Canada, 27 April 1975. Journal of Geophysical Research, 112(F02):028, https://doi.org/10.1029/2006JF000499.

Sobie, S. (2020). Future changes in precipitation-caused landslide frequency in British Columbia. Climatic Change, 162, 465–484, https://doi.org/10.1007/s10584-020-02788-1.

Stacey, C. D., Lintern, D. G., Shaw, J., & Conway, K. W. (2020). Slope stability hazard in a fjord environment: Douglas Channel, Canada. Geological Society, London, Special Publications, 500, 427-451, https://doi.org/10.1144/SP500-2019-191.

Stacey, C., Hill, P., Talling, P., Enkin, R., Hughes Clarke, J., & Lintern, D. (2019). How turbidity current frequency and character varies down a fjord-delta system: combining direct monitoring, deposits and seismic data. Sedimentology, 66(1), 1-31, https://doi.org/10.1111/sed.12488.

Stasiuk, M., Hickson, C., & Mulder, T. (2003). The vulnerability of Canada to volcanic hazards. Natural Hazards, 28, 563-589.

Stephenson, F., & Rabinovich, A. (2009). Tsunamis on the Pacific coast of Canada recorded in 1994–2007. Pure applied geophysics., 166, 177–210, https://doi.org/10.1007/s00024-008-0440-7.

Sugawara, D. (2021). Numerical modeling of tsunami: advances and future challenges after the 2011 Tohoku earthquake and tsunami. Earth-Science Reviews, 214, 103498, https://doi.org/10.1016/j.earscirev.2020.103498.

Suleimani, E., Combellick, R., Marriott, D., Hansen, R., Venturato, A., & Newman, J. (2005). Tsunami hazard maps of the Homer and Seldovia areas, Alaska. Report of Investigations 2005-2, Published by State of Alaska, Department of Natural Resources, Division of Geological and Geophysical Survey, 33, 2 sheets, scale 1:12,500, https://doi.org/10.14509/14474.

Sumner, E., & Paull, C. (2014). Swept away by a turbidity current in Mendocino submarine canyon, California. Geophysical Research Letters, 41(21), p.7611-7618.

Suriñach, E., Vilajosana, I., Khazaradze, G., Biescas, B., Furdada, G., & Vilaplana, J. (2005). Seismic detection and characterization of landslides and other mass movements. Natural Hazards and Earth System Sciences, 5 (6), 791-798, https://doi.org/10.5194/nhess-5-791-2005.

Talandier, J., & Okal, E. (1998). On the mechanism of conversion of seismic waves to and from T waves in the vicinity of island shores. Bulletin of the Seismological Society of America, 88(2), 621–632.

Talandier, J., Hyvernaud, O., Hébert, H., Maury, R., & Allgeyer, S. (2020). Seismic and hydroacoustic effects of the May 29, 2010 submarine South Sarigan volcanic explosion: energy release and interpretation. Journal of Volcanology and Geothermal Research, 394(0377-0273), 106819, https://doi.org/10.1016/j.jvolgeores.2020.106819.

Talling, P., Wynn, R., Masson, D., Frenz, M., Cronin, B., Schiebel, R., Akhmetzhanov, A., Dallmeier-Tiessen, S., Benetti, S., Weaver, P., Georgiopoulou, A., & Zühlsdorff, C. & Georgiopoulou, A. (2007). Onset of submarine debris flow deposition far from original giant landslide. Nature, 450(7169), p. 541-544.

Tan, F., Kao, H., Nissen, E., & Visser, R. (2020). Tracking earthquake sequences in real time: application of Seismicity-Scanning based on Navigated Automatic Phase-picking (S-SNAP) to the 2019 Ridgecrest, California sequence. Geophysical Journal International, 223(3), 1511-1524, https://doi.org/10.1093/gji/ggaa387.

Tannant, D., & Morgenroth, J. (2020). Kemano Project–70 Years of Development. Conference: GeoVertual 2020, Resilience and Innovation, 6, https://www.researchgate.net/publication/348606733.

Tappin, D., & Grilli, S. (2021). The continuing underestimated tsunami hazard from submarine landslides. In: Sassa, K., Mikoš, M., Sassa, S., Bobrowsky, P.T., Takara, K., Dang, K. (eds) Understanding and Reducing Landslide Disaster Risk. WLF 2020, ICL Contribution to Landslide Disaster Risk Reduction. Springer, Cham, https://doi.org/10.1007/978-3-030-60196-6.

Tehranirad, B., Kirby, J., Ma., G., & Shi, F. (2012). Tsunami benchmark results for non-hydrostatic wave model NHWAVE (version 1.0). Research Report:CACR-12-03, Center for Applied Coastal Research, University of Delaware, Newark, 43.

ten Brink, U., Geist, E., & Andrews, B. (2006). Size distribution of submarine landslides and its implication to tsunami hazard in Puerto Rico. Geophysical Research Letters, 33(11).

Tepp, G., & Dziak, R. (2021). The seismo-acoustics of submarine volcanic eruptions. Journal of Geophysical Research: Solid Earth, 126, e2020JB020912, https://doi.org/10.1029/2020JB020912.

Tepp, G., Chadwick, W., Haney, M., Lyons, J., Dziak, R., Merle, S., Butterfeild, D., & Young III, C. (2019). Hydroacoustic, seismic, and bathymetric observations of the 2014 submarine eruption at Ahyi Seamount, Mariana Arc. Geochemistry, Geophysics, Geosystems, 20, 3608–3627, https://doi.org/10.1029/2019GC008311.

Thomson, R., Fine, I., Krassovski, M., Cherniawsky, J., Conway, K., & Wills, P. (2012). Numerical simulation of tsunamis generated by submarine slope failures in Douglas Channel, British Columbia. Department of Fisheries and Oceans, Canadian science advisory research document, 115, 38.

Tinti, S. (2003). Needs and perspectives of tsunami research in Europe. In: Yalçiner A.C., Pelinovsky E.N., Okal E., Synolakis C.E. (eds) Submarine Landslides and Tsunamis. NATO Science Series (Series IV: Earth and Environmental Sciences), vol 21. Springer, Dordrecht, https://doi.org/10.1007/978-94-010-0205-9_2.

Tinti, S., Maramai, A., Armigliato, A., Graziani, L., Manucci, A., Pagnoni, G., & Zaniboni, F. (2005). Observations of physical effects from tsunamis of December 30, 2002 at Stromboli volcano, southern Italy. Bulletin of volcanology, 68, 450-461, https://doi.org/10.1007/s00445-005-0021-x.

Tolstoy, I., & Ewing, M. (1950). The T phase of shallow-focus earthquakes. Bulletin of the Seismological Society of America, 40(1), 25–51.

Tolstoy, M., Cowen, J., Baker, E., Fornari, D., Rubin, K., Shank, T., & et, a. (2006). A sea-floor spreading event captured by seismometers. Science, 314(5807), 1920–1922, https://doi.org/10.1126/science.1133950.

Torres, M., & Nadal-Caraballo, N. (2021). Rapid tidal reconstruction with UTide and the ADCIRC tidal database. StormSim: metamodelling of coastal storm hazards for parabolistic applications; ERDC SR-21-3; US Army Corps of Engineers, Engineer Research and Developm Center: Vicksburg, MS, USA.

Tsai, Y. B., & Wu, H. (1997). A study of the errors in locating earthquakes due to the geometry of the Taiwan seismic network. Terrestrial Atmospheric and Oceanic Sciences, 8, 355–370. doi:10.3319/TAO.1997.8.3.355(T).

Uhira, K., Yamasato, H., & Takeo, M. (1994). Source mechanism of seismic waves excited by pyroclastic flows observed at Unzen Volcano, Japan. Journal of Geophysical Research, 99, 17757–17773, https://doi.org/10.1029/94JB00110.

Van Zeyl, D. P., Stead, D., Sturzenegger, M., Bornhold, B. D., & Clague, J. J. (2015). Structure, stability, and tsunami hazard associated with a rock slope in Knight Inlet, British Columbia. Natural Hazards and Earth System Sciences, 15(6), 1425–1436, https://doi.org/10.5194/nhess-15-1425-2015.

Vancouver Fraser Port Authority. (2020). Guidelines: shoreline protection (Vancouver Harbour), inspection, maintenance, design and repair, Version 1.0. Engineering and Maintenance Department, Part of Vancouver, 42, https://www.portvancouver.com/wp-content/uploads/2020/01/WEB-COPY-317071-16152-00-MA-REP-0003_R1.pdf.

Verbovšek, T., Košir, A., Teran, M., Zajc, M., & Popit, T. (2017). Volume determination of the Selo landslide complex (SW Slovenia): integrating field mapping, ground penetrating radar and GIS approaches. Landslides, 14, 1265-1274, https://doi.org/10.1007/s10346-017-0815-x.

Viola, C., Verdon-Kidd, D., Hanslow, D., Maddox, S., & Power, H. (2021). Long-term dataset of tidal residuals in New South Wales, Australia. Data, 6(10), 101, https://doi.org/10.3390/data6100101.

Wall, C. C., Haver, S. M., Hatch, L., Miksis-Olds, J., Bochenek, R., Dziak, R. P., & Gedamke, J. (2021). The next wave of passive acoustic data management: how centralized access can enhance science. Frontiers in Marine Science, 8, 703682, https://doi.org/10.3389/fmars.2021.703682.

Walter, T., Haghshenas Haghighi, M., Schneider, F., Coppola, D., Motagh, M., Saul, Babeyko, A., Dahm, T., Troll, V., Tilmann, F., Heimann, S., Valade, S., Triyono, R., Khomarudin, R., Kartadinata, N., Laiolo, M., Massimetti, F., & Gaebler, P. (2019). Complex hazard cascade culminating in the Anak Krakatau sector collapse. Nature Communications, 1–11.

Wang, J., Xiao, Z., Liu, C., Zhao, D., & Yao, Z. (2019). Deep learning for picking seismic arrival times. Journal of Geophysical Research: Solid Earth, 124(7), 6612–6624, https://doi.org/10.1029/2019JB017536.

Wang, Y., Heidarzadeh, M., Satake, K., Mulia, I., & Yamada, M. (2020). A tsunami warning system based on offshore bottom pressure gauges and data assimilation for Crete Island in the Eastern Mediterranean Basin. Journal of Geophysical Research: Solid Earth 125, no. 10 (2020): e2020JB020293, https://doi.org/10.1029/2020JB020293.

Warwick, R., Williams-Jones, G., Kelman, M., & Witter, J. ( 2022). A scenario-based volcanic hazard assessment for the Mount Meager Volcanic Complex, British Columbia. Journal of Applied Volcanology, 11 (1), 5, https://doi.org/10.1186/s13617-022-00114-1.

Watts, P., Grilli, S., Tappin, D., & Fryer, G. (2005). Tsunami generation by submarine mass failure. II: predictive equations and case studies. Journal of Waterway, Port, Coastal, and Ocean Engineering, 131(6), 298–310, https://doi.org/10.1061/(ASCE)0733-950X(2005)131:6(298).

Westmar. (2005). Tsunami probability and magnitude study, summary report. Report to Village of Lions Bay, Lions Bay (Report No.: 05670).

Westra, S., Fowler, H., Evans, J., Alexander, L., Berg, P., Johnson, F., Kendon, E., Lenderink, G., & Roberts, N. (2014). Future changes to the intensity and frequency of short-duration extreme rainfall. Reviwes of Geophysics, 52(3):2014RG000464.

Whitmore, P., Benz, H., Bolton, M., Crawford, G., Dengler, L., Fryer, G., Goltz, J., Hansen, R., Kryzanowski, K., Malone, S., Oppenheimer, D., Petty, E., Rogers, G., & Wilson, J. (2008). NOAA/West Coast and Alaska tsunami warning center Pacific Ocean response criteria. Science of Tsunami Hazards, 27(2), 1–19, http://pubs.er.usgs.gov/publication/70010016.

Widiyanto, W., Hsiao, S., Chen, W., Santoso, P., Imananta, R., & Lian, W. (2020). Run-up, inundation, and sediment characteristics of the 22 December 2018 Sunda Strait tsunami, Indonesia. Natural Hazards and Earth System Sciences, 20(4), 933-946, https://doi.org/10.5194/nhess-20-933-2020.

Williamson, A., Melgar, D., Crowell, B., Arcas, D., Melbourne, T., Wei, Y., & Kwong, K. (2020). Toward near-field tsunami forecasting along the Cascadia subduction zone using rapid GNSS source models. Journal of Geophysical Research: Solid Earth, 125, e2020JB019636, https://doi.org/10.1029/2020JB019636.

Wright, I., Chadwick, W., de Ronde, C., Reymond, D., Hyvernaud, O., Gennerich, H., & Bannister, S. (2008). Collapse and reconstruction of Monowai submarine volcano, Kermadec arc, 1998–2004. Journal of Geophysical Research, 113, B08S03, doi:10.1029/2007JB005138.

Yavari-Ramshe, S., & Ataie-Ashtiani, B. (2017). Subaerial landslide-generated waves: numerical and laboratory simulations. Sassa, K., Mikoš, M., Yin, Y. (eds) Advancing Culture of Living with Landslides. WLF 2017. Springer, Cham, https://doi.org/10.1007/978-3-319-59469-9_3.

Yin, Y., Huang, B., Chen, X., Liu, G., & Wang, S. (2015). Numerical analysis on wave generated by the Qianjiangping landslide in Three Gorges Reservoir, China. Landslides, 12(2), 355–364, https://doi.org/10.1007/s10346-015-0564-7.

Youd, T. (1978). Major cause of an earthquake damage is ground failure. Civil Engineering, 48(4), 6.

Zhang, C., Kirby, J., Shi, F., Ma, G., & Grilli, S. (2021b). A two-layer nonhydrostatic landslide model for tsunami generation on irregular bathymetry. 1. Theoretical basis. Ocean Model, 159, 101749, https://doi.org/10.1016/j.ocemod.2020.101749.

Zhang, X., Chen, H., Zhang, W., Tian, X., & Chu, F. (2021a). Generalized neural network trained with a small amount of base samples: Application to event detection and phase picking in downhole microseismic monitoring. Geophysics, 86(5), KS95-KS108.

Zhu, W., & Beroza, G. (2019). PhaseNet: A deep-neural-network-based seismic arrival-time picking method. Geophysical Journal International, 216(1), 261-273.